Imperial College London

Metal Oxide Semiconductors Employed as Photocatalysts during Water Splitting

Federico M Pesci

Department of Chemistry

Imperial College London

Supervisor: David R Klug

Thesis Submitted for Degree of Doctor of Philosophy

I hereby declare that the material contained in this thesis is the result of my own work except when specific reference is made. This manuscript does not exceed 100 000 words and has not been submitted in whole or in part of a degree at this or any other university.

Federico M Pesci

July 2014

"Where vegetation is rich, photochemistry may be left to the plants and by rational cultivation solar radiation may be used for industrial purposes. In the desert regions, unadapted to any kind of cultivation, photochemistry will artificially put their solar energy to practical uses.

On the arid lands there will spring up industrial colonies without smoke and without smokestacks; forests of glass buildings will rise everywhere; inside of these will take place the photochemical processes that hitherto have been the guarded secret of the plants, but that will have been mastered by human industry which will know how to make them bear even more abundant fruit than nature, for nature is not in a hurry and mankind is. And if in a distant future the supply of coal becomes completely exhausted, civilization will not be checked by that, for life and civilization will continue as long as the sun shines!" [1]

Giacomo Ciamician
The Photochemistry of the Future
Science, September 1912

Abstract

Photocatalytic water splitting has attracted significant interest in recent decades as it offers a clean and environmentally friendly route for the production of hydrogen. A key challenge remains the development of systems that employ abundant, non-toxic and inexpensive materials to dissociate water efficiently using sunlight. Titanium dioxide (TiO_2), tungsten trioxide (WO_3) and hematite (α-Fe_2O_3) are among the most studied photoanodes employed during water splitting because of the position of their valence band which is suitable for oxidising water to oxygen, and their low costs. However reported efficiencies for these materials are below the reported theoretical maximum values. A good understanding of the factors that are limiting the efficiency of these photoanodes is therefore desirable if improvements in the photocatalytic activity are to be achieved.

This thesis is divided in four main sections. Chapters 3 and 4 describe transient absorption spectroscopy (TAS) studies in the microsecond-second timescales carried out on WO_3 photoelectrodes and TiO_2 nanowires respectively. TAS has been employed to follow the charge carriers dynamics in WO_3 highlighting the presence of relatively long-lived holes (30 ms), which have been described as a requirement for the water oxidation reaction to take place. The electrons also appear to be long-lived (0.1 s), and this has been proposed to be due to slow electron transport through the film. TAS measurements have also been carried out on oxygen-deficient hydrogen-treated TiO_2 nanowires, highlighting a more efficient suppression of the electron/hole recombination process in comparison with conventional anatase TiO_2 photoanodes.

Chapter 5 describes TAS and sum frequency generation (SFG) studies on TiO_2 films which are designed to investigate the surface mechanisms of water oxidation. The dependence of the hole lifetime on the pH of the electrolytes employed has been examined by TAS and substantially faster decay rates have been found in highly alkaline solutions suggesting a change in the mechanism of water oxidation. Consequently, SFG has been employed in order to detect any possible intermediate at the interface TiO_2/water. Initial measurements have provided the evidence of physisorbed and chemisorbed methanol (model probe) on the TiO_2 surface and further studies at the TiO_2/water interface have been carried out.

Chapter 6 describes the development of a hybrid solar fuel reactor coupling a α-Fe_2O_3 based photoelecrochemical cell with luminescent solar concentrator plates. Initial tests have been carried out on a proof of principle prototype providing encouraging results.

Acknowledgments

First of all I would like to thank my supervisor Professor David Klug for his support and guidance over the duration of this PhD project. Thanks also to Professor James Durrant for his copious suggestions given during several meetings. A special thanks goes to Dr Alex Cowan for his precious help in the lab, his numerous advices and suggestions and for sharing with me his extensive knowledge. Thanks also to Dr Chris Barnett and Dr Fred Fournier for their indispensable help with the lab equipments.

Also thanks to Dr Xiaoe Li, Dr Bruce Alexander, Dr Anna Hankin and Prof Yat Li for providing me the samples used over the course of this project and to Dr Amanda Chatten, Martyn Fisher and Jose Videira for the help in the development of the solar fuel reactor.

I am really grateful to all the member of the solar fuel group for the constructive discussions and suggestions given over these years.

Last but not least, a special thank goes to my mum and dad, for their precious and unique support and guidance given to me over the course of my life. I will never lose sight of the values that you have taught me.

Table of Contents

List of Figures

List of Symbols and abbreviations

A	Absorbance
α	Hyperpolarisability of first order
ABPE	Applied-Bias Photon-to-current Efficiency
APCE	Absorbed Photon-to-Current Efficiency
β	Hyperpolarisability of second order
CB	Conduction Band
c	Speed of light
γ	Hyperpolarisability of third order
D	Electron diffusion coefficient
DSSC	Dye Sensitised Solar Cells
E	Electric field
EE	Electrode/Electrolyte illumination (front side illumination)
E_{CB}	Energy position of the Conduction Band
E_F	Energy position of the Fermi level
E_g	Band gap energy
e^-	Electron
e_0	Elemental charge (1.602×10^{-19} C)
ε	Dielectric constant
ε_0	Permittivity of the free space
η	Efficiency
F	Flux gain
FQY	Fluorescence Quantum Yield
$\Delta\varphi_{SC}$	Potential drop across the depletion layer
G	Geometrical gain
h	Plank constant
I	Intensity
i	current density
IPCE	Incident Photon-to-Current Efficiency
λ	Wavelength
J_{OP}	Current in Operational Conditions

LMA	Lauryl methacrilate
LSC	Luminescent Solar Concentrator
mp	Mesoporous
μ	Electric dipole
nc	Nanocrystalline
OD	Optical Density
P	Polarisation
PEC	Photoelectrochemical
PEEK	Polyether ether ketone
PMMA	Polymethylmetacrylate
PV	Photovoltaic
RHE	Reversible Hydrogen Electrode
SCL	Space-Charge Layer
SCLJ	Semiconductor/Liquid Junction
SE	Substrate/Electrolyte side illumination (back side illumination)
SFG	Sum Frequency Generation
STH	Solar-to-Hydrogen Efficiency
TAS	Transient Absorption Spectroscopy
TIR	Total Internal Reflection
TPC	Transient Photocurrent
U_{OP}	Potential in operational conditions
V	Potential
VB	Valence Band
V_{OC}	Open Circuit potential
ω	Space charge width
ω_{IR}	Infrared frequency
ω_{Vis}	Visible frequency
W	Electrode thickness
χ	Susceptibility

List of Publications

"Charge Carrier Dynamics on mesoporous WO_3 during Water Splitting"

Pesci, F. M., Cowan, A. J., Alexander, B.D., Durrant, J. R. and D. R. Klug

The Journal of Physical Chemistry Letters, **2011**, *2*, 15, 1900-1903

"Efficient Suppression of Electron–Hole Recombination in Oxygen-Deficient Hydrogen-Treated TiO_2 Nanowires for Photoelectrochemical Water Splitting"

Pesci, F. M., Wang, G., Klug, D. R., Li, Y. and A. J. Cowan

The Journal of Physical Chemistry C, **2013**, *117*, 48, 25837-25844.

"Interfacial Charge Separation in Cu_2O/RuO_x as Visible Light Driven CO_2 Reduction Catalyst"

Pastor, E., Pesci, F. M., Reynal, A., Handoko, A. D., Guo, M., An, X., Cowan, A. J., Klug, D. R., Durrant, J. R. and J. Tang

Physical Chemistry Chemical Physics, **2014**, *16*, 13, 5922-5926.

Chapter I

Theory and Background

In this chapter the theory behind photoelectrochemical water splitting is introduced. The electronic processes occurring at the semiconductor/electrolyte interface are discussed and an overview of the principles of operation of the techniques employed during the course of this project is provided.

1.1 Theory of Photoelectrochemical Water Splitting

A rapid increase in the concentrations of greenhouse gasses and concerns over the reserves of fossil fuels have led part of the scientific community to research technologies based on renewable and carbon free form of energy.

The annual incident solar radiation on the earth's surface (120 000 TW of electromagnetic radiation) is far in excess of the current consumption levels,[2] however given the intermittent nature of solar energy at ground level, to realise the potential of this vast energy resource, efficient energy conversion and storage technologies have to be developed.

Photoelectrochemical water splitting to produce oxygen and hydrogen has the potential to be a clean and environmentally sustainable route for the production of solar hydrogen. However, to realise this goal, efficient photo-active mediums based upon abundant, non-toxic and accessible raw materials need to be developed. Metal oxide semiconductor photoelectodes have attracted interest since the 1970s, following a pivotal series of papers from Honda and Fujishima[3], and previously Boddy,[4] on the use of TiO_2 for photoelectrochemical water oxidation. Since these early works a wide range of materials have been investigated with particular interest in large band gap semiconductors such as TiO_2, α-Fe_2O_3 and WO_3 because of their band energies which are suitable for the evolution of O_2 and their stability under conditions in which photoelectrochemical water oxidation occurs and these are described in several comprehensive reviews.[5-7] However, the large band gap of TiO_2 and, to a lesser extent, WO_3 and α-Fe_2O_3, limits the maximum Solar energy-To-Hydrogen (STH) efficiencies achievable (TiO_2= 1.3 %, WO_3 = 4.8 %, α-Fe_2O_3 = 12.9%, *Figure 1.1*).[8,9]
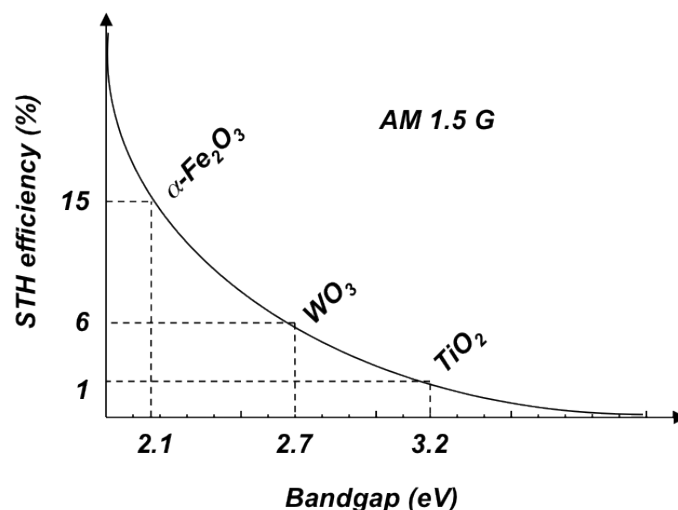
Figure 1.1:   *Theoretical solar to hydrogen (STH) efficiency versus band gap for TiO_2, a-Fe_2O_3 and WO_3. Figure adapted from reference 9.*

Nonetheless, the actual STH values determined experimentally are still significantly below those required for an economically viable device.[10] Therefore in the last 40 years the synthesis of new materials and the surface modifications of existing semiconductors have been widely investigated with the aim of increasing their efficiency.[5-7,11]

A more limited number of fundamental studies have also been carried out in order to understand the mechanisms involved during photo-assisted water splitting and define the factors which are limiting the efficiency of the materials currently employed.[12-16] A deeper understanding of these factors would allow researchers to accurately engineer new and more efficient materials.

In order to discuss the experiments reported in this thesis it is necessary to first introduce the general theory behind photoelectrochemical water splitting and the techniques used to investigate water splitting on metal oxide semiconductors. Towards the end of this introductive chapter a discussion of the practical development of water splitting reactors is also reported.

1.1.1 Semiconductor/Electrolyte Interface

A description of the electronic processes occurring at the interface between a semiconductor and an electrolyte is fundamental in order to understand the chemistry behind the electrochemical processes discussed during the course of this thesis. When a semiconductor is placed in contact with an electrolyte a potential difference is established.[17-22] In an n-type semiconductor (such as TiO_2, WO_3 and α-Fe_2O_3), the Fermi level is generally higher than the redox potential of an aqueous electrolyte, therefore, to equalise their energies and reach electronic equilibrium, electrons are transferred from the electrode into solution causing an electric current to flow across the junction. This electron transfer causes the valence and conduction bands to bend upward and the concentration of the electrons at the surface is reduced in comparison to the bulk of the semiconductor, forming what is known as depletion or space-charge layer (SCL), *Figure 1.2*. The electron transfer also leads to the formation of an electric field in the electrolyte at the semiconductor liquid junction (SCLJ), however the higher charge density typically limits its width to less than 150 nm (for a WO_3 based electrode).[23] The width of the depletion layer within the semiconductor electrode (Equation 1.1) depends on its charge density ($e_0\,N_D$),

$$\omega = \sqrt{\Delta\varphi_{SC}\,\frac{2\varepsilon\varepsilon_0}{e_0 N_D}} \qquad\qquad \text{Eq. 1.1}$$

Where ω is the width of the depletion layer, $\Delta\varphi_{SC}$ the potential drop across it, ε the dielectric constant of the semiconductor, ε_0 the permittivity of free space, e_0 the elemental charge and N_D the donor density of the semiconductor, for instance the dopant concentration. This equation is very similar to the Mott-Schottky equation for a

semiconductor-metal interface[17-18] and in both cases a decrease in the donor density leads to an increase in the width of the SCL. *Figure 1.2* shows the band bending occurring in a n-type semiconductor when electronic equilibrium is reached (E_F and E_{Redox} are equal).
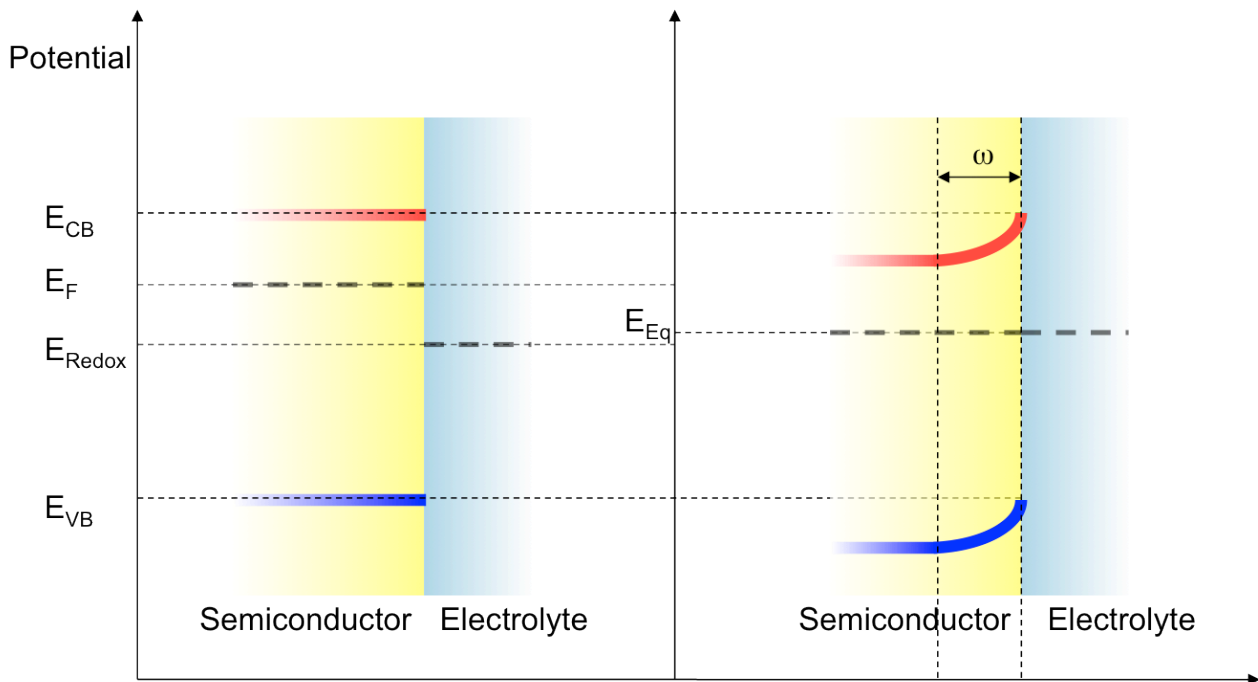
Figure 1.2: Semiconductor-electrolyte junction. The electronic equilibrium (E_{Eq}) is reached when the energy of the Fermi level (E_F) in the semiconductor is equal to the redox potential of the electrolyte (E_{Redox}). ω represents the width of the space charge layer which is the region in which the charge distribution differs from the bulk material. The separation of the charge carriers leads to band bending across the space charge layer, resulting in the electrons having higher energy at the surface than in the bulk.

The formation of a significant electric field at the SCLJ requires the size of the semiconductor particles to be bigger than the SCL width. Over the past few decades there has been interest in the use of nanostructured (nc) and mesoporous (mp) materials because the small size of their particles leads to a very high surface area, enabling the generation of a higher concentration of charges close to the SCLJ.[17-19,24] The

nanostructuring can lead to a large contact area at the electrode/electrolyte junction and to a very small or even non-existent space-charge layer at the interface, due to the fact that the material become fully depleted with only a minimal voltage drop.

If a photon of energy higher than the E_g (energy gap between valence and conduction bands) hits a semiconductor, a valence band (VB) electron can be excited into the conduction band (CB) with the consequent generation of an electron-hole pair. In the case of an n-type semiconductor with sufficient domain size to maintain a large internal electric field, the pair is separated in the space-charge region by the electric field, which minimises the chance of recombination. The electron then moves toward the bulk of the semiconductor while the hole is swept towards the surface of the electrode where it can accept an electron from a reduced species. Under steady state illumination there is a situation of non-equilibrium between the quasi Fermi levels of holes and electrons (which describe the electrochemical potential of one charge carrier at a time). The voltage generated at the semiconductor/electrolyte junction by the difference in electron and hole quasi Fermi levels is known as the open circuit potential (V_{oc}). *Figure 1.3* shows an outline of the generation of a photogenerated charge pair in an n-type semiconductor under steady state irradiation.
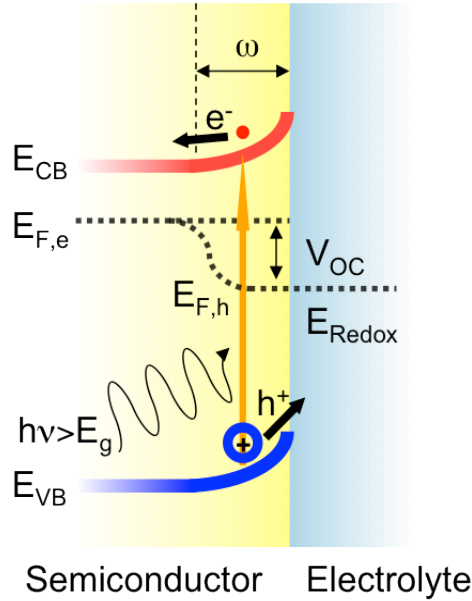
Figure 1.3: *Charge carriers separation in an n-type semiconductor. When a photon with energy greater than E_g hits the semiconductor an electron/hole pair is generated. The electrons move toward the bulk of the semiconductor while the holes move to the solution. E_{VB} and E_{CB} represent the energies of the valence and conduction band respectively. $E_{F,e}$ and $E_{F,h}$ are the energies of the quasi-Fermi levels of electrons and holes whose difference describes the open circuit potential (V_{OC}).*

In an ideal metal oxide semiconductor whose valence and conduction band edges straddle the water oxidation and reduction potentials, the holes in the valence band can act as oxidising species, leading to oxygen production, and the electrons in the conduction band can act as reducing species, leading to hydrogen evolution, as described in the following equations:

$$2H_2O + 4h^+ \rightarrow O_2 + 4H^+ \qquad (+1.23 \text{ V vs RHE}) \qquad \text{Eq. 1.2}$$

$$4H^+ + 4e^- \rightarrow 2H_2 \qquad (0 \text{ V vs RHE}) \qquad \text{Eq. 1.3}$$
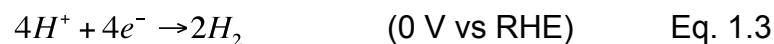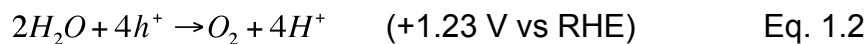
To give the overall reaction expressed by equation 1.4:

$$2H_2O \rightarrow 2H_2 + O_2 \quad (\text{+1.23 V vs RHE}) \qquad \text{Eq. 1.4}$$

Where the redox potentials are expressed versus the reversible hydrogen electrode (RHE).

From the equations reported above, it is noted that a suitable metal oxide semiconductor must meet certain requirements in order to be employed in photocatalytic water splitting. These requirements include a value of the band gap energy higher than the Gibbs free energy required to dissociate water (1.23 V), but at the same time low enough to allow an efficient absorption of the sunlight. In reality, however, taking into account all the possible energy losses, the practical lower limit is often quoted to be closer to 2.5 V.[25] Furthermore, equation 1.2 shows that the production of an oxygen molecule requires the presence of four holes, recalling the natural water splitting mechanism occurring during photosynthesis; evidence of this has been given by Tang *et al.* in 2008.[16]

A system in which both water oxidation and proton reduction occurs in the same semiconductor particle in the absence of an additional applied electrical field, is commonly known as photocatalytic system and I will also employ this terminology throughout this thesis. Semiconductor photocatalytic approaches are of significant interest given the potential low costs of the materials involved. However the limited subset of materials that are active for both water oxidation and reduction under visible light, combined with the potential hazards involved with the simultaneous evolution of oxygen and hydrogen, has led many groups to explore photoassisted, or photoelectrochemical (PEC), systems.[11] In a PEC system, the application of an external bias to a semiconductor electrode material is required in order to achieve water splitting.[19] In the experiments discussed in this thesis,

the oxygen is evolved at the semiconductor photoanode with the hydrogen produced at a separate, typically platinum, counter electrode (cathode). *Figure 1.4* shows the band position for some of the most studied semiconductors in contact with an aqueous electrolyte at pH 1.
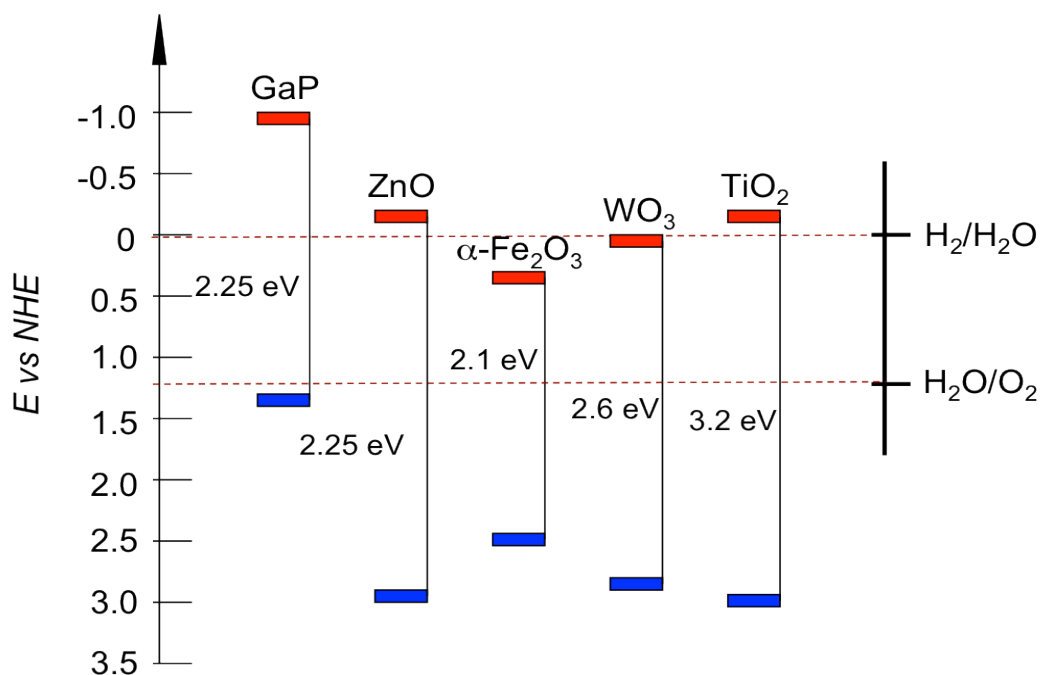
Figure 1.4: *Band positions for some of the most common metal oxide semiconductors in contact with aqueous electrolyte at pH 1. The band gaps are expressed in electron volts and the band energy is expressed versus the Normal Hydrogen Electrode (NHE). Figure adapted from reference 19.*

As it can be seen in TiO_2, WO_3 and α-Fe_2O_3 the valence band sits well below the redox potential of the H_2O/O_2 couple (with values close to the practical lower limit of 2.5 V) making water oxidation viable. Whereas the conduction band and, therefore, the Fermi level of α-Fe_2O_3 and WO_3 sits at lower (more positive) potential than the redox potential of the H^+/H_2 couple. For this reason these materials are usually employed in PEC cells in

which the application of an external bias is required in order to drive the proton reduction at the counter electrode.

1.1.2 Photoelectrochemical (PEC) Cells

In a dual band gap PEC cell the, anode and the cathode are both light absorbers and are an n-type and p-type semiconductors respectively, whilst in a single band gap configuration the anode or the cathode consists of a semiconductor which can adsorb photons and the other electrode is usually a metal. During the course of this thesis a three electrode, single band gap PEC cell consisting of a semiconductor photoanode, a Pt counter electrode and a commercial Ag/AgCl (3 M KCl) reference electrode has been used, *Figure 1.5*.
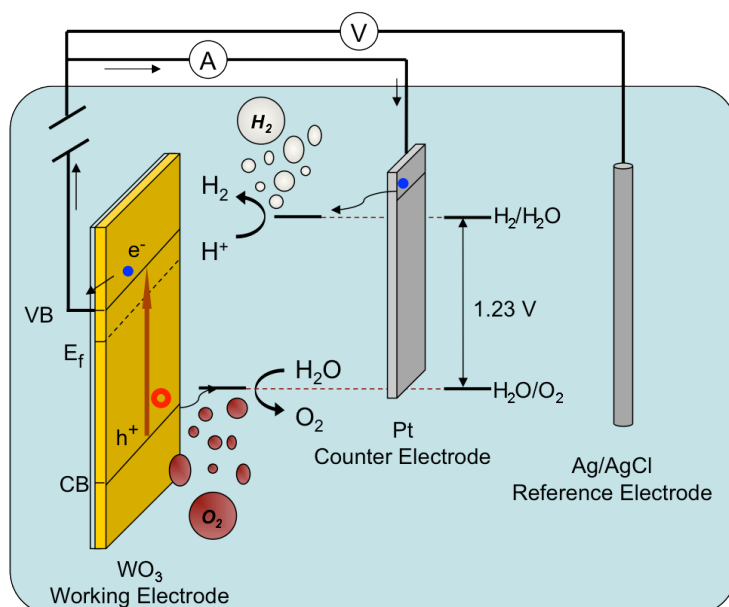
Figure 1.5*: **Pictorial representation of the principle of operation of a three electrode PEC cell. After charge carrier photogeneration the holes in the VB oxidise water, whereas the CB electrons are moved to the counter electrode by the application of a positive bias and reduce protons into hydrogen.***

Following the photo-generation of charge carriers, the application of an external electric bias between working and reference electrodes leads to a change in the position of the Fermi level in the bulk of the semiconductor.[19] In this situation conduction band electrons flow to the counter electrode where they can act as reducing species while the valence band holes can act as oxidising species. In the case of photoassisted water splitting, the reactions of water oxidation and proton reduction take place at the working and counter electrodes respectively.

Four main processes involving the photogenerated charge carriers in a PEC cell are now considered:

i) Electron/hole pair generation following the absorption of a photon of suitable energy.

ii) Charge carrier transport (holes toward the semiconductor surface and electrons toward the semiconductor bulk then to the counter electrode)

iii) Chemical reaction between charge carriers and surface species.

iv) Recombination between electrons and holes.

If the chemical reaction with the surface species is fast enough or if charge carrier separation and transport is very efficient, the step which determines the rate of the whole water splitting process is the generation of the charge carriers.

Figure 1.6 provides an illustration of a typical current/voltage plot for a n-type photoanode with domain sizes suitable for maintaining a significant voltage drop at the SCLJ. Under a moderate applied external anodic bias in the dark, the current at the semiconductor/electrolyte junction is minimal and it is known as dark current (black trace, regions I, II). As the anodic potential (in the dark) is increased further, a sharp increase in

current is observed, correlating to the onset of electrocatalytic water oxidation (black trace region III).

The flatband potential is defined as the potential at which the semiconductor has no depletion layer, for example when the electrode is under intense illumination and in the absence of an additional electrical input. At potentials close to the flatband potential and under illumination (region I red trace), no photocurrent is present as rapid electron hole recombination prevents its generation. As the applied bias is increased from the photocurrent onset potential (region II), the width and depth of the space charge layer increases enabling improved charge carriers separation efficiency. This leads to the presence of suitably long-lived electrons and holes to allow the transport and utilisation of charges to compete with recombination, and the photocurrent rises until it reaches a plateau. In the plateau regions (region III), the efficiency of charge separation for electron/hole pairs generated within the space charge layer is very high and the photocurrent becomes limited by the light intensity and the ability to generate charge carriers close to the SCLJ.
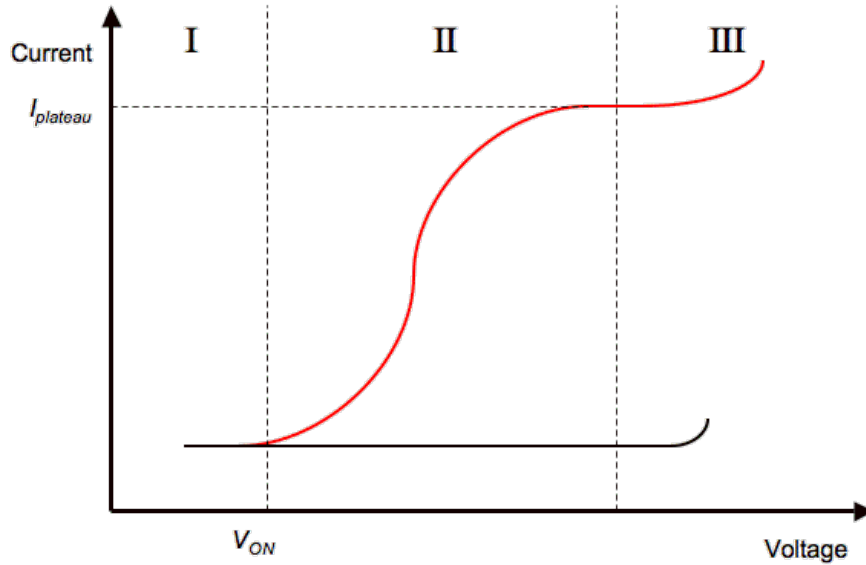
Figure 1.6: *Example of an I/V plot for an n-type semiconductor in the dark (black line) and under illumination (red line). When the electrode is irradiated with UV light three distinctive areas can be observed: I) no photocurrent is present, II) the photocurrent starts to rise at the onset potential (V_{ON}) until it reaches a plateau ($I_{plateau}$), III) an overpotential is applied and electrolysis begins.*

From the analysis of an *I/V* graph, it is possible to determine the voltage that must be applied to a photoelectrode in order to maximise its performances. Precisely, the value of *V* in which the current reaches a plateau represents the voltage where charge carrier separation is more efficient and is therefore the optimal operational *V* of the PEC cell. Clearly, materials with high photocurrent values when irradiated are preferable as they are more efficient catalysts for the production of oxygen. The efficiency of a PEC cell can be defined in different ways and in the next section the various definitions are reported.

1.1.3 Efficiency Definitions

There are several efficiency definitions for a PEC cell such as i) Solar to Hydrogen (STH) conversion efficiency, ii) Applied-Bias Photon to current Efficiency (ABPE), iii) Incident

Photon to Current Efficiency (IPCE) and iv) Absorbed Photon to Current Efficiency (APCE).[9]

i) STH conversion efficiency (Eq. 1.5) defines the overall efficiency of a PEC cell exposed to Air Mass 1.5 Global (AM 1.5 G) illumination under zero bias conditions, where no bias is applied between working and counter electrodes.

$$STH = \left[\frac{(mmol\,H_2\,/s) \cdot (237kJ\,/mol)}{P_{tot}\left((mW\,/cm^2) \cdot Area(cm^2)\right)} \right]_{AM1.5G} \qquad \text{Eq. 1.5}$$

Where ($mmol\,H_2/s$) is the rate of hydrogen production, ($237\,kJ/mol$) is the change in Gibbs free energy per mol of H_2, P_{tot} is the incident illumination power density and $Area$ is the geometric area of illumination of the photoelectrode.

ii) ABPE (Eq. 1.6) describes the efficiency of a PEC cell exposed to AM 1.5 G considering the effect of an applied bias between working and counter electrodes:

$$ABPE = \left[\frac{\left| j_{ph}\left(mA\,/cm^2\right) \right| \cdot \left(1.23 - |V_b|\right)(V)}{P_{tot}\left(mW\,/cm^2\right)} \right]_{AM1.5G} \qquad \text{Eq. 1.6}$$

Where J_{ph} is the photocurrent density obtained under the applied bias V_b, and P_{tot} the incident illumination power density.

iii) IPCE (Eq. 1.7) describes the photocurrent collected per incident photon flux as a function of illumination wavelength.

$$IPCE = 1239 \left(\frac{V \cdot nm}{C \cdot s} \right) \frac{j_{ph}\left(A/cm^2\right)}{P_{mono}\left(W/cm^2\right) \lambda(nm)} \qquad \text{Eq. 1.7}$$

Where 1239.8 represents the multiplication of h (Plank constant) and c (speed of the light) divided by e (elemental charge). J_{ph} is the photocurrent density obtained under applied bias, P_{mono} is the illumination power intensity and λ is the wavelength at which the illumination power is measured.

In a PEC system, IPCE values are normally obtained from chronoamperometry measurements where the current from illuminating the working electrode with monochromatic light at different wavelengths is measured while a bias is applied between working and counter electrode.

iv) APCE (Eq. 1.8) defines the photocurrent collected per incident photon absorbed and is defined by:

$$APCE = \frac{IPCE}{1 - 10^{-A}} = 1239.8 \left(\frac{V \cdot nm}{C \cdot s} \right) \frac{j_{ph}\left(A/cm^2\right)}{P_{mono}\left(W/cm^2\right) \cdot \lambda(nm) \cdot \left(1 - 10^{-A}\right)} \qquad \text{Eq. 1.8}$$

Where 10^{-A} represents the transmittance and the absorbance A is defined by:

$$A = -\log\left(\frac{I}{I_0}\right) \qquad \text{Eq 1.9}$$

Where A defines the absorbance of the sample as the logarithmic ratio of the measured output light intensity I versus the initial input light intensity I_0. This is determined experimentally by UV-Vis Spectroscopy.

1.1.4 Metal Oxide Semiconductors Employed in Photoassisted Water Splitting

As mentioned in the introduction, TiO_2, WO_3 and α-Fe_2O_3 are among the most studied metal oxide semiconductors because of their high stability, which is attributable to their large band gap that gives strength to the chemical bond. However, their relatively large band gap limits the region of the solar spectrum that can be absorbed. In the following section, a brief overview on the main characteristics of these materials is presented and a more detailed discussion on each metal oxide will be presented in the relevant chapters.

The position of the conduction and valence bands in anatase TiO_2 are suitable for both water oxidation and proton reduction, however the large band gap of ~3.2 eV limits its absorption to wavelengths up to ~390 nm and, therefore, restricts its practical use. Despite its low conversion efficiency (1.3% of maximum theoretical photoconversion)[8], TiO_2 has been broadly studied and is considered an ideal model material for mechanistic studies because of its stability in a wide range of pHs. Considering the proximity of its conduction band to the redox potential of the H^+/H_2 couple and taking into account any possible energy loss, anatase TiO_2 has been primarily employed as photoanode in PEC systems. I will discuss the use of TiO_2 photoanodes in Chapter 5.

With the aim of increasing TiO_2 photocatalytic activity, several material modifications such as main group doping or the use of co-catalysts have been reported in the literature.[26,27] In recent years, a novel approach to extend the absorption profile of TiO_2, consisting on the hydrogen treatment of TiO_2 nanoparticles at a moderate pressure (20 bar, 200 °C for 5 days) has been reported.[28] The effect of hydrogen treatment on TiO_2 nanowires has also been recently investigated highlighting a substantial increase in the oxygen vacancies lying below the conduction band and leading to an improvement of the absorption of visible light.[29] This increase of oxygen vacancies has been proposed to be responsible to facilitate charge transport and separation leading to increased IPCE values in comparison with conventional anatase TiO_2 photoanodes. This topic will be discussed in details in Chapter 4.

WO_3 is an n-type semiconductor with a band gap value of ~2.7 eV, equivalent to an absorption edge of ~460 nm corresponding to part of the blue region of the solar spectrum. Its valence band sits at a potential more positive than the redox potential of the H_2O/O_2 couple enabling WO_3 to be used as a photoanode in PEC cells. However, since the conduction band is also more positive than the redox potential of the H^+/H_2 couple, proton reduction can only occur at a counter electrode in the presence of an external applied bias. The theoretical maximum photoconversion of 4.8% for WO_3 and the high photocurrent values reported in literature make WO_3 a promising photoanode for photoassisted water splitting.[8] As for TiO_2 material modifications and the use of co-catalysts have been investigated in order to increase its photoconversion efficiency.[30,31] However, recent studies have suggested that water oxidation does not occur through the surface of WO_3 using several electrolytes such as HCl, H_2SO_3 and $HClO_4$. Instead an

indirect oxidation takes place and involves radical electrolyte intermediates.[32,33] This topic will be discussed in more detail in Chapter 3.

α-Fe$_2$O$_3$ (hematite) is also a widely employed photoanode for water splitting systems because of its abundance, low cost and stability (at neutral-alkaline pH)[34] under water oxidation conditions. Its band gap (~2.1 eV) corresponds to an absorption of wavelengths up to ~600 nm, which represents a significant portion of the solar spectrum. The position of the α-Fe$_2$O$_3$ valence band enables its use as a water oxidation photoanode, but an external electric bias is required in order to reduce protons as its conduction band edge is more positive than the proton reduction potential. For α-Fe$_2$O$_3$ the maximum theoretical photoconversion efficiency has been calculated to be 12.9%,[8] however its performance has been reported to be limited by fast charge carriers recombination which results in a short hole diffusion length.[35] As for TiO$_2$ and WO$_3$ the effect of surface modification and co-catalysts has been investigated and current state of the art electrodes based on single-crystal wormlike hematite showed a high and stable photocurrent of 4.3 mA/cm^2 which corresponds to 34% of the maximum theoretical photoconversion efficiency.[36]

Despite intense research into the synthesis and catalytic characterization of these highly studied materials, the mechanism of reaction behind photoassisted water splitting remains unclear and is still under investigation. A good understanding of the processes involving the charge carriers generated in the photoelectrodes is required in order to define the factors which are limiting the photoconversion efficiency of these materials. Once there is a good understanding of these factors, targeted development of new and efficient materials and photoanode design will be enabled.[37] Many techniques have been employed

to study photoelectrodes used in water splitting systems; in the next section I will give a description of the techniques employed during the course of this thesis.

1.2   Studies of Water Splitting Systems

In this thesis four main techniques have been employed for the study of water oxidation photoelectrodes:

i) Photoelectrochemical measurements have been carried out in order to test the quality of the photoelectrodes and their capability to oxidise water into oxygen;

ii) Oxygen measurements have been employed in order to confirm the evolution of oxygen;

iii) Transient absorption spectroscopy (TAS) has been employed in the study of charge carrier dynamics following UV excitation of the semiconductors;

iv) Sum Frequency Generation (SFG) spectroscopy has been used for the study of intermediates during photochemical water splitting.

In this section a general overview on the non-standard techniques (i, iii and iv) is given and a more detailed description of the setup used during the experiments is discussed in Chapter 2.

UV-Vis spectroscopy has also been used to locate the region of the spectrum where an electrode absorbs light, to estimate the portion of the solar spectrum employable, but is not described in this section.

1.2.1 Photoelectrochemical Measurements.

Photoelectrochemical measurements are generally carried out in order to estimate the photocatalytic activity of an electrode. During the course of these thesis studies steady state and transient photocurrent measurements were employed.

Steady state photocurrent is generally recorded in a complete PEC cell in order to test the capability of a photoanode (photocathode) to oxidise water (reduce protons) and to determine the operational conditions of the PEC cell. Current vs. voltage plots are recorded in the dark and under steady state illumination. The subtraction of the dark from the light current gives the value of the photocurrent produced as an effect of charge carrier separation. *Figure 1.7* shows an example of a current/voltage plot recorded both in the dark and under UV illumination
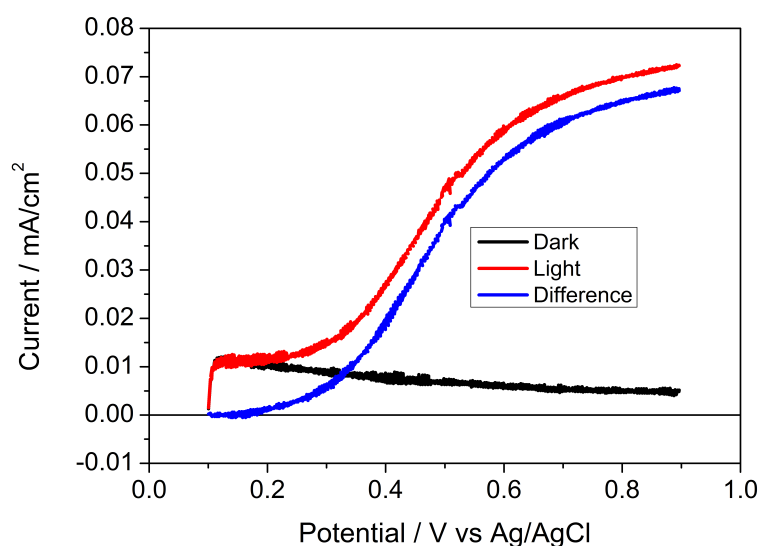
Figure 1.7: *Current vs Voltage plot recorded for a WO$_3$ photoanode in the dark (black line) and under UV (355 nm, 75Xe lamp) irradiation (red line) in 0.5 M NaClO$_4$, pH 2 (HClO$_4$). The difference between light and dark current, i.e. the photocurrent, is also showed (blue line). (Scan rate: 20 mV/s; WO3 W.E., Ag/AgCl (KCl 3M) R.E., Pt C.E.; SE side illumination.)*

45

Transient photocurrents are also recorded using a complete PEC cell in order to estimate the internal quantum efficiency of a metal oxide semiconductor. Current vs. time plots are recorded applying the PEC operational potential between working and counter electrode and using a pulsed light in order to generate charge carrier separation. *Figure 1.8* shows a transient photocurrent graph.

The plot reported below describes the behaviour of the photocurrent over a period of one second. Following excitation of the anode with a pulsed laser (6 ns pulse width), charge carrier separation and electron transport occur. The photocurrent rise is related to both the transport rates and, at very short times, the capacitance of the FTO-semiconductor interface. After initial excitation the charges recombine and the photocurrent decreases until all the electrons have recombined with the holes and the current is equal to zero.
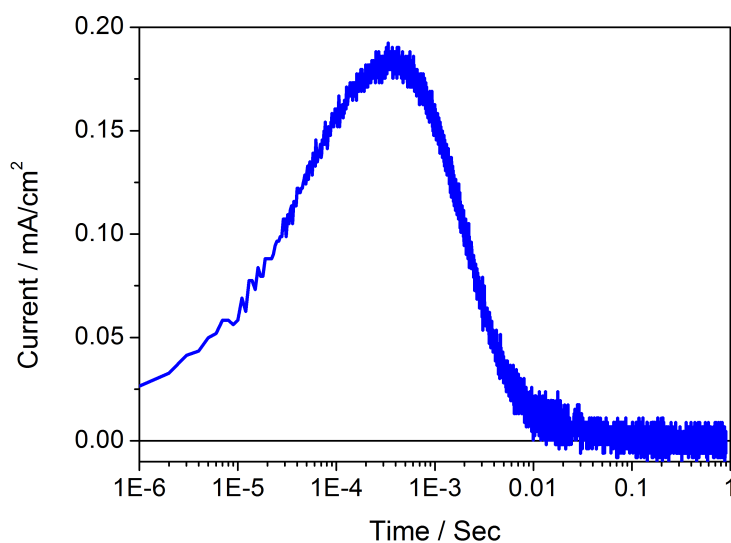
Figure 1.8: *Transient photocurrent recorded for a mesoporous WO$_3$ electrode in 0.5 M NaClO$_4$ (pH 2, HClO$_4$). Following pulsed irradiation of the electrode (355 nm, 0.33 Hz, 250 μJ/cm^2), the photogenerated charge carriers generate a current which decreases over time due to charge carriers recombination.*

By integrating the photocurrent over the time it is possible to determine the total charge collected as the result of a single light pulse.

1.2.2 Transient Absorption Spectroscopy

Transient absorption spectroscopy (TAS) is a spectroscopic technique employed to measure the absorbance of a sample as a function of time. TAS is an extension of flash photolysis, a pump/probe technique developed shortly after the Second World War by Eigen, Norrish and Porter who were awarded the Nobel Prize in 1967 for this invention. They developed flash photolysis in order experimentally give proof of the existence of free radicals and short lived intermediate whose presence was only deducted from kinetic studies and product analysis.[38] In 1950 George Porter published a paper describing the principles of operation of flash photolysis and spectroscopy using gas-filled flash discharge tubes of very high power as spectroscopic and photochemical sources and providing the transient spectra of various molecules and intermediates proving the capability and the power of this technique for the study of short lived intermediates.[39]

In 1970 another paper published by Porter and Topp described a nanosecond flash photolysis system employing a pulsed laser as excitation source and used in the study of events with a duration of few nanoseconds, in particular they described the observation of the absorption spectra of excited singlet states, short lived excited triplet states and chemical events in the nanosecond time region. The use of a laser as excitation source led to a time resolution improvement by a factor of a thousand over the conventional flash photolysis techniques described until then.[40] Since these pioneering studies flash photolysis has been used in the study of various photochemical system with particular interest in semiconductor chemistry. During the course of my PhD transient absorption

spectroscopy has been used in order to follow the charge carriers dynamics in metal oxides semiconductors employed as photocatalysts during water splitting in order to retrieve important information on their kinetics. In the next paragraph a brief description of the use of TAS on photocatalytic system based on semiconductors is briefly discussed.

TAS is described as a pump/probe technique where a pump beam is employed to excite a photoactive sample and subsequently a probe beam of a fixed wavelength is used to follow the absorbance of photoexcited states as a function of time. With TAS it is possible to follow processes ranging from the fs – s timescales.

In the case of a semiconductor, the electrons are excited to the conduction band by the pump beam, which is typically a pulsed laser. The photogenerated charge carrier concentration is probed by following the change in the UV/Vis absorption due to photogenerated species using a probe light, which can either be a steady state lamp or another pulsed laser, *Figure 1.9*.
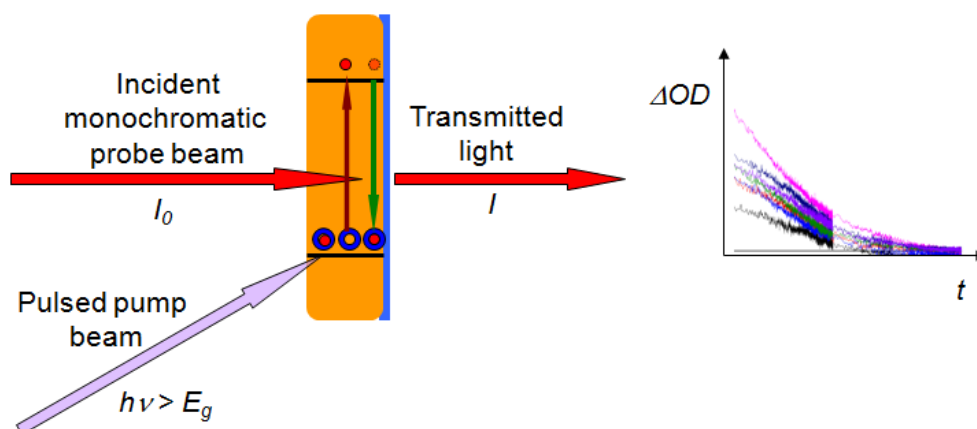
Figure 1.9*: Pictorial representation of the principle of operation of transient absorption spectroscopy on an isolated metal oxide semiconductor electrode. A pulsed pump beam with hv>E$_g$ generates charge carriers. Their absorption is followed by an incident probe beam at a fixed wavelength over time and ΔOD vs. t graphs are plotted.*

The absorbance or optical density (*OD*) of a sample is, therefore, recorded as a function of the probe wavelength and the difference in optical density (*ΔOD*) before and after pump excitation is expressed as a function of time, equation 1.11 and 1.12:

$$OD_{(\lambda)} = \log \frac{I_0(\lambda)}{I(\lambda)} \qquad \text{Eq. 1.11}$$

$$\Delta OD_{(t)} = OD_{a.e.(t)} - OD_{b.e.} = \log \frac{I_0}{I_{a.e.(t)}} - \log \frac{I_0}{I_{b.e.}} = \log \frac{I_{b.e.}}{I_{a.e.(t)}} \qquad \text{Eq. 1.12}$$

Where I_0 and I are the intensities of incident and transmitted radiation respectively, *ΔOD*$_{a.e.}$ and *ΔOD*$_{b.e.}$ are the optical densities before and after pump excitation.

By the analysis of the charge carrier absorption profiles over the time, important information on their dynamics such as lifetime, recombination times and charge transport can be obtained.[12-16]

TAS becomes an even more powerful technique when employed to study charge carriers dynamics in a complete PEC cell, *Figure 1.10*:
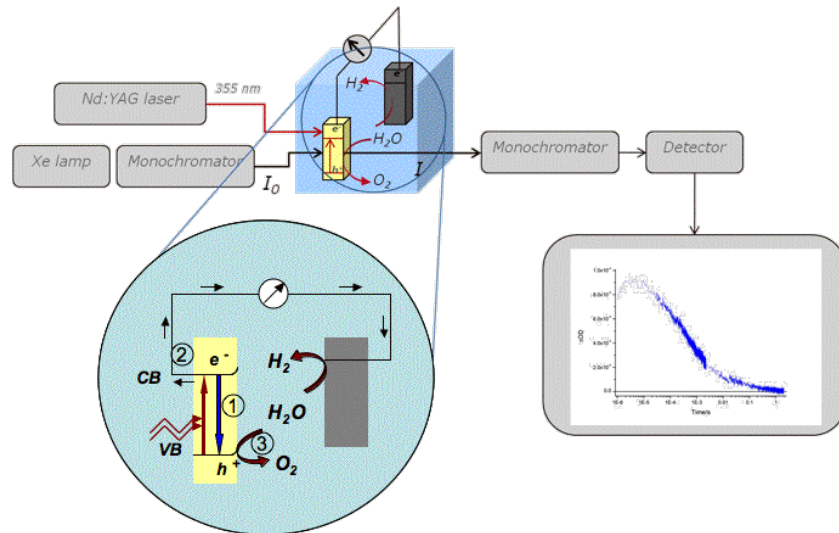
Figure 1.10: *Transient absorption spectroscopy employed to study a PEC system. Charge carrier separation is enhanced in the PEC cell by the application of an external bias, facilitating the study of the three main processes occurring in a PEC: 1) charge recombination, 2) charge transport and 3) chemical reaction with water.*

As it has been mentioned in section 1.1.2, in a semiconductor based PEC cell, following charge carrier separation the photoelectrons and holes are mainly involved in three processes:

1)   Charge carrier recombination;

2)   Charge transportation;

3)   Chemical reactions

By fitting the TAS traces recorded in a complete PEC cell, it is possible to obtain important information about the dynamics of these three processes and understand which, if any, is the process that limits the efficiency of a given material. A thorough understanding of the kinetics of these processes is of fundamental importance for a targeted development of new materials.

1.2.3 Progresses in Transient Absorption Studies on Metal Oxide Semiconductors Used During Photoassisted Water Oxidation

TAS has been used in recent years in order to follow the charge carriers dynamics in metal oxide semiconductors including TiO_2, α-Fe_2O_3 and WO_3. In this section I will summarise some of the progresses that have been made in the study of these photoanode materials in photoelectrochemical systems and a more detailed discussion on this topic will be reported at the beginning of each relevant chapter.

- As mentioned in section 1.1.4 TiO_2 has been one of the most studied materials employed during photoassisted water oxidation because of its high stability in conditions in which water splitting can occur, its abundance and its low costs. The transient absorption features of the charge carriers in a colloidal solution of TiO_2 were first assigned by Bahnemann and co-workers in 1984; they identified two characteristic absorption peaks at 475 nm and at wavelengths higher than 650 nm which were assigned to photogenerated holes and electron respectively. [41] The position of these absorption peaks was then confirmed by several authors including Tang et al. who, using TAS, proved that the water oxidation process involve a four holes reaction.[16] By defining the spectral position of the charge carriers absorption features it has been possible to follow their kinetics in several experimental condition in order to retrieve information on hole and electron life times, and subsequently define kinetic parameters describing the processes involving photogenerated charge carriers such as electron/hole recombination, electron transport and hole reaction with water. The lifetime of photogenerated hole during photoassisted water oxidation in a complete PEC cell was also defined by Cowan et al. to be ~0.3 s at pH 12.6.[15] Despite several TAS studies on anatase TiO_2 electrodes there is not record of transient studies carried out in a wide range of pH, therefore I have investigated the

dependence of the hole life-time on the H^+ concentration of the electrolytes employed during TA measurements. This topic will be described in details in chapter 5.

- The use of hydrogen-treated TiO_2 nanowires has recently attracted interest because of the reported increase in the concentration of oxygen vacancies lying below the TiO_2 conduction band which leads to an improved visible light absorption and consequently to high values of IPCE closed to the unit.[42] However from the best of our knowledge no TA studies has been carried out on this material in the past. By follow the charge carrier dynamics in hydrogen treated TiO_2 nanowire therefore will be possible to determine the electron/hole recombination rate and gain important information on the improved electrical property of this material. This topic will be discussed in details in chapter 4.

- From the best of our knowledge only one TAS study has been reported in the past on WO_3.[43] However only the electron spectrum was assigned and the transient absorption of photogenerated hole has never been studied. Therefore a we decided to carried out transient absorption studies on WO_3 with the aim of identify the hole absorption features and define the kinetic parameters required in order to have a better understanding of the factors limiting the efficiency of this material. I will discuss in detail this topic in Chapter 3.

- Hematite (α-Fe_2O_3) has also been investigated using TAS and the presence of two distinct photogenerated species absorbing at around 575 and 625 nm has been identified and assigned to the absorption of photogenerated holes. [44,45] Under the application of an external bias, the photogenerated holes have been found to be enough long-lived (hundreds of milliseconds to seconds lifetime) in order to enable water oxidation. This has been ascribed to the fact that a positive electric bias not only increases the reduction potential of electrons at the cathode, but also reduces the background electron density in hematite, leading to a decrease in electron/hole recombination and increased hole lifetime. Being known as one of the most efficient photocatalysts currently used in PEC cell, we

have decided to employ α-Fe_2O_3 in a novel solar fuel reactor whose caracteristics will be discussed in details in Chapter 6.

1.2.4 Sum Frequency Generation Spectroscopy

Sum Frequency Generation (SFG) spectroscopy is a non-linear optical technique which provides the vibrational spectra of molecules at interfaces.[46,47] Here we have employed SFG spectroscopy with the aim of obtaining information about the surface species involved during water oxidation. SFG occurs when one pulsed laser beam with a fixed visible frequency (ω_{VIS}) and another tuneable infrared pulsed beam (ω_{IR}) are spatially and temporally overlapped at the surface of a material or at the interface between two materials (it can be applied to gas/solid, gas/liquid and liquid/solid interfaces), *Figure 1.11*. The emission occurs at a frequency which is the sum of the two incident frequencies ($\omega_{SF}=\omega_{VIS}+\omega_{IR}$) and the intensity of the emission light is enhanced when the frequency of the IR beam matches a vibrational mode of the molecule at the interface. When the sum frequency light is detected as a function of the infrared frequency it is possible to obtain a vibrational spectrum, which is shifted into the visible region of the electromagnetic spectrum. Detection systems for visible photons are significantly more sensitive than those for infrared photons, making the detection of even sub-monolayer concentrations possible. Furthermore, a molecule must be asymmetric at both macroscopic and molecular levels and have a net polar orientation in order to be sum frequency active, making SFG spectroscopy a powerful technique for the study of solvated interfaces, such as that of TiO_2/Water.
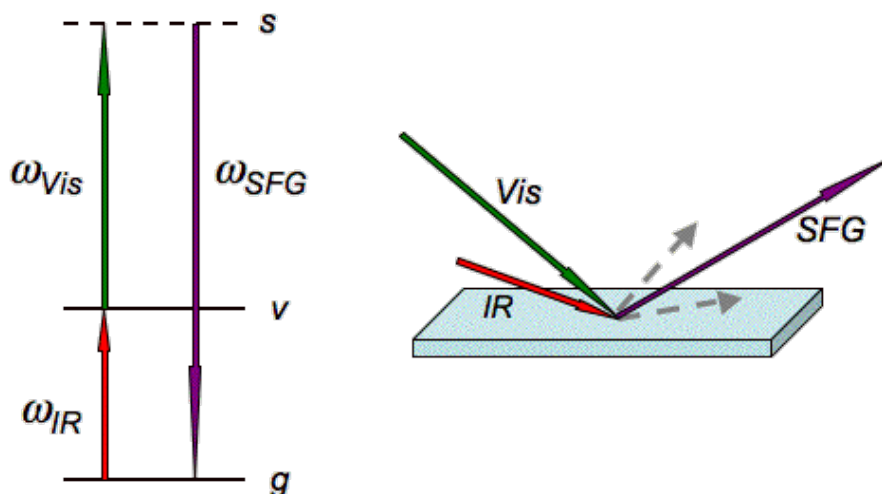
Figure 1.11: *Pictorial representation of the principle of operation of sum frequency generation spectroscopy. When a fixed Visible beam and a tuneable IR beam are spatially and temporally overlapped at a surface SF light is generated with a frequency (ω_{SFG}) which is the sum of the visible (ω_{Vis}) and IR (ω_{IR}) frequencies.*

Figure 1.11 provides a pictorial illustration of the SFG mechanism: *g*, *v* and *s* indicate the ground state, the excited state and any other state respectively. Information on the interfacial molecules can be obtained by the analysis of the position, intensity and phases of the vibrational resonances. The origin of the SFG term and its surface selectivity is now discussed in more detail:

The propagation of an electric field across an isotropic material can induce an electric dipole, μ (see equation 1.13), as a result of the force applied to the electrons in the medium, which can be expressed by:

$$\mu = \mu_0 + \alpha E \qquad \text{Eq. 1.13}$$

Where μ_0 is the permanent dipole of the material, α is the polarisability of the electrons and E is the applied electric field. In the bulk of a material the sum of the electric dipoles can be expressed by the polarisation P (equation 1.14):

$$P = \varepsilon_0 \chi^{(1)} E \qquad \text{Eq. 1.14}$$

Where χ is the first order susceptibility (the response of a material to an applied field) and is given by the average of α; ε_0 is the permittivity in the vacuum. Linear optical properties such as reflection and refraction are then produced as the dipoles oscillate and emit at the same frequency of the incident electric field. However, the non-linear properties increase with increasing E and additional terms must be added in order to define the induced dipole, see equation 1.15:

$$\mu = \mu_0 + \alpha E + \beta E^2 + \gamma E^3 + ... \qquad \text{Eq. 1.15}$$

Where β and γ represent the hyperpolarisability of first and second order respectively. Taking into account these non-linear terms, the bulk polarisation can be re-expressed by equation 1.16 :

$$P = \varepsilon_0 \left(\chi^{(1)} E + \chi^{(2)} E^2 + \chi^{(3)} E^3 + ... \right) = P^{(1)} + P^{(2)} + P^{(3)} + ... \qquad \text{Eq. 1.16}$$

Where $\chi^{(1)}$ and $\chi^{(2)}$ are the non-linear susceptibilities of second and third order. SFG is a second-order non-linear process, therefore, it is dependent on the second order susceptibility, which is zero in centrosymmetric mediums such as the majority of bulk

phases, and therefore only asymmetric mediums are sum frequency active. The polarisation can then be rewritten as:

$$P_{SF}^{(2)} = \varepsilon_0 \chi^{(2)} E_{Vis} E_{IR}$$ Eq. 1.17

The second order susceptibility is solely responsible for the vibrational information that can be obtained from a SF spectrum as it changes significantly with changes in the infrared wavenumber; when the infrared pulsed beam is tuned to a resonant wavenumber and its frequency coincides with the frequency of a vibrational mode, the susceptibility increases leading to an increase in the intensity of the SF signal which is directly proportional to the square of the second order susceptibility and to the intensities of the visible and infrared beams, equation 1.18:

$$I(\omega_{SFG}) \propto \left| \chi^{(2)} \right|^2 I(\omega_{Vis}) + I(\omega_{IR})$$ Eq. 1.18

From the position and the intensity of a sum frequency peak it is possible to determine the nature of the vibrational mode observed, this therefore provides information on the species present at the interface. A more detailed discussion on the principles behind sum frequency generation spectroscopy can be found in references 46 and 47.

As a result, SFG can be employed in the study of photoactive systems based on metal oxide semiconductors and represents a very powerful technique for determining the surface species involved during water splitting and clarifying the mechanism of reaction which, despite several decades of research, still remain unclear.

1.3   Reactors for Solar Hydrogen Production

Over the past few years, devices for solar hydrogen production have been refined with the aim of supplying a realistic solution to the global energy demand. In the final chapter of this thesis, a hybrid solar concentrator/photoelectrochemical solar fuel reactor that has been developed and tested is described, providing positive initial results and representing a step toward a feasible device for medium to large scale solar fuel production.

1.3.1 Grätzel Tandem Cells Based on Metal Oxide Semiconductors

Grätzel tandem cells represent an example of a solar fuel device developed over the last decade. A standard tandem cell consists of a metal oxide photoanode coupled with one or two dye-sensitized solar cells (DSSCs) which provides the potential required for the water splitting reaction to take place.[48-50] *Figure 1.12* shows a standard sandwich configuration for a tandem cell using a α-Fe_2O_3 anode coupled with a DSSC.
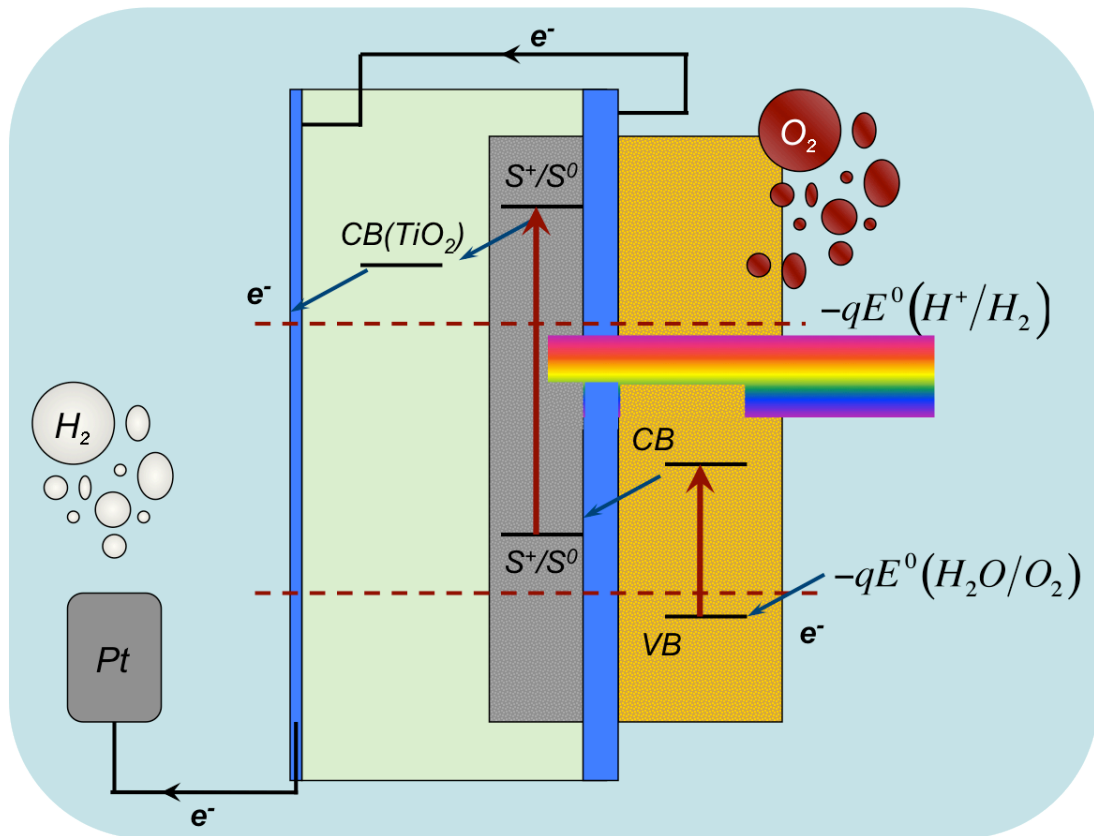
Figure 1.12: *Outline of a Grätzel tandem cell based on an α-Fe$_2$O$_3$ photoanode with relative energy levels. The red dotted lines represent the reduction and oxidation potentials of water. This figure has been adapted from reference 50.*

However, the need to use transparent conductive substrates could lead to large potential drops across the electrodes with increasing active area, limiting the efficiency of this type of device with increasing dimensions. A detailed discussion of this can be found in the introduction of Chapter 6.

The vertical design of the Grätzel tandem cells represents a further limitation to the reachable STH efficiency as wavelengths shorter than 600 nm are absorbed by the photoanode (considering a state of the art α-Fe$_2$O$_3$ photoanode),[48] limiting the portion of the solar spectrum usable by the DSSC. To overcome this limitation and enhance the light

harvesting of a similar solar fuel device, a hybrid reactor which couples luminescent solar concentrators and a PEC cell has been developed and tested.

1.3.2 Luminescent Solar Concentrators

A Luminescent Solar Concentrator (LSC) is a non-imaging optical device consisting of a transparent plate (e.g., glass or polymethyl methacrylate, PMMA) doped with luminescent species such as dyes or nanocrystals which absorb incident solar radiation and re-radiate it at red-shifted wavelengths with high quantum efficiency.[51-53] The photons which enter the upper face of the plate are absorbed by the dyes and luminescent photons are emitted. A large portion of the emitted light is trapped into the plate by total internal reflection (TIR) and guided towards the edges of the LSC by successive reflections where it can be collected by a photovoltaic (PV) cell or a photoelectrode. A portion of the emitted photons can be lost due to several factors such as i) losses within the escape cones, ii) re-absorption due to an overlap of the absorption and emission spectra of the luminescent molecules, iii) transmission of longer wavelength radiation and iv) surface reflection. *Figure 1.13*:
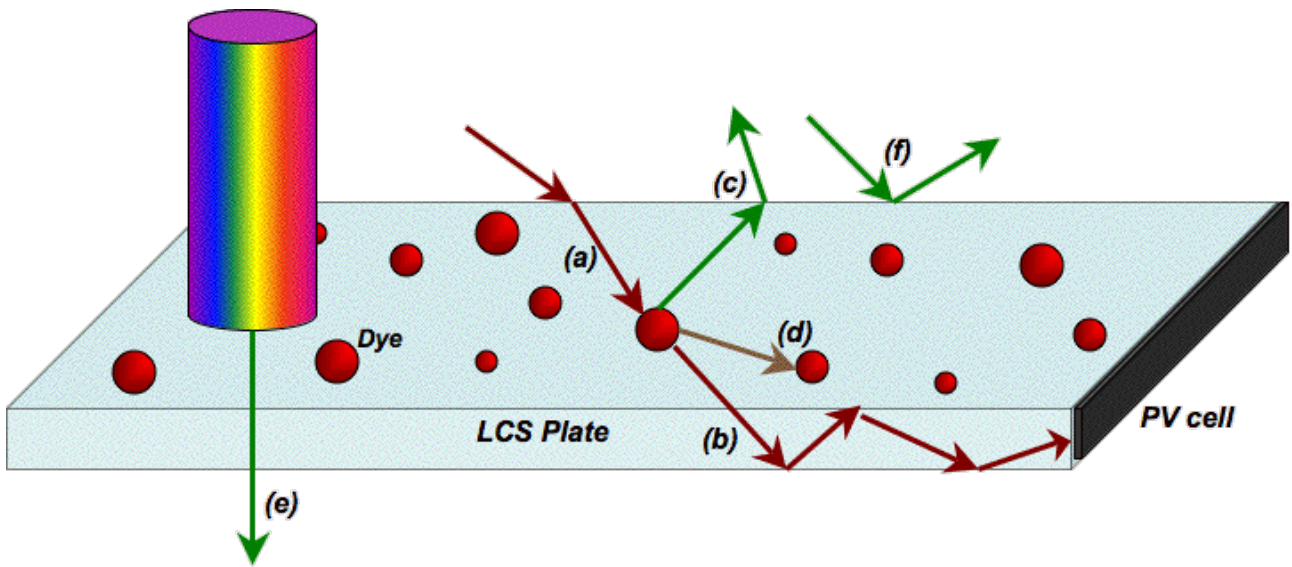
Figure 1.13: *Pictorial representation of the cross section of a LCS plate doped with dye molecules. Incident sunlight is adsorbed by a fluorescent dye molecule (a) and re-radiated isotropically with a longer wavelength and high quantum efficiency. When the angle of incidence is beyond the critical angle the light is totally internally reflected (b) toward the edge of the LSC. When the light is emitted within the escape cone it is lost from the LSC (c). Other processes leading to light losses are: re-absorption by another dye molecule (d), transmission through the LSC plate (e) and reflection by the surface (f).*

Two main factors must be taken into consideration during the optimisation of a LSC plate: the choice of the luminescent dye and the geometry of the plate.

When coupled with a LSC plate, the efficiency of an absorbing device such as a PV cell is higher when there is a good overlap between the emission spectra of the luminescent dye and the absorption spectra of the PV itself. Therefore, it is clear that the choice of the luminescent species plays a key role in the optimisation of the performances of a LSC/PV device. When choosing a luminescent dye, certain factors must be taken into consideration: i) Its Fluorescence Quantum Yield (FQY) which is expressed by equation 1.19 and represents the amount of the absorbed photons which are re-emitted.

$$FQY = \frac{n° photons_{Emitted}}{n° photons_{Absorbed}} \qquad \text{Eq. 1.19}$$

In the ideal case in which every absorbed photon is re-emitted FQY has a value of 1.

ii) The capability of the fluorescent species to absorb photons in the region of the solar spectrum of interest.

iii) A minimum overlap between the absorption and emission spectra which leads to re-absorption losses.

iv) A narrow emission spectrum which matches the absorption profile of the species that needs to be irradiated.

By an accurate choice of the luminescent species, it is possible to optimise the LSC overall efficiency expressed by equation 1.20 :

$$\eta_{opt} = \eta_{waveguiding} \cdot \eta_{capturing} \qquad \text{Eq. 1.20}$$

Where η_{opt} represents the optical efficiency which is given by the multiplication of capture and waveguide efficiencies ($\eta_{capturing}$ and $\eta_{waveguiding}$ respectively).

Two more parameters must be taken in account when considering the overall performance of the LSC: the geometrical gain (G) and the flux gain (F).

The geometrical gain is expressed as the ratio of the area of the concentrator A_{LSC} to the area of the solar cells connected to its four sides (A_{PV}), equation 1.21 :

$$G = \frac{A_{LSC}}{A_{PV}} = \frac{l^2}{4ld} = \frac{l}{4d} \qquad \text{Eq. 1.21}$$

Where l and d are the length and the depth of the square LSC respectively.

The flux gain is given by the geometrical gain multiplied by the optical efficiency of the LSC, equation 1.22 :

$$F = \frac{\varphi_{Out}}{\varphi_{In}} = G\eta_{opt} \qquad \text{Eq. 1.22}$$

Where φ_{in} and φ_{out} are the incident flux and the outbound flux from side emission respectively. As it can be seen, F increases with increasing G, however it reaches a maximum when any benefit of additional G is cancelled by high self-absorption losses. Conventionally, the LSC used are squared-planar as high values of G can be achieved even in thin plates.[54]

If two LSC square plates with different absorption spectra are coupled and placed one on top of the other, the portion of the solar spectrum that can be absorbed substantially increases and two different photoactive materials with complementary absorptions can be photoexcited, *Figure 1.14*.
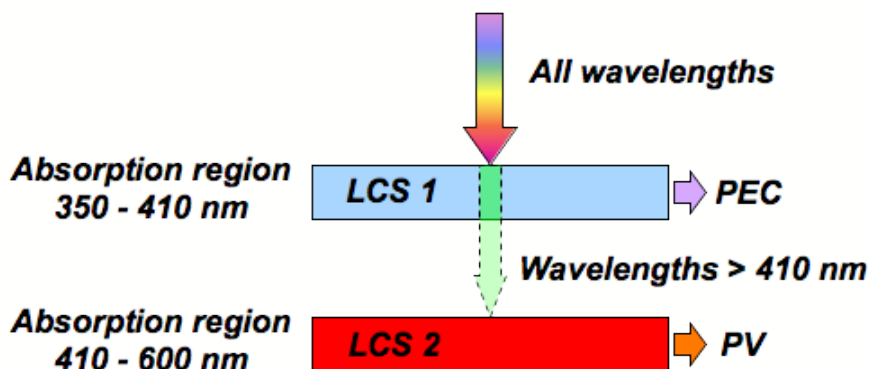
Figure 1.14: *Outline of two LSC plates with different absorption regions placed horizontally one on top of the other. Wavelengths up to 410 nm are absorbed by LSC 1 whereas longer wavelengths pass through it and are absorbed by LSC 2.*

In the reactor developed during my PhD and described in detail in Chapter 6, two LSC are placed horizontally on top of each other. One is coupled with a α-Fe_2O_3 photoanode contained in a complete PEC cell and the other to three PV cells connected in series that provide the external potential required to split water in the PEC cell.

1.4   Project Objectives

As highlighted in sections 1.1.3 and 1.2.2, an improved understanding of the kinetics and the mechanisms involving the photogenerated charge carriers in metal oxide semiconductors is extremely important to enable a targeted development of new and more efficient materials. The main purpose of the project was to investigate the charge carrier dynamics in mesoporous WO_3 electrodes, which were poorly understood prior to these studies. TAS was used in order to identify the charge carrier absorption features and to follow the electron and hole dynamics on the millisecond to second timescales which are believed to be most relevant to water oxidation processes, (Chapter 3).

TAS was also employed in order to investigate the charge carriers dynamics in hydrogen treated rutile TiO_2 nanowires with particular interest in following the electron/hole recombination process in order to highlight any possible suppression of it and explain the high values of IPCE reported for this material. (Chapter 4)

A pH-dependence transient absorption study was also carried out on nanocrystalline anatase TiO_2 electrodes with the aim of elucidating any possible dependence of the hole dynamics on the electrolyte pH. However, TAS does not provide sufficient information on the nature of the intermediate involved during the water oxidation reaction and, as already mentioned in the previous sections, this surface intermediate and the mechanisms still remain unclear. Therefore, SFG spectroscopy was employed during the course of these thesis studies in order to clarify the nature of the intermediates present on the surface of an isolated TiO_2 electrode when irradiated with UV light and in contact with water (Chapter 5).

Toward the end of my PhD a medium-scale hybrid reactor, based on a α-Fe_2O_3 PEC cell and two solar concentrators, was developed. Initial photochemical measurements were carried out in order to test its efficiency, (Chapter 6).

Chapter II

Methods and Materials

A general description of the main techniques and materials used during the course of these thesis studies was given in Chapter 1. Here I provide a detailed description of the setup of the instruments and the materials employed.

Methods

2.1 Transient Absorption Spectroscopy and Photoelectrocemical Cells

2.1.1 Transient Absorption Spectroscopy

In section 1.2.2 TAS was described as a time resolved pump/probe spectroscopic technique which uses short pulses of light as pump beams to irradiate the sample and a continuous probe beam at a fixed wavelength to follow the absorption of the photogenerated species. In the case of a semiconductor, the kinetics of the reactive intermediates (charge carriers) which are formed following pump excitation can be monitored by examining the change in absorption at a chosen wavelength in the UV-Visible region.

The UV excitation source (pump beam) was the third harmonic of a Nd:YAG laser (Continuum, Surelite I-10, 355 nm, 6 ns pulse width) operating between 0.33 and 10 Hz repetition rate. The laser pulse was transmitted to the sample using a liquid light guide (Newport). The output energy of the laser was set by changing the Q-switch timing on the laser and varying the aperture of an iris placed prior the sample area, and was measured using a power meter (Newport model 1918-R).

The probe beam was a 75W Xe lamp (Hamamatsu Photonics) coupled with a monochromator (OBB Corp.), which allowed the choice of the wavelength. Another monochromator was placed after the sample area and prior to the detector (a silicon PIN photodiode, Hamamatsu Photonics) in order to select the same wavelength of the probe beam and reduce scattered laser light reaching the detector. The Si photodiode was mounted in a customized case with a homebuilt preamplifier with two different

gain/frequency settings to enable a minimum rise time of either ~100 ns or 1 µs. DC and AC signals were recorded on a DAQ card (National Instruments, Ni-6221) and on a digital oscilloscope (Tektronix TDS220) coupled with a home-built amplifier filter respectively; the oscilloscope data were used to study the microsecond to millisecond time scale while the DAQ card covered the millisecond to seconds time scale. *Figure 2.1* shows an outline of the TAS system employed during the course of these thesis studies.
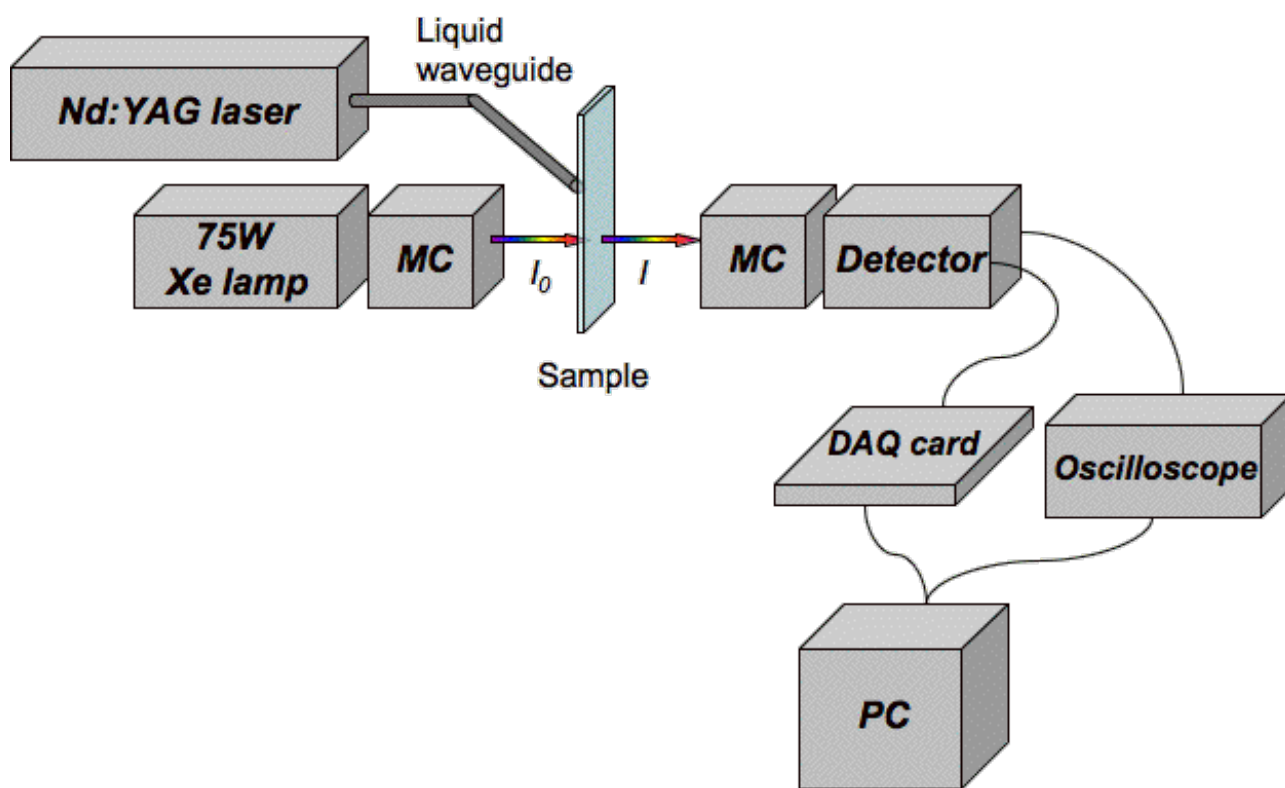
Figure 2.1:** **Outline of the TAS system employed during the course of these PhD studies. The Nd:YAG laser and the Xe lamp coupled with a monochromator represent the pump and the probe beams respectively. The pump beam excites the sample while the change in intensity of the transmitted probe beam is recorded. A monochromator is also placed between the sample and the detector in order to minimize interference from scattered pump laser light. AC and DC signals are recorded on a DAQ card and an oscilloscope connected to a PC. Custom labview software was employed for data acquisition.

The Nd:YAG laser typically operated at 0.33 Hz in order to allow the charge carriers to fully decay between two consecutive excitation events. For a typical experiment, the laser energy was chosen to be ~250 μJ/cm^2. The data were collected by averaging 500–1000 laser pulses and the ΔOD signals were acquired between 1 μs and 2 s. The TAS system described in this section was used to study isolated metal oxide semiconductors and photoanodes in a PEC cell with an external applied bias.

2.1.2 PEC cell

The PEC cell used during TAS and electrochemical measurements was a two compartment borosilicate glass cell described in *Figure 2.2*.
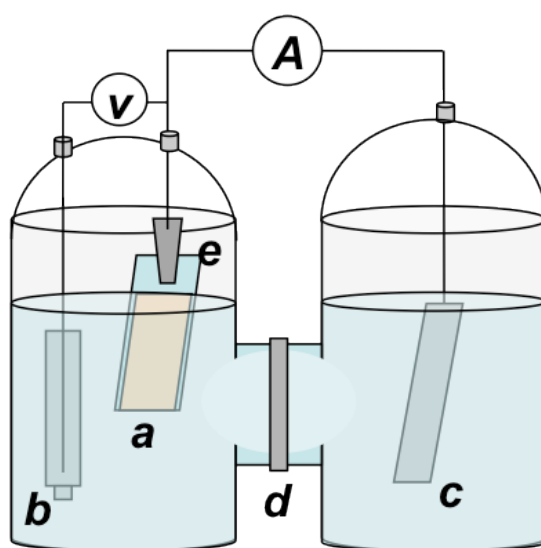
Figure 2.2*: Outline of a two-compartment PEC glass cell with an n-type semiconductor photoanode (working electrode). An external electrical bias is applied between working (a) and reference (b) electrodes while the current flows between working and counter (c) electrode. The working electrode is held by a metal clip (e, kept above the electrolyte level) in order to create an electric contact. When separate gas extraction is required the anodic and cathodic compartments can be separated by an ion exchange membrane (Nafion-115) (d).*

One compartment contains the working (semiconductor photoanode) (a) and reference (b) electrodes and the other contains the counter electrode (c). The two compartments can be separated by an ion exchange membrane (Nafion 115) (d) in order to extract hydrogen and oxygen separately. The working electrode is usually an electrode consisting of a metal oxide film deposited by various techniques on top of a conductive glass substrate (FTO or ITO). The working electrode was held by a metal clip (e) which was kept above the electrolyte level in order to avoid contamination of the electrolyte solution with metal ions, and was illuminated from the substrate (SE) or from the electrode (EE) side depending on the type of experiment carried out. The reference electrode employed was an Ag/AgCl (3 M KCl) commercial electrode (Bioanalytical Systems Inc) protected with a double junction when working with highly alkaline pHs in order to avoid degradation of the vycor glass frit at the end of the electrode. The counter electrode was a platinum gauze. The electrolyte was typically a 0.5 M $NaClO_4$ (reagent grade, Sigma-Aldrich) solution prepared using Milli-Q water (Millipore Corp., 18.2 MΩ cm at 298 K) and adjusted in pH using NaOH and $HClO_4$ (reagent grade, Sigma Aldrich); the solution pHs were measured using a digital pH-meter (Philips, PW9420). Before any measurement, the solutions were de-aerated for 30 minutes using Ar gas (BOC, Pureshield grade) in order to remove any possible dissolved oxygen. In the text the potentials are usually reported versus the Ag/AgCl electrode and can be converted to RHE using equation 2.1:

$$E_{RHE} = E^0_{Ag/AgCl} + E_{Ag/AgCl} + 0.059 pH \qquad \text{Eq. 2.1}$$

Where $E°_{Ag/AgCl}$ is the standard potential of the Ag/AgCl reference electrode used (0.21 V$_{RHE}$ at 298 K) and $E_{Ag/AgCl}$ is the measured potential versus the Ag/AgCl electrode.

2.1.3 Current/Voltage and Chronoamperometry Measurements

Steady state photocurrent measurements were carried out using the PEC cell described in the previous section. A potentiostat (Ministat 251, Thompson Electrochemical), connected to a PC *via* homebuilt Labview software, was used in a 3-electrode mode. The current-potential response of the semiconductor electrode was measured in the dark and under illumination (using the 75W Xe lamp employed in the TAS system). Part of the PEC cell was covered with black tape in order to avoid irradiation of the reference electrode which could lead to increasing noise levels. Before each experiment the electrolytes were purged with Ar gas for 30 minutes to remove any possible dissolved oxygen which, under illumination, leads to an increase in the photocurrent and, therefore, to possible misinterpretations of the capability of a photoanode to oxidise water.

Chronoamperometry measurements were carried out using a homebuilt PTFE cell with a quartz window connected to an Autolab potentiostat (PGSTAT12) controlled by a Nova v1.6 software. The light source was a 75 W Xe lamp (Hamamatsu Photonics) coupled with a monochromator in order to select a fixed wavelength. The current was recorded under a constant applied bias in the dark, until stable, and under monochromatic light until it reached a plateau. The dark current was subtracted from the light current and IPCE was calculated using equation 1.7.[9]

2.1.4 Transient Photocurrent

Transient Photocurrent (TPC) measurements were carried out using an adaptation of the system employed to record steady-state photocurrent. The potential applied between working and counter electrode was maintained at a constant value using the potentiostat (Ministat 251, Thompson Electrochemical) and the photoanode was excited by a short pulse of light from the Nd:YAG laser described above. A resistor (usually 47 Ω) was placed between the working and the counter electrode and the voltage drop across it was recorded as a function of time using an oscilloscope probe (Tektronix TekP6139A) connected to a digital oscilloscope (Tektronix TDS 220). The data recorded were converted from voltage to current using the Ohm's law ($V=IR$) in order to obtain the photocurrent as a function of time following the sample excitation.

2.1.5 Oxygen Measurements

Oxygen measurements were carried out using an oxygen membrane polarographic microelectrode (Instech Laboratories, Inc.),[55] also known as Clark electrode.[56] The photoactive sample was placed in a chamber connected with a thermostatic bath and maintained at 293 K, as the response of the polarographic electrode is known to be extremely sensitive to temperature. The Clark electrode consists of two electrodes, a platinum cathode and an Ag/AgCl anode, covered by a gas permeable Teflon membrane. Conduction between the two electrodes is achieved using a 3 M KCl (≥99%, Sigma Aldrich) solution. When an electric potential is applied between cathode and anode the gaseous oxygen that reaches the Teflon membrane is reduced at the cathode producing a

current, while the Ag anode is oxidised as the overall reaction expressed in equation 2.3 shows.

$$4Ag + O_2 + 2H_2O + 4Cl^- + 4e^- \rightarrow 4AgCl + 4OH^- + 4e^- \qquad \text{Eq. 2.3}$$
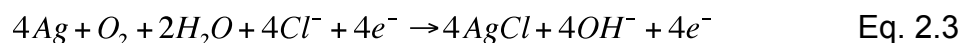
The Clark electrode was connected to a homebuilt potentiostat connected to a PC. The oxygen concentration in the cell was monitored as a function of the illumination time using homebuilt Labview software. *Figure 2.3* shows an outline of the Clark electrode employed during this thesis.
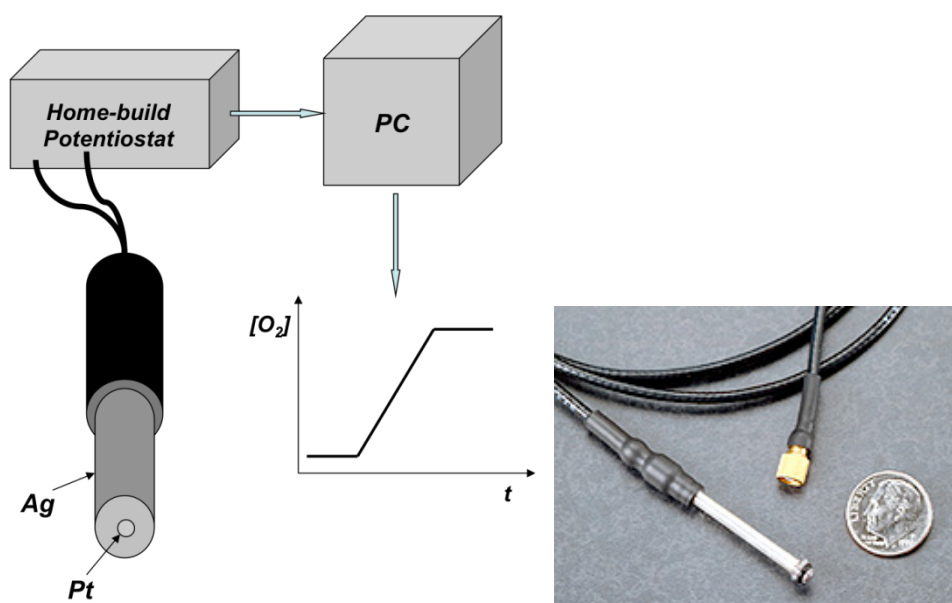
Figure 2.3: Outline of the system used to measure oxygen evolution. A commercial Clark electrode consisting in a Pt cathode and an Ag/AgCl anode is connected to a homebuilt potentiostat. By applying an external bias between cathode and anode the oxygen that reaches the cathode is reduced producing a current. Current versus time graphs are then recorded using a PC with a Labview software. The picture on the right has been reproduced from reference 55.

Next to the cathode the concentration of oxygen is zero, therefore a concentration gradient appears across the membrane resulting in the diffusion of oxygen through it. The concentration of oxygen in the bulk solution affects the rate of oxygen flow and therefore the current.[55]

2.2 Sum Frequency Generation Spectroscopy

The SFG setup was based on a Spectra-Physics laser system which included a Spitfire Pro XP Ti:Sapphire regenerative amplifier pumped by an Empower frequency-doubled Nd:YFL laser and seeded by a Tsunami mode-locked laser operating in the femtoseconds. 1 ps pulses at around 800 nm were generated at 1 kHz with a energy of ~2 mJ. The as-generated laser beam was split in two halves; one half was used to pump an optical parametric amplifier (OPA-800C) aligned, motorised and calibrated to deliver infrared light tuneable between 2700 and 3200 cm^{-1}. The other half passed through an empty OPA to remain at 800 nm. *Figure 2.4* shows an outline of the system used during the course of this work. The same laser system was used in various experiments, therefore part of the outline (OPAs 1 and 2) refers to another system but has been included in the scheme for completeness. Prior to the measurements, the wavelength of the IR beam was calibrated using a monochromator (Newport 77700). The visible beam passed through a delay stage in order to have spatial and temporal overlap with the IR beam at the sample area and obtain SFG generation. The signal was then detected using a photo multiplier (Hamamatsu H7422-40) connected to a PC through a National Instrument interface and with a homebuilt Labview program.

The samples were placed in a commercial cell Harrick (DLC525) and SFG was recorded in transmission mode.
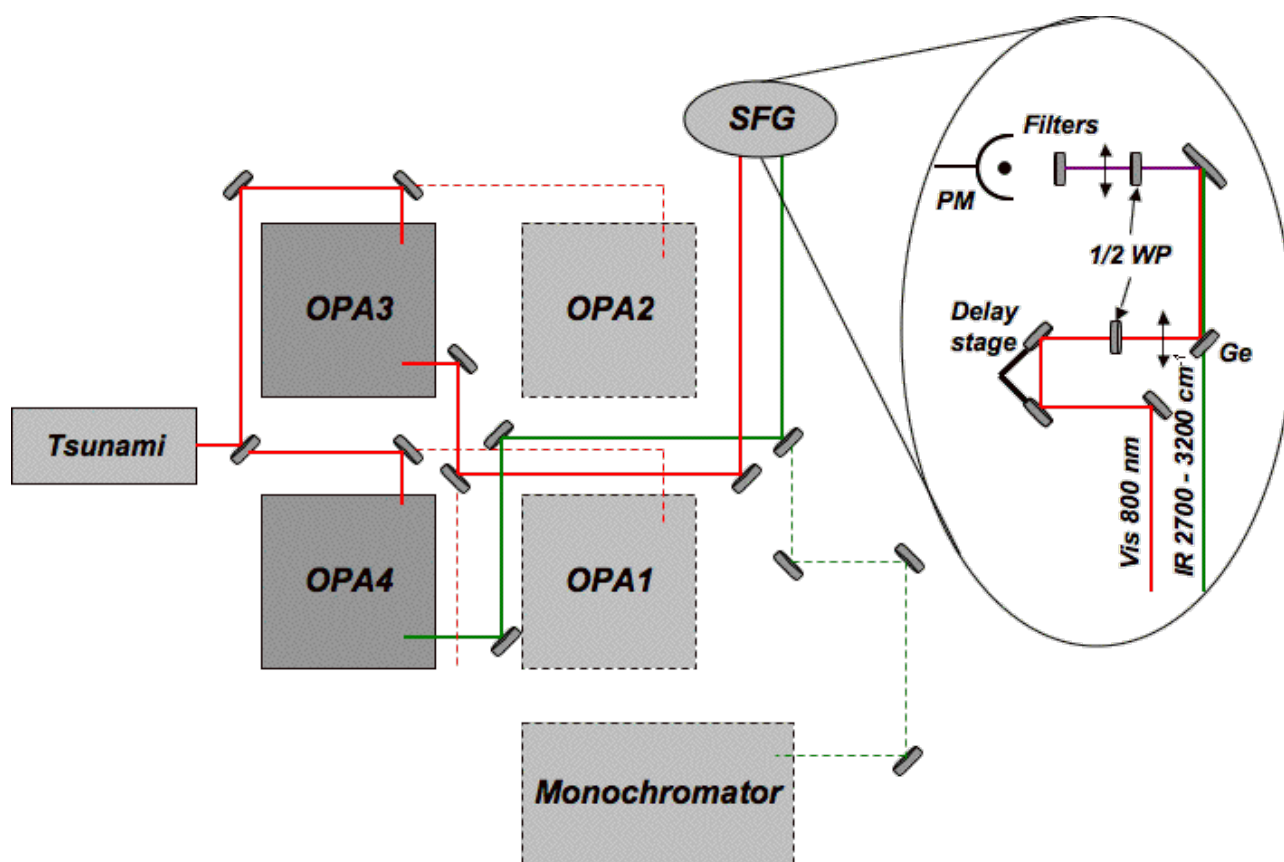
Figure 2.4: *Outline of the SFG system employed during the course of these PhD studies. Half of the laser beam passes through an OPA-800C aligned, motorised and calibrated between 2700 and 3200 cm^{-1} (IR beam) while the other half passes through an empty OPA (Vis beam). The Visible beam then passes through a delay stage in order to control the temporal overlap with the IR beam on the sample. SFG signal is detected by a PM connected to a gated integrator (Boxcar) and interfaced to a PC using National Instrument hardware. The control and signal acquisition is done using a homebuilt Labview program.*

2.3 Luminescent Solar Concentrators

The LSC plates used during the course of these thesis studies were prepared by the Chatten group in the Imperial College Department of Physics. A general description of the principle of operation of a LSC can be found in Section 1.3.2.

As already noted (Section 1.3.2), an LSC is a non-imaging optical device consisting of a transparent plate doped with a luminescent species which absorb incident solar radiation and re-radiate it at a red shifted wavelength with high quantum efficiency. Two LSC plates were prepared and characterised.

A 10 cm x 10 cm x 0.5 cm glass plate was used as substrate and a thin film was wire bar coated on it. The solution employed to make the thin film consisted of a matrix (a mixture of poly methyl methacrylate (PMMA) crystals and poly lauryl methacrylate (LMA) in a 85:15 ratio) with a total mass of 4 g dissolved in 10 ml of chlorobenzene in which was dissolved a dye species. Two LSC plates with different absorption and emission profiles were prepared by adding to the matrix 2.5 (wt)% of Fluorescent Violet (Kremer) and 5 (wt)% of Lumogen red 305 solutions respectively. The concentration of the dyes was chosen in order to optimise the absorption of light at the relevant wavelength.[57] More details on the preparation of the LSC plates are given in Chapter 6.

Materials

During the course of this research three main materials have been employed in PEC cells.

- TiO$_2$ electrodes were screen-printed by the author from a TiO$_2$ paste (obtained from Dr Xiao Li) of ~15 nm anatase TiO$_2$ nanoparticles (Durrant Group, Chemistry Department, Imperial College London);

- Hydrogen-treated TiO$_2$ (H:TiO$_2$) nanowires were prepared by Prof Yat Li (University of California, Santa Cruz);

- WO$_3$ electrodes were prepared by Dr Bruce Alexander (University of Greenwich);

- α-Fe$_2$O$_3$ electrodes were prepared by Dr Anna Hankin (Geoff Kelsall Group, Chemical Engineering Department, Imperial College London).

2.4   TiO$_2$

Nanocrystalline (nc) anatase TiO$_2$ electrodes were prepared by a doctor blade deposition of TiO$_2$ paste on a conductive fluorine doped tin oxide (FTO) glass substrate. Detailed information on the paste preparation procedure can be found in reference 58.[58] Prior to depositing the TiO$_2$, the substrate was cleaned by two successive sonications of 30 minutes each in acetone and deionised water, dried in air and heat treated (450 °C for 30 minutes) in order to remove any possible organic contamination left on the surface. A colloid paste with 15 nm TiO$_2$ particle size was spread on the surface of the FTO glass, the films were dried in air for 20 minutes and calcined at 450°C in air for 30 minutes in order to remove the organic components present in the paste. The thickness of the films was measured with a profilometer (Alpha-Step 200, Tencor Instruments). During TAS experiments films with a thickness of ~4 μm were employed. *Figure 2.5* shows a SEM

image of a similar nanocrystalline TiO_2 film at high resolution. Before any experiment, each film was heat treated at 450°C for 30 minutes in order to remove possible impurities.
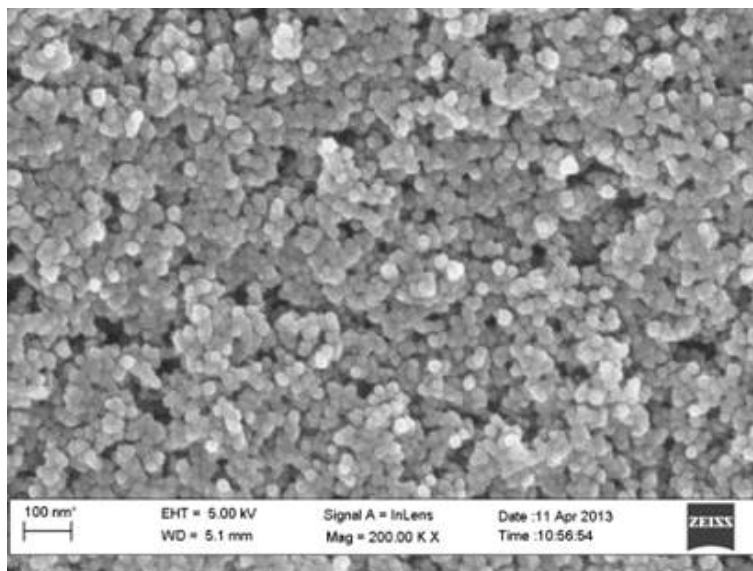
Figure 2.5: *SEM image of a 4 μm thick TiO_2 electrode. Image courtesy of Dr Xiaoe Li.*

During SFG spectroscopy measurements the FTO glass substrates were replaced with CaF_2 windows in order to allow the IR beam to be transmitted. Details on the preparation of these samples can be found in section 5.3.2.

2.5   H:TiO_2 nanowires

Hydrogen-treated nanowires were prepared by electrochemical anodisation as described in several recent reports and were deposited on a fluorine-doped tin oxide (FTO) glass.[59] Rutile TiO_2 nanoarrays were characterised by nanowire bundles of 100 – 200 nm diameter consisting of individual 10 – 20 nm diameter elements with a typical lengths of 2 – 3 μm. The as prepared samples were annealed in air at 550 °C for 3 hours or under a hydrogen atmosphere at 350 °C for 30 minutes in order to prepare air-treated (A:TiO_2) or hydrogen-

treated (H:TiO$_2$) photoelectrodes respectively. *Figure 2.6* shows a SEM image of TiO$_2$ nanotube arrays prepared by electrochemical anodisation on a FTO substrate. This figure has been reproduced from reference 42.
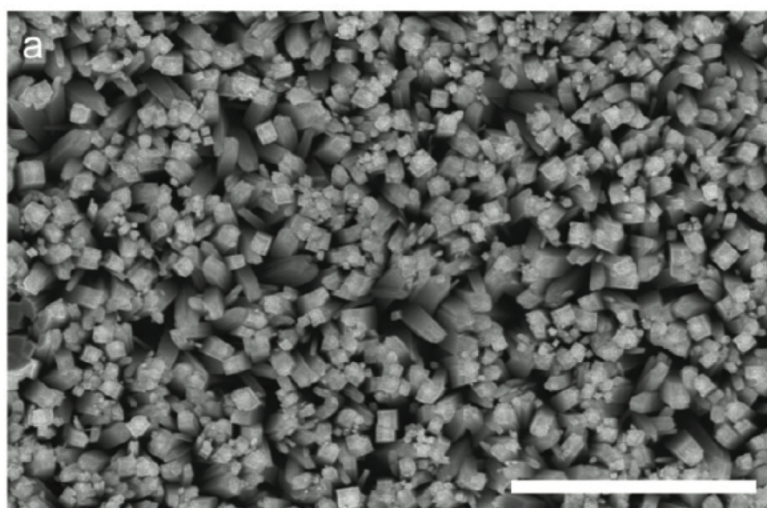
Figure 2.6: *SEM image of TiO$_2$ nanotube arrays prepared by electrochemical anodisation on a FTO substrate. Figure reproduced from reference 42.*

2.6   WO$_3$

WO$_3$ electrodes were prepared on a conductive indium tin oxide (ITO) glass substrate by depositing polytungstic acid/PEG 300 obtained by the passage of a solution of Na$_2$WO$_4$ through a cation exchange column. A detailed description of the procedure employed can be found in reference 60.[60] Electrodes with three different thicknesses were prepared by depositing three, six or nine layers (~1.2 μm per layer). The electrodes were annealed at 550 °C in order to remove the organic component and to form well-crystallised WO$_3$. Before each experiment the electrodes were heat treated at 400 °C for 30 minutes in order

to remove possible organic impurities. *Figure 2.7* shows a SEM image of a three-layer electrode
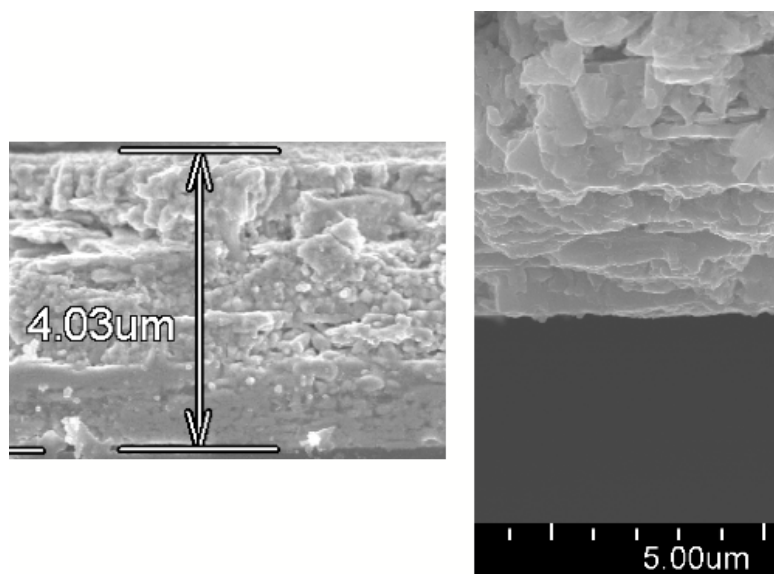
Figure 2.7:   *SEM images of a 4 μm thick WO$_3$ electrode. Image courtesy of Dr B. Alexander.*

2.7 α-Fe$_2$O$_3$

Hematite electrodes were prepared by Chin Kin Ong and Anna Hankin (Chemical Engineering Department, Imperial College London), who also provided the description of the procedure used in this section. Iron oxide electrodes were prepared using spray pyrolysis on a TEC-8 fluorine-doped tin oxide (FTO) coated glass substrate (Hartford Glass Inc., USA).[61] The FTO substrate (120 mm x 13 mm) was first cleaned with acetone and then with high purity water in an ultrasonic bath for 15 minutes. A quartz nebuliser (Meinhard, US) which acted as the spray nozzle was attached onto a computer numerical control machine (Heiz T-720, Germany) at 15 cm above the substrate surface, and the Fe(III) precursor was delivered by a syringe pump at 2 cm^3 min^{-1}. The precursor solution

comprised 0.1 M $FeCl_3$ (Sigma Aldrich, UK) and 6×10^{-4} M $SnCl_2$ (Sigma Aldrich, UK) dissolved in ethanol absolute (AnalaRNormapur, VWR BDH Prolabo). Air was supplied to the nozzle at 50 psig and acted as the oxidising agent for the formation of α-Fe_2O_3. The nozzle was passed width-wise and length-wise over the heated substrate in order to ensure a uniform coating; the movement of the nebulizer was software-automated (WinPC-NC CNC Software, BobCad-CAM, USA).

40 layers of hematite, generating a ca. 200 nm film, were deposited; subsequently the sample was heat treated (Elite, UK) in air at 500 °C for 1 hour to form Sn^{IV}-Fe_2O_3. *Figure 2.8* shows two SEM images of a 200 nm thick α-Fe_2O_3 film deposited on FTO.
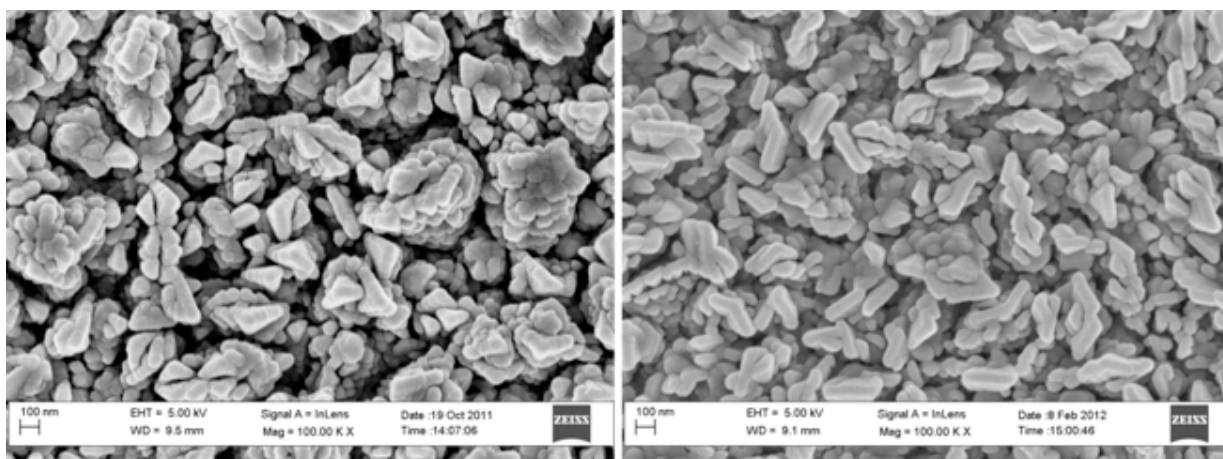
Figure 2.8*: SEM image of a 200 nm thick α-Fe$_2$O$_3$ film, Images courtesy of Dr A. Hankin.*

Chapter III

Transient Absorption Studies on WO$_3$

In this chapter results on mesoporous WO$_3$ electrodes obtained using transient absorption spectroscopy are discussed. Studies on isolated WO$_3$ films in the presence of chemical scavengers and on WO$_3$ photoanodes employed in a complete photoelectrochemical cell are reported. The identification of transient absorption signals attributable to photogenerated electrons and holes and the study of their decay under the effect of an applied bias are described.

3.1   Introduction

Thanks to its photochromic and electrochromic properties, tungsten trioxide has found many applications in the technology industry, i. e. in the fabrication of smart windows[62,63] and gas sensors.[64,65] In addition to these applications WO_3 is considered among the most suitable metal oxide semiconductors employed as a photocatalyst during photoassisted water oxidation thanks to the position of its valence and conduction bands,[19] its high reported values of IPCE[60,66,67] and its relatively high STH efficiency[8,9] (see section 1.1.3 for details).

Several different techniques have been employed to prepare nanostructured WO_3 films, such as vacuum evaporation,[68] reactive sputtering,[69] electrodeposition,[70] sol-gel methods,[58,65,66] and spry pyrolysis.[71] However, some reports suggest that the sol-gel method allows control of the film morphology, in particular their porosity.[60] At present mesoporous and nanostructured films prepared by spry pyrolysis and sol-gel routes are among the most common WO_3 electrodes employed in PEC systems because of their high surface area which could facilitate the hole transfer into solution.[17-19] Augustynski and co-workers investigated the effect of annealing temperature on the phase of WO_3 thin films prepared by sol-gel method. They found the presence of two phases (hexagonal and monoclinic) at low annealing temperatures, whereas the WO_3 was found to be only in the monoclinic phase at annealing temperatures higher than 500 °C.[66]

The effect of WO_3 particle size on its electrochemical properties has also been investigated by Lee and co-workers who determined that in photoelectrochemical systems the maximum photoactivity is provided by small crystal (60 nm particle size) because of

the reduced distance that the holes must travel to reach the SCLJ. On the other hand, the photoactivity decreases for even smaller crystals (30 nm particle size) because of dominant surface recombination.[23]

In order to further enhance the photoelectrochemical performances of WO_3, the effect of dopants has also been investigated. Augustynski and co-workers reported an improvement in the electrochromic behaviour of WO_3 using dopants such as tin, molybdenum and silicon while its electronic conductivity was significantly enhanced using ruthenium.[72] The effect of nitrogen doping has also been investigated by Cole *et al.* who found that nitrogen doping results in a decrease of the optical band-gap of WO_3 (< 2 eV) which also leads to a substantial decrease of the photocurrent density attributable to the degradation of the electron transport properties as a result of a high defect density.[73] Lewis and co-workers also recently reported a decrease in the absorption threshold of WO_3 as a result of nitrogen doping.[30] On the other hand, an increase in the photocurrent and IPCE values of WO_3 electrodes has been reported when mesoporous WO_3 is deposited on plasmonic silver nanoparticles.[74] The photocatalytic activity of WO_3 is also enhanced by surface modification by a cobalt phosphate (Co-Pi) catalyst which decreases the recombination of the photogenerated charge carriers.[75,76]

The photooxidation of water on WO_3 powder was investigated by Darwent and Mills in the presence of Fe^{3+} as an electron acceptor: oxygen evolution was found to be inhibited by Fe^{2+} and a high concentration of Fe^{3+} (see Section 3.3.1 for details).[77] Desilvestro and Grätzel also investigated the photoelectrochemical properties of polycrystalline n-WO_3 in the presence of several ions including HSO_4^-, Fe^{2+}, and Ce^{3+} which could be oxidised with faradaic efficiencies up to 100% leading to a steeper photocurrent when compared with SO_4^{2-} and ClO_4^- containing solutions.[78]

Concerns over the photoelectrochemical performances of WO_3 in different electrolytes have been recently raised by Augustinski and co-workers.[79] By comparing the photocurrent evolution in CH_3HSO_3, H_2SO_4 and $HClO_4$ as a function of illumination time they noted a current decrease in H_2SO_4 and $HClO_4$ attributable to the formation of H_2O_2 as a secondary photo-oxidation product which leads to the deactivation of the WO_3 photoanode. Whereas, the current recorded in CH_3HSO_3 was substantially higher and remained constant over an illumination period of 14 hours. Further studies on the competition between electrolyte ions and water for the WO_3 valence band photoholes have also been carried out by Lewis and co-workers, who suggested that water oxidation does not directly occur through the surface of WO_3 using electrolytes such as HCl, H_2SO_3 and $HClO_4$ but an indirect oxidation takes place involving radical electrolyte intermediates.[32,33] Details on these proposed mechanisms are given in Section 3.3.2. Although several electrochemical studies on WO_3 have been published over the last few decades, only one transient absorption study has been reported previously (by Kamat and co-workers).[43] However a better understanding of the factors that control the quantum yield of WO_3 is likely to provide insights into the engineering rules required for an efficient modification of this material for water splitting. Therefore, we decided to use TAS to investigate the dynamics of the processes involving the photogenerated charge carriers in WO_3 photoanodes.

WO_3 films prepared by sol-gel method were firstly investigated in the presence/absence of chemical scavengers in order to facilitate the identification of the transient absorption fingerprints of holes and electrons (section 3.3.1). Then they were employed as photoanodes in a complete PEC cell in order to better understand the kinetics of the charge carriers in conditions in which water oxidation is enabled (sections 3.3.2, 3 and 4).

3.2   Experimental

The samples used in the experiments discussed in this chapter were prepared in Greenwich University by Dr B. Alexander in the manner described in section 2.6. Unless where stated, the films were three layers thick (~1.2 μm each layer) and the WO_3 was deposited on ITO glass with dimensions of 1x3x0.3 cm. Prior to each experiment the samples were heat-treated at 400°C for 30 minutes to remove any possible organic contaminants. UV-Vis spectra were recorded before and after heat treatments in order to monitor any possible change in the absorption profile. *Figure 3.1* shows the recorded UV-Vis spectra.
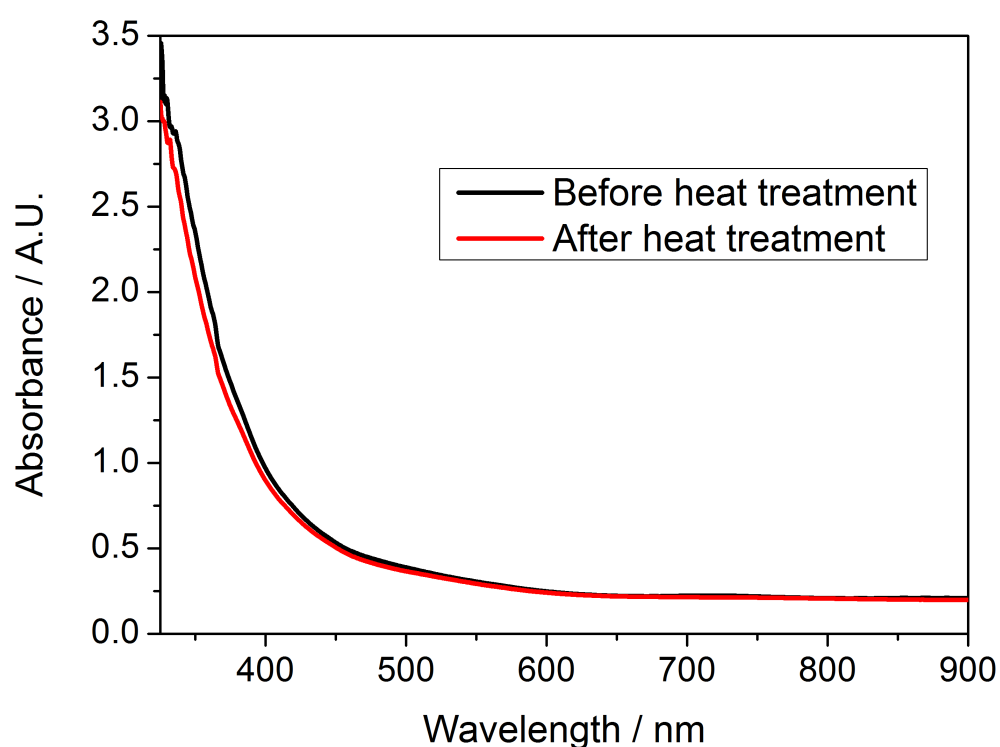
Figure 3.1:   *UV-Vis spectra recorded in air between 300 and 900 nm before (black line) and after (red line) heat treatment.*

The WO_3 was found to have an absorption edge at ~450 nm, in line with the reported value of 2.7 eV for the WO_3 band-gap. The small absorption in the region 450 – 900 nm is assigned to the light scattered by the WO_3 sample, which has a particles size of ~50 nm.

Transient absorption spectra were recorded initially under an Ar atmosphere and in the presence/absence of chemical scavengers. CH_3OH (>99.9%, Sigma Aldrich), 0.02 M $FeCl_3$ (reagent grade, Sigma Aldrich) and 0.01 M $AgNO_3$ (reagent grade, Sigma Aldrich) solutions were used in the TA experiments carried out on isolated WO_3 thin films.

For the measurements in a complete PEC cell, an electrolyte consisting of 0.5 M $NaClO_4$ (>98.0 %, Sigma Aldrich) at pH ~2, reached through addition of $HClO_4$ (ACS grade, Sigma Aldrich) was employed. TA, photocurrent, chronoamperometry and oxygen measurement experiments were carried out using the equipment described in Chapter 2. Unless stated, the laser energy used during TA measurements was ~250 $\mu J/cm^2$ at the sample and the samples were irradiated from the substrate/electrolyte (SE) side with an average of 1000 laser shots for each wavelength examined. No substantial differences in the response of all the WO_3 electrodes used during the course of these thesis studies were noted.

3.3 Results and Discussion

3.3.1 Initial Transient Studies on Isolated WO_3 Films – Electron and Hole Absorption Features

The results reported in this section have already been published by the author of the thesis and some of the figures used are adapted from *J. Phys. Chem. Lett.*, **2011**, 2, 15, pp 1900–1903 (Reference 13).

Following heat treatment the TA traces and spectrum of an isolated WO$_3$ film were recorded in an Ar atmosphere in the region 450 – 950 nm and are reported in *Figure 3.2*.
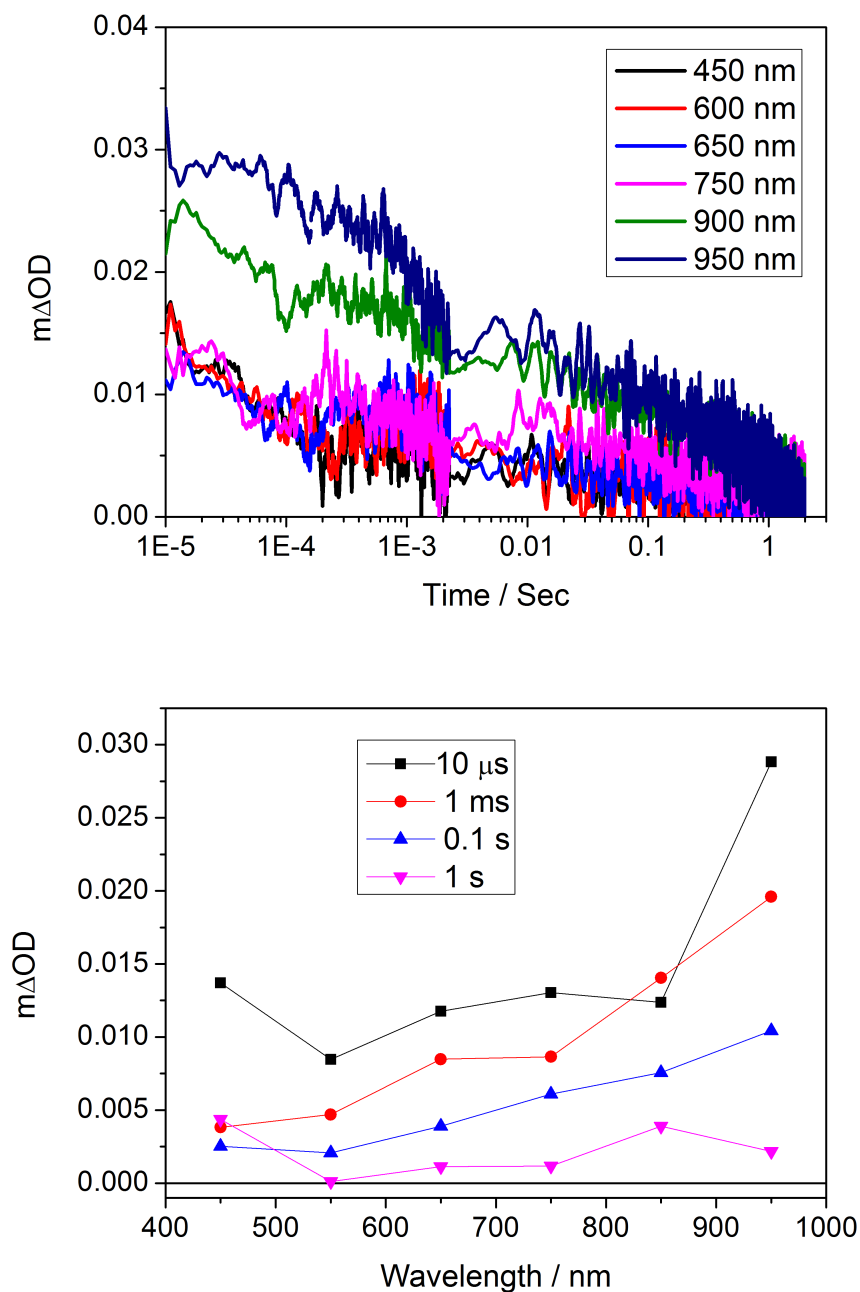
***Figure 3.2**: Transient absorption decay traces (top) and spectrum (bottom) recorded in an Ar atmosphere following UV excitation (355 nm, 0.33 Hz, 250 $\mu J/cm^2$) of a WO$_3$ film illuminated from the SE side.*

In the absence of any chemical scavenger the TA signal is relatively weak at the wavelengths examined when compared with comparable TA data from other metal oxide photoelectrodes such as TiO_2 and α-Fe_2O_3 (which are an order of magnitude stronger).[14,44,45] However, we do note an increase of the TA signal amplitude with increasing wavelengths. The weakness of the transient signal is proposed to be due to fast electron/hole recombination, which is expected to be the main process involving the photogenerated charge carriers in an inert atmosphere. A previous microwave spectroscopy study on a similar mesoporous WO_3 film also suggested that >80% of electron/hole recombination occurs very fast, within 500 ns from UV excitation (using a higher laser energy, ~2.3 mJ/cm^2).[80] This fast process would in fact give rise to a very weak TA signal in the microseconds to seconds timescales.

Electron/hole recombination is also believed to be the predominant process when a WO_3 film is immersed in an electrolyte in the absence of any applied bias. In order to determine the best excitation intensity to use during TAS measurements, it is necessary to investigate the dependence of electron/hole recombination rate on the intensity of the incident laser light. The TA traces of the charge carriers (assigned to photoelectrons in the following subsection) were recorded at 900 nm in an aqueous solution of $NaClO_4$ (0.5 M) at pH 2 ($HClO_4$) between 18 and 1500 μJ/cm^2, *Figure 3.3*.
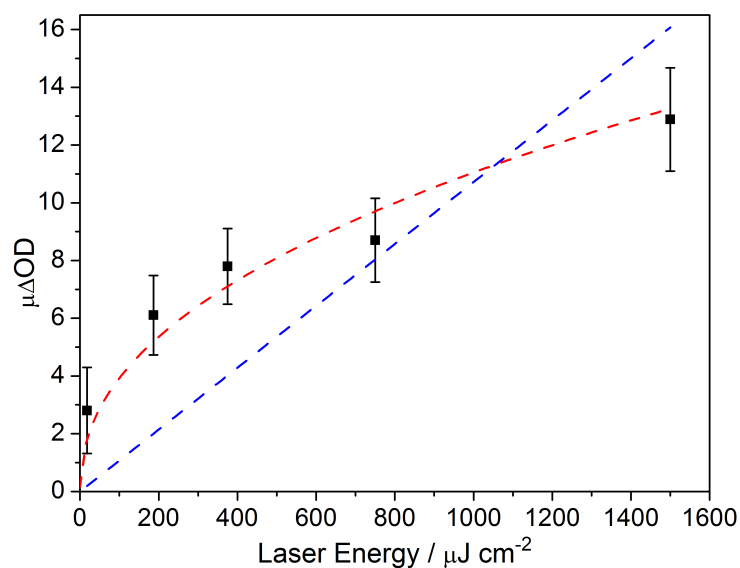
Figure 3.3: *Dependence of the WO$_3$ photogenerated electron transient absorption signal on the UV excitation intensity. The kinetic traces were recorded after 10 μs from UV excitation at 900 nm between 18 and 1500 $\mu J/cm^2$ in NaClO$_4$, 0.5 M, pH 2. The blue line shows a linear fitting while the red line is a non-linear fitting of the form y=Ax^b with b~0.5. (Figure adapted from reference 13)*

The recombination shows a non linear dependence on the laser energy. The TA signal amplitude is well fitted by a power function of the form $y=Ax^b$ where b~0.5. The amplitude of the signal, which reflects the relative electron population in the conduction band, tends to saturation with increasing laser energy, indicating increasing rate of electron/hole recombination with increasing pump intensity. These results could suggest that a certain population of electrons relaxes into deep trap states until these states are saturated and the deep-trapped electrons avoid initial recombination with the holes. These results also suggest the need to carry out transient experiments using an excitation intensity which is low enough to simulate solar fluxes as recombination, transfer and transport kinetics are likely to be highly dependent on the nature of the trap states populated, which will vary with excitation density

In order to minimise electron/hole recombination and to facilitate the identification of the transient absorption fingerprints of electrons and holes, it is necessary to isolate one of the two charge carriers by the use of a chemical scavenger. A charge scavenger is usually a chemical which selectively quickly removes either photogenerated electrons or holes minimising charge carrier recombination, as showed in *Figure 3.4*. Several examples of hole and electron scavenging are reported in the literature. Commonly used hole scavengers are ethanol and methanol, whereas ions Ag^+ or Fe^{3+} are usually employed as electron scavengers.
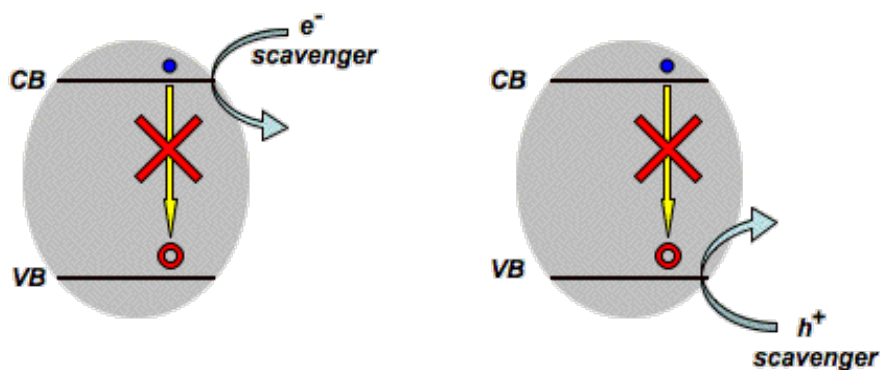
***Figure* 3.4:** *Pictorial representation of the role played by a charge scavenger on an excited metal oxide semiconductor. Following UV excitation, a chemical scavenger can be employed to selectively remove electrons (left) or holes (right) minimising charge carrier recombination and facilitating the identification of the absorption features of the carrier left in the sample.*

The fast scavenging of photoholes by CH_3OH has been reported and used to identify the photoelectron absorption features in TiO_2.[16] Also, photoelectrochemical studies carried out in the past on a WO_3 based system have shown that the addition of CH_3OH to an aqueous electrolyte significantly enhances the anodic photocurrent indicating that the photoholes in WO_3 can easily oxidise methanol.[81] In light of these facts CH_3OH was employed in this work as a hole scavenger with the aim of identifying the electron signal.

A WO$_3$ film was placed in a glass cuvette containing ~10 ml of methanol and the solution was bubbled with Ar for 20 minutes in order to remove any dissolved oxygen. The TA traces and spectrum were recorded in the region 450 -950 nm and are shown in *Figure 3.5.*
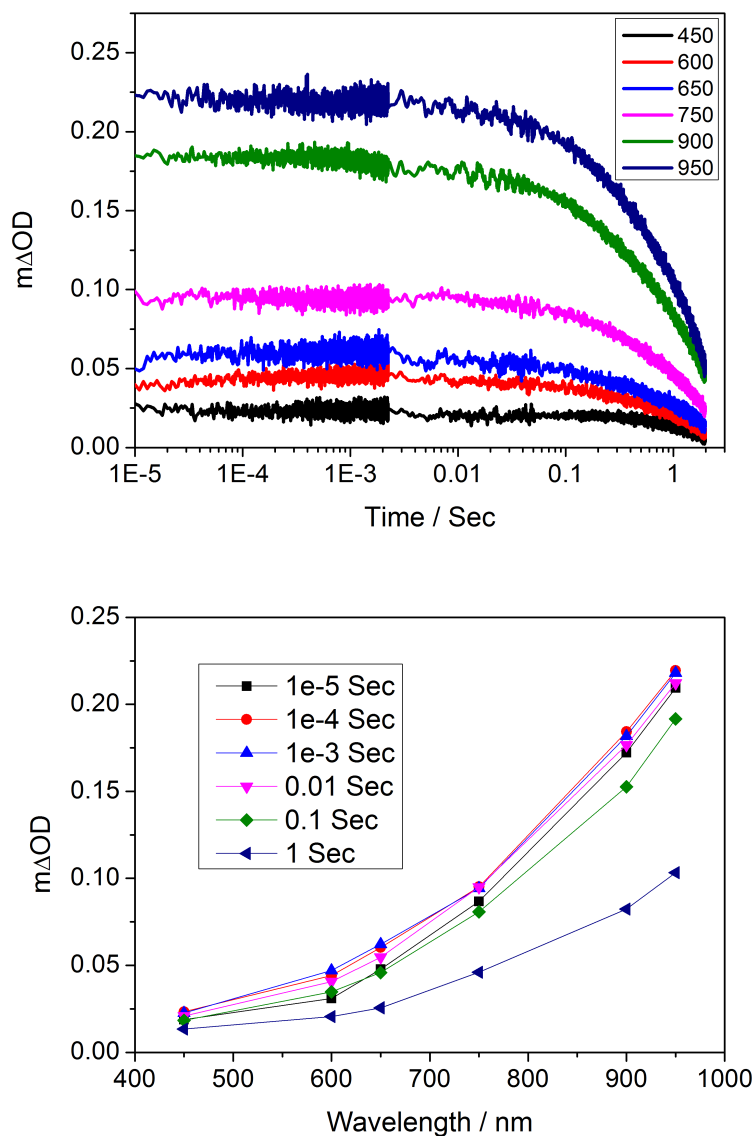
Figure 3.5: *Transient absorption decay traces (top) and spectrum (bottom) recorded in CH$_3$OH (99%) following UV excitation (355 nm, 0.33 Hz, 250 μJ/cm^2) for a WO$_3$ film illuminated from the SE side.*

From *Figure 3.5* it is observed that the signal amplitude increases with increasing wavelength. From the comparison of the spectra recorded in Ar and methanol (*Figure 3.6*), it is apparent that the addition of methanol results in a strong increase in TA signal amplitude (~10 times) at wavelengths >700 nm suggesting that we are looking at a broad electron signal.
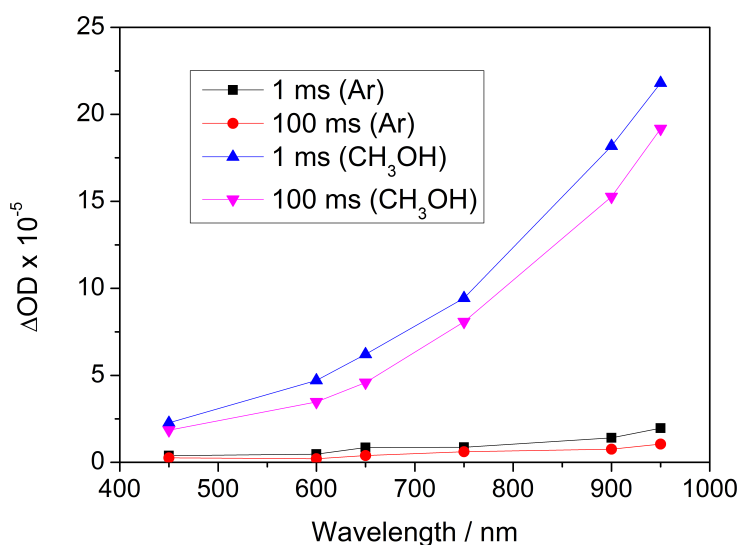
Figure 3.6: Transient absorption spectra recorded at 1 and 100 ms in the presence/absence of CH$_3$OH (99%) as a hole scavenger following UV excitation (355nm, 0.33 Hz, 250 μJ/cm^2) of a WO$_3$ film illuminated from the SE side. Figure adapted from reference 13

The signal assigned to the photogenerated electrons however does not decay completely after 3 seconds following the UV excitation (*Figure 3.5* top). This is attributable to a very slow electron scavenging reaction possibly by any residual oxygen or methanol oxidation intermediates within the cell.

Examples of electron scavenging by ions Fe^{3+} and Ag^+ on WO_3 have been reported in the past by Mills and Grätzel,[77,82] and the use of both these chemical scavengers presents both advantages and disadvantages. Fe^{3+} is known to scavenge electrons via a reversible reaction; equations 3.1 and 3.2 show that the same sample can be used in consecutive experiments.

$$2H_2O + 4Fe^{3+} \xrightarrow{\ hv,WO_3\ } 4Fe^{2+} + O_2 + 4H^+ \qquad \text{Eq. 3.1}$$

$$Fe^{2+} + h^+ \rightarrow Fe^{3+} \qquad \text{Eq. 3.2}$$
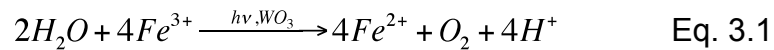
Following initial charge carrier separation within the semiconductor, it is proposed that Fe^{3+} rapidly scavenges conduction band electrons leading to the formation of $Fe^{2+}_{(aq)}$. However, it is known that $Fe^{2+}_{(aq)}$ is itself an active hole scavenger leading to a kinetic competition with the desired process of water oxidation. This competition leads to low quantum yield for the scavenging reaction.

Ag^+ ions are known to efficiently scavenge electrons because of the irreversibility of their reduction on the WO_3 surface (equation 3.3). However, the reduction of Ag^+ leads to the coating of the film with Ag nanoparticles that can have distinct UV absorption features[83] and prevents the reuse of the same sample in different sets of experiments.

$$2H_2O + 4Ag^+ \xrightarrow{\ hv,WO_3\ } O_2 + 4H^+ + 4Ag \qquad \text{Eq. 3.3}$$
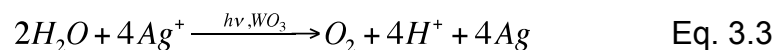
The TA spectra of UV excited WO_3 in the presence of ions Fe^{3+} and Ag^+ ions were recorded in the 450- 950 nm region averaging 500 shots for each wavelength examined.

Prior to any measurement, both the solutions were bubbled with Ar for 20 minutes in order to remove any dissolved oxygen which could compete with the scavengers by reaction with conduction band electrons. *Figure 3.7* shows the spectra recorded in FeCl$_3$ (top) and AgNO$_3$ (bottom).
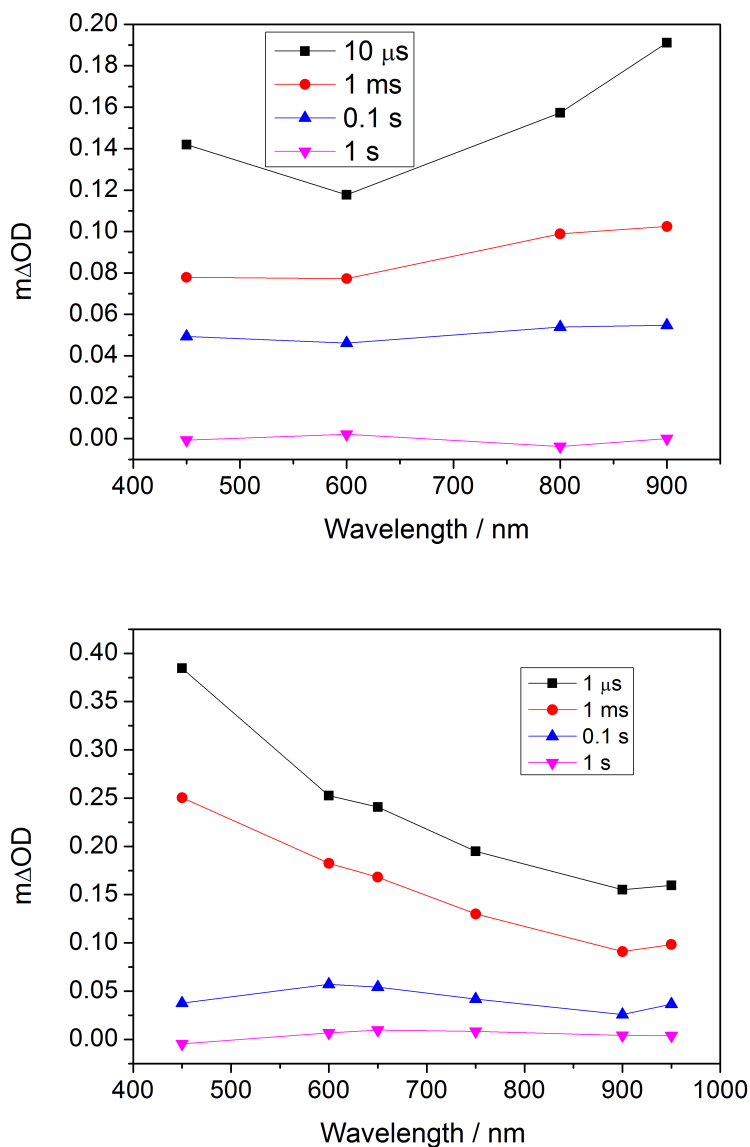
Figure 3.7*:   Transient absorption spectra recorded in the presence of 0.02 M FeCl$_3$ (top) and 0.01 M AgNO$_3$ (bottom) following UV excitation (355 nm, 0.33 Hz, 250 μJ/cm^2) of a WO$_3$ film illuminated from SE side.*

In the presence of $FeCl_3$ the amplitude of the TA signal is enhanced at both short and long wavelengths; the signal at short wavelengths could be attributable to the presence of long-lived holes which are prevented from recombining with the electrons due to the reversible scavenging of photoelectrons by Fe^{3+}. The low scavenging efficiency of Fe^{3+} mentioned above could explain the presence of a strong signal at long wavelengths which has been assigned to the photoelectrons.

It is also important to note that both Fe(III) and Fe(II) absorb in the visible region and this could lead to misinterpretation of the TA spectrum, hence, in order to minimise any contribution from the scavenger absorption to the TA data, a low concentration of $FeCl_3$ was used, leading to very low reaction yield. However, the TA spectrum recorded in $FeCl_3$ is difficult to interpret and it is not possible to rule out any contribution from the Fe(III) and Fe(II) species. Therefore, the scavenging effect of Ag^+ ions was also examined. The spectrum recorded in $AgNO_3$ shows a strong increase in the amplitude of the signal at short wavelengths suggesting a higher scavenging efficiency of Ag^+, and also the presence of TA signal at long wavelengths at 0.1 seconds, which could indicate slow electron scavenging by Ag^+. This spectrum was recorded after leaving the WO_3 sample immersed in $AgNO_3$ in the dark for 12 hours in order to allow the $AgNO_3$ molecules to penetrate the sample and be more accessible by the conduction band electrons.

When comparing the spectra recorded in $AgNO_3$ and in an Ar atmosphere (*Figure 3.8*) it is evident that at early times the signal at short wavelengths increases ~40 times in the presence of $AgNO_3$, providing confirmation of the assignment of the hole signal at 450 nm.
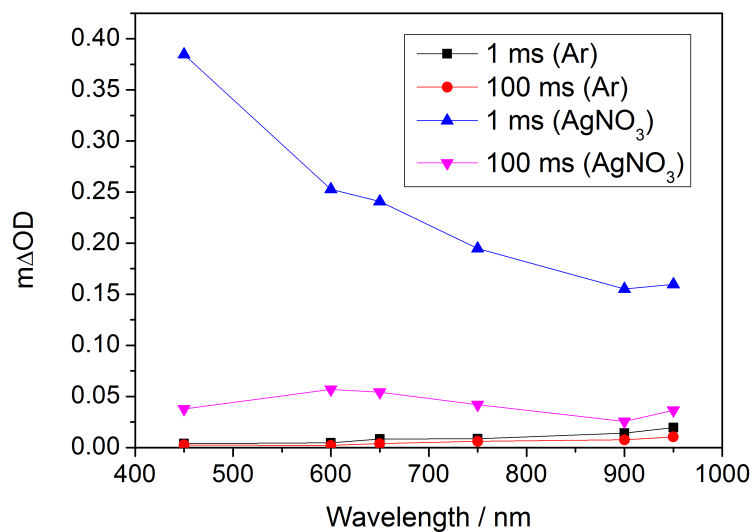
Figure 3.8: *Transient absorption spectra recorded in the presence/absence of 0.01 M AgNO$_3$ at 1 ms and 100 ms after UV excitation (355 nm, 0.33 Hz, 250 μJ/cm^2) of a WO$_3$ film illuminated from the SE side. Figure adapted from reference 13.*

As mentioned above, the irreversible reduction of ions Ag$^+$ leads to the deposition of Ag nanoparticles on the WO$_3$ surface, which could lead to characteristic absorption features and complication of the TA spectrum. Therefore, it was necessary to record a TA spectrum in the presence of both AgNO$_3$ and CH$_3$OH in order to rule out the possibility of the TA hole signal being due to the absorption of silver nanoparticles. *Figure 3.9* shows the recorded TA spectrum at 1ms in the presence of both electron and hole scavengers compared with the spectrum recorded in the presence of solely AgNO$_3$. In the 450–500 nm region it is not possible to identify a distinct absorption when both scavengers are presents, confirming the assignment of this absorption to be due exclusively to the presence of the hole signal.
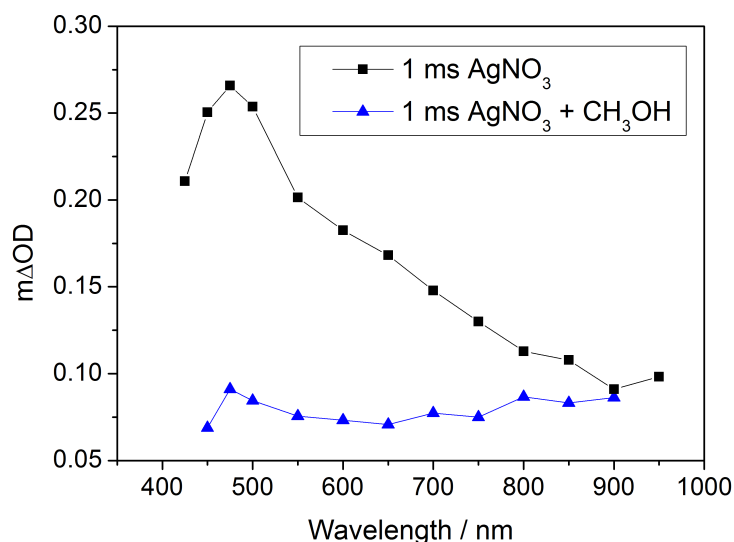
Figure 3.9: *Transient absorption spectra recorded in solely AgNO₃ (blue line) and both AgNO₃ and CH₃OH (black line) at 1 ms after UV excitation (355 nm, 0.33 Hz, 250 µJ/cm²,) of a WO₃ film illuminated from the SE side. Figure adapted from the supporting information of reference 13*

The scavenging efficiency of AgNO₃ can be confirmed by qualitatively detecting the oxygen evolved when the WO₃ sample is exposed to UV irradiation. In fact, following UV excitation and in the presence of an efficient electron scavenger, holes are left in the WO₃ valence band and can react with water leading to oxygen evolution as described in equation 1.2. The irreversible scavenging of photoelectrons by Ag$^+$ is expected to lead to photoholes with a lifetime long enough to enable water oxidation.

A WO₃ sample was immersed in a 0.01 M AgNO₃ solution placed in a glass chamber kept at a constant temperature (293 K) using a thermostat (Grant LTD6G) and the increase of current due to an oxygen concentration rise in bulk solution was detected using the Clark electrode described in section 2.1.5. The solution was stirred at a constant speed and the WO₃ sample was irradiated using a Xe lamp (150W (Photophysics), using a KG1 filter). The current was recorded for 500 seconds in the dark in order to ensure that the reading

was stable, then was recorded for 1000 seconds when the WO$_3$ film was under UV illumination and again for 1000 seconds in the dark at the end of the experiment. The reading of the Clark electrode (in a.u.) versus time is shown in *Figure 3.10* for a WO$_3$ photoanode in an AgNO$_3$ solution (black line) and in milliQ water (red line).
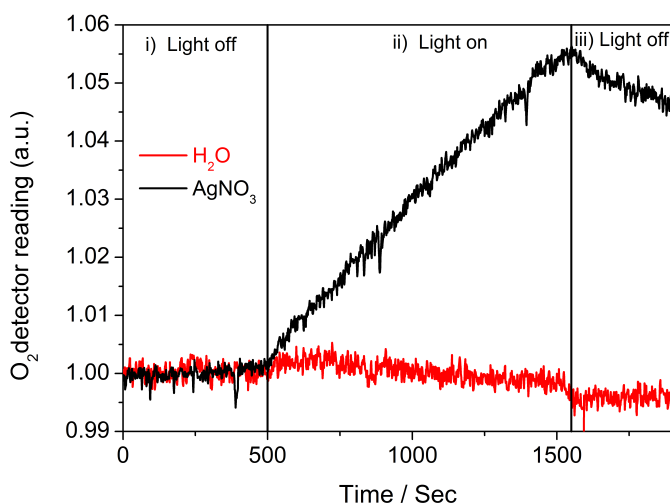
Figure 3.10: *Graph showing the Clark electrode reading versus time when a WO$_3$ film is immersed in a 0.01 M AgNO$_3$ solution (black line) and in milliQ water (red line). The film was i) kept in the dark for 500 seconds, ii) exposed to UV illumination for 1000 seconds and iii) kept again in the dark for 500 seconds. The rise in the O$_2$ detector reading in (ii) suggest that oxygen evolution is occurring at the WO$_3$ surface thanks to the oxidation of water by long-lived photoholes. Figure adapted from reference 13*

The oxygen reading is constant and stable in the first 500 seconds when the sample is kept in the dark (i), prior to a sharp increase when the WO$_3$ film is exposed to UV irradiation (ii), confirming that water oxidation occurs in the presence of a chemical scavenger capable of removing electrons and leaving solely photogenerated holes. The lack of further increase in the O$_2$ reading when the UV light is switched off again (iii)

confirms that water oxidation occurs due to the presence of long-lived photoholes when the WO_3 is under UV light. In the absence of an electron scavenger (red line), the slow and linear decay of the signal when under UV illumination (ii) suggests that the O_2 dissolved within the cell is consumed with a zero order kinetics as already shown in previous publications [16,84] and is ascribed to O_2 reduction by photoelectrons.

In other metal oxide semiconductors (i.e. TiO_2 and α-Fe_2O_3) the capability to oxidise water has been attributed to the presence of long-lived photoholes with lifetimes of 0.3 – 3 s.[14,15,44,85] *Figure 3.11* shows the WO_3 hole and electron kinetic traces recorded in the presence of Ag^+.
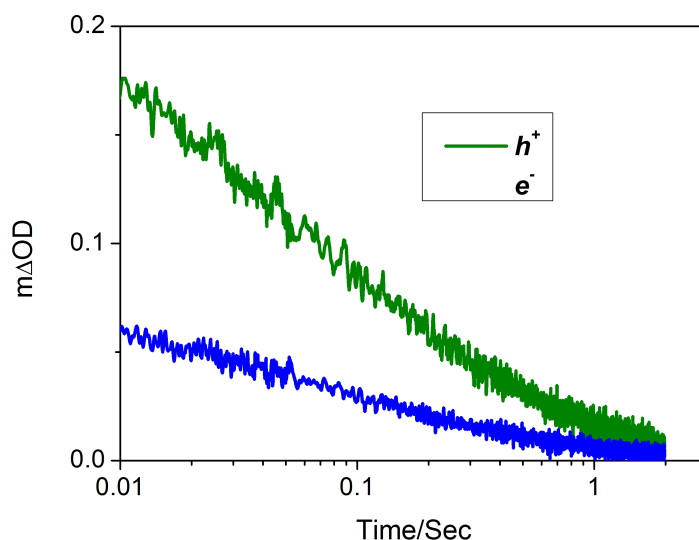
Figure 3.11: *Transient absorption decay traces recorded at 450 nm (h^+, green line) and 900 nm (e^-, blue line) in 0.01 M $AgNO_3$ following UV excitation (355 nm, 0.33 Hz, 250 $\mu J/cm^2$) of a WO_3 film illuminated from the SE side.*

It is noted that the hole trace (green line) fully decays only on the seconds timescale suggesting the presence of long-lived holes. In the following section we examine the slow rate of hole decay under conditions where PEC water oxidation occurs.

3.3.2 Transient Studies on WO$_3$ Photoelectrodes Employed in a Complete PEC Cell – Electron and Holes Signals in HClO$_4$.

In order to investigate the kinetics of the photogenerated charge carriers in conditions in which water oxidation take place, WO$_3$ has been used as photoanode in a complete PEC cell (see section 2.1.2 for details). Prior to any experiment, the samples were heat treated (400 °C for 30 minutes) and the electrolyte contained in the PEC cell was purged with argon for 20 minutes in order to remove any residual oxygen.

Before any TA measurement, current/voltage curves were recorded in order to test the photocatalytic activity of the WO$_3$ samples. *Figure 3.12* shows an example of I/V plot recorded in the dark (black dots) and under UV irradiation (red dots).
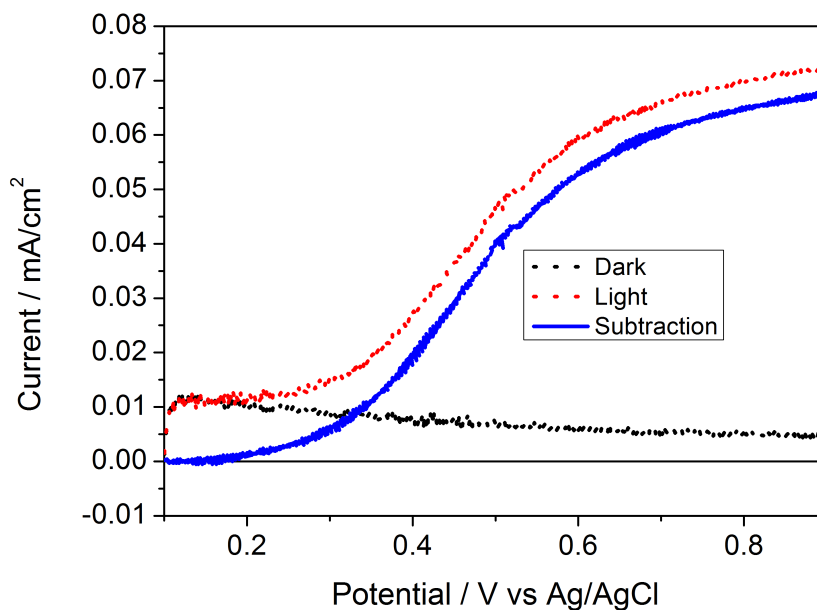
Figure 3.12: *Current vs. voltage plot recorded in the dark (black dots) and under 355 nm UV irradiation (red dots) of a WO_3 electrode in 0.5 M $NaClO_4$, pH 2 ($HClO_4$). The blue line represents the subtraction of the dark (black line) from the light (red line) current, i. e. the photocurrent. Scan rate 20 mV/sec, WO_3 W.E., Ag/AgCl (KCl 3M) R.E., Pt C.E. Illumination from the SE side*

The photocurrent (blue line) is the result of subtracting the dark current from the light current; the potential is expressed versus the Ag/AgCl reference electrode.

The photocurrent shows the onset at ~0.2 V and rises until it reaches a plateau at ~0.65 V which represents the optimal potential to be applied under PEC operational conditions and where WO_3 is expected to oxidise water under UV irradiation, in accord with other publications.[86] The TA traces and spectrum were recorded under +0.7 V (vs Ag/AgCl) applied bias. *Figure 3.13* shows the comparison between the spectra recorded under a positive applied bias (solid lines) and in an Ar atmosphere in the absence of an electrolyte and applied bias (dotted lines).
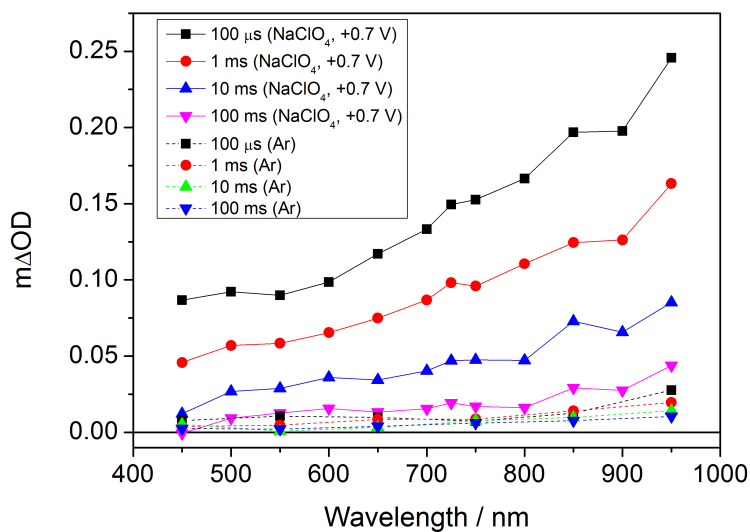
Figure 3.13: *Transient absorption spectra recorded in 0.5 M NaClO₄ (pH 2, HClO₄) at +0.7 V vs Ag/AgCl (solid lines) and in an Ar atmosphere (dotted lines) following UV excitation (355 nm, 0.33 Hz, 250 μJ/cm²) of a WO₃ electrode illuminated from the SE side.*

At early times both hole and electron signals increase when compared with the spectrum recorded under an Ar atmosphere suggesting that electron/hole recombination is minimised as an effect of applied bias as previously reported for other metal oxide photoanodes such as α-Fe$_2$O$_3$ and TiO$_2$. [14,16,44] *Figure 3.14* shows the TA kinetic traces recorded at 450 nm (holes) and 900 nm (electrons) in this experiment.
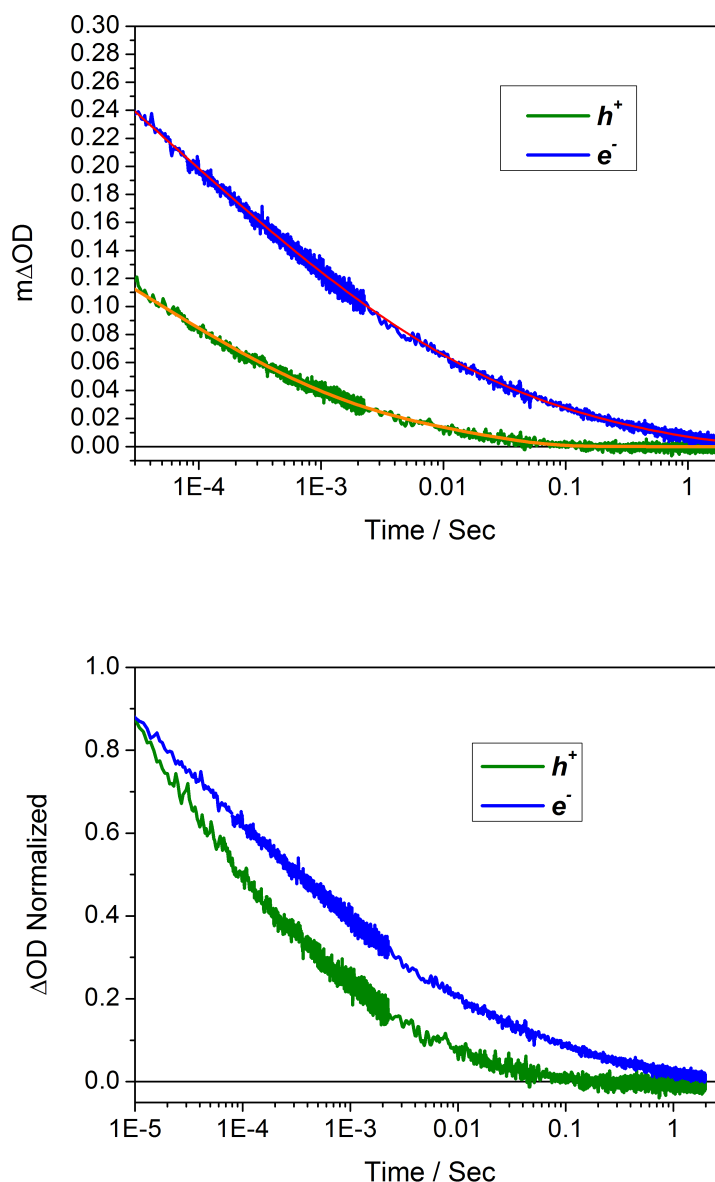
Figure 3.14: *Transient absorption decay traces recorded at 450 nm (h[+], green traces) and at 900 nm (e[-], blue traces) at +0.7 V vs Ag/AgCl following UV excitation (355 nm, 0.33 Hz, 250 $\mu J/cm^2$) of a WO$_3$ electrode illuminated from the SE side in 0.5 M NaClO$_4$ (pH 2, HClO$_4$). The raw data (top) and the normalised traces (bottom) are shown. Both traces were fitted with a combination of two stretched exponential functions (red and orange lines, top figure).*

From *Figure 3.14* it is evident that the decay of the holes (450 nm) is relatively fast, being

completed within 100 ms, non-consistent with the TA data recorded in the presence of an

electron scavenger. Both the electron and holes traces were fitted by a combination of two stretched exponential functions of the form (equation 3.4):

$$y = A_1 \cdot \exp\left(-\frac{x}{t_1}\right)^{b_1} + A_2 \cdot \exp\left(-\frac{x}{t_2}\right)^{b_2} + y_0 \qquad \text{Eq. 3.4}$$

Where the first and the second terms are used to fit the fast and slow components of the decay trace respectively, for instance electron/hole recombination and hole transfer into solution. A_1 and A_2 indicates the amplitude of the two exponential functions, t_1 and t_2 the decay time of the TA traces and b_1 and b_2 the stretching component of the functions. From the decay fittings the hole lifetime was found to be 30 ms under a positive applied bias. Given the expectation that the terminal hole reaction will be transfer into solution, we tentatively assign the required hole lifetime for oxygen evolution to be 30 ms at pH 2. The hole reaction with water, therefore, appears to be significantly faster than in other materials such as α-Fe_2O_3 ($\tau\sim3$ seconds at pH 13) and TiO_2 ($\tau\sim0.3$ seconds at neutral pH). [14,15,44,85]

Interestingly, the photoelectron decay is also extremely slow – on the order of milliseconds. The electron spectrum can be fitted with a lifetime of 0.1 seconds. This indicates that some of the electrons are not involved in fast electron/hole recombination, which has been described as one of the limiting factors in the efficiency of TiO_2.[15]

Figure 3.15 shows the kinetic traces recorded at 450 nm (green line) fitted by the combination of the two stretched exponential functions described above (red and blue lines). It is noted that the blue line better describes the early times (micro- to milli-seconds, attributable to electron/hole recombination) while the red line better describes the slow times (milliseconds to seconds, attributable to hole transfer into solution). Previous

published works have proposed that the magnitude of the stretched exponential function describing the hole transfer into solution is related to the relative hole population; in this case, being about ten times smaller than the fast component assigned to electron/hole recombination, a low quantum yield for the reaction between photoholes and water is expected.[15]
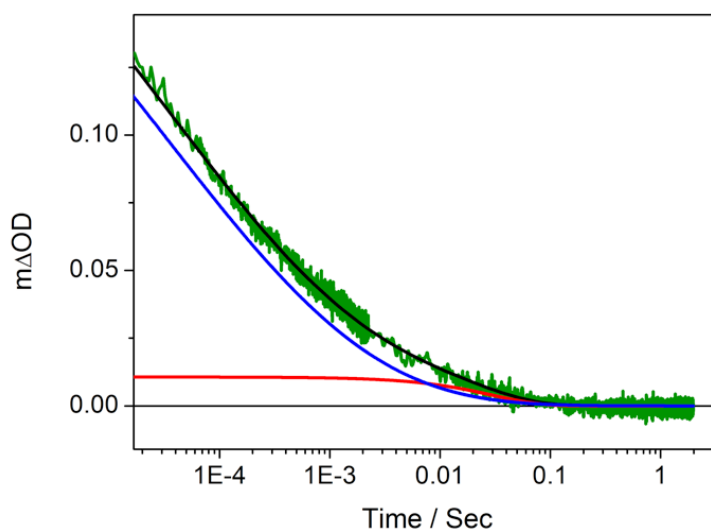
Figure 3.15: *Transient absorption decay trace recorded at 450 nm (h$^+$) at +0.7 V vs Ag/AgCl following UV excitation (355 nm, 0.33 Hz, 250 μJ/cm^2) of a WO$_3$ electrode illuminated from the SE side in 0.5 M NaClO$_4$ (pH 2, HClO$_4$) The trace is fit by a combination of two stretched exponential functions (blue and red lines).*

Using the Clark electrode described in section 2.1.5, the current rising as an effect of increasing oxygen concentration in the bulk electrolyte was recorded over time while the WO$_3$ electrode was placed under UV illumination in the presence/absence of a positive applied bias. *Figure 3.16* shows the recorded graph where the sample was constantly kept under UV illumination in a complete PEC cell; for the first 500 seconds no bias was provided in order to allow a stable reading of the oxygen sensor. When a positive external bias (+0.7 V vs Ag/AgCl) was applied to the WO$_3$ electrode for 1500 seconds the oxygen

sensor reading increased suggesting that water oxidation is taking place. The O_2 reading stabilised again when the bias was turned off.
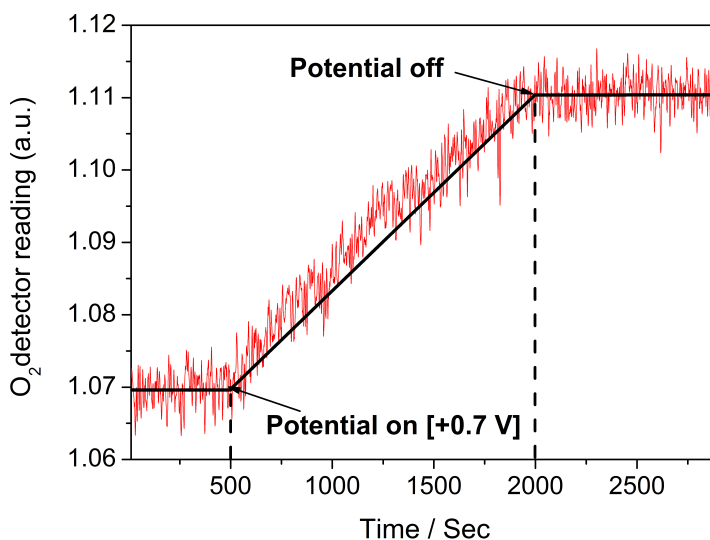
Figure 3.16: *Graph showing the Clark electrode reading versus time recorded under UV irradiation (150W Xe lamp) of a WO₃ electrode in the presence/absence of +0.7 V applied vs Ag/AgCl in 0.5 M NaClO₄ (pH 2, HClO₄).*

Although the increase in the O_2 sensor reading indicates that water is oxidised, no gas bubbles were observed at the surface of the WO_3 electrode. As discussed in the introduction of this chapter, in a recent publication Lewis and co-workers described the competition between water and anion oxidation at a similar porous WO_3 photoanodes in various electrolytes including $HClO_4$, and proposed the presence of an indirect water oxidation mechanism involving perchlorate radical formation.[32,33] This was proposed as oxygen bubbles were also not found to directly form on the surface of the WO_3 electrode. From an analysis of the positions of the redox couples accessible to the VB photoholes (*Figure 3.17*) they proposed that a strong thermodynamic driving force is required in order

to obtain direct water (or OH⁻) oxidation by the WO_3 photoholes. The mechanism of Lewis et al. is envisaged due to a proposed fast reaction between holes and the perchlorate ions which leads to the formation of a perchlorate radical (equation 3.4) and prevents the reaction between photoholes and water. An indirect mechanism of photoelectrochemical oxidation involving radical intermediates has also been proposed for different electrolytes such as HCl, CH_3SO_3H and H_2SO_4. Although the mechanisms and the intermediate involved in the photoelectrochemical oxidation of $HClO_4$ still remain unclear, they proposed that the perchlorate radical is adsorbed at the surface of the WO_3 via an O-O bond. Nevertheless perchlorate radicals do not tend to form stable peroxides in aqueous solution and, therefore, lead to the formation of oxygen as the final oxidation product.

Transient absorption spectroscopy, however, cannot directly provide experimental evidence of the nature of the intermediates involved during photocatalytic oxidation, and therefore can not prove or disprove the mechanism described above.
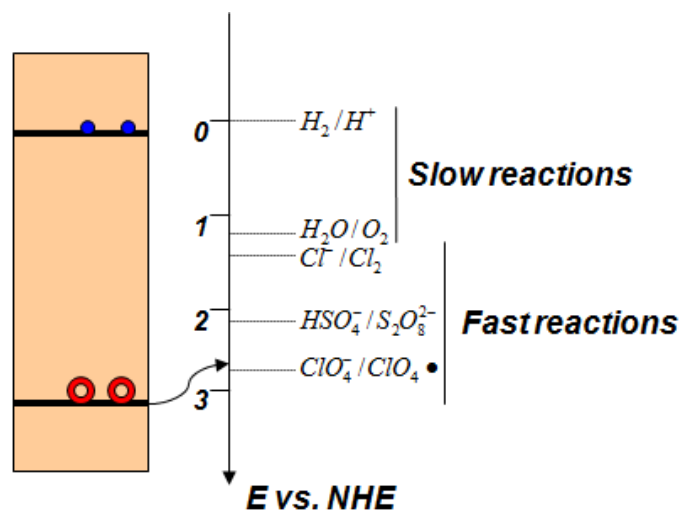
Figure 3.17: Redox couples accessible to the VB holes generated following UV excitation of a WO_3 electrode. The reactions involving the electrolytes ions are proposed to be faster than the reaction involving the H_2O/O_2 couple. (Figure adapted from reference 32)

$$ClO_{4(aq)}^- \rightarrow ClO\bullet_{(aq)} + e^- \qquad E^0 = 2.75\ V \qquad Eq.\ 3.4$$

The TA kinetic traces and spectrum of a WO_3 electrode were also recorded under 355 pulsed light and positive applied bias in the presence of 10% methanol (*Figure 3.18*). When comparing the spectra recorded in the presence/absence of methanol there is an increase in the signal amplitude at long wavelengths at early times (microseconds) attributable to the fast reaction between methanol and photoholes which prevents charge carriers recombination and is consistent with the electron signal assignment proposed in the previous section. However the signal attributable to the photoholes at short wavelengths does not change substantially in the presence of methanol. In fact, under these conditions the photoholes are likely to be rapidly scavenged by the methanol and the TA signal is expected to be weaker in amplitude. Hence any TA signals observed in the 450–500 nm region is proposed to be due to the tail of the broad photoelectron absorption. By comparing the normalised traces of the holes and electrons it can be evident that in the µs to ms region the shape of the 450 nm kinetic decay (photoholes) matches that seen at 900 nm (photoelectrons) (*Figure 3.18* top), suggesting that similar kinetics are observed. This also indicates that the transient absorption at short wavelengths could be due to an overlap of the hole and electron individual signals and, in this case, the determination of the individual components of the hole and electron lifetime are likely to be non-trivial.
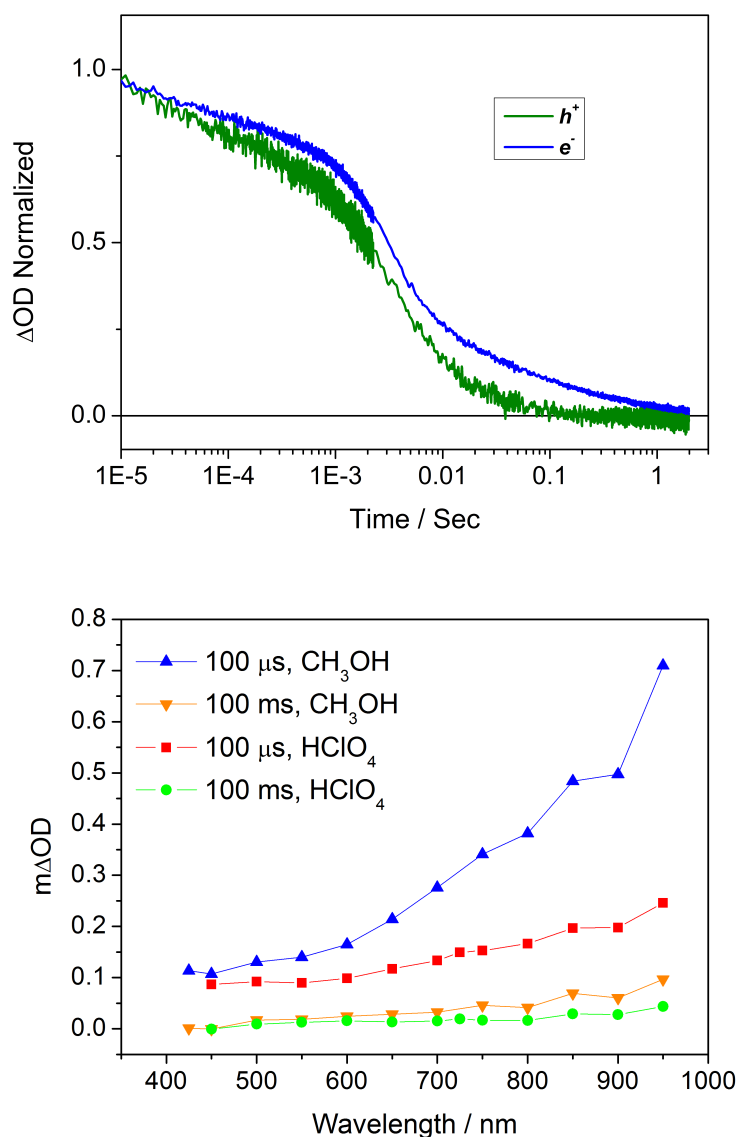
Figure 3.18: *Transient absorption decay traces (top, holes and electrons probed at 450 nm and 900 nm respectively) and spectra (bottom) recorded in 0.5 M NaClO₄ (pH 2, HClO₄) with and without the addition of 10% CH₃OH (99%) under +0.7 V applied vs Ag/AgCl following UV excitation (355 nm, 0.33 Hz, 250 μJ/cm²) of a WO₃ electrode illuminated from the SE side.*

When comparing the decay of the hole traces recorded between 100 ms and 1 sec in HClO₄, CH₃OH and methansulfonic acid (*Figure 3.19*), significant overlap in the decay kinetics are observed. This could also be due to an overlap between the hole and electron

signals at short wavelengths or could suggest that even in the absence of methanol, the photogenerated holes are involved in an equally fast process.
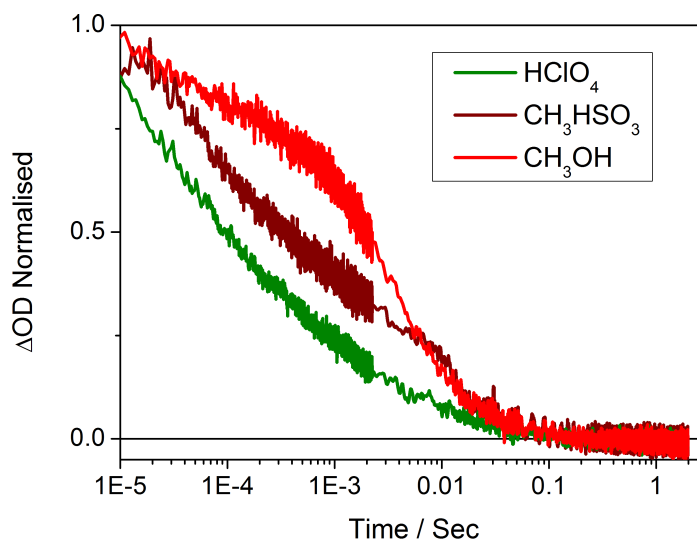
Figure 3.19: *Transient absorption decay traces of photogenerated holes recorded at 450 nm in 0.5 M NaClO$_4$ (pH2, HClO$_4$) (green line) with the addition of 10% CH$_3$OH (red line) and in 1 M CH$_3$HSO$_3$ (brown line) under +0.7 V applied vs Ag/AgCl following UV excitation (355 nm, 0.33 Hz, 250 μJ/cm^2) of a WO$_3$ electrode illuminated from SE side.*

From chronoamperometry measurements it has been possible to calculate the experimental values of IPCE% (using equation 1.7). The shape of the IPCE plot (*Figure 3.20*) matches the UV/Vis absorption spectrum for WO$_3$ (*Figure 3.1*) however the magnitude of the IPCE is significantly lower than that reported in the literature for similar WO$_3$ electrodes (80% in H$_2$SO$_4$).[66]

The low IPCE (maximum 15% at 325 nm) could be attributable to two main factors: i) the low quality of the electrodes used during the course of these experiments and ii) more significantly the IPCE values reported in the literature refer to measurements carried out in H$_2$SO$_4$.

In fact, in 1987 Desilvestro and Grätzel suggested that the high IPCE values in H_2SO_4 were due to the oxidation of SO_4^{2-} and HSO_4^{-} to form $S_2O_8^{2-}$, which was found to be the primary product of photo-oxidation over polycrystalline WO_3.[78]

Lewis *et. al* also ascribe the high photocurrent values in H_2SO_4 to the oxidation of the electrolyte rather than water, which leads to low $\eta(O_2)$.[32,33]

The low values of IPCE reported herein could also be explained by a recent study on nano-crystalline WO_3 carried out by Augustynski and co-workers which proposes the deactivation of the WO_3 surface when the measurements are carried out in $HClO_4$.[79] In fact they report the formation of hydrogen peroxide as a secondary oxidation product; the accumulation of H_2O_2 on the WO_3 surface prevents the hole transfer in solution leading to a decrease in the photocurrent over time which could explain the low IPCE values observed.
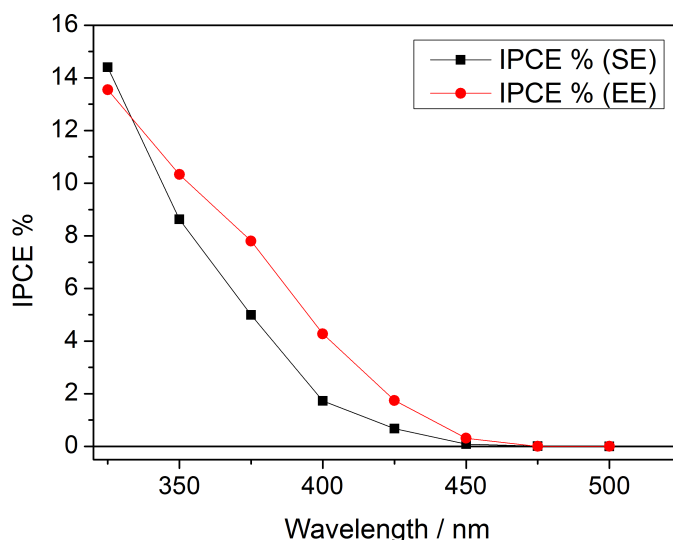
Figure 3.20: *Incident Photon-to-Current Efficiency (IPCE%) determined by chronoamperometry measurements between 300 nm and 500 nm, illuminating the WO₃ photoanode from the SE (black squares) and EE (red circles) sides in 0.5 M NaClO₄ (pH 2, HClO₄) at +0.7 V vs Ag/AgCl.*

3.3.3 Correlation of Photocurrent with Charge Carrier Population as a Function of Applied Bias.

A good correlation between photohole TA amplitude and photocurrent has been reported in materials such as α-Fe_2O_3 where the presence of long lived holes has been experimentally proven.[87] This suggests an increase in the hole population with increasing positive applied potential until saturation is reached.

TA kinetic traces for a WO_3 electrode were recorded as a function of applied bias between +0.1 V (before the photocurrent onset) and +0.9 V (where the photocurrent reaches a plateau and charge carrier separation is optimised) and were compared with the photocurrent/voltage plot. *Figure 3.21*.
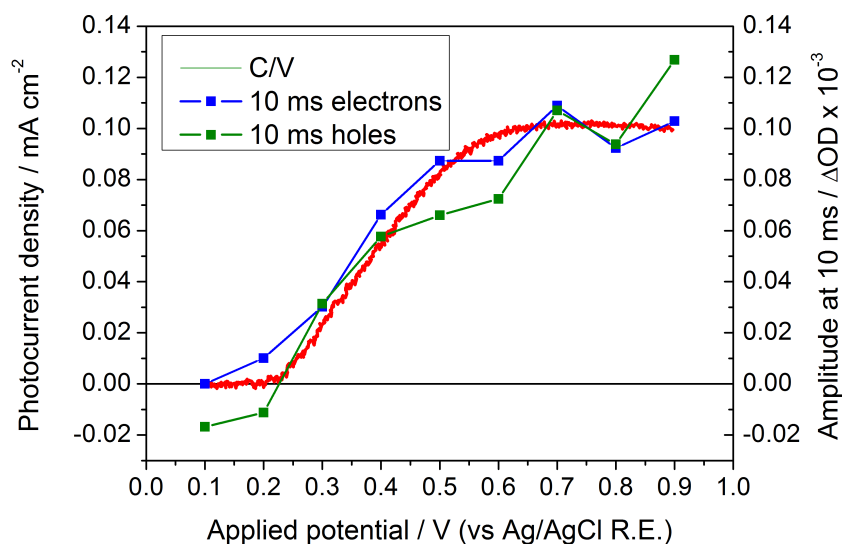
Figure 3.21: *Correlation between photogenerated holes probed at 450 nm (green squares) and electrons probed at 900 nm (blue squares) signal amplitudes recorded at +0.7 V vs Ag/AgCl at 10 ms after UV excitation (355 nm, 0.33 Hz, 250 $\mu J/cm^2$) of a WO_3 electrode with the photocurrent (red line) recorded under 355 nm (75 Xe lamp) illumination in 0.5 M $NaClO_4$ (pH 2, $HClO_4$).*

From *Figure 3.21* it can be seen that there is a relatively good match between the hole and electron TA amplitude recorded at 10 ms and the photocurrent, suggesting that both the hole and electron populations reach saturation before the charge carriers are transferred into solution or transported toward the counter electrode. Furthermore, in contrast to TiO_2 where a poor correlation to the TA signal of the photoelectron and the PC measurement is observed,[88] we achieve an excellent agreement. The lifetime of the WO_3 electron signals in experiments where water oxidation is occurring was found to be very long (see *Figure 3.11*). This indicates that electron transport is very slow and the slow component of the TA trace is likely to be due to the charge transport to the ITO interface. Slow charge transport may indicate that the nano-particles have poor interconnectivity, or alternatively this could be due to significant levels of trapping of photoelectrons at defect sites.

Figure 3.22 shows a simplified kinetic model where k_{t1}, k_{t2} and k_r represent the kinetic rates of electron transport to the FTO, electron trapping and electron/hole recombination respectively. In this model, following fast recombination losses, a subset of the initial electron population becomes trapped at defect sites. Thermal de-trapping would be required for charge transport to the FTO interface, leading to slow electron decay kinetics. In kinetic competition with both the slow charge transport and hole transfer would be recombination following electron de-trapping.[89] Tachiya and co-workers reported that the survival probability of charge carriers in the presence of fast recombination are well described by stretched exponential functions, as they follow the exponential distribution of the density of localised states below the conduction band.[90] The electron traces were in fact fitted by a combination of two stretched exponential functions, one describing the fast electron/hole recombination and the other describing electron trapping.
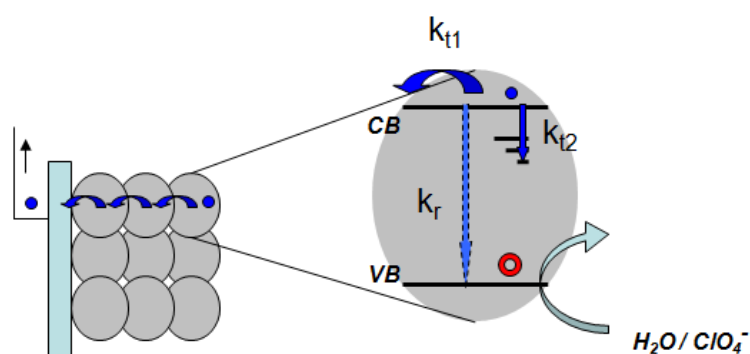
Figure 3.22: *Outline of the proposed model of the processes involving the photogenerated electrons. k_{t1}, k_{t2} and k_r represent the rate of electron transport, electron trapping and electron/hole recombination respectively.*

The presence of trapped electrons in WO_3 colloids was proposed by Kamat and co-workers;[91] by applying a negative bias, they observed a blue coloration attributable to the trapped electrons whose TA absorption was identified at wavelengths >620 nm. They also estimated the rate constant for electron trapping to be $10^{10}s^{-1}$.[43] On the other hand, the electron transfer kinetics in WO_3 have been investigated by Leland and Bard by investigating the steady state photocurrent as a function of applied bias in a system consisting of a colloidal solution of WO_3 placed in a PEC cell containing a Pt counter electrode in the presence of a hole scavenger; they suggested that reduction of WO_3 decreased the electron transport rate, whereas platinisation slightly increased it.[92]

In the next section the electron diffusion through WO_3 electrodes as a function of excitation intensity and thickness of the electrodes is discussed in more detail.

3.3.4 Dependence of the Electron Diffusion on the Excitation Intensity and the WO$_3$ Thickness

In order to investigate the effect of different excitation intensities on the electron transport, transient photocurrent measurements under variable excitation intensity were recorded. *Figure 3.23* shows the recorded TPC in the range 1.5–1500 µJ/cm^2 using an adaptation of the system used during TA measurements (see Section 2.1.4)

It is clear that the amplitude of the transient photocurrent increases with increasing excitation intensities, and that the current peaks do not show substantial difference in time at excitation intensities higher than 0.6 mJ/cm^2.
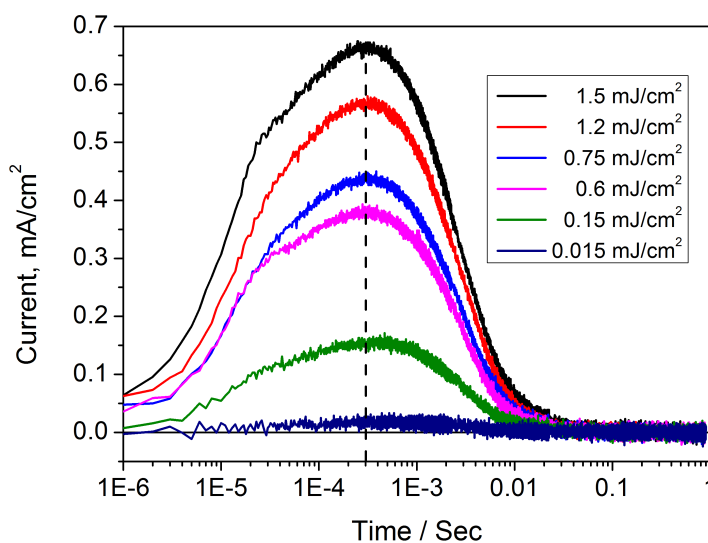
Figure 3.23: Transient photocurrent recorded at +0.7 V vs Ag/AgCl in 0.5 M NaClO$_4$ (pH 2, HClO$_4$) following pulsed UV excitation (355 nm, 0.33 Hz, 46Ω resistor) in the range 15–1500 µJ/cm^2 of a WO$_3$ electrode illuminated from the SE side.

From *Figure 3.23* above, it can be seen that the electron transport through the film is relatively slow, (~0.3 ms), however it should be noted that the resistors used during the

measurements could limit the time constants associated with the photocurrent rise. In fact the time constant of the photocurrent can be expressed as:

$$\tau_{PC} = C_{SCL} \cdot (R_m + R_e + R_{SC})$$ Eq. 3.5

Where C_{SCL} is the capacitance of the space charge layer, and R_m, R_e and R_{SC} are the resistance of the measurement, of the electrolyte and of the semiconductor respectively. The TPC response in the μs timescales is known to be dependent on the resistance of the measurement resistor employed while the photocurrent decay are independent.[93]

Assuming that at 355 nm the majority of the incident photons are absorbed by the WO_3 (see Figure 3.1), the electron diffusion coefficient can be estimated according to equation 3.6.[94, 95]

$$D = \frac{W^2}{2\tau_{peak}}$$ Eq. 3.6

Where D is the electron diffusion coefficient, W is the thickness of the WO_3 electrode and τ_{peak} is the temporal position of the transient photocurrent peak. The values of the electron diffusion coefficients calculated at each laser excitation intensity examined are reported in *Table 3.1*.

Table 3.1: *Position of the transient photocurrent peak and electron diffusion coefficient measured for each laser excitation intensity.*

Excitation Intensity (mJ/cm^2)	1.5	1.2	0.75	0.6	0.15	0.015
τ_{peak} (s)	3.06×10^{-4}	3.27×10^{-4}	3.46×10^{-4}	3.51×10^{-4}	6.7×10^{-4}	1.05×10^{-3}
D (cm^2/s)	2.12×10^{-4}	1.98×10^{-4}	1.87×10^{-4}	1.85×10^{-4}	9.67×10^{-5}	4.32×10^{-5}

When comparing the electron diffusion coefficients calculated at 1200 and 0.015 mJ/cm^2 it is evident that the electrons move faster through the WO_3 electrode with increasing laser excitation intensities, suggesting a faster filling of the trap states by the photogenerated electrons which survive initial recombination with holes. However with this model we assume a minimal electron/hole recombination after charge carrier separation. By integrating the photocurrent over the time it is possible to determine the total charge collected as a result of a single light pulse. *Figure 3.24* shows the integrated TPC versus the excitation intensity fit by a non-linear fitting function of the form $y=Ax^b$ with b~0.5.
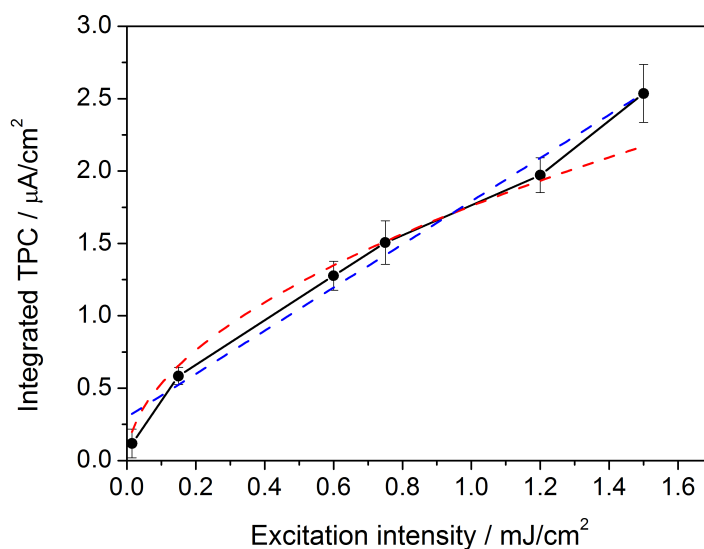
Figure 3.24: *Integrated transient photocurrent recorded at +0.7 V vs Ag/AgCl in 0.5 M NaClO₄ (pH 2, HClO₄) following pulsed UV excitation (355 nm, 0.33 Hz, 46 Ω resistor) in the range 55–550 μJ/cm² of a WO₃ electrode illuminated from the SE side. The dotted red and blue lines indicates a linear and non linear fitting function respectively.*

This is in agreement with the transient absorption data shown in *Figure 3.2*, which indicates that the relative population of electrons in the CB tends toward saturation when using high excitation intensities.

The dependence of electron transport on the thickness of the films was also investigated by recording the TPC for two electrodes prepared by depositing 3 and 9 layers of WO_3 which correspond to a thickness of 3.6 and 10.8 μm respectively. *Figure 3.25* shows the normalised TPC traces recorded using an excitation intensity of 250 μJ/cm².
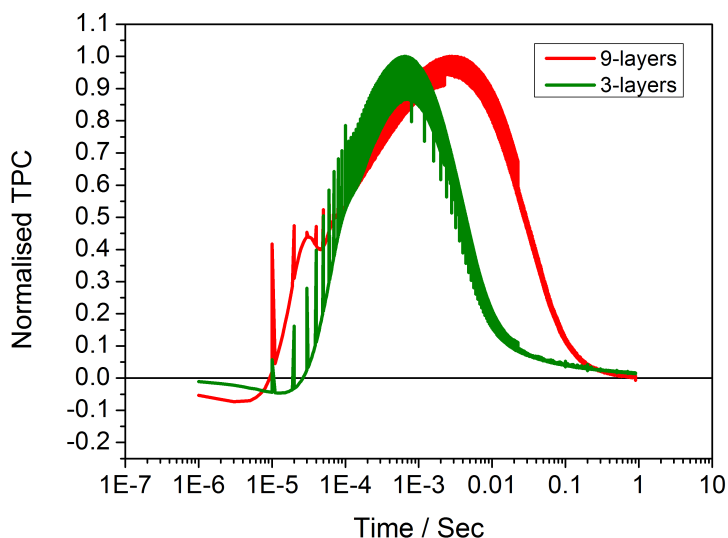
Figure 3.25: *Transient photocurrent recorded at +0.7 V vs Ag/AgCl in 0.5 M NaClO$_4$ (pH 2, HClO$_4$) following pulsed UV excitation (355 nm, 0.33 Hz, 250 μJ/cm^2, 46 Ω resistor) of a 3 layer (green trace) and nine layer (red trace) WO$_3$ electrode illuminated from the SE side.*

From *Figure 3.25* above it can be seen clearly that there is a shift of the TPC peak towards early times for the 3-layer electrode, in accordance with Bisquert and co-workers who also reported a shift of the TPC peaks at shorter times using thinner electrodes.[96] The electron diffusion coefficients have been calculated to be 1.46 x 10^{-4} cm^2/s and 9.3 x 10^{-5} cm^2/s for the 3- and the 9-layer electrodes respectively, which indicate that in thicker electrodes the electrons need a longer time in order to reach the ITO substrate, as expected.

Electrodes prepared by the deposition of six WO$_3$ layers were also investigated, however they did not behave as expected because of problems that occurred during the preparation of these films. From SEM images, some delamination was observed in the 6-layer electrodes where the WO$_3$ layer had come away from the ITO. Furthermore, given the method for preparing the thin sections, it was difficult to say if this delamination had

occurred during the synthesis of the electrodes or if it was during the embedding and polishing of the SEM samples.[97]

3.4 *Conclusions*

Transient absorption studies on isolated mesoporous WO_3 films suggested the presence of two distinct absorption features at 450 and 900 nm attributable to photogenerated holes and electrons respectively. In the presence of an efficient electron scavenger charge carrier recombination was minimised and the valence band holes were found to be relatively long-lived, enabling water oxidation to occur without an external electric bias.

Transient absorption studies in a fully operational photoelectrochemical cell have also confirmed the presence of two distinct absorption features, however, the very broad signal assigned to photoelectrons presents a tail at short wavelengths which overlaps the hole signal and leads to complications in determining the individual components of the charge carrier lifetimes. We have identified the presence of a slow (30 ms lifetime) kinetic component in the hole dynamics which correlates with the magnitude of the photocurrent measured, and this is tentatively assigned to hole transfer to solution. Although different mechanisms of reactions of the photohole leading to oxygen evolution have been proposed, transient absorption spectroscopy cannot provide detailed information on the intermediates involved during photocatalytic processes.

The decay of the photogenerated electrons was found to be particularly slow (0.1 s), even in a complete photoelectrochemical cell where electron/hole recombination is believed to be minimised. The accumulation of electrons in the conduction band has been confirmed by a quantitative correlation between the yield of photogenerated electrons and

photocurrent density. This close correlation has been ascribed to two main processes: i) electron trapping at defect sites and ii) slow electron transport through the film.

By examining the transient photocurrent trend as a function of excitation intensity, it has been possible to investigate the rate of electron transport through the WO_3 electrode. The electron diffusion coefficients were found to increase with increasing excitation intensities.

The effect of the electrodes thickness on the electron diffusion coefficient has also been investigated, with evidence for slower electron transport in thicker films.

Further studies on the other processes involving the photogenerated electrons could provide more detailed information on the rate of individual components.

Chapter IV

Transient Absorption Studies on Oxygen-Deficient Hydrogen-Treated TiO$_2$ Nanowires

In this chapter results on oxygen-deficient hydrogen-treated titanium dioxide (H:TiO$_2$) nanowires obtained using transient absorption spectroscopy are discussed. Evidence of efficient spatial separation of electron-hole pairs in the submicrosecond time scale leading to an improvement of the photoelectrochemical activity of H:TiO$_2$ is given.

4.1 Introduction

The result and discussion reported in this Chapter have already been published by the author of the thesis and the figure used are adapted from *J. Phys. Chem. C*, **2013**, 117, pp 25837-25844. (Reference 12)

As already mentioned in section 1.1.4 anatase TiO_2 has been employed as a photoanode since the early seventies,[3,4] however its theoretical maximum solar to hydrogen efficiency is limited by its large band gap (3.2 eV).[8] Therefore in recent years several material modifications such as main group doping or the use of co-catalysts have been attempted with the aim of increase its photochemical activity.[26,27] Recently has also been proposed that TiO_2 STH efficiency could be substantially increased by narrowing its band gap (and therefore extend its absorption profile) and minimising electron/hole recombination losses. Hydrogen treatment of TiO_2 nanoparticles has been proposed by Mao and co-workers to be an efficient route to narrow the TiO_2 band gap as a result of the formation of black TiO_2 with highly disordered surfaces and crystalline cores.[28] Following density functional theory (DFT) calculations they proposed that the increased photocatalytic efficiency of black TiO_2 could be attributable to limited electron/hole recombination losses as a result of the presence of localised mid-gap holes spatially separated from the conduction band electrons.

In 2011 a new benchmark STH efficiency value of 1.1% was reported by Li et al. for rutile TiO_2 as a result of low pressure hydrogen treatment on TiO_2 photoanodes employed during water oxidation.[42] When rutile TiO_2 nanowires were treated at 350°C under an hydrogen atmosphere for 30 minutes ($H:TiO_2$) they showed a pale yellow colour and substantially increased values of photocurrent under simulated solar irradiation were recorded in comparison with air-treated samples ($A:TiO_2$). The high value of STH

efficiency was proposed to be due to the substantial increase in the IPCE values under UV illumination at relatively low applied biases. However, only a small increase in the visible light activity was observed (despite a significant improvement in the visible light absorption properties) in comparison with the black TiO_2 photoanodes described by Mao and co-workers also in 2011.[28] In fact, no change in the valence band edge was observed in $H:TiO_2$, however X-ray photoelectron spectroscopy (XPS) showed an increase in the concentration of oxygen vacancies lying below the conduction band edge of $H:TiO_2$. This is in agreement with a proposed improvement of the portion of visible light absorbed by hydrogen-treated single crystals rutile TiO_2 as a result of the presence of oxygen vacancies. More importantly, the high values of IPCE were attributed to an improved separation and transport of the photogenerated charge carriers as a result of the fact that the oxygen vacancies situated below the conduction band edge of $H:TiO_2$ were proposed to act as electron donors.

More recently, the same authors have investigated the role of low pressure hydrogen treatments in several metal oxide semiconductors employed as photoanodes during water splitting such as α-Fe_2O_3, WO_3 and ZnO. For all of these materials the hydrogen treatment resulted in an improvement of their photocatalytic activity without noticing a substantial change in their optical band gap, suggesting that these performance improvements were caused by the presence of oxygen vacancies which act as electron donor as suggested for $H:TiO_2$.[29]

As mentioned earlier in this introduction, the increased concentration of oxygen vacancies in $H:TiO_2$ nanoparticles is proposed to lead to a decrease in electron/hole recombination even if the mechanism behind this still remain unclear. Li and co-workers have proposed hole trapping at Ti^{3+} sites as a result of the partial reduction of Ti^{4+} sites during

hydrogenation;[29] other authors have instead ascribed the decrease in electron/hole recombination to electron trapping by O_2 absorbed at the $H:TiO_2$ surface defects or electron trapping at oxygen vacancy sites.[98,99]

As mentioned in section 1.1.1, a decrease in the donor density leads to an increase in the width of the space charge layers and *vice versa*, therefore, under an applied bias, a photoelectrode characterised by a high donor density caused by the presence of oxygen defects, a decrease in recombination is expected because of the voltage drop obtainable in the depletion layer of highly structured material is greater in materials with higher donor density.

Despite increasing interest in oxygen-deficient metal oxide semiconductors and a recent TA study on ZnO,[100] no fundamental transient absorption studies have been reported in the literature for $H:TiO_2$, therefore, toward the end of my PhD I have been investigating rutile $H:TiO_2$ nanowires in a complete PEC cell employing TAS, with the aim of following the dynamics of the photogenerated charge carriers and investigate how an applied potential could modify the rate of recombination, transport and charge transfer.

In section 1.2.3 it has been mentioned that TiO_2 has been widely studied with TAS for over 25 years and the photogenerated holes and electrons have been found to have their absorption features at ~450-500 nm and ~800-900 nm respectively.[16,101,102] Several information regarding hole and electron dynamics have been retrieved employing TAS in the past, these include the rate of hole and electron trapping which has been found to occur within 500 ps from the laser excitation[103] and the required lifetime of hole transfer into solution in order to enable water oxidation which has been found to be ~0.03-0.4 seconds, depending on the electrolyte pH[14,15] (a detailed discussion regarding the hole lifetime in a wide range of pH will be discussed in Chapter 5).

H:TiO$_2$ nanowires were studied using TAS in order to i) identify the possible role that hydrogen treatment could have on the electron/hole recombination process; ii) compare the hole lifetime in hydrogen- and air-treated TiO$_2$ nanowire which is expected to be similar as a result of an unmodified valence band edge; and iii) investigate the factors which sit behind the low level of visible light activity reported for H:TiO$_2$ nanowires.

4.2   Experimental

The samples used in the experiments discussed in this chapter were prepared in University of California, Santa Cruz, by Prof Y. Li in the manner described in section 2.5. The H:TiO$_2$ and A:TiO$_2$ nanowires were deposited on FTO glasses with dimensions of 1x3x0.3 cm. Prior to each experiment the samples were UV cleaned for 30 minutes in order to remove any possible organic contamination. UV-Vis spectra were recorded before and after heat-treatment and did not shown any substantial difference. *Figure 4.1* shows the recorded UV-Vis spectra for A:TiO$_2$ (black line) and H:TiO$_2$ (red line). From the figure reported below it is possible to note a slight increase in the absorption profile for H:TiO$_2$ when compared with the control A:TiO$_2$ sample with an absorption edge at ~575 nm which could be attributable to a slight increase in the optical absorption of the hydrogen-treated sample. However it is important to consider that there can be a possible contribution to this absorption in the visible region due to the light scattered by the H:TiO$_2$ sample whose particle size is 10-20 nm.
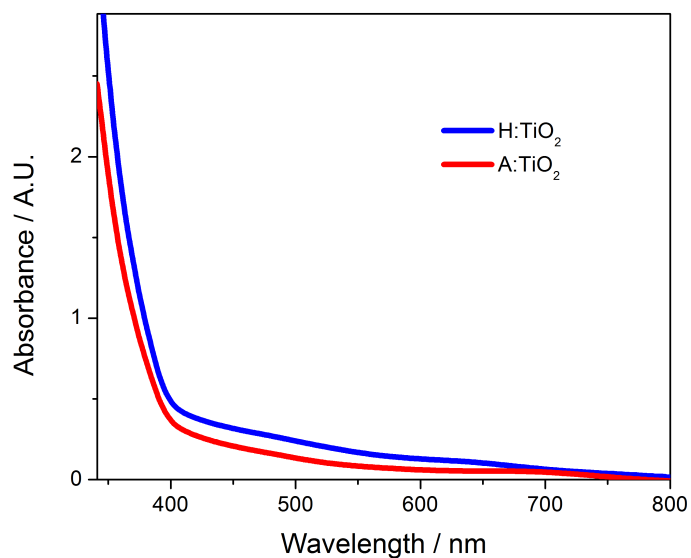
Figure 4.1: *UV-Vis spectra recorded between 325 and 800 nm in an Ar atmosphere for a A:TiO$_2$ (black line) and a H:TiO$_2$ (red line) electrode. Figure adapted from reference 12*

Electrochemical measurements were carried out employing the instrumentation described in section 2.1.2 and 2.1.3 using an electrolyte consisting in 1 M NaOH (Sigma Aldrich) prepared with Mill-Q water (Millipore Corp, 18.2 MΩ cm at 25 °C). After UV cleaning of the samples and prior each experiment the electrolyte was replaced and the solution was bubbled with Ar for 30 minutes in order to remove any possible dissolved oxygen within the cell. In order to prevent degradation of the reference electrode (Ag/AgCl, 3 M KCl) during long measurements, a double junction containing an intermediate solution 0.5 M NaClO$_4$ was employed.

Transient absorption spectra were recorded using the apparatus described in section 2.1.1 when using the UV excitation source (355 nm). When using the visible excitation source (575 nm) an OPO (Continuum, Surelite OPO plus) pumped by 355 nm from the Nd:YAG laser was used. The laser intensity used was 70 μJ/cm^2 at 355 nm and 250 μJ/cm^2 at 575

nm. The samples were irradiated from the electrolyte/electrode (EE) side and an average of 300 laser shots were recorded for each wavelength examined in order to record the spectra, while an average of 600 laser shots was recorded for lower noise kinetic traces. No substantial differences in the response of all the A:TiO$_2$ or H:TiO$_2$ samples used during the course of this studies were noted.

4.3   Results and Discussion

4.3.1 Initial Transient Studies on Rutile TiO$_2$ Photoanodes in a Complete PEC Cell – Assignment of the Hole and Electron Spectra

Following UV cleaning of the samples the photocurrent vs. voltage curves were recorded for both an A:TiO$_2$ and a H:TiO$_2$ electrodes in order to estimate the photocatalytic activity of the sample prior TA measurements. *Figure 4.2*.
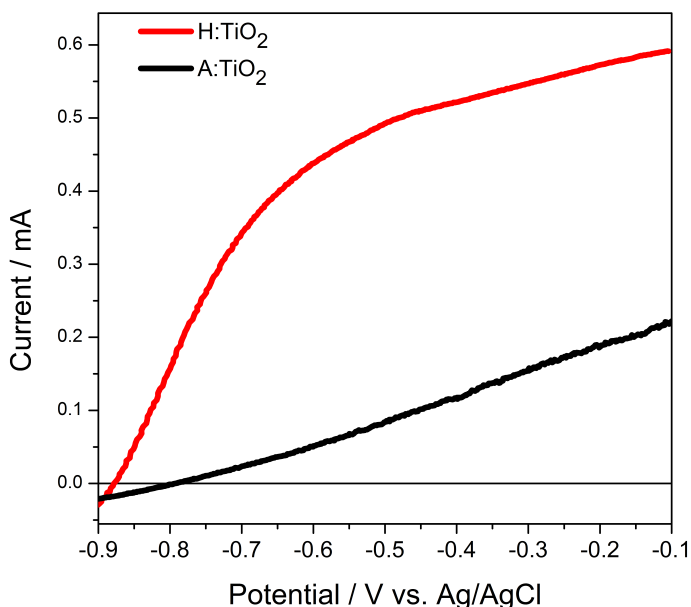
Figure 4.2: *Linear current vs voltage plot recorded under UV illumination (355 nm, 75W Xe lamp) from negative to positive potentials in 1M NaOH of A:TiO$_2$ (black line) and H:TiO$_2$ (red line) electrode illuminated from the EE side with a scan rate of 20 mV/s. Figure adapted from reference 12.*

When comparing the two curves, it is possible to notice an earlier onset and a substantial increase of the photocurrent for the H:TiO$_2$ sample, in agreement with previous reports which suggest that H:TiO$_2$ is significantly more active for water oxidation under UV

irradiation than a A:TiO$_2$. In fact *Figure 4.2* shows a 10-time enhancement of the photocurrent between A:TiO$_2$ and H:TiO$_2$ at -0.6 V vs Ag/AgCl.[42]

The TA traces and spectra of both samples were recorded by scanning the region 450 – 900 nm every 25 nm. *Figure 4.3* shows the recorded spectra.
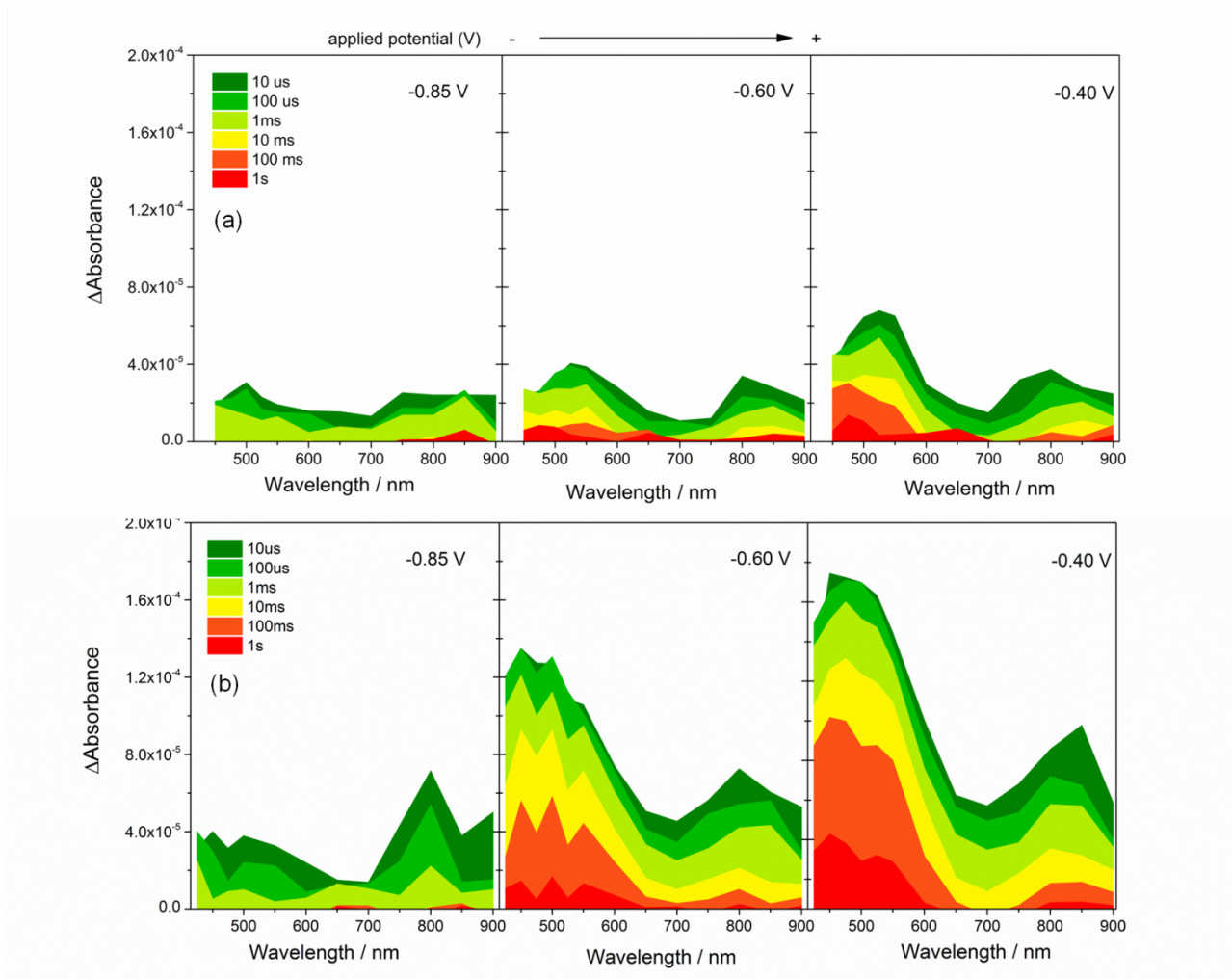
Figure 4.3: *Transient absorption spectra recorded in 1 M NaOH following UV excitation (355nm, 0.33 Hz, 70μJ/cm^2) of (a) A:TiO$_2$ and (b) H:TiO$_2$ illuminated from the EE side, at the bias (vs Ag/AgCl) indicated in the figure captions. Figure reproduced from reference 12.*

Previous TA studies on anatase TiO_2 published in the past suggest the presence of the hole and electron signals at ∼ 450 – 550 nm and ∼ 800 – 900 nm respectively.[16] More specifically, the hole spectrum in anatase has been experimentally assigned to transitions which occur between surface and sub-surface O^- centres and in rutile TiO_2 has been proposed a similar trapping mechanism employing DFT calculations.[104,105] Therefore, in light of these previous reports, the signal visible at short wavelengths (450 – 550 nm) in *Figure 4.3* has been assigned to trapped photoholes. Similarly, the absorption feature at long wavelengths (750 – 900 nm) has been assigned to trapped photoelectron, also in agreement with previous publications.[16]

As mentioned in Section 3.3.3 a good correlation between the amplitude of the TA signal and the photocurrent has been reported in several materials such as anatase TiO_2, α-Fe_2O_3 and WO_3 indicating the presence of photoholes sufficiently long lived to take part to water oxidation and providing a good quantitative measure of the level of charge separation.[87,88] *Figure 4.4* shows an overlap of the photocurrent curve with the TA signals recorded at 500 nm at 10 ms under an increasing applied bias for both a $A:TiO_2$ and a $H:TiO_2$ sample. For both samples there is a very good overlap between the two sets of data further reinforcing the assignment of the transient absorption signal at short wavelengths to trapped photoholes. This excellent overlap between the amplitude of the TA signal recorded under pulsed laser and the photocurrent recorded under UV illumination of the electrodes also indicates that the transient measurements employed during the course of this set of experiments are a reasonable model for the same photoelectrochemical cell under continuous irradiation.
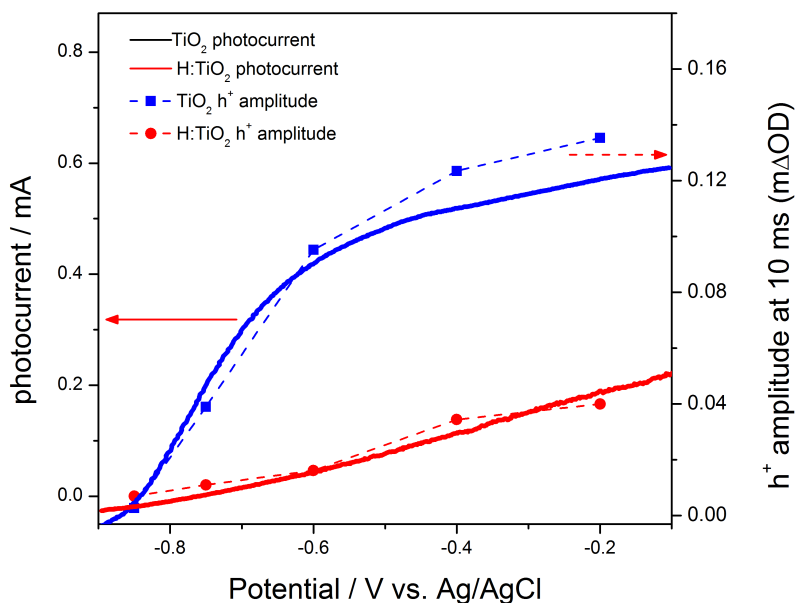
Figure 4.4: *Correlation between linear sweep voltammogram recorded under UV irradiation (355 nm, 75W Xe lamp, 50 mV/s) of A:TiO₂ (red line) and H:TiO₂ (blue line) photoanodes and the photohole transient absorption amplitude recorded at 500 nm after 10 ms from UV excitation (355 nm, 0.33 Hz, 70 μJ/cm²,) of A:TiO₂ (black circles) and H:TiO₂ (blue squares) electrodes illuminated from the EE side. Figure adapted from reference 12.*

From both *Figure 4.3* and *Figure 4.4* it can be seen a sharp increase of the yield of the long-lived photoholes between –0.85 and –0.6 V which then slightly levels at potentials more positive than – 0.6 V. From *Figure 4.3* (b) it can be assumed that the level of electron/hole recombination in H:TiO₂ is very sensitive to the applied electrical bias, in fact it can be noted a substantial increase of the relative electron and hole yields between – 0.85 and –0.6 V, suggesting an efficient charge carrier separation with increasing applied potential. On the other hand, *Figure 4.3* (a) shows that the increase in the overall hole and electron yield in A:TiO₂ is much more slow and gradual in the whole potential window examined, reaching a relatively high level of charge separation (matching the one seen on H:TiO₂ at –0.55 V) only with far greater electrical energy input (–0.2 V) suggesting that

electron/hole recombination is the predominant process at lower applied bias. However, in order to rationalise these assumption it has been necessary to examine the potential dependence of the photogenerated hole and electron kinetics more in details.

4.3.2 Electron/hole Recombination Dynamics – The Role of Applied Bias

As mentioned in the previous chapter, in the absence of an applied external bias or in the presence of an applied bias below the photocurrent onset, the predominant process involving the photogenerated charge carriers is proposed to be electron/hole recombination. From *Figure 4.2* it is possible to see a minimum photocurrent at –0.85 V and this is also attributable to fast electron/hole recombination being the main process involving hole and electrons. Also, the TA traces recorded at this potential show very weak and short-lived signals and the kinetics of both electrons and holes are indistinguishable on the microseconds to seconds time scale supporting the suggestion that recombination is the predominant process. *Figure 4.5*.

Both the TA decay traces have been fitted using power law functions, of the form $y = Ae^{(-b)} + y_0$, which have been employed in the past by several group in order to describe the fast electron/hole recombination process in a large number of semiconductor materials with a high density of trap states in which the recombination process take place via multi trapping-detrapping steps.[89,106]
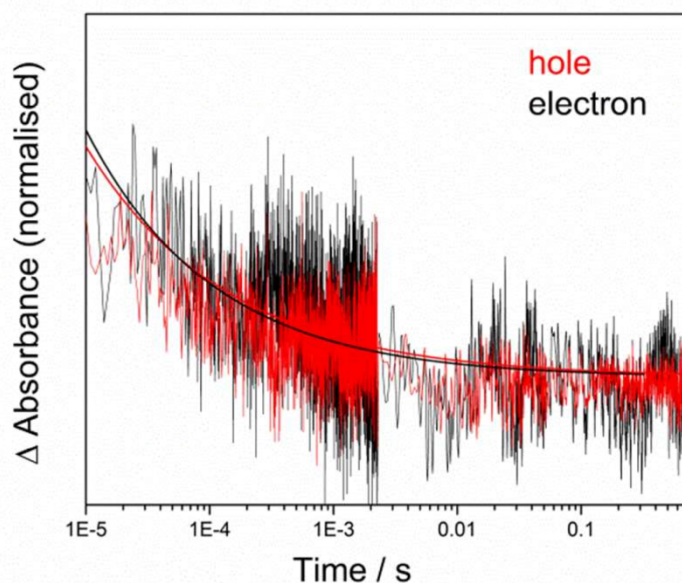
Figure 4.5: *Transient absorption decay traces of photoholes (500 nm, red trace) and electrons (800 nm, black trace) recorded in 1 M NaOH at –0.85 V vs Ag/AgCl after UV excitation (355 nm, 0.33 Hz, 70 μJ/cm^2) of a H:TiO$_2$ electrode illuminated from the EE side. Figure reproduced from Supporting Informations of reference 12.*

The TA signal amplitude increases with increasing applied bias as it can be seen from the spectra reported in *Figure 4.3*; it is in fact possible to notice a substantial increase in the electron-hole relative yields at early times (microseconds time scale) with applied potential more positive than –0.85 V and a decrease and decoupling of the rate of decay of the hole and electron TA signals on the microsecond to second timescale. This evident increased yield of both holes and electrons in the microsecond timescale (10 μs for instance) suggests a retardation of fast electron/hole recombination as a result of the application of an anodic applied bias. Cowan *et al*. have recently employed TAS results in order to derive the concentration of photogenerated charge carriers in anatase TiO$_2$ knowing its extinction coefficient.[88] Herein an estimated value describing the relative charge carrier

yield at 10 μs after laser excitation has been calculated. It is important to note that the earliest timescales studied in this set of experiments has been 1 μs, however given the very week nature of the TA signals (~10^{-5} – 10^{-4} ΔOD) it is not desirable to average both several hundred laser shots and several time delays together to minimise the chances of electrical or optical noise giving rise to an erroneous result, making 10 μs a practical lower limit for accurate measurements on the 10^{-5} scale with this apparatus.

The extinction coefficient of single crystal rutile TiO$_2$ has been reported in the literature to be 600 M^{-1} cm^{-1} at 850 nm.[107] Using this value in the Beer-Lambert equation (Eq. 4.1) it is possible to estimate a maximum value of $\Delta A_{850\,nm}$.

$$A = \varepsilon l c \qquad \text{Eq. 4.1}$$

Where A is the absorbance of the sample, ε is it extinction coefficient, l the path length and c the concentration of a given specie, in this case the photoelectrons generated per laser pulse.

c has been calculated considering the light harvesting efficiency of A:TiO$_2$ ($\eta_{LH,\,355\,nm}$ = 0.98) and H:TiO$_2$ ($\eta_{LH,\,355\,nm}$ = 0.99) and the incident light intensity at 355 nm (70 μJ/cm^2), giving an estimate number of photons absorbed by the TiO$_2$ samples of 2 x 10^{-10} mol/cm^2 per laser pulse. Therefore it is possible to estimate that a maximum value of $\Delta A_{850\,nm}$ $\approx$ 1.2 x 10^{-4} from trapped photoelectrons, corresponding to 100% of photons going to trapped photoelectrons, is achievable. By dividing this value to the measured $\Delta A_{850\,nm}$ at 10 μs in *Figure 4.3* it is possible to estimate the photoelectron yield. By doing this it is possible to approximate that, 10 μs after the laser flash, 30%, 55% and 75% of photoelectrons remain in the H:TiO$_2$ film at –0.85, –0.6 and –0.4 V respectively. In contrast, considering A:TiO$_2$ it

is possible to notice only a minimal change in the photoelectron yield as the applied bias is varied between –0.85, –0.6 and –0.4 V by considering the estimate values of 20%, 25% and 30%. This could be ascribed to a substantially more efficient initial charge carrier separation in H:TiO$_2$ which is more sensitive to the applied bias and could explain the enhanced activity of the hydrogen-treated TiO$_2$ samples in comparison to the air-treated samples. Nonetheless, it is important to note that absolute values of charge carrier yields could be still characterised by potentially large errors, as the extinction coefficient employed in their determination has been reported for a single crystal sample, however the relative differences between the applied potentials are still an important measure of fast electron/hole recombination losses.

It is important to note that the presence of two distinctive kinetics for holes and electrons in the microseconds to seconds timescale at potential more positive than –0.6 V both in A:TiO$_2$ and H:TiO$_2$ suggest the fact that other processes rather than electron/hole recombination can occur in these materials under the application of an external electrical input. In order to define kinetic parameters for electrons and holes in both materials it is necessary to singularly analyse the recorded TA decay traces. *Figure 4.6* shows the hole and electron TA traces recorded for H:TiO$_2$ (top) and A:TiO$_2$ (bottom) at –0.6 V vs Ag/AgCl. From the figure reported below it can be seen that the signal of the photoelectrons in H:TiO$_2$ (black line, top figure) decays by more than 50% between 10 μs and 1 ms, whereas the signal of the photoholes (red line, top figure) remain almost unchanged. In accord with several other publication the photoelectron decay is well fitted by a power law or the tail of a stretched exponential type function of the form $y = Ae^{\left(x/_t\right)^\beta} + y_0$ with $\tau \sim 1.4 \times 10^{-4}$ s.[89,106] The fact that the hole signal does not decay in this timescale allow the electron signal to be assigned to electron transport through the film

toward the external circuit. The H:TiO$_2$ hole decay trace has also been fitted using a single stretched exponential with a lifetime of 0.15 ± 0.03 s.
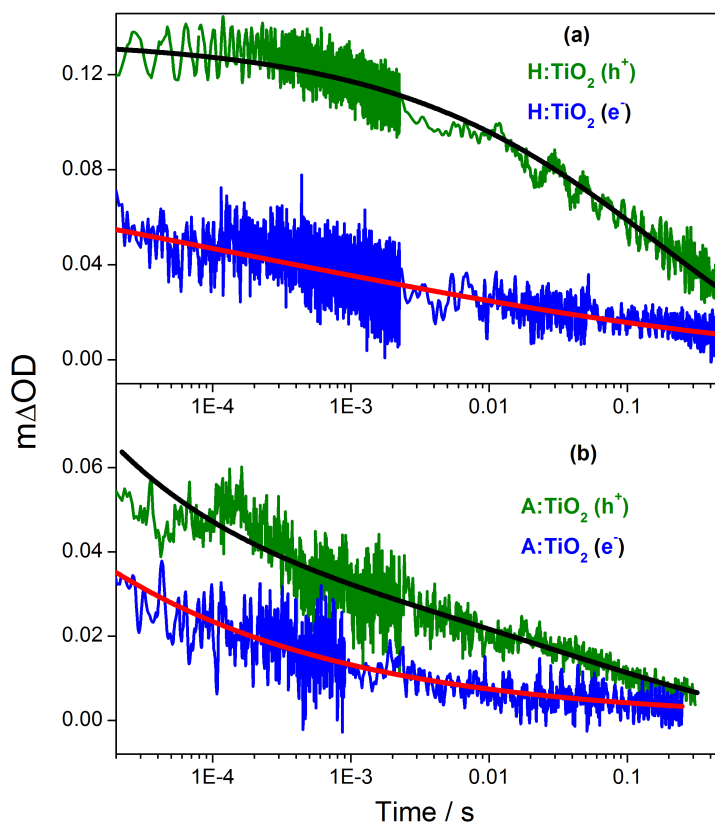
Figure 4.6: *Transient absorption decay traces of photoholes (500 nm, green traces) and electrons (800 nm, blue traces) recorded in 1 M NaOH after UV excitation (355 nm, 0.33 Hz, 70 μJ/cm^2) of H:TiO$_2$ (top) and A:TiO$_2$ (bottom) electrodes illuminated from the EE side. Figure adapted from reference 12.*

This calculated lifetime is assigned to the hole transfer into solution which is the slowest process measured. As mentioned in the introduction of this chapter, water oxidation on anatase TiO$_2$ requires holes with a lifetime between 0.03 and 0.4 s therefore it is possible to assume that the holes in H:TiO$_2$ photoelectrode have a lifetime long enough to oxidise water.[14-16] Moreover, the use of a single stretched exponential function to fit the hole decay in all the time range suggests that electron/hole recombination has been effectively blocked in H:TiO$_2$ on the microseconds to seconds timescale. In order to confirm this

assumption, the TA decay trace of the photogenerated holes in A:TiO$_2$ has been examined. From the fitting of the hole trace in *Figure 4.6* (red line, bottom figure) it has been observed a high level of electron/hole recombination on the microseconds to seconds timescale. In fact at –0.6 V the hole trace on A:TiO$_2$ can be fitted by a combination of both a stretched exponential function ($y = Ae^{\left(x/_t\right)^B} + y_0$) which well describe the slow component and a power law decay ($y = Ae^{(-b)} + y_0$) which well describe the early times.[14-16] This indicates that it is possible to distinguish two different kinetic pathways. The power law decay (*b*=0.35) is assigned to fast electron/hole recombination whereas the slow (τ~0.1 s) exponential decay component is assigned to the hole transfer into solution. The magnitude of this component (A = 2.6x10^{-5}) is proposed to be due to the kinetic competition with electron/hole recombination, which is also in line with the low IPCE reported in the literature (15%).[42] On the other hand, the signal assigned to the A:TiO$_2$ photoelectrons is relatively week, therefore the fitting of its decay appear to be non-trivial. From the fitting of the charge carriers decay discussed above it has been possible to demonstrate that initial charge separation (submicroseconds timescale) and suppression of electron/hole recombination on the microseconds to seconds timescale at –0.6 V vs. Ag/AgCl is substantially more efficient in H:TiO$_2$ than A:TiO$_2$. The difference between the recombination kinetics in hydrogen- and air- treated TiO$_2$ could be ascribed to the presence of localised electron or hole traps as a result of the hydrogenation process in accord with a model described by Shen and co-workers in 2013.[108] However, the overall similarity of the spectra recorded for both A:TiO$_2$ and H:TiO$_2$ (*Figure 4.3*) suggests that the nature of the trap states in both material is similar. Therefore the differences in the role of the applied potential on the recombination kinetics must be considered and they can be interpreted within the context of the model developed by Gartner[109] and Gerischer.[110,111]

They proposed that electron/hole pair separation is driven by the presence of a depletion layer that drives the holes toward the semiconductor/liquid interface (SCLJ) and the electrons away from the interface toward the bulk of the material. As previously discussed in section 1.1.1, the application of a positive bias to a TiO_2 electrode leads to an increase of the width and depth of its space-charge layer (SCL), enhancing the charge separation yield. From Eq. 1.1 it is possible to see that the width of the depletion layer depends upon the donor density of the semiconductor and its dielectric constant; however, it is necessary to consider the cylindrical geometry of the material employed during the course of these studies. Bisquert et al. have discussed in detailed the potential distribution in the axial and radial directions for a cylindrical semiconductor in 1999;[112] herein the same method has been used to calculate the maximum potential difference between the centre and the surface of the cylindrical TiO_2 at point $z \gg a$, where a is the radius of the cylinder and z the axial position (the FTO interface is defined as $z = 0$).

Equation 4.2 defines the potential drop between the centre and the surface of the cylindrical semiconductor:

$$\Delta \phi_M = \frac{1}{4} \left(\frac{a}{L_D} \right)^2 \qquad \text{Eq. 4.2}$$

where ϕ is the reduced potential (Eq. 4.3) and L_D the extrinsic Debye length (Eq. 4.4).

$$\phi = -\frac{qV}{k_B T} \qquad \text{Eq. 4.3}$$

$$L_D = \sqrt{\frac{\varepsilon_0 \varepsilon_r k_B T}{2q^2 N_d}}$$ Eq. 4.4

Where q is the fundamental electric charge, V is the electric potential, k_B is the Boltzmann constant, T the temperature, ε_0 is the permittivity of free space, ε_r is the dielectric constant of the semiconductor and N_d is the donor density particle of radius r. Li and co-workers have reported that for rutile TiO_2 ε_r is 130 and that in $A:TiO_2$ $N_d \sim 5 \times 10^{18}$ cm^{-3} and in $H:TiO_2$ $N_d \sim 1 \times 10^{22}$ cm^{-3}.[112] Considering the dimension of the materials used during the course of these studies ($a \sim 10 - 20$ nm, maximum z = 2-3 μm), this give a maximum voltage drop of 0.03 – 0.11 V for $A:TiO_2$ compared to 53 – 215 V for $H:TiO_2$, which suggest that $H:TiO_2$ is more able to support a sizeable radial electric field along its length. This can be attributable to the fact that the numerous oxygen vacancies which seat below the conduction band of $H:TiO_2$ act as electron donors, increasing its N_d and causing a dramatic decrease of the width of the SCL (Eq. 1.1) which leads to both a high initial charge carrier yield and an efficient suppression of slow (> μs) electron/hole recombination. In contrast, the lower N_d in $A:TiO_2$, therefore its wider SCL width, does not allow to maintain a significant large radial electric field, leading to higher level of recombination losses and lower IPCE values. However electron transport and hole transfer into solution are still viable thanks to the fact that the Fermi level and the background electron density are lowered as a result of the application of an external electrical bias, in accord with previous published studies on TiO_2 and Fe_2O_3.[15,87]

Figure 4.7 shows an outline of the model proposed above for $A:TiO_2$ (a) and $H:TiO_2$ (b) where K_{ct}, K_r and K_{et} are the rate of charge transfer into solution, recombination and

electron transport and collection at the FTO respectively. E_{1O} and E_{2O} represent the oxygen vacancies in H:TiO$_2$ at 0.75 and 1.2 eV below its conduction band edge respectively.
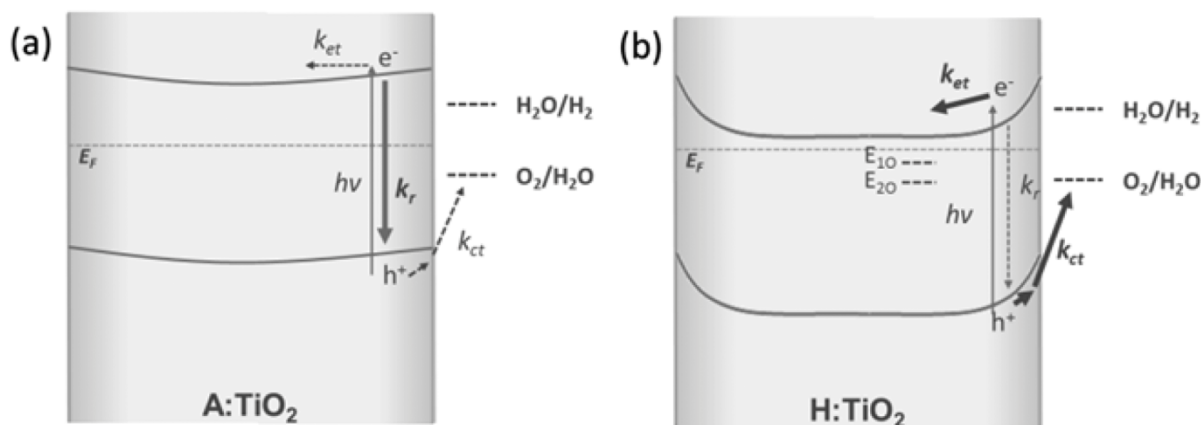
Figure 4.7: *Outline of the energy diagram for a cross section af A:TiO$_2$ (a) and H:TiO$_2$ (b) under a positive applied bias at a distance away from the FTO interface and following UV irradiation. K_{ct}, K_r and K_{et} are the rate of charge transfer into solution, recombination and electron transport and collection at the FTO respectively. E_{1O} and E_{2O} represent the oxygen vacancies in H:TiO$_2$ at 0.75 and 1.2 eV below its conduction band edge respectively. A:TiO$_2$ is represented to be fully depleted at even moderate applied bias. Figure reproduced from reference 12.*

In order to assess a possible contribution of modified hole transfer kinetics to the activity of H:TiO$_2$ it is necessary to examine in detail and compare the slow hole kinetics for both H:TiO$_2$ and A:TiO$_2$. This topic will be discussed in the following section.

4.3.3 Transient Studies on the Hole Transfer Kinetics in A:TiO$_2$ and H:TiO$_2$

From the fittings of the TA decay profile reported in *Figure 4.6* it was possible to assign the slow hole decay at 500 nm on H:TiO$_2$ at –0.6 V (τ = 0.15 ± 0.03 s) to the transfer of photogenerated holes into solution. The fitting of the TA traces recorded at –0.4 V also gives a comparable lifetime (τ = 0.13 ± 0.04 s), suggesting that in both conditions the

average rate of hole transfer into solution is not very sensitive to the applied bias. Additionally, despite an overlap of the electron/hole recombination kinetics, which leads to limited fitting accuracy, also in A:TiO$_2$ the hole transfer lifetime has been calculated to be ~0.1 s. (Refer to section 4.3.2 for detailed fitting information). When a substantially more positive bias is applied to A:TiO$_2$ the electron/hole recombination process is further reduced and the hole transfer kinetic can be accurately fitted using a single stretched exponential function with τ = 0.13 ± 0.02 s, value which is very similar to that observed on H:TiO$_2$ at –0.6 V. *Figure 4.8* shows an overlap of the TA traces recorded at 500 nm at –0.6 V for H:TiO$_2$ (red trace) and at –0.2 V for A:TiO$_2$ (black trace).
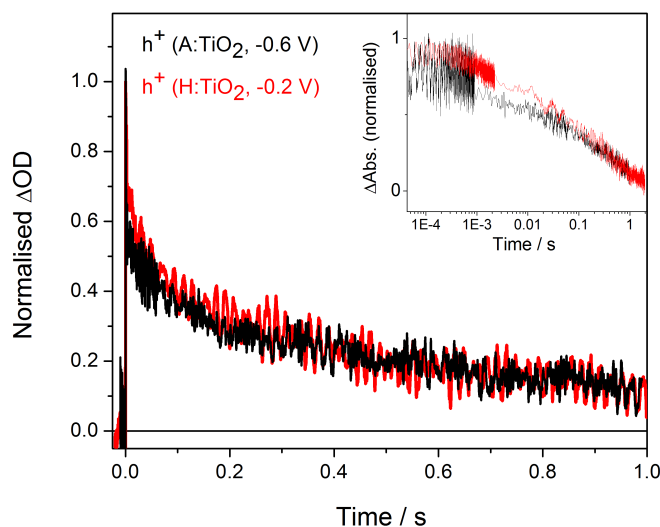
Figure 4.8: *Transient absorption decay of photoholes (500 nm) on H:TiO$_2$ at –0.6 V (red trace) and A:TiO$_2$ at –0.2 V (black trace) recorded following UV excitation (355 nm, 0.33 Hz, 70 μJ/cm^2) of the samples illuminated from the EE side. In the inset the traces are reported on a logarithmic scale. Figure adapted from reference 12.*

In the introduction of this chapter it has been mentioned that published XPS studies carried out on H:TiO$_2$ by Li et al. have showed no shift in the valence band edge as a result of hydrogenation.[29,113] This could explain the fact that both the TA spectrum recorded and surface kinetics of trapped holes are insensitive to hydrogen treatment. It is also important to note that with the equipment used during the course of these experiments, an average hole transfer rate over 300 to 600 laser shots has been recorded and it is hard to identify any change induced in the rate of individual steps which occur on the H:TiO$_2$ photoelectrodes. Despite this, the TA experiments carried out show that the average rate of hole transfer into solution on H:TiO$_2$ is not sufficiently different from that in A:TiO$_2$ to account for the approximate 10 time increase in the IPCE under UV illumination. This indicates that enhanced surface reaction kinetics are not responsible for the improved photocatalytic activity of H:TiO$_2$, which instead is suggested to be due to an efficient suppression of the fast recombination process as suggested in section 4.3.2.

The rate of electron decay on H:TiO$_2$ over a small range of applied biases has also been examined. The recorded TA decay are shown in *Figure 4.9*.

Between –0.75 V and –0.6 V it is possible to notice a substantial decrease in the level of electron/hole recombination. At –0.6 V the electron decay could be assigned to electron transport to the external circuit. However it is not possible to see a clear change between the photoelectron kinetics at –0.4 V and –0.6 V. It may be anticipated that the increase in applied bias would lead to faster electron transport through the H:TiO$_2$, however it is important to note that the majority of the voltage drop occurs close to the SCLJ. The slow electron transport processes probed here involve the movement of charges through the bulk of the H:TiO$_2$ toward the FTO interface and this is occurring at a distance away from the SCLJ which would be expected to limit the bias dependence.
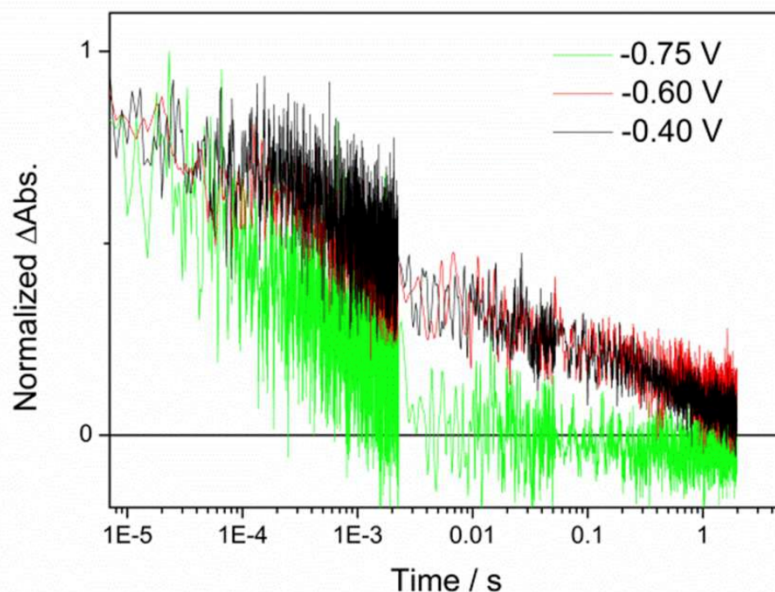
Figure 4.9: *Transient absorption decay traces of photoelectrons (800 nm) recorded following UV excitation (355 nm, 0.33 Hz, 70 μJ/cm^2) of H:TiO$_2$ photoanodes illuminated from the EE side, at the applied bias indicated in the figure caption. Figure adapted from Supporting Informations of reference 12.*

Considering the absorption profile of H:TiO$_2$ (*Figure 4.1*) and its capability to absorb light effectively in the visible region of the electromagnetic spectrum, the role of visible light on H:TiO$_2$ has been investigated and it is briefly discussed in the next section.

4.3.4 Effect of Visible Light on the Transient Absorption Spectrum of H:TiO$_2$

In order to monitor the effect of visible light on the transient absorption spectrum of H:TiO$_2$ the TA spectrometer was modified as described in section 4.2 in order to modify the wavelength of the pump beam to 575 nm. This wavelength was chosen considering the

IPCE profile of H:TiO$_2$ in the visible region recorded by Li and co-workers in 2011.[42] *Figure 4.10* has been reproduced from reference 42 and shows the aforementioned IPCE %.
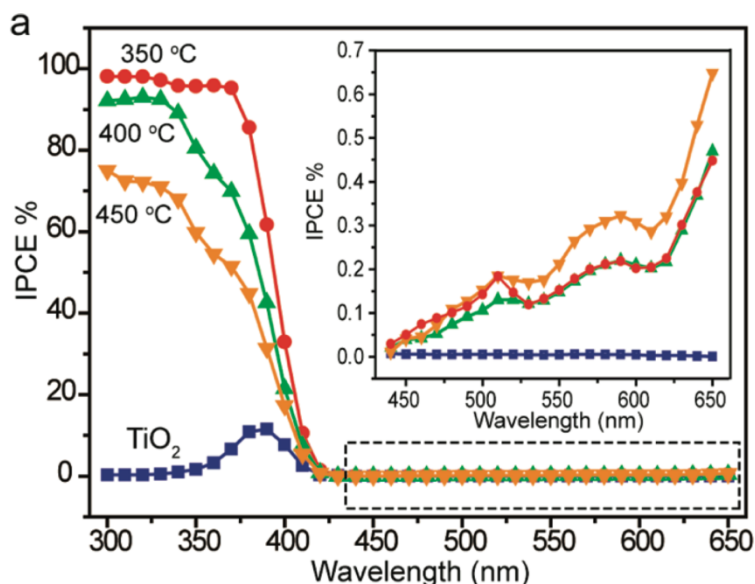
Figure 4.10: *IPCE spectra of A:TiO$_2$ (blue symbols) and H:TiO$_2$ nanowires prepared at 350, 400 and 450 °C, collected at the incident wavelength range from 300 to 650 nm at a potential of 0.6 V vs Ag/AgCl. Inset: Magnified IPCE spectra that highlighted in the dashed box, at the incident wavelength range from 440 to 650 nm. Figure reproduced from reference 42.*

The intensity of the laser was adjusted in order to have an equivalent number of photons absorbed by the H:TiO$_2$ at the sample area. The spectra at 100 μs and 10 ms from the laser shot were recorded in the 450 – 900 nm region and a comparison with the spectra recorded using the 355 nm excitation source is shown in *Figure 4.11*.

Despite H:TiO$_2$ absorbs light at 575 nm, no long-lived photohole or photoelectron signal can be seen in the spectrum reported below, in accord the very low recorded IPCE yields at λ > 400 nm, indicating that any electron/hole pairs that are generated are rapidly recombining. Oxygen vacancies in rutile TiO$_2$ are localised at 0.75 and 1.2 eV below the

conduction band edge, and charge carriers generated following photoexcitation to and from the E_{1O} and E_{2O} states have been proposed to be inactive as a result of their decreased energy and mobility.
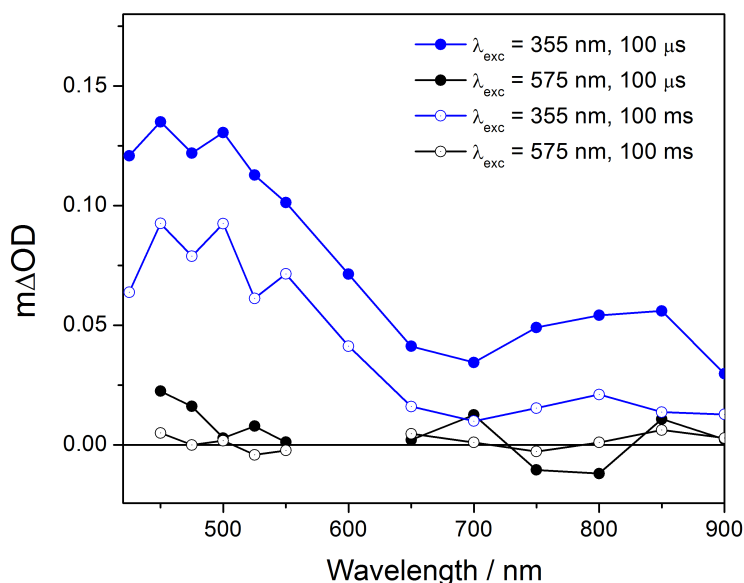
Figure 4.11: *Transient absorption spectra recorded in 1 M NaOH at the timescales indicated in the caption following UV (355 nm, 0.33 Hz, 70 $\mu J/cm^2$, blue traces) and visible (575 nm, 0.33 Hz, 250 $\mu J/cm^2$, black traces) excitation of H:TiO$_2$ illuminated from the EE side at −0.6 V vs Ag/AgCl. Figure adapted from reference 12.*

From the results reported herein, the low level of photocatalytic activity of H:TiO$_2$ at 575 nm is attributable to the inability of generating suitably long-lived charge-separated states for water oxidation.

4.4   Conclusions

Transient absorption studies on oxygen-deficient hydrogen-treated rutile TiO_2 ($H:TiO_2$) nanowires suggested that the improved electrical properties of $H:TiO_2$ allow an efficient charge separation to be achieved under an external applied bias in accord with the literature.[42] Transient absorption measurements in a fully operational photoelectrochemical cell and carried out in a range of applied potentials (–0.85, –0.6 and –0.4 V vs Ag/AgCl) have shown that near a complete suppression of electron/hole recombination can be achieved at only –0.6 V vs Ag/AgCl on $H:TiO_2$ following UV excitation. From the fitting of the TA decay traces recorded at 500 nm the rate of the hole transfer into solution was calculated to be τ = 0.15 ± 0.03 s, indicating that the photogenerated holes are enough long-lived in order to enable water oxidation in line with previous TA studies carried out in anatase TiO_2.[14,15] In contrast, air-treated TiO_2 ($A:TiO_2$) nanowires require a substantially more positive external applied electric current (–0.2 V vs Ag/AgCl) in order to reach an effective electron/hole separation and hole lifetime comparable with that achieved in $H:TiO_2$. A significant change in surface kinetics in $H:TiO_2$ has also been ruled out and an efficient suppression of fast electron/hole recombination was confirmed to be the key factor behind the improved IPCE values under UV illumination in this material when compared with $A:TiO_2$. The presence of oxygen vacancies as a result of hydrogenation of TiO_2 has been proposed to lead to an improvement in charge separation yields and consequentially to higher STH efficiency in line with other reports on several metal oxide semiconductors such as α-Fe_2O_3 and WO_3. Further transient absorption experiments on hydrogen-treated TiO_2 could further clarify this proposed mechanism and are under way in the laboratories of Dr Cowan (Liverpool University).

Chapter V

Examination of the Hole Reaction Mechanism on TiO$_2$ using TAS and SFG

In this chapter results on nanocrystalline titanium dioxide (nc-TiO$_2$) electrodes obtained using transient absorption spectroscopy and sum frequency generation spectroscopy are discussed. Transient absorption studies in a complete photoelectrochemical cell carried out at different pH are described. Initial sum frequency generation measurements on similar nc-TiO$_2$ films are also discussed.

5.1   Introduction

Titanium dioxide (TiO_2) has been the most widely investigated photocatalyst because of its low cost, high stability and the position of its valence and conduction bands which are suitable for water oxidation and proton reduction respectively. The main factor limiting the efficiency of TiO_2 is the high value of its energy band gap (~3.2 eV for anatase TiO_2) which restricts its absorption only in the UV region of the solar spectrum leading to a maximum theoretical photoconversion efficiency of 1.3%.[8] Despite its low conversion efficiency TiO_2 is a suitable model material for mechanistic investigations. Furthermore the potential to enhance its light harvesting capabilities through doping and sensitization is being explored and it is also widely studied in photo-oxidation and organic degradation reactions.[114,115] Several papers have previously examined possible mechanisms and the intermediates involved in the reaction of water oxidation, however, the exact surface mechanism has not been elucidated.[116-119]

TAS was first employed to study charge carriers dynamics in TiO_2 in 1984 by Bahnemann et al. who observed the TA spectra of photogenerated holes and electrons in colloidal TiO_2 identifying their characteristic absorption peaks at 475 and at wavelengths higher than 650 nm respectively.[41] By monitoring the evolution of the TA spectra on ultra-fast (fs-ps) timescales, trapping and recombination of holes and electrons has also been investigated, providing a hole and electron trapping time of <50 fs and 260 fs respectively.[120] Tang et al. also confirmed the position of the absorption peak of holes to be at 460 nm and suggested that the absorption feature of conduction band electrons increases with increasing wavelength;[16] several studies have indicated that trapped electrons in anatase TiO_2 can

be probed between 800-900 nm.[15,16] TA has also been used to study the charge carrier dynamics of holes during the water oxidation reaction and the required hole lifetimes for oxygen evolution in the presence of an $AgNO_3$ electron scavenger have been reported to be ~0.3 s.[16] The charge carrier dynamics of TiO_2 films in a complete PEC cell have also been reported at pH 12.6 on the microsecond to seconds timescale;[15] very long hole lifetimes (~0.3 s) were also found to be required for water oxidation. Furthermore, by reducing electron/hole recombination, nc-TiO_2 has been found to be a very selective catalyst for the formation of O_2 from water oxidation.[15,16] Here we further examine the effect of electrolyte pH on the photogenerated hole lifetime in TiO_2 as a probe of potential surface mechanisms. Of particular relevance to this study is a series of papers briefly discussed below.

In 2004 and 2007 Nakamura and Nakato studied the mechanism of the intermediates involved in the oxygen photoevolution reaction in the pH range 1–13 using photolumienescence and FTIR measurements, which suggested a nucleophilic attack mechanism at pH ≤ 13. However, the photoluminescence measurements showed a decrease in intensity with increasing solution pH and the presence of two minima at pH 4 and 13. The first minimum was attributed to the increased rate of nucleophilic attacks of water molecules to surface holes bridging oxygen, the density of which increases with increasing pH, and this was proposed as the first step of the photooxidation reaction at pH <13. The second minimum was attributed to a change in mechanism of reaction; an initial oxidation of a Ti-O- group by a photohole as initial step at pH >12 followed by the formation of the same key intermediate involved at lower pHs was proposed.[116,118] In section 4.3.1 a more detailed discussion of these mechanisms will be provided.

In 2007 Yoshihara et al. also investigated the effect of pH changes in absorption spectra of photogenerated holes in nc-TiO$_2$ suggesting the presence of two different types of holes in acidic and neutral/alkaline pHs respectively (*Figure 5.1*). The first type was suggested to be produced in the bulk of TiO$_2$ particles through an ultra-fast process before reaching the surface. The second type was thought to be related to the presence of OH$^-$ ions on the TiO$_2$ surface which generate charge transfer complexes with holes.[101]
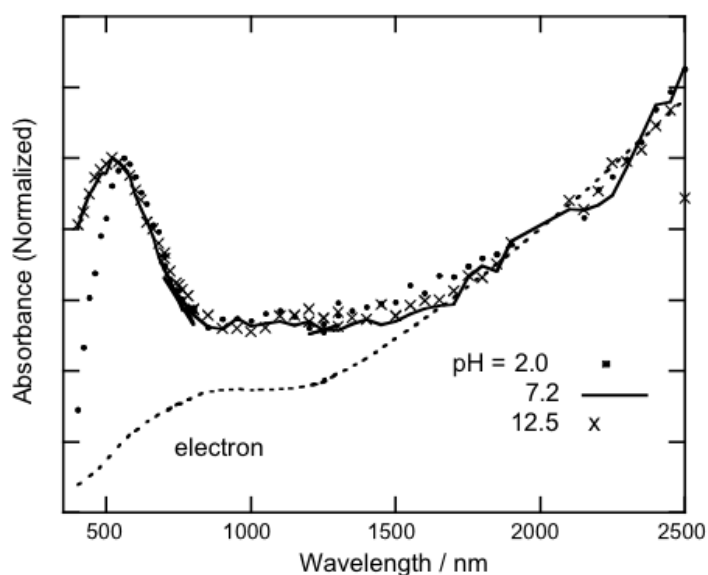
Figure 5.1: *Transient absorption spectra of nc-TiO$_2$ films recorded at pH 2, 7.2 and 12.5. The dashed line represents the electrons TA spectrum. Figure reproduced from reference 102.*

In 2009 Crawford et al. also investigated the effect of pH changes on the H$_2$ evolution rate using gas-chromatography. They reported a constant water splitting rate between pH 3 and 10 and a substantial increase between pH 11 and 13, attributed to a more effective water splitting mechanism which involves the direct oxidation of OH$^-$ ions rather than water molecules.[121]

In order to rationalize the studies above I carried out a range of TAS experiments to explore the mechanisms occurring. TAS is a powerful technique for the study of reaction dynamics, however UV/Vis spectroscopy only provides a limited insight into the chemical nature of the short lived intermediates. Direct experimental evidence of the nature of the surface intermediates involved during water oxidation on TiO_2 could lead to a better understanding of the reaction mechanisms, which is a basic requirement for a rational development of new metal oxide photocatalysts for water splitting. In Section 1.2.4 sum frequency generation spectroscopy was described as a powerful technique to probe vibrational spectra of molecules at interfaces. By employing SFG in the study of TiO_2/water interfaces in conditions in which water oxidation occurs it could be possible to determine the nature of the intermediates involved during the reaction and retrieve information on their structure and geometry. This would represent an important step forward for the study of photoassisted systems on metal oxide semiconductors. In 2003 Wang et al. detected for the first time traces of hydrocarbons and hydroxyl groups on nanoparticulate anatase TiO_2 films surfaces by SFG, proving the applicability and suitability of this technique for molecular level characterisation of metal oxide films.[122] Investigating a freshly prepared TiO_2 film they noticed the presence of two resonant SFG features between 2800 and 3000 cm^{-1} which were assigned to $-CH_3$ and $-CH_2-$ groups, attributed to a contaminating hydrocarbon layer formed during the film preparation under ambient conditions. The disappearance of these SFG resonances upon UV irradiation confirmed this assignment. In the presence of methanol and after UV irradiation of the sample, four new SFG features were detected in the same region; two were attributed to molecular methanol and two to methoxy chemisorbed to the TiO_2 film surface (see Section 5.3.2 for details). The SFG

signals attributed to molecular methanol altered with changes in the temperature and pressure of the system, whereas the signals assigned to chemisorbed methoxy did not, suggesting that this latter specie was strongly adsorbed on the TiO_2 surface. The same group carried out a study on the competitive adsorption between methanol and water on TiO_2, showing that when H_2O vapour was introduced into the system the molecular methanol signal dropped below the SFG detection limit while the signal of chemisorbed methoxy remained appreciable.[123-125] A new broad peak also appeared beyond 3000 cm-1 corresponding to hydrogen-bonded OH groups indicating that methoxy species on TiO_2 were hydrolyzed by water addition. However methanol appeared to be more strongly adsorbed to the TiO_2 surface than water. In 2004, Uosaky et al also studied the interfacial water structure at TiO_2 surfaces, showing that UV illumination of the film led to an increase of the amount of adsorbed water and specifically ordered adsorbed water on the TiO_2 surface as a result of increasing hydrophilicity of the surface.[126]

5.2 Experimental

The TiO_2 electrodes used during TA experiments were prepared by doctor blade deposition of a TiO_2 paste courtesy of Xiaoe Li (Durrant group, Imperial College London) on a FTO glass (dimensions 1x3x0.3 cm) as described in section 2.4. All the films used were ~4 μm thick and were heat treated at 450°C for 30 minutes prior to carrying out any measurement in order to remove any possible organic contamination. UV-Vis spectra were recorded before and after thermal treatment in order to monitor any possible change in the absorption profile.

Transient absorption traces were recorded using the equipment described in section 2.1.1 in $NaClO_4$ 0.5 M in pH 2–13; $HClO_4$ and NaOH were used to reach acidic and alkaline pHs

respectively. Before any measurement, each solution was purged with Ar for 20 minutes in order to remove any dissolved oxygen within the PEC cell. The laser intensity used to excite the TiO_2 was ~70 $\mu J/cm^2$. Hole and electron traces were recorded at 460 and 900 nm respectively, in accordance with previously published studies.[15,16] An average of 1000 shots was recorded at each wavelength examined. No notable differences were found between the different electrodes prepared on different days during these studies, indicating that the TiO_2 paste employed for the film fabrication was stable and the electrode preparation was reproducible.

A description of the preparation of the nc-films used during SFG measurements is discussed in detail in section 5.3.2.

5.3 Results and Discussion

5.3.1 TAS Studies on nc-TiO$_2$ Electrodes – Dependence of the Hole Lifetime on the Electrolyte pH

After thermal treatment, hole and electron traces were recorded at 460 and 900 nm respectively in pH range 2-13 in a complete photoelectrochemical cell. The photocatalytic activity of each film used in this study was tested by recording current vs. voltage plots. *Figure 5.2* shows an I/V curve recorded under 355 nm illumination for a TiO$_2$ electrode in NaClO$_4$ 0.5 M (pH 8)
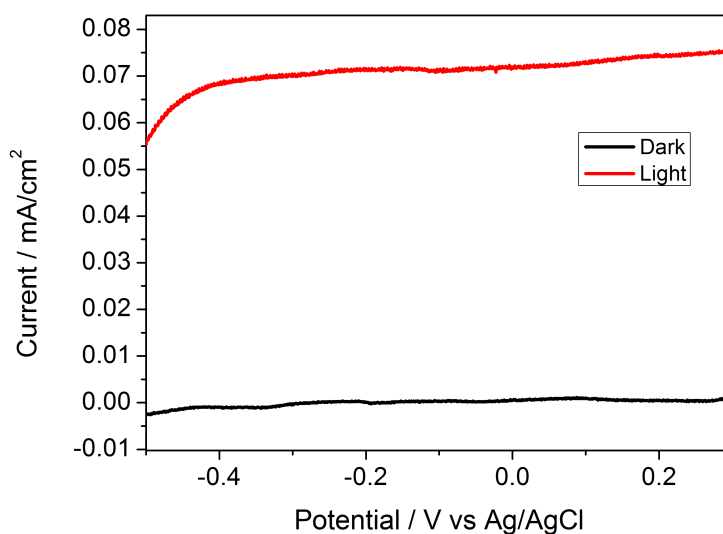
Figure 5.2: *Linear current vs voltage voltammogram recorded in the dark (black line) and under UV illumination (red line, 355 nm, 75W Xe lamp) of a TiO$_2$ electrode illuminated from the SE side in 0.5 M NaClO4 (pH 8, NaOH). Scan rate 20 mV/s.*

The potential applied to the working electrode during TA measurements was corrected by 59mV pH^{-1} in order to account for the shift in the potential of the water splitting potentials with pH. *Table 5.1* shows the applied potentials at different OH⁻ concentrations.

Table 5.1: *Electrolyte pH's and relative applied potentials*

pH	2	4	8	10	11	12	12.5	13
[OH-]	1×10^{-12}	1×10^{-10}	1×10^{-6}	1×10^{-5}	1×10^{-3}	0.01	0.05	0.1
V $_{(Ag/AgCl)}$	+0.32	+0.15	-0.07	-0.17	-0.22	-0.28	-0.30	-0.33

Figure 5.3 shows the TA kinetic traces for the electrons (top) and the holes (bottom) probed at 900 and 460 nm respectively at the pH's and applied potentials listed in *Table 5.1*.

Significant differences were not observed in the hole decay dynamics between pH 2 and 12, therefore in *Figure 5.3* (bottom) only the normalised traces recorded at pH 10 and 13 are reported for clarity.

In previous published works, the electron decay was modelled with a continuous time random walk model were a power function law fits the TA kinetic traces well, indicating that the recombination process occurs via a trapping-de-trapping model suggestive of bimolecular recombination.[89,127,128] We decided to fit the electrons traces with a power law function (equation 5.1) whereas the hole traces were fitted with a combination of a power and exponential function (equation 5.3).
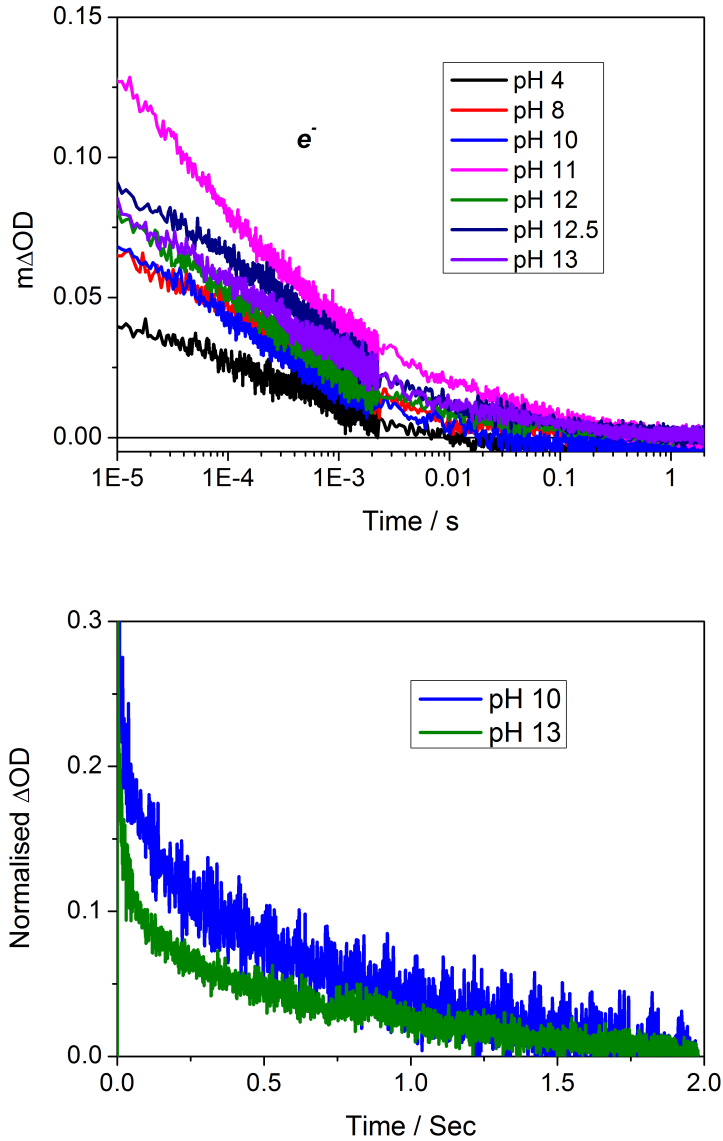
Figure 5.3: *Transient absorption decay traces of photoelectron (900 nm, top) and hole (460 nm, bottom) recorded after UV excitation (355 nm, 0.33 Hz, 70 $\mu J/cm^2$) of a nc-TiO₂ electrode illuminated from the SE side, in 0.5 M NaClO₄ (pH range 2–13, HClO₄ and NaOH). As no substantial differences were observed in the hole decay between pH 2 and 12, the hole traces (bottom) recorded at pH 10 and 12 are shown in a linear scale in order to simplify the identification of a different decay profile.*

$$y = a_2 \cdot \left| x - x_c \right|^P + y_0 \quad \text{Eq. 5.1}$$

$$y = a_1 \cdot \exp\left(-\frac{x}{t_1} \right)^b + y_0 \qquad \text{Eq. 5.2}$$

$$y = a_1 \cdot \exp\left(-\frac{x}{t_1}\right)^b + a_2 \cdot x^c + y_0 \qquad \text{Eq. 5.3}$$

Where a_1 and a_2 describe the amplitude of the two functions, t_1 the decay time of the stretched exponential function, b represents the stretching of the exponential function and P the slope of the power function. The power law describes the fast recombination process it dominates the early times. The stretched exponential function dominates the slow component of the hole decay and its amplitude describe the yield of the hole transfer into solution.[15] *Figure 5.4* shows the fitting functions used overlapped on the TA kinetic trace of photoholes at pH 8.
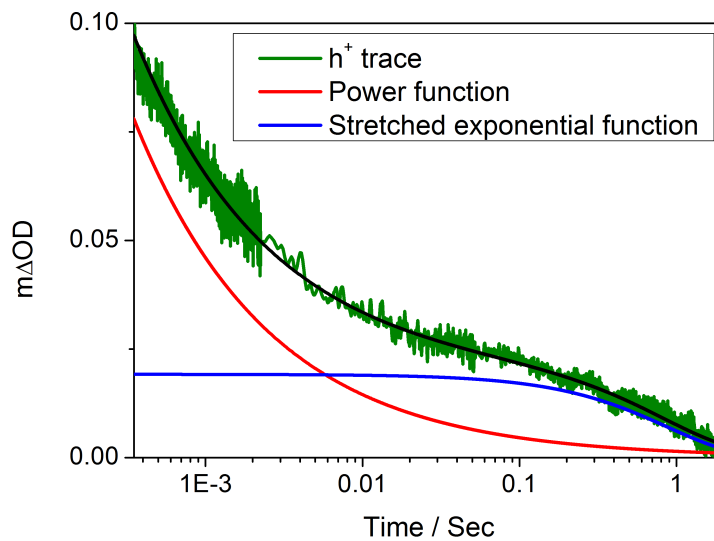
Figure 5.4: *Transient Absorption decay trace of photoholes recorded at 460 nm in 0.5 M NaClO₄ (pH 8, NaOH) after UV excitation (355 nm, 0.33 Hz, 70 $\mu J/cm^2$) of a nc-TiO₂ electrode illuminated from the SE side. The TA trace is fitted by a combination of a power function (red line) which dominates the early times and a stretched exponential function (blue line) which dominates the slow component.*

The lifetime of the hole TA decay at different pH were all fitted using equation 5.3 and are reported in *Table 5.2*.

Table 5.2: *Electrolyte pH's and relative hole lifetime.*

pH	2	4	8	10	11	12	12.5	13
[OH-]	1×10^{-12}	1×10^{-10}	1×10^{-6}	1×10^{-5}	1×10^{-3}	0.01	0.05	0.1
τ (s)	0.72 ±0.003	0.75 ±0.008	0.84 ±0.003	0.75 ±0.004	0.95 ±0.006	0.5 ±0.007	0.04 ±0.001	1.8×10^{-3} ±5.7 x 10^{-6}
K_{obs} (s^{-1})	1.39	1.33	1.19	1.33	1.05	2	24.85	555.56

From the table reported above it is noted that the holes are relatively long-lived in the pH range 2–12 whereas they decay faster under more alkaline conditions (pH >12). *Figure 5.5* shows the calculated K_{obs} versus the electrolyte [OH⁻], where $K_{obs}=1/\tau$.
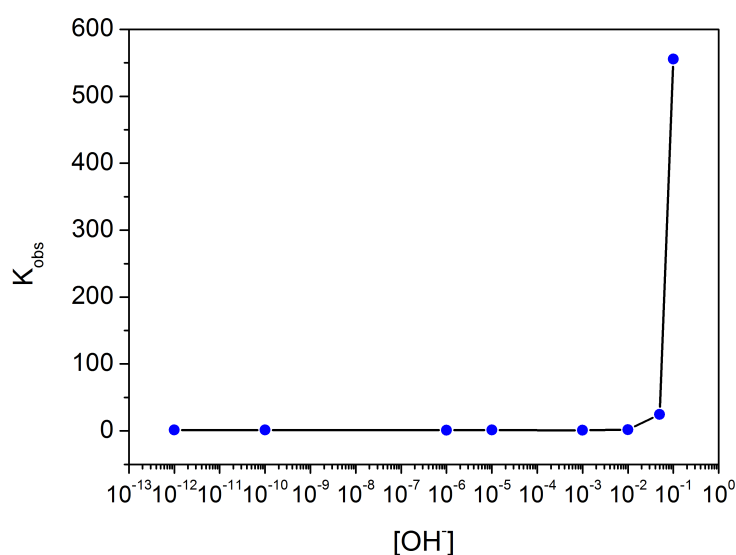
Figure 5.5: K_{obs} *vs. [OH⁻] graph. The value of K at pH 13 is clearly several orders of magnitude greater than the values observed between pH 2 and 12.*

This results show that the hole lifetime drastically decreases in the presence of an elevated concentration of OH⁻, with a step change in the measured rate at pH >13. Whilst it is important to note that the exact lifetime values obtained were sensitive to the initial fitting parameters, the slow component of the hole decay decreased by a factor far greater than the fitting uncertainty at pH >13. Furthermore, several TiO_2 electrodes were investigated and no substantial differences in the fitting results were observed. It should also be noted that with the model used in these studies we assumed that the electron decay was exclusively attributable to fast electron/hole recombination. From the calculation of τ carried out during the course of these experiments, it can be assumed that there is a change in the photohole kinetics at pH >13. This is in agreement with a previous publication by Nakamura and Nakato, which proposed a change in water photo-oxidation reaction mechanism at pH ~13, as briefly discussed in the introduction to this chapter.[116-118] A rapid decrease in photoluminescent intensity at pH ~13 was attributed by these authors to the formation of surface anionic species (Ti-O⁻) which could rapidly react with photogenerated holes. *Scheme 5.1* shows the two proposed mechanisms at pH ≤ and ≥ 13. At pH <13 a first step involving a nucleofilic attack of water molecules on the TiO_2 surface-trapped holes was proposed.
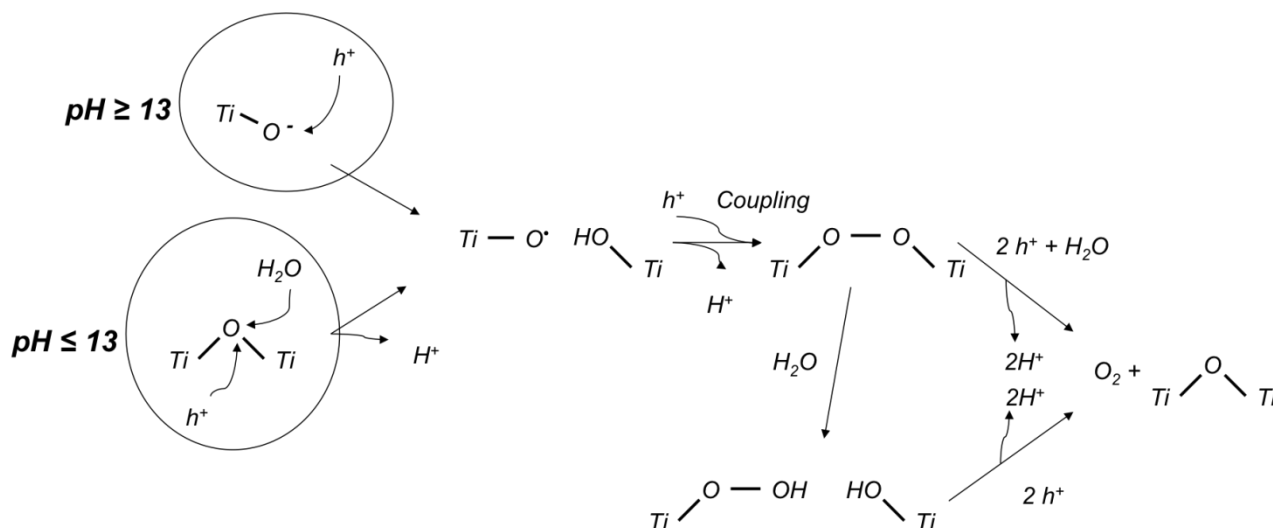
Scheme 5.1: *Reaction scheme for oxygen photo-evolution on TiO$_2$ in contact with aqueous electrolytes with pH ≤ 13 and ≥ 13. This scheme has been adapted from reference 116.*

However, transient absorption spectroscopy provides only limited information on the chemical nature of the intermediates involved during photo-assisted water oxidation on metal oxide semiconductors. Therefore initial experiments employing sum frequency generation spectroscopy (section 1.2.4) were carried out to provide structural information on the species at the TiO$_2$/water interface.

5.3.2 Initial SFG Studies at the Surface of nc-TiO$_2$ Films – Physisorbed and Chemisorbed Methanol

Towards the end of my PhD the SFG spectrometer described in section 2.2 was built with the aim of carrying out initial SFG experiments on nc-TiO$_2$ films in order to enable future detailed studies on water splitting systems and identify signals attributable to interface species involved during the water oxidation reaction. The data reported in this section were recorded and analysed in collaboration with Dr. Frederic Fournier.

To the best of our knowledge, the TiO_2 films employed in the existing SFG published works were prepared by depositing and drying in air a drop of a colloidal solution of nanoparticulate TiO_2 on a CaF_2 window,[122-125] or by spry pyrolysis.[126] However, this approach provides limited control and, in order to prepare samples that were of greatest similarity to those used in our TAS studies, the films were prepared by doctor blade deposition of a TiO_2 paste onto a CaF_2 window, that was previously cleaned at 450 °C for 30 minutes. Following drying in air the CaF_2/TiO_2 films were calcined for a final time in air at 450 °C to give a 4 μm film which was expected to be free of organic contaminants.

The samples were left several days in air and in milliQ water in order to monitor any degradation of the films and possible detachment of the TiO_2 layer from the CaF_2 substrate. No noticeable damage to the samples was noted in both conditions.

An initial spectrum of the freshly calcined TiO_2 sample on CaF_2 was recorded under argon flow in the region 2400 – 3000 cm^{-1} and it is shown in *Figure 5.6*.
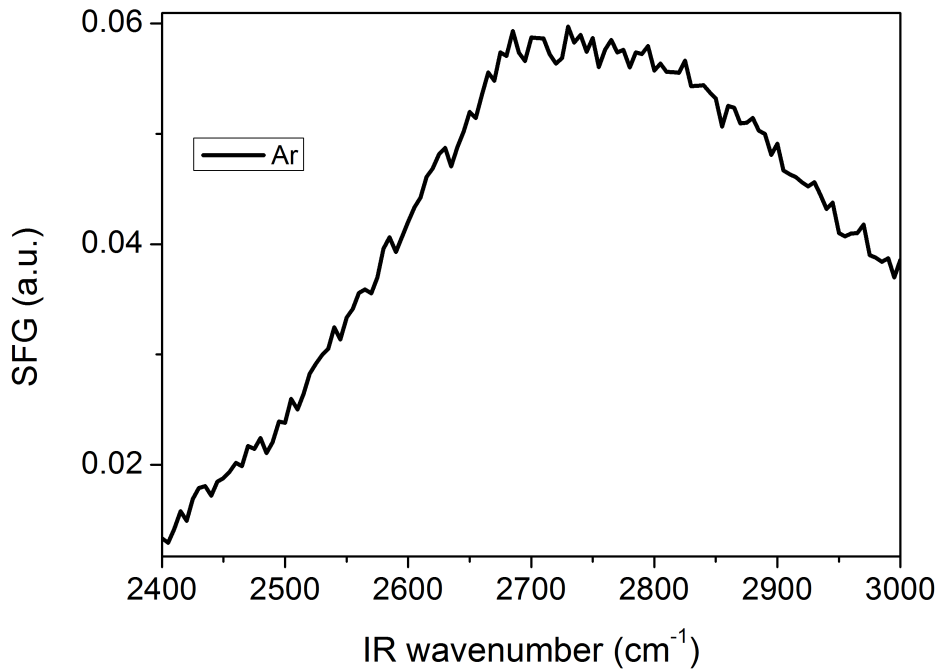
Figure 5.6: *Sum frequency generation spectrum recorded at the interface of a TiO$_2$ film kept under an Ar flow in the region 2400 – 3000 cm^{-1}. The signal is attributed to a high non-resonant signal which follows the IR profile (Gaussian type shape) across the wavelength range.*

The signal shown in the above figure is attributable to a high non-resonant background which follows the IR profile (IR intensity as a function of the IR frequency). Its non-symmetric Gaussian type shape is attributable to the fact that the intensity of the IR beam is lower at 2400 cm^{-1} than at 3000 cm^{-1}. The non-resonant signal is dependent on the second order susceptibility ($\chi_{NR}^{(2)}$) of the material at which the SFG signal is generated. The amplitude of the non-resonant signal is also related to the symmetry of the material where the SFG signal is generated. For example, in centro-symmetric materials the SFG signal is generated only at the surface, therefore, the non-resonant signal is expected to be weaker than in non-centro-symmetric materials where the SFG is generated in the bulk (up to the penetration depth of the IR and visible beams). In section 1.2.4 the intensity of the SF

signal was defined without taking into account the non-resonant contribution, therefore, it can be re-written as in equation 5.4:

$$I_{SFG} \propto \left\| \left| \chi_R^2 \right| + \left| \chi_{NR}^2 \right| \right\|^2 \qquad \text{Eq. 5.4}$$

A further contribution to the non-resonant signal can be given by the visible beam when its wavelength is close to an electronic resonance on the material investigated.[46,47]

In the literature, the absorption of methanol on the TiO_2 surface is reported to give rise to characteristic SFG peaks.[122-124] In the studies reported herein CH_3OH was flowed through the cell using Ar as a carrier gas; the SFG spectrum was recorded in the region 2775–3025 cm^{-1} in the dark and under UV irradiation. *Figure 5.7* shows the SFG intensity measured and normalised to the peak maximum value. From the comparison with the non-resonant background recorded in an Ar atmosphere it is observed that there is an additional presence of two negative peaks at around 2850 and 2960 cm^{-1} under methanol, which could indicate the presence of molecular methanol adsorbed on the TiO_2 surface.
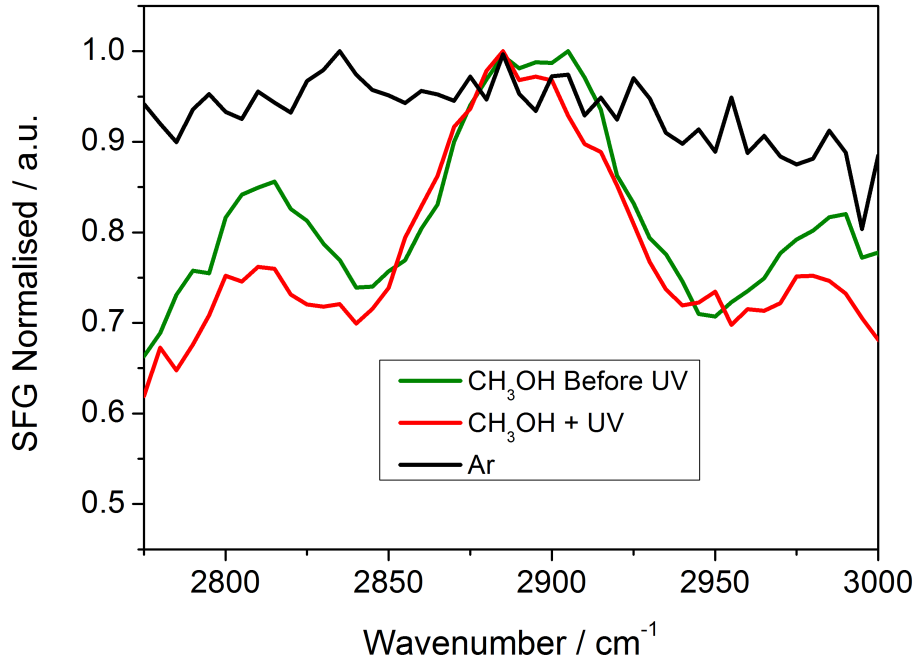
Figure 5.7: Sum frequency generation spectra recorded at the interface of a freshly calcined TiO$_2$ film on CaF$_2$ in an Ar atmosphere (black line), in the presence of a CH$_3$OH (99%, Sigma Aldrich) flow in the dark (green line), under UV irradiation (355 nm, UV LEDs) of the sample (red line).

The presence of these negative peaks is attributable to the fact that SFG signals are not simply additive. To explain these results it is necessary to take into account all the possible interferences. Using equation 5.4 the SFG signal can be expressed by equation 5.5:

$$
\begin{aligned}
I_{SFG} &\propto \left| P_{Res} + P_{N\,Res} \right|^2 = \left| \chi_{Res} E_{Vis} E_{IR} + \chi_{N\,Res} E_{Vis} E_{IR} \right|^2 = \\
&= \left| \chi_{Res} E_{Vis} E_{IR} \right|^2 + \left| \chi_{N\,Res} E_{Vis} E_{IR} \right|^2 + 2\left(\chi_{Res} E_{Vis} E_{IR} \right)\left(\chi_{N\,Res} E_{Vis} E_{IR} \right) = \\
&= Signal_{SFG_{Res}} + Signal_{SFG_{N\,Res}} + Interference
\end{aligned}
\qquad \text{Eq. 5.5}
$$

Where P_{Res} and P_{NRes} are the resonant and non-resonant polarisation vectors respectively, E_{Vis} and E_{IR} are the laser electric field for the visible and IR beams and χ_{Res} and χ_{NRes} are the resonant and non-resonant second order susceptibility tensors.[35-36] The interference signal can be expressed in terms of sin and cos dependent on phases; it is possible to have negative, positive and half-half (similar to a dispersion shape) resonant signals on top of the non-resonant background (refer to references 46 and 47 for a more detailed description of the theory behind non-resonant susceptibility). However, it is non-trivial to predict the shape of a resonant signal as it depends on several factors such as the geometry of the beams on the sample, the orientation of molecules on the surface of the sample and the nature of the material and molecules.

In order to confirm the presence of any SFG signal it was necessary to extract the peaks by subtracting the non-resonant background which was found to be well fitted by a Gaussian function. *Figure 5.8* (top) shows an example of normalised raw data (black line) recorded in the presence of CH_3OH interpolated with a fitting function (red dots), which is the combination of two Lorentzian functions (*Figure 5.8* bottom).[46]
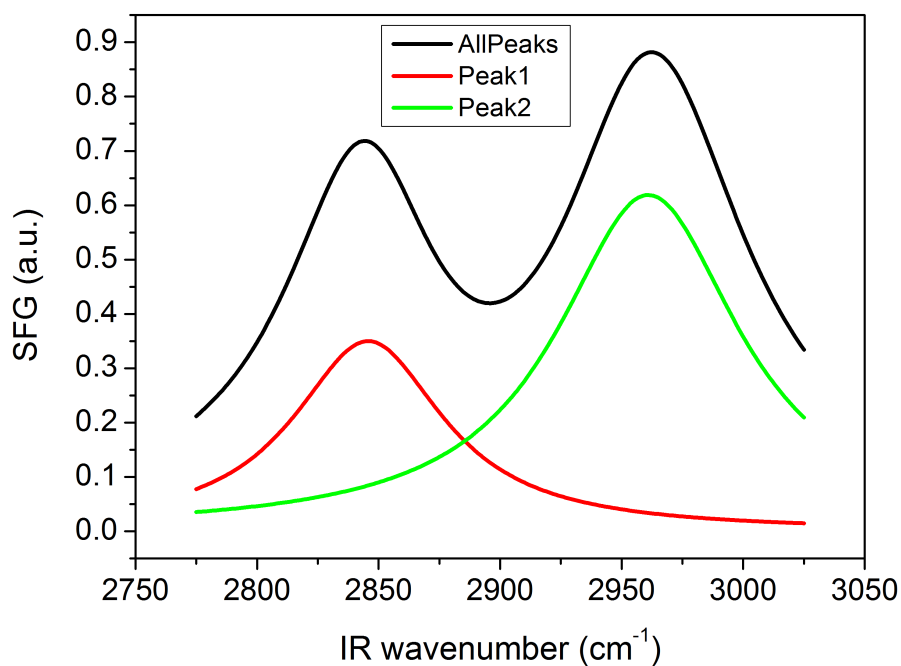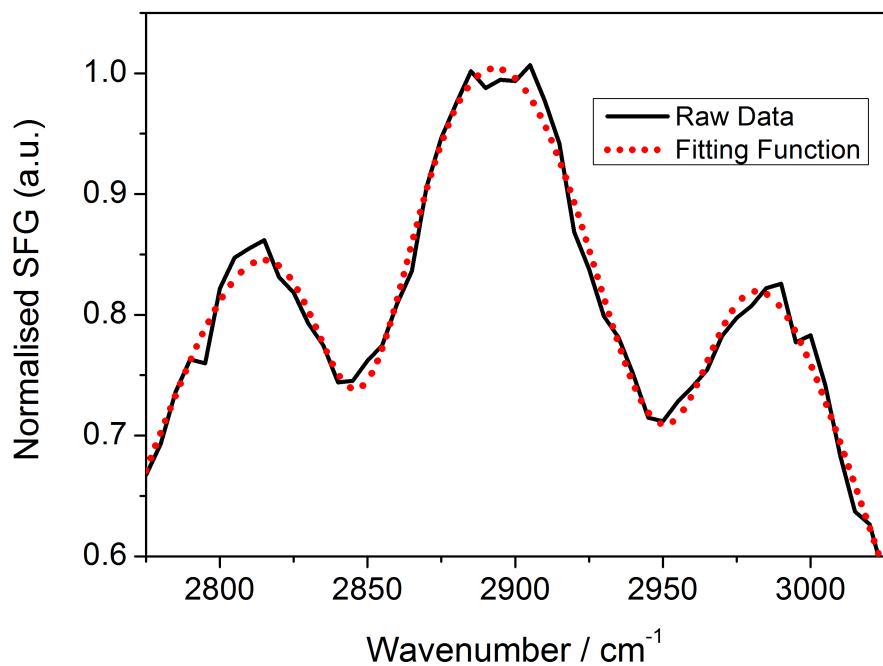
Figure 5.8: *Example of sum frequency generation raw data (black line, top graph) interpolated by a fitting function (red dots, top graph) which is the combination of two Lorentzian functions (red and green lines, bottom graph).*
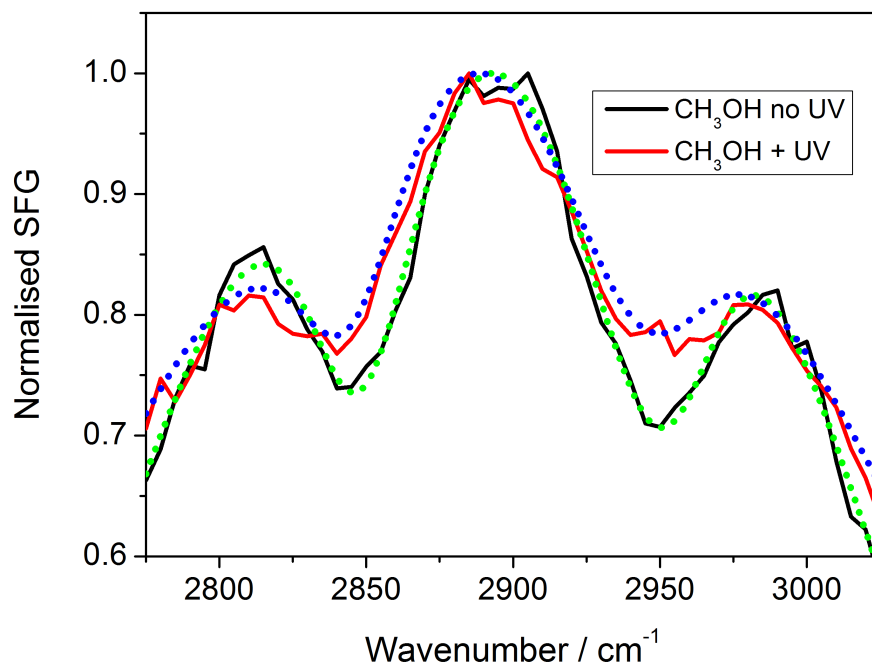
Figure 5.9: *Normalised sum frequency generation spectra recorded at the interface of a TiO₂ film in the presence of a CH₃OH (99%, Sigma Aldrich) flow when the sample was kept in the dark (black line) and under UV illumination (red line, 355 nm, UV LED's) of the sample. The dots represent the Lorentzian fitting functions employed.*

The normalised SFG spectra of a TiO_2 film recorded in the presence of a CH_3OH flow in the dark and under UV illumination of the sample area were compared and are showed in *Figure 5.9*.

The raw data were interpolated with the fitting functions mentioned above and the extracted peaks are shown in *Figure 5.10*.
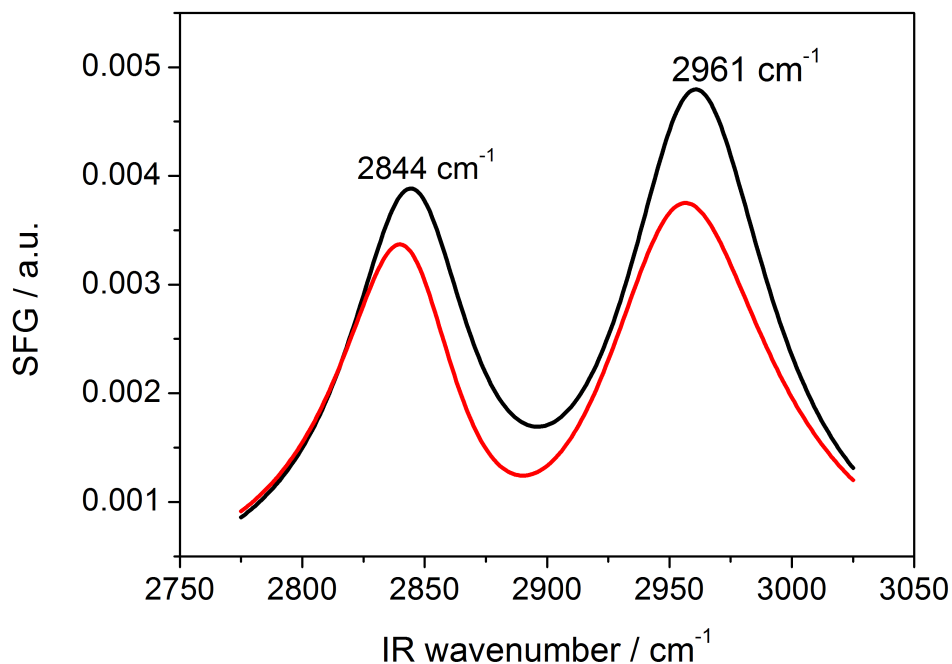
Figure 5.10: *Extracted fittings of the sum frequency generation spectra recorded at the interface of a TiO₂ film in the presence of CH₃OH (99%, Sigma Aldrich) in the dark (black line) and under UV irradiation (355 nm, UV LEDs) of the sample (red line). It is possible to note a decrease in the SFG signal magnitude when the TiO₂ film is exposed to UV light, although no significant changes in the position of the peaks are observed.*

From the fitting of the SFG spectra reported above it is possible to see two relatively strong peaks at 2844 and 2961 cm^{-1} when the TiO_2 film is kept in the dark (black line). Under UV light the peaks decrease in intensity and a slight red-shift in wavenumber is observed (red line). The two peaks recorded in the dark and under UV irradiation are assigned to molecular methanol physisorbed on the TiO_2 surface in accordance with the results reported by Shultz and co-workers.[123-125] They noted the presence of four distinct peaks: i) two peaks at 2855 and 2968 cm^{-1}, which were assigned to molecular methanol physisorbed on the TiO_2 surface, and ii) two peaks at 2828 and 2935 cm^{-1} which were assigned to methoxy produced by dissociative chemisorption of methanol on the TiO_2

surface providing the first evidence of methoxy generation on nanoparticulate TiO_2 films. In a freshly prepared film the peaks assigned to molecular methanol were predominant, whereas after the TiO_2 film was exposed to UV light the peaks assigned to chemisorbed methanol substantially increased in intensity indicating an activation of the TiO_2 surface.

In order to confirm the presence of chemisorbed methanol on the TiO_2 surface after activation by UV light, the sample was kept under UV illumination for 60 minutes while the cell was purged with an Ar flow. An SFG spectrum was then recorded in the presence of a CH_3OH flow under UV illumination and was compared with the spectrum recorded in the dark in the presence of methanol (*Figure 5.11*)

When comparing the spectra it is noted that there is a shift of the peaks to lower wavenumbers after prolonged UV irradiation of the TiO_2 film. The peaks were extracted and a comparison of the fits is shown in *Figure 5.12*.
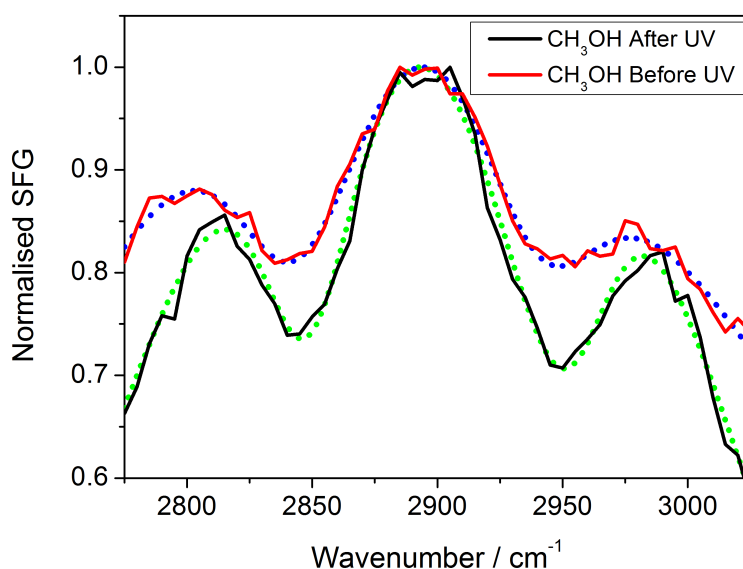
Figure 5.11: *Normalised sum frequency generation spectra recorded at the interface of a TiO₂ film in the presence of CH₃OH (99%, Sigma Aldrich) when the sample was kept in the dark (red line) and following prolonged UV illumination (black line, 355 nm, UV LEDs)*
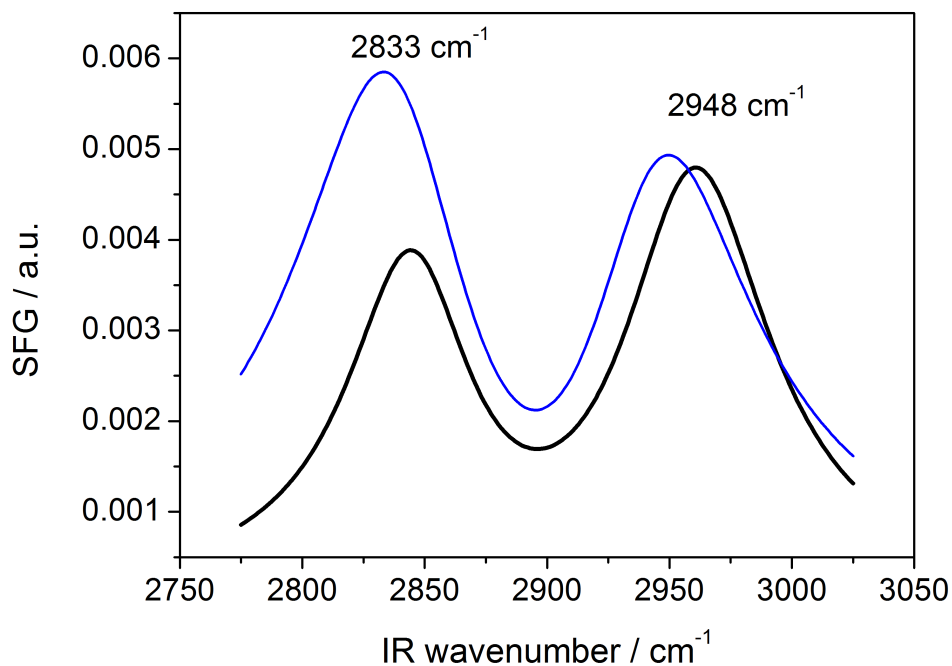
Figure 5.12: **Extracted fittings of the sum frequency generation spectra recorded at the interface of a TiO₂ film in the presence of CH₃OH (99%, Sigma Aldrich) in the dark (black line) and following prolonged UV illumination (blue line, 355 nm, UV LEDs). After UV irradiation it can be seen a substantial increase in the signal magnitude and a shift of the peaks toward lower wavenumbers, which could indicate the presence of chemisorbed methoxy species on the TiO₂ surface.**

After prolonged UV irradiation of the sample the peaks were at 2833 and 2948 cm^{-1} which indicates that these signals could be assigned to chemisorbed methoxy on the TiO_2 surface, indicating an efficient activation of the sample by UV irradiation as suggested by Shultz and co-workers.[123-125]

However, given the number of Lorentzian functions employed in the data analysis it is not possible to assign the peaks at 2833 and 2948 cm^{-1} exclusively to methoxy, in fact there may be a contribution to these peaks by the signals assigned previously to the physisorbed methanol.

5.3.3 SFG Studies at the Surface of TiO$_2$ Films in the Presence of Water

Using Ar as a gas carrier, D$_2$O was introduced in the cell and a SFG spectrum was recorded in the dark in order to monitor any change in the signal attributable to D$_2$O micro-drops deposited on the surface of the TiO$_2$ film. *Figure 5.13* shows the comparison between the spectra recorded solely in Ar and in the presence of D$_2$O.
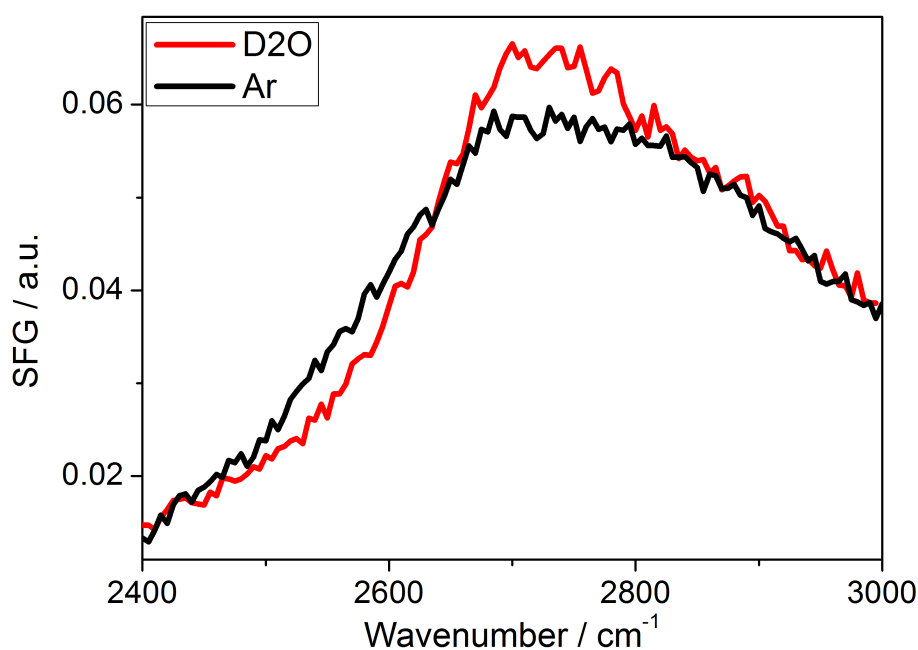
Figure 5.13: *Sum frequency generation spectra recorded at the interface of a TiO$_2$ film in the dark under an Ar flow (black line) and a D$_2$O flow (red line).*

From the SFG spectra reported above a slightly steeper slope at short wavenumbers and a higher peak at 2725 cm^{-1} is observed. The spectrum recorded in Ar (assigned exclusively to non-resonant signal) was subtracted from the spectrum recorded in D$_2$O and the difference is reported in *Figure 5.14*.
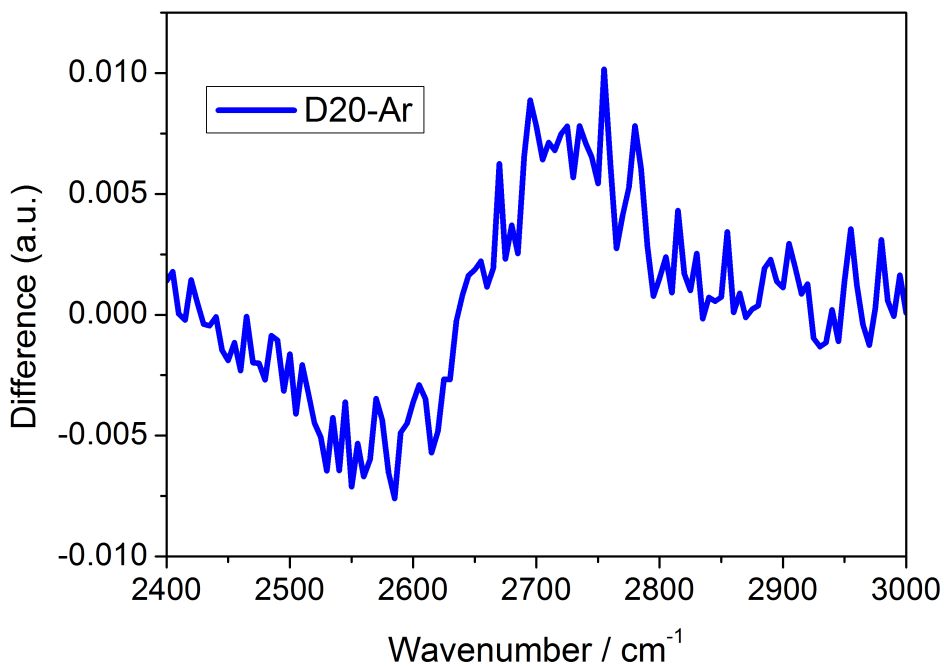
Figure 5.14: Sum frequency generation signal obtained by subtracting the non-resonant background from an SFG spectrum recorded at the interface of a TiO_2 film in the dark under a D_2O flow.

The subtraction of the spectra shows a broad negative peak at 2575 cm^{-1} and a positive, and sharper peak at 2750 cm^{-1} which could be assigned to the presence of molecular D_2O adsorbed on the TiO_2 surface.

The same measurements were carried out under UV illumination of the sample area and the spectra recorded in Ar and D_2O are shown in *Figure 5.15* (top). *Figure 5.15* (bottom) shows the difference between the two spectra.
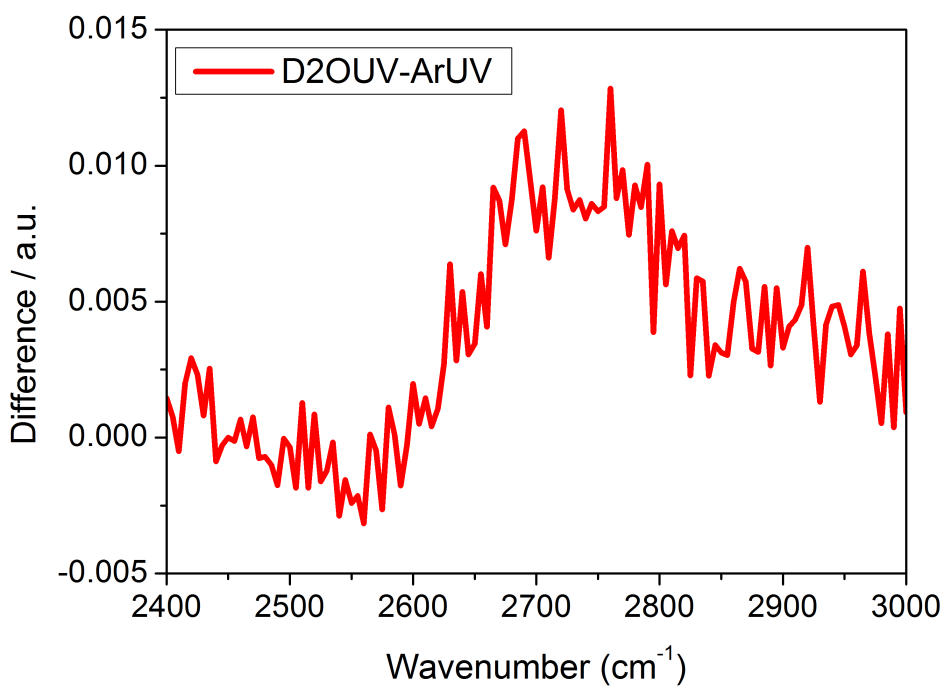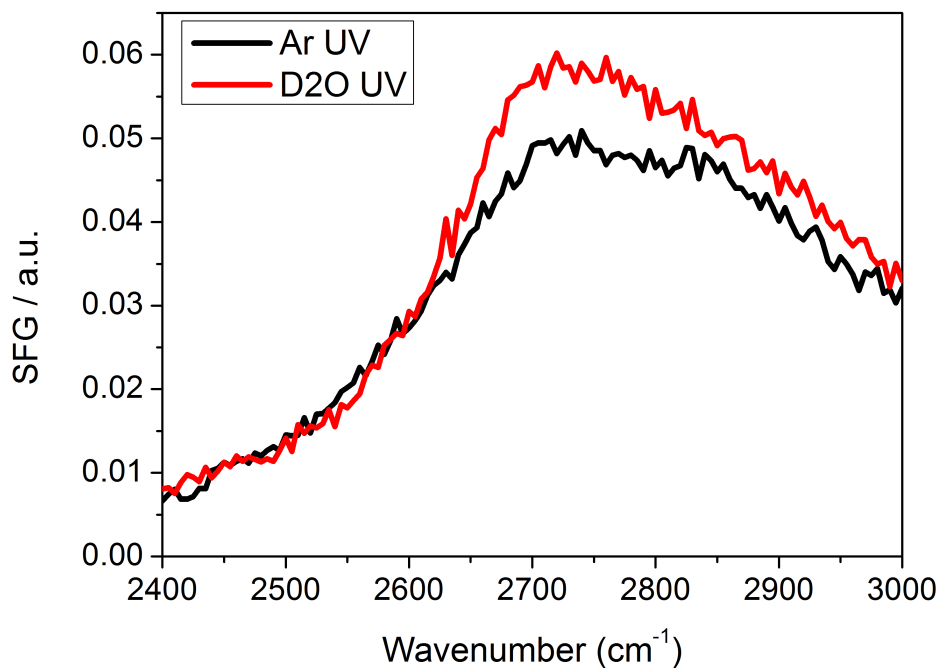
Figure 5.15: *Sum frequency generation spectra (top) recorded at the interface of a TiO$_2$ film during UV illumination (355 nm, UV LEDs) under an Ar flow (black line) and a D$_2$O flow (red line) and (bottom) SFG signal obtained by subtracting the non-resonant background from a SFG spectrum recorded at the interface of a TiO$_2$ film during UV illumination (355 nm, UV LEDs) under a D$_2$O flow.*
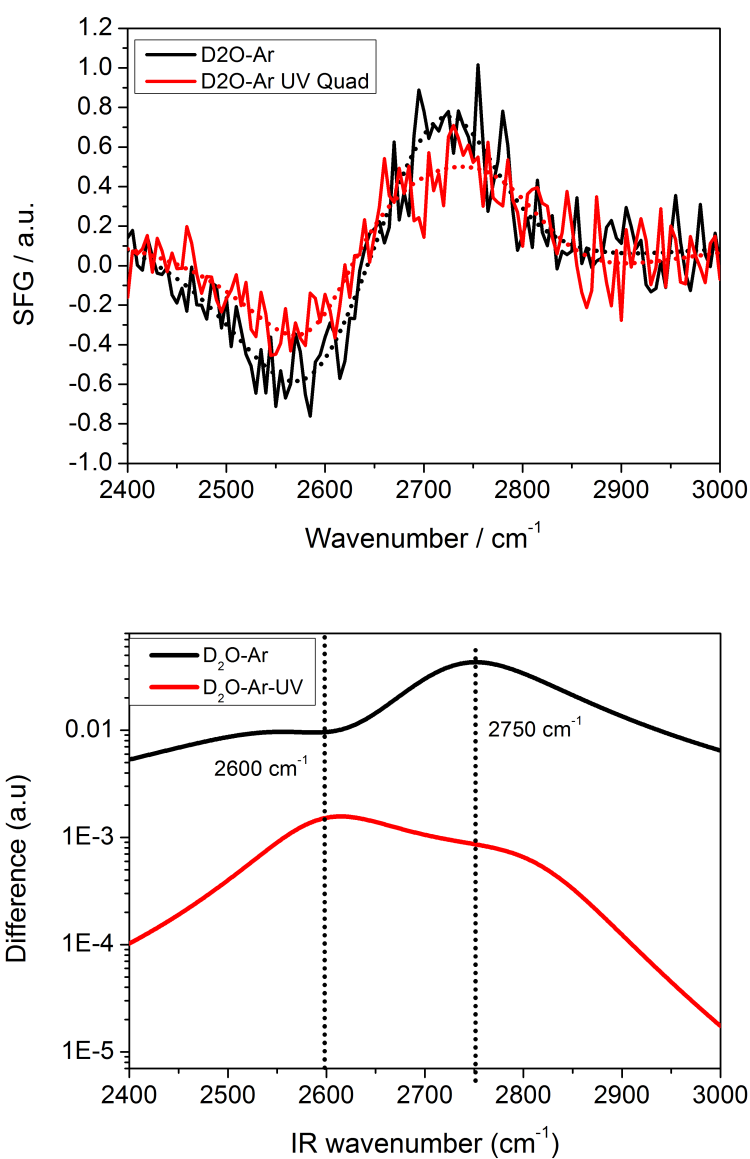
Figure 5.16: *(Top) Comparison between the sum frequency generation spectra recorded at the interface of a TiO₂ film under a D2O flow in the dark (black line) and during UV illumination (red line, 355 nm, UV LEDs) and (bottom) extracted fitting of the aforementioned spectra.*

The spectra reported in *Figure 5.13* and *Figure 5.15* (top) present similarities, however, it is necessary to compare the subtraction spectra (*Figure 5.16* top) and especially the extracted peaks (*Figure 5.16* bottom) in order to highlight any differences. From the

analysis of the extracted fitting it is possible to identify two main broad peaks. One at 2750 cm^{-1}, which is predominant when the sample is kept in the dark, and one at 2600 cm^{-1}, which is predominant when the TiO$_2$ film is exposed to UV light. Although it is not possible to accurately determine the position of these broad peaks they could be attributable to the symmetric and asymmetric stretches of D$_2$O, which are known to have characteristic peaks at ~2650 and ~2740 cm^{-1} respectively.[129,130] However, given the magnitude and the shape of these peaks it is not possible to assign them with certainty to adsorbed D$_2$O on the TiO$_2$. Furthermore, the reason for the difference noted in the intensities of the peaks as a result of UV irradiation still remains unclear, although this could be ascribed to a possible increase in the hydrophilicity of the TiO$_2$ surface as described by Uosaky et al. in 2004.[126]

Nevertheless, in the absence of any chemical scavenger the main process involving the photogenerated charge carriers is recombination, therefore it was decided to use Ag$^+$ as an electron scavenger in order to generate long-lived holes which could react with water,[16] and to identify any possible signal attributable to reaction intermediates.

A drop of 0.01 M AgNO$_3$ was left to dry on a freshly calcined TiO$_2$ sample kept in the dark then SFG spectra were recorded under a D$_2$O flow while the sample was irradiated with UV light.

However, two main problems arose, as described below, which prevented the collection of any useful data.

- Following AgNO$_3$ deposition on the sample surface, the TiO$_2$ layer which in previous experiments appeared to be strongly attached to the CaF$_2$ substrate, easily exfoliated from the window preventing the acquisition of any data. To overcome this problem we attempted to deposit two different layers of TiO$_2$ on the CaF$_2$ substrate, the first by spry

pyrolysis and the second by the doctor blade method as described in section 5.3.2. The samples prepared following this procedure were treated with $AgNO_3$ and the SFG measurements were repeated. The TiO_2 films showed a higher stability and no exfoliation was noted, however, the colour of the film rapidly turned brown/black when the samples were exposed to UV irradiation indicating the deposition of Ag nanoparticles on the TiO_2 surface.

- The dark coloration of the sample as a result of Ag particle deposition led to difficult identification of any SFG signal and a high level noise, attributable to an increase in the scattering at the TiO_2 surface.

These problems that arose have prevented the acquisition of any spectra in the presence of $AgNO_3$ as an electron scavenger.

5.4 Conclusions

Transient absorption studies on TiO_2 photoanodes in the pH range 2-13 showed a substantial decrease of the hole lifetime at high concentrations of OH^-. By fitting the TA kinetic traces recorded at 460 nm, where the valence band holes are known to absorb, it has been possible to estimate the hole lifetime dependence on the pH of the electrolyte. The slow decay between pH 2 and 12 indicated the presence of relatively long-lived photoholes capable of oxidising water in accord with previous studies, whereas a significant decrease of the hole lifetime at pH >12.5 suggested a change in the mechanism of water oxidation at this pH. However, transient absorption spectroscopy does not provide detailed information on the mechanism of reaction and cannot identify reaction intermediates.

Initial SFG studies on TiO_2 films showed the capability of samples prepared by doctor blade method for use with these measurements. The presence of two distinct SFG peaks assigned to physisorbed methanol (2850 and 2970 cm^{-1}) and two peaks attributable to chemisorbed methanol (2830 and 2940 cm^{-1}) were confirmed, highlighting the potential of sum frequency generation spectroscopy for the study of the intermediates involved during water oxidation on metal oxide semiconductors. From the analysis of SFG spectra recorded in the presence of D_2O in the dark and under UV illumination of the TiO_2 sample it has been possible to identify the presence of two broad peaks which could be ascribed to the symmetric and asymmetric stretch modes of adsorbed D_2O on the TiO_2 surface. However, the relatively low resolution used during the course of these experiments has not enabled a definitive assignment. SFG studies at the TiO_2/D_2O interface in the presence of an efficient electron scavenger have underlined the need to improve the stability of the samples in order to determine the presence of surface intermediates.

Particular attention has been given to the optimisation of the system employed, however several problems encountered during the course of these experiments such as difficulties in spatially and temporally overlapping the ps beams and finding the interface and the correct collection angle, have not allowed any further investigation.

Chapter VI

Design and Initial Measurements on a Medium Scale LSC/PEC Reactor

In this chapter a medium scale hybrid reactor consisting of a luminescent solar concentrator connected to a α-Fe_2O_3 based photoelectrochemical cell is described. The driving force required to enable water oxidation is provided by a photovoltaic cell placed in contact with a second luminescent solar concentrator. Initial testing experiments are also reported.

6.1   Introduction

As previously discussed in section 1.3, over the past few years the development of reactors for solar hydrogen production has attracted increasing interest. The Grätzel tandem cells represent the most significant example of solar fuel devices coupling a metal oxide semiconductor photoanode with one or two dye sensitised solar cells connected in series which provides the potential required for the water splitting reaction to take place (Figure 1.12).[48-50] At present, the small size of the photoanodes (~1 cm^2) allows these reactors to reach promising STH efficiency (3.1 % STH for a WO_3 based device)[50] which however decreases with increasing active area of the semiconductor electrodes because transparent conductive substrates are used and their high sheet resistance in a full scale device leads to substantial voltage drops across the electrode decreasing the overall STH efficiency.[131] In fact, based on reported efficiencies for state of the art photoelectrodes, it has been calculated that for a 10 x 10 cm α-Fe_2O_3 planar electrode on FTO, biased to enable a total voltage difference between the counter electrode and the contacts of an FTO/α-Fe_2O_3 electrode of 2.0 V (0.77 V electrical input) under illumination, up to 90 % of the planar photoanode becomes inactive due to the extent of the voltage drop across the material.[132] A further limitation of the Grätzel tandem cells is represented by their vertical design as the wavelengths shorter than 600 nm (considering a state of art α-Fe_2O_3 photoanode) are absorbed by the photoanode limiting the portion of the solar spectrum usable by the DSSCs.[48] Therefore, it is clearly desirable to develop systems that can use photoanodes deposited on highly conductive materials which are unlikely to be optically transparent (e.g. metal substrates), whilst maintaining the ability to drive a PV solar cell

using the longer wavelength photons (> 600 nm) that are not used by the most promising water splitting electrodes.

This chapter describes the development of a medium scale hybrid reactor which couples two luminescent solar concentrator (LSC) plates and a α-Fe$_2$O$_3$ based PEC with a novel design approach that also allows front side illumination of the photoelectrode. *Figure 6.1* shows a pictorial illustration of the PEC cell in a back side illumination (top) and front side illumination (bottom) configuration.
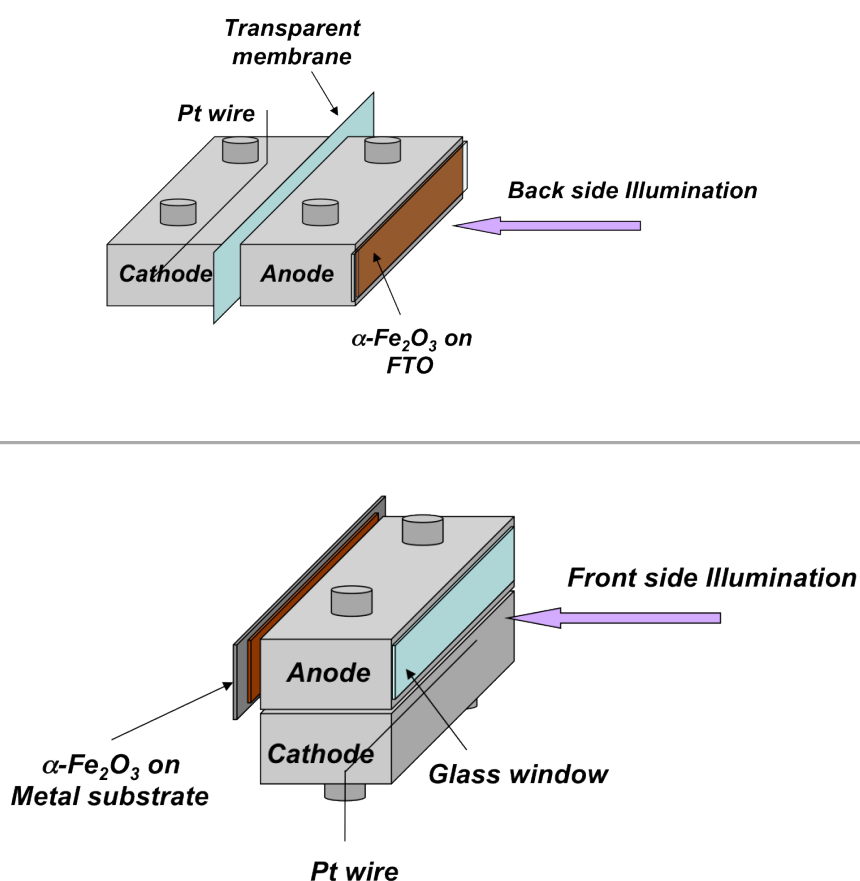
Figure 6.1: *Pictorial representation of the photoelectrochemical cell designed in two different configurations: (top) Illumination of the photoanode from the back side (SE) and (bottom) illumination of the photoanode from the front side (EE).*

By concentrating the incident light onto a smaller area with a geometry designed to minimize resistive losses, we are able to circumvent many of the issues associated with medium to large scale tandem photoreactors. During the development of the reactor we gave particular attention to the cost per unit efficiency and the PEC cell has been designed in order to enable limited dimensions of a ion exchange transparent membrane, which are currently employed in large scale reactors and substantially increasing their cost per unit. In fact, in both configurations the area of the membrane (5 cm^2) is significantly smaller than that employed (100 cm^2) in large scale devices currently used. The costs can further be reduced when using highly conductive metal substrates (instead of conductive transparent glasses) which could also be suitable for roll to roll manufacturing.

In order to prove the applicability of the reactor, we demonstrate the system using a α-Fe_2O_3 on FTO glass photoelectrode as proof of concept. However, in this prototype reactor a back side illumination configuration (*Figure 6.1* top) has been employed which implies a rise in the effective cost per unit as a result of the use of a transparent conductive substrate.

As already mentioned in section 1.1.4 hematite is one of the most commonly employed photoanodes because of its stability under water splitting conditions, its low cost and the position of its band gap (~2.1 eV) which allows the absorption of wavelengths up to ~600 nm (in state of the art materials). However, its absorption profile presents a maximum peak in the violet region of the electromagnetic spectrum (~400 nm) which constitutes only a smaller portion of the solar spectrum. In the reactor described herein a LSC plate with an emission profile in the UV region has been employed in order to irradiate the α-Fe_2O_3 photoanode and generate charge carrier separation, whereas another LSC plate coated with a dye with different absorption and emission features has been used to concentrate

the light on three Si-PV connected in series which provide the required electrical energy input to run the PEC cell off-grid. A first test with less expensive GaAs PV cells has also been carried out, however the poor quality of the cells employed and difficulties in modulating their electric output did not allow their use.

In the following paragraph an introduction on the development of LSCs is discussed.

The principle of planar luminescent solar concentrators was introduced in 1976 by Weber and Lambe when they described a planar solar collector which utilised a luminescent medium to absorb radiation and total internal reflection to collect it in order to concentrate the light onto a high efficiency semiconductor solar cell.[133] Two ideal types of luminescent materials with a strong absorption in the visible portion of the solar spectrum, a high luminescent efficiency and a high transmittance in the emission region were proposed: the rare-earth-doped laser glasses and the dyes used in dye lasers. However, the estimated efficiency for a system coupling incident photons into a high index semiconductor collector was found to be ~10%, limited by gaps in the absorption spectra of the luminescent material. In 1977 Goetzberger and Greubel proposed the use of a stack of transparent sheets of material doped with fluorescent dyes as luminescent medium in order to achieve a higher overall theoretical efficiency of 35% for a system with four semiconductor collectors.[134] The problems which arose from this study were i) the identification of plastic materials with high transparency and ii) the light losses due to self-absorption in the fluorescent dyes because of their overlap between absorption and emission spectra. Over the last few decades different kinds of LSC have been developed with particular interest in planar LSC consisting in glass sheets coated with an organic thin-film which are reported to reach a quantum efficiency >50% in a tandem-waveguide configuration.[135] At present, in state of the art LSCs, the organic dyes are replaced by quantum dots (QDs) which allow

the absorption threshold to be tuned by choosing the diameter of the dots and lead to high luminescence quantum efficiency.[136-138] The choice of the QDs size limits the overlap between the luminescence and absorption minimising the re-absorption losses and improving the quantum efficiency of LSC systems.

Herein we decided to employ LSC because of their capability to collect both direct and indirect solar radiation concentrating it by a factor of 5-10 and consequentially increasing the solar energy harvesting of PV and PEC systems. Once the principle of operation of the prototype device has been proven, it would be possible to develop a reactor based on a photocathode/photoanode design which could lead to a complete water splitting reaction with no need for an external applied bias.

6.2 Experimental

In collaboration with the Chatten Group (Physics Department, Imperial College London) a proof of principle reactor in a back side configuration has been developed and its outline is shown in *Figure 6.2*.
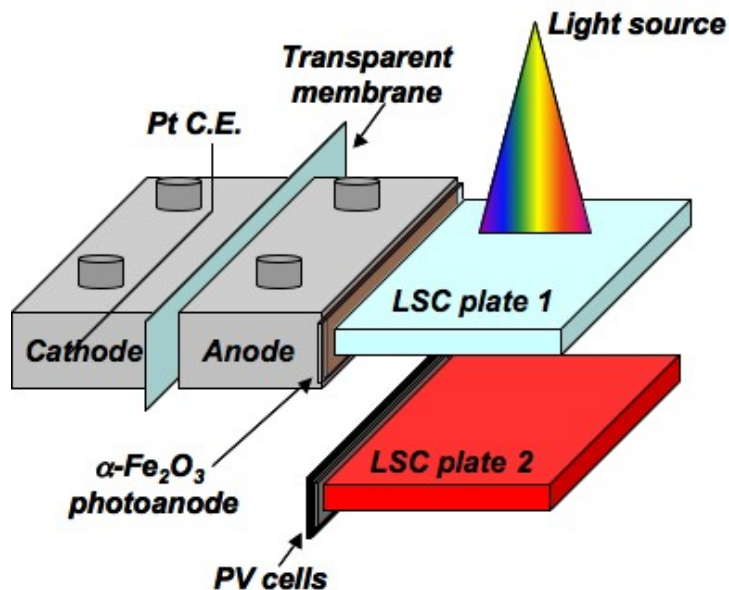
Figure 6.2: *Pictorial representation of the LSC/PEC reactor developed in a back side (SE) illumination configuration. The UV emitting LSC plate is placed in contact with the photoanode, whereas the Vis emitting LSC plate is placed in contact with three Si PV cells connected in series.*

The proof of principle device consists of a PEC cell with a 10x5 cm active area based on a $5cm^2$ α-Fe_2O_3 photoelectrode coupled with two 10x10x0.5 cm LSC plates used to irradiate both the photoanode and the Si PV cells. The α-Fe_2O_3 samples were prepared by Dr A. Hankin (Prof. G. H. Kellsal Group, Department of Chemical Engineering, Imperial College London) following the procedure described in Section 2.7. The PEC cell contained a 10 cm long Pt wire acting as counter electrode and was filled with an aqueous solution of NaOH 1 M. A Nafion-115 membrane was placed between the anode and the cathode chambers. The Si PV cells were provided by Dr J. Goldschmidt (Fraunhofer-Institute for Solar Energy Systems ISE, Freiburg, Germany). The front of the cells was inverted pyramids with 105 nm anti-reflection and surface passivating SiO_2 and Ti/Pd/Ag fingers provided electric contact whereas the back was coated with evaporated Al. The characterisation of the PV cells and of the LSC plates was carried out by M. Fisher and J. Videira (Chatten group,

Imperial College London) which provided some results and data showed in this the following section. The LSC plates were prepared by coating a matrix material consisting of a mixture of PMMA and LMA, with a total mass of 4g (15% of LMA), dissolved in 10 ml of chlorobenzene in which were added different dyes. 2.5(wt)% of Fluorescent Violet (Kremer) dye was desolved to the matrix/solvent material to coat plate 1, whereas 3(wt)% Lumogen red 305 was added to coat plate 2. Photon flux measurements were performed on both the red and violet LSC using a Steuernagel Lichttechnik solar simulator as light source removing the UV filter to give a spectrum closer to that of the AM1.5g solar spectrum and measuring the output from the four edges of each plate.

Photocurrent vs voltage plots and chronoamperometry measurements were carried out using an Autolab potentiostat (PGSTAT101) connected to a PC where the data were acquired using a Nova v1.4 software.

6.3 *Results and Discussion*

6.3.1 PEC Cell Design

The PEC cell consists in an anodic and a cathodic compartment containing the photoanode (α-Fe_2O_3 electrode) and a counter electrode (Pt wire) respectively. PEEK was chosen as the manufacturing material after taking into account its high chemical stability in a wide range of pHs including highly alkaline solutions which have been used during these studies.[139] The cell was designed in order to allow both front or back side illumination of the photoelectrode. *Figure 6.3* shows the outline of the PEC cell in a back side illumination configuration.
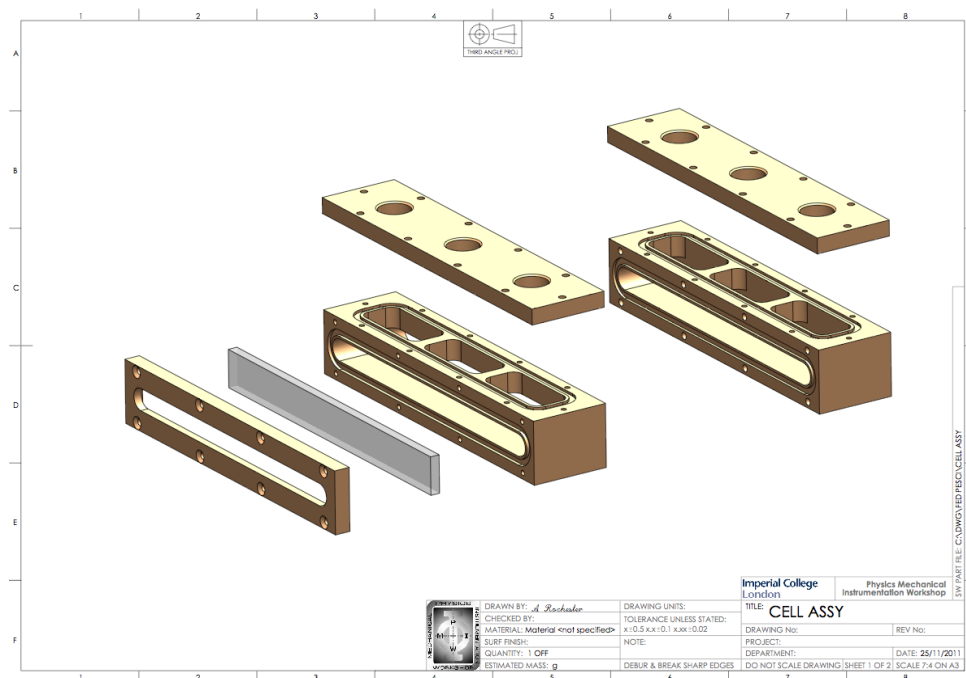
Figure 6.3: *Outline of the PEC cell showing a back side (SE) illumination configuration.*

Both configurations present advantages and disadvantages. In an SE configuration the α-Fe_2O_3 photoanode is deposited on a transparent conductive substrate which also acts as the front window of the PEC cell. The photoanode, therefore, is easily accessible by incident UV light and charge carrier separation is expected to be maximised. However the use of large transparent substrates leads to substantial potential drops across the electrode as a result of a large sheet resistance.[131-132] Higher are the potential drops and lower is the overall quantum efficiency of the reactor. Furthermore, in an SE configuration the cathode and anode chambers need to be separated by an ions exchange membrane in order to avoid the recombination of gaseous oxygen and hydrogen evolved during photoassisted water splitting. Nevertheless, the highly alkaline pH of the electrolyte used during the course of these experiments limits the choice of the membrane to be employed because of stability issues. In the prototype reactor a Nafion-115 membrane was utilised

and replaced after every set of experiments in order to avoid its degradation and subsequent contamination of the cell. Nafion is in fact known to be subject to degradation over time when in the presence hydrogen peroxide.[140] Furthermore, the use of transparent conductive substrate leads to resistance losses and increase in the costs of the unit. On the contrary, the use of a EE configuration enable the α-Fe$_2$O$_3$ to be deposited on a highly conductive metal substrate which are characterised by low sheet resistance in contrast with conductive glass substrates and, therefore, their use minimise the potential drops across the electrode increasing the overall efficiency of the reactor. However, in the EE configuration the incident UV light must follow a relatively long path before reaching the photoanode and the risk of losses derived by light diffraction in the electrolyte could lead to a less efficient charge carrier separation.

During the course of the measurements described in the following section the SE configuration has been employed and the glass electrode was coated at the edge with a silver paste (Electrolube SCP03B) in order to decrease the sheet resistance along the substrate increasing the length of the current collector.

6.3.2 LSC Choice and Preparation

As shown in *Figure 6.2* two LSC plates have been coupled to the PEC cell; plate 1 has been used to irradiate the photoanode and induce charge carrier separation and plate 2 has been used in order to drive a series of Si PV cells needed to provide the electrical energy input required to minimise electron/hole recombination and enable the reaction of water oxidation on the α-Fe$_2$O$_3$. The luminescent dyes employed in the coating of the glass plates have been chosen considering their absorption and emission profiles in order

to both optimise the portion of the solar spectrum used and match the absorption spectra of the photoanode and the PV cells:

- The choice of the dye employed in plate 1 has been carried out by considering the IPCE% profile of the α-Fe$_2$O$_3$ electrode used (*Figure 6.4*). IPCE% values were determined experimentally by chronoamperometry measurements employing the equipment described in Section 2.1.3.
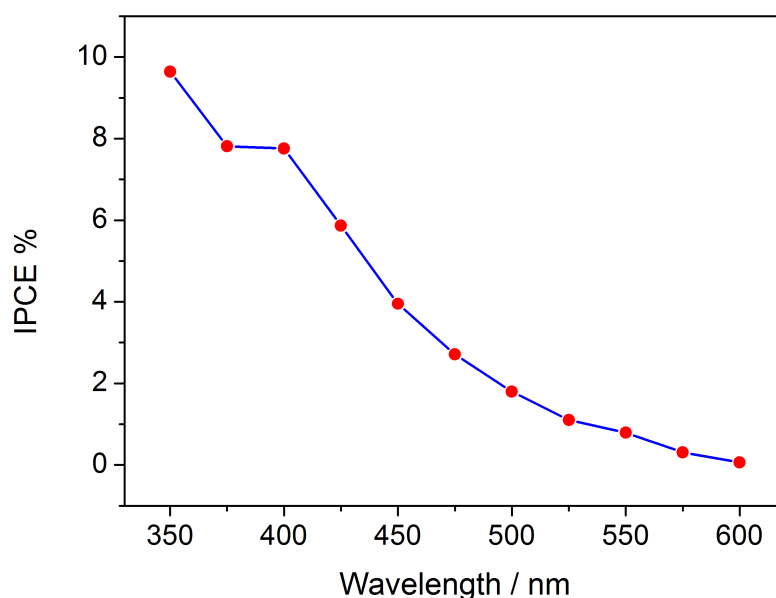
Figure 6.4: *Incident Photon-to-Current Efficiency (IPCE%) determined by chronoamperometry measurements between 300 nm and 675 nm, illuminating the α-Fe2O3 photoanode from the SE side on 1 M NaOH.*

As it can be seen from *Figure 6.4*, the IPCE% reaches a maximum value at an irradiation wavelength of 350 nm indicating an efficient charge carrier separation, and rapidly declines until it reaches a minimum at 600 nm. Therefore, a dye with a narrow emission profile close to 350 nm is preferable.

- The choice of the dye employed in plate 2 has been carried out by considering the external quantum efficiency of the Si PV cells (*Figure 6.5*). No substantial differences were noted when testing the three PV cells. When irradiated between 650 and 800 nm each cell reached a maximum EQE value close to 90%. This suggested the choice of a dye with an emission profile in the visible region.
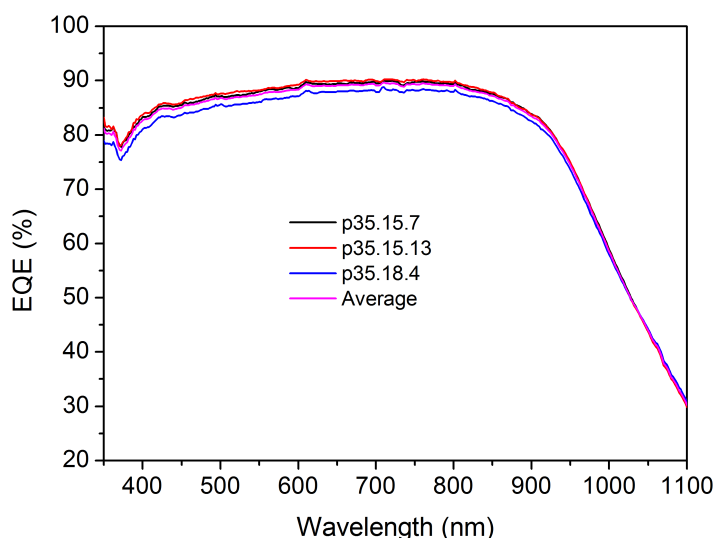
Figure 6.5: *External Quantum Efficiency (EQE%) recorded for the three PV cells between 350 and 1100 nm. Figure courtesy of M. Fisher.*

In operational conditions the LSC are placed one on the top of the other (*Figure 6.2*), therefore, the absorption profiles of both the dyes have been considered in order to avoid any substantial overlap between their absorption spectral regions which could lead to the loss of a portion of the solar spectrum employable. Also, the dyes concentrations were chosen in order to be sufficiently high so as to ensure the maximum absorption of light but also to be low enough to avoid noticeable dye agglomeration.

Figure 6.6 top and bottom shows the absorptivity (expressed as the fraction of radiation absorbed at a given wavelength) spectra for the dyes used for coating plate 1 and 2 respectively.
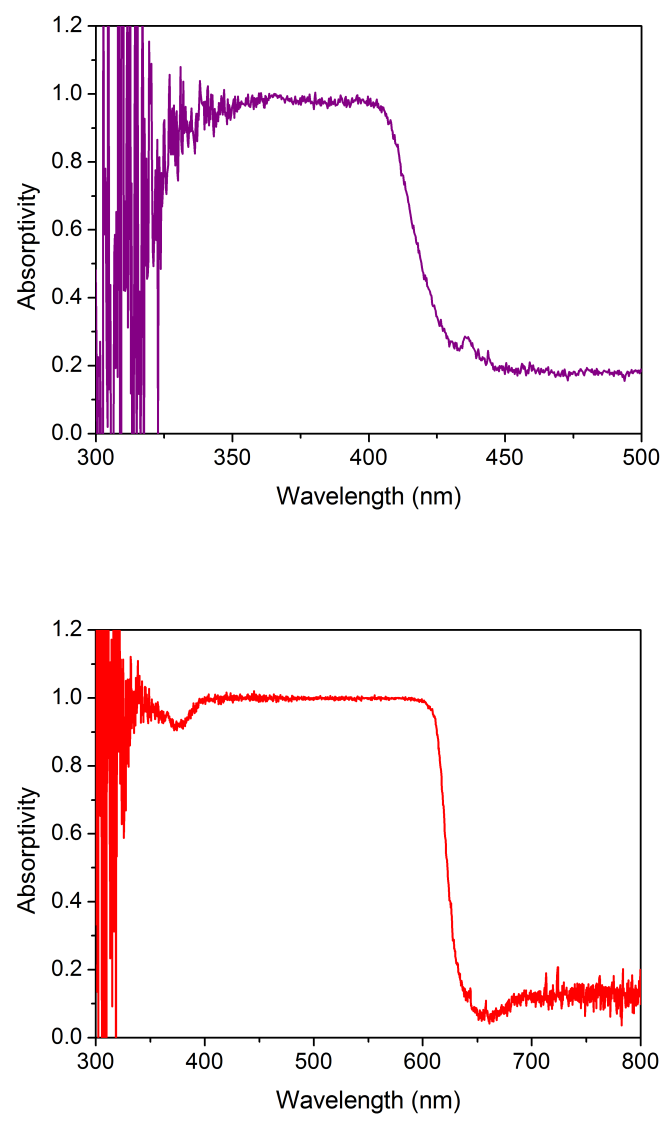
Figure 6.6: *Absorptivity spectra of the 2.5(wt)% Lumogen Violet LSC plate (top) and the 3(wt)% Lumogen red 305 LSC plate (bottom). Figure courtesy of M. Fisher.*

As it can be seen in *Figure 6.6* (top) the Fluorescent Violet dye presents a saturation of the absorption spectrum between ~350 nm and ~410 nm whereas in the Lumogen red 305 dye (*Figure 6.6* bottom) the absorption saturation occurs between ~400nm and ~610 nm. The edge emission spectra were recorded for both plates both independently taken and when mounted inside the plates holder. *Figure 6.7* top and bottom shows the emission spectra in terms of normalised photon flux recorded for the UV and the red plates respectively.
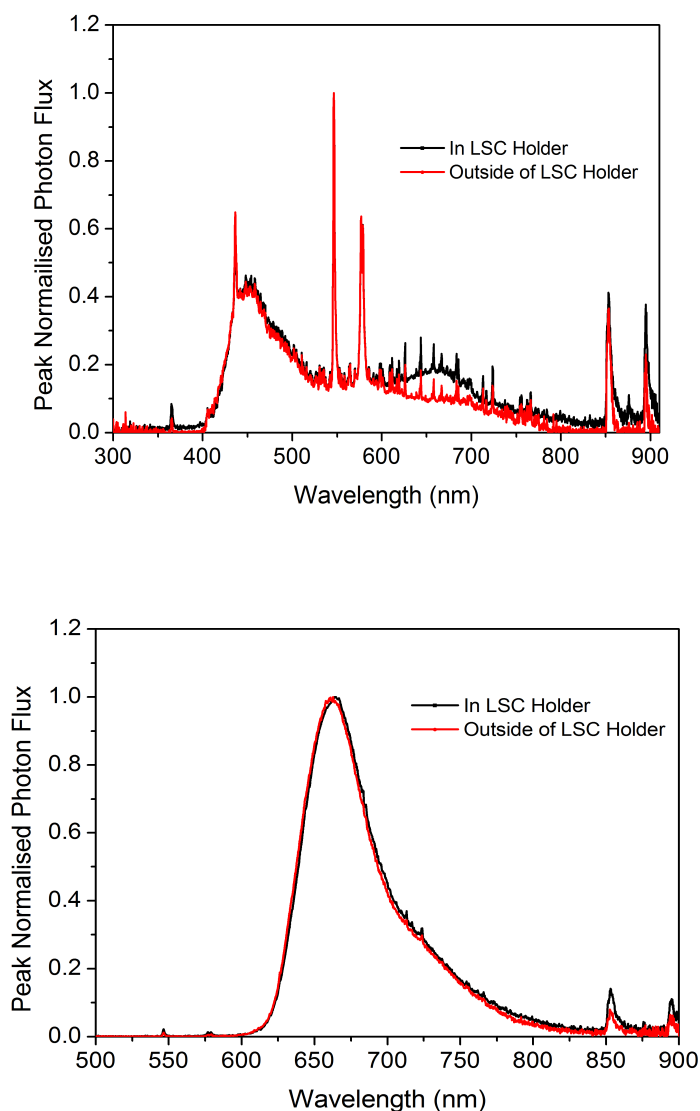
Figure 6.7: *Edge emission spectra of the Lumogen Violet LSC plate (top) and the Lumogen red 305 LSC plate (bottom). The spectra were recorded outside (red lines) and inside (black lines) the sample holder. Figure courtesy of M. Fisher.*

As shown in *Figure 6.7*, the Lumogen violet LSC presents an emission peak at ~450 nm, which does not match the maximum IPCE% of the α-Fe_2O_3 electrode. On the contrary, the Lumogen red 305 shows an emission peak at ~650 nm which perfectly matches the region where the EQE efficiency of the PV cell reaches a maximum value.

The Lumogen Violet emission spectrum presents an additional peak in the spectrum when inside the LSCs holder (~650 nm). This is the result of some of the red photoluminescence emission scattered to the edges of the violet LSC. Both spectra presents a slight red-shift when inside the sample holder as a result of an increase in re-absorption losses due to PTFE white diffuse scattering that lines the inside of the LSC sample holder.

Table 6.1 and *Table 6.2* show the results of photon flux measurements for the violet and the red LSCs respectively from each of the four edges.

Table 6.1: *Photon flux, optical efficiency and photon concentration data for the Lumogen violet LSC measured from each edge. Data courtesy of M. Fisher.*

Violet LSC	*Edge 1*	*Edge 2*	*Edge 3*	*Edge 4*	*Average*
Photon Flux	1.721±0.017	1.688±0.017	1.636±0.016	1.635.0.016	1.670±0.209
Optical Efficiency	2.90±0.03%	2.80±0.03%	2.70±0.03%	2.70±0.03%	2.80±0.08%
Photon Concentration	0.553±0.006	0.542±0.005	0.526±0.005	0.525±0.005	0.536±0.012

Table 6.2: *Photon flux, optical efficiency and photon concentration data for the Lumogen red 305 LSC measured from each edge. Data courtesy of M. Fisher.*

Red LSC	*Edge 1*	*Edge 2*	*Edge 3*	*Edge 4*	*Average*
Photon Flux	2.298±0.023	2.367±0.024	3.267±0.033	3.226±0.032	2.790±0.458
Optical Efficiency	3.7±0.04%	3.8±0.04%	5.2±0.05%	5.2±0.05%	4.5±0.73%
Photon Concentration	0.715±0.007	0.737±0.007	1.017±0.010	1.004±0.010	0.868±0.143

As it can be seen from the tables above, the average photon concentration is 0.536 and 0.868 for the violet and the red LSCs respectively. This suggests that on average, using a LSC is less efficient than directing the PEC or the Si PV cells directly at the solar simulator light source. However regarding the red LSC, two edges (3 and 4) emit more light than could be collected by aiming the PV cells directly at the incident light source. The photon concentration variation is attributed to the variation in the optical density of the LSCs at different regions across the surface of the plate.

On the other hand the level of photon concentration in the violet LSC is far below the desirable values grater than 1 indicating that the photoanode is supplied with almost half of the light that might be collected if placing it directly under the incident light source, leading to a less efficient charge carrier separation. An increase of the dye concentration leads to an increase of the photon concentration, however in this case an increase of the concentration of the Lumogen violet dye would lead to visible dye agglomerations which have a quenching effect resulting in less light emitted from the edge of the plate. The use of a different UV absorbing dye with higher photon concentration is under consideration.

6.3.3 Reactor Operation

By placing the UV plate in contact with the α-Fe_2O_3 electrode and the Red plate in contact with the Si PVs connected to the counter electrode, charge carrier separation can be achieved and water oxidation occurs at the photoanode whereas proton reduction takes place at the Pt wire.

A commercial acrylic matching fluid (Cargille) with a refractive index of 1.4917 (very similar to glass) was placed between the LSC plates and the anode and PV cells to remove any air gap and stop photons from being totally internally reflected at the interface.

In order to determine the optimal operational conditions in which run the photoelectrochemical cell, photocurrent measurements were carried out with a two electrode setup in the dark and under UV irradiation between +0.6 and +1.85 V vs the RHE using the equipment described in the experimental section. *Figure 6.8* shows the recorded traces for the α-Fe_2O_3 photoanode before and after $Co(NO_3)_2$ treatment. The treatment of α-Fe_2O_3 with $Co(NO_3)_2$ results in an earlier onset of the photocurrent which also reaches a higher value in the plateau region. The steep rise of the current at potential higher than +1.7 V vs RHE indicates the potential in which classic electrolysis begins. In order to avoid electrolysis taking place it is necessary to keep the applied potential during operational conditions at value lower than +1.7 V.
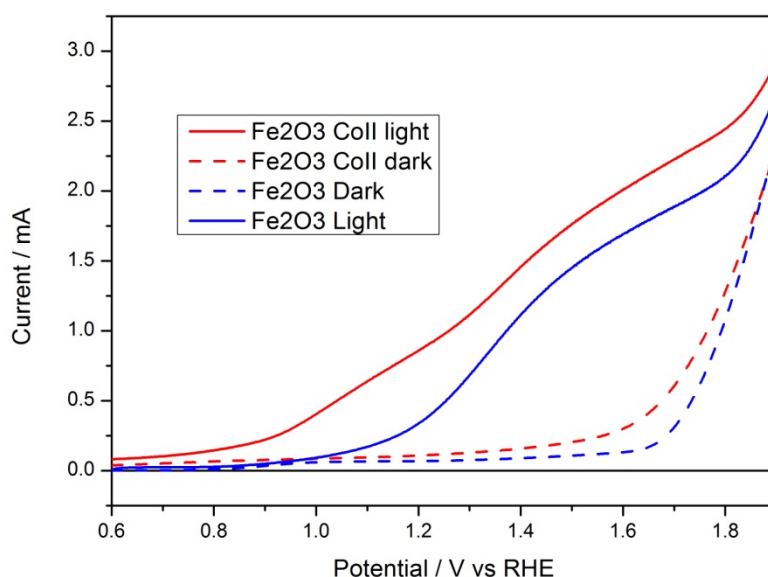
Figure 6.8: *Linear sweep voltammogram recorded at a scan rate of 20 mV/s in the dark (dotted lines) and under UV illumination (solid lines, 355 nm, 75W Xe lamp) before (blue lines) and after (red lines) $Co(NO_3)_2$ treatment of the α-Fe_2O_3 photoanode in 1 M NaOH.*

The output of the Si PV cells connected in series was also recorded in the dark and under illumination between 0 and +1.85 V. The potential has been scanned at different light intensity covering part of the red luminescent plate with the aim of regulating the current output of the PV cells in order to avoid the application of an overpotential when the PV cells are connected to the PEC cell. A good fill factor is maintained over the range of intensities and a small current is still present even when 100% of the LSC area is covered because of possible light reflection on the walls of the box containing the plates. The recorded traces are shown in *Figure 6.9*.
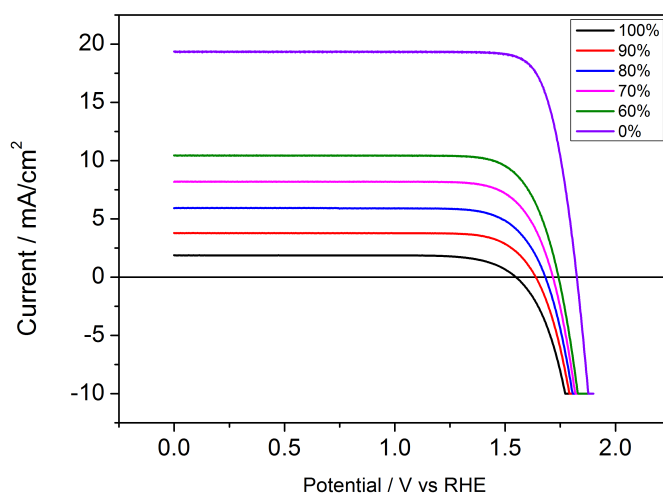
Figure 6.9: *Current recorded versus the applied potential for the three Si PV cells connected in series covering up to 100% of the area of the Lumogen red 305 LSC plate.*

By overlapping the photoanode photocurrent with the current output of the PV cells it is possible to define the optimal operational conditions for the reactor.
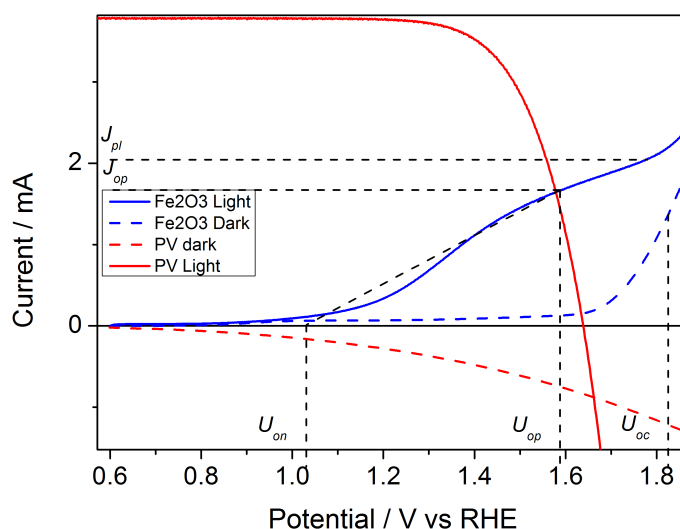
Figure 6.10: *Overlap of the linear sweep voltammogram recorded at a scan rate of 20 mV/s for the α-Fe₂O₃ photoelectrode in the dark (blue dotted line) and under UV illumination (blue solid line, 355 nm, 75W Xe lamp) in 1 M NaOH and current output of the three Si PV cells connected in series in the dark (red dotted line) and when placed in contact with the lumogen red 305 LSC plate (red solid line).*

Figure 6.10 shows in blue the α-Fe₂O₃ dark and light photocurrent curves (dotted and solid lines respectively) and in red the dark and light (90% of LSC area covered) current output for the Si PV cells (dotted and solid lines respectively). Where J_{op} and U_{op} represent the current and voltage at operational condition respectively; U_{on} and U_{oc} the onset and open circuit potential and J_{pl} the plateau photocurrent.

6.3.4 Chronoamperometry Measurements and Efficiency Definition

Chronoamperometry measurements were carried out when the PV cells were connected to the PEC cell in order to supply the required electrical bias to allow electrons to flow to the counter electrode.

The sample holder containing the two LSC plates was placed under the solar simulator, the Si PV cells and the PEC were placed on the free edge of the LSCs and the reactor was connected to the potentiostat as shown in a pictorial illustration in *Figure 6.11* left. The positive pole of the PV cells was connected to the photoanode while the negative pole, together with the counter electrode (Pt wire), were connected to the potentiostat.
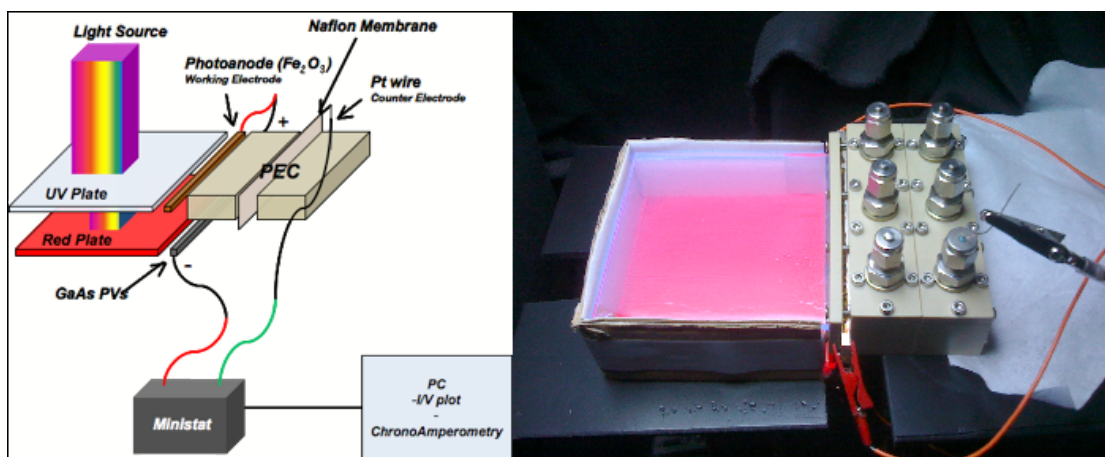
Figure 6.11: *(Left) Pictorial outline of the LSC/PEC – LSC/PV device connected to the potentiostat to carry out I/V and chronoamperometry measurements. (Right) Picture of the reactor placed under the solar simulator light source.*

For each set of experiments the light source was blocked using a black card for 100 seconds in order to allow the dark current to stabilise, subsequently the LSCs were irradiated and the current recorded until reaching a plateau. *Figure 6.12* shows the recorded current density vs time.
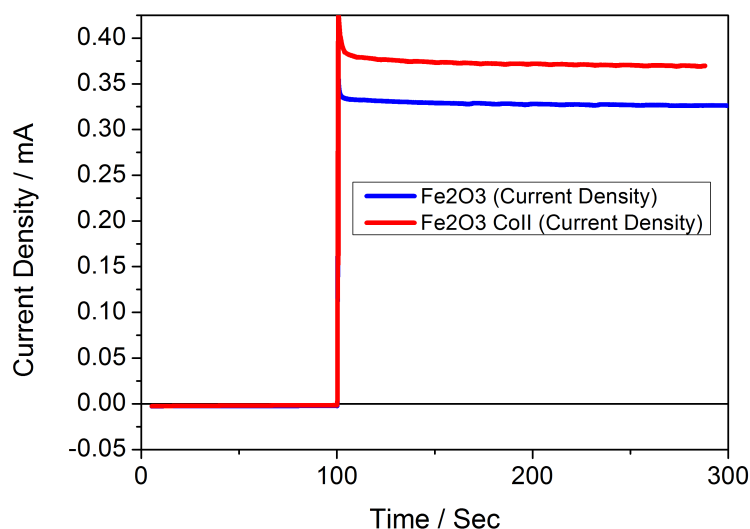
Figure 6.12: *Chronoamperometry graph recorded for both a CoII doped (red line) and undoped (blue line) α-Fe₂O₃ electrode in 1 M NaOH at +1.6 V vs RHE. For the first 100 seconds the photoanode was kept in the dark by totally covering the Lumogen UV LSC plate then it was exposed to irradiation by exposing the Lumogen UV LSC plate to the solar simulator and the current was recorded until reaching a plateau.*

An average of the current density was taken for the plateau region in the dark and in the light resulting in an average of 0.30 mA/cm² and 0.37 mA/cm² for the undoped and doped electrode respectively.

Relatively high current was recorded indicating an efficient charge carrier separation. From the current values it is possible to estimate the STH efficiency for the reactor using equation 6.1.

$$STH = \frac{J_{(OP)}(mA/cm^2) \cdot 1.23(V)}{P(mW/cm^2)} \qquad \text{Eq. 6.1}$$

Considering the photocurrent density (J_{op}) recorded by chronoamperometry and the power output on the edge of the LSC plate (4.5 mW/cm^2),[57] we obtain a STH value of 0.1% for a cobalt treated sample.

The so determined STH efficiency is substantially lower than the current efficiency reported for α-Fe$_2$O$_3$ based Grätzel tandem cells (1.16%),[48] this is ascribed to three main factors, i) the lower quality of the photoanodes employed in these experiments, ii) the lack of photon concentration occurring at the violet LSC plate and iii) the slight mismatch between the emission spectra of the UV plate and the IPCE% profile of the photoanode. By optimising these parameters a higher STH efficiency would be reached. For example, if we consider state of the art α-Fe$_2$O$_3$ photoanodes[141] with a maximum photocurrent density of 1.3 mA/cm^2 at 450 nm (*Figure 6.13* left) and an IPCE% several times greater than the efficiency of the electrode used herein, we could reach a theoretical STH efficiency of ~0.5%, substantially higher than the one recorded with the photoanode employed in this study.
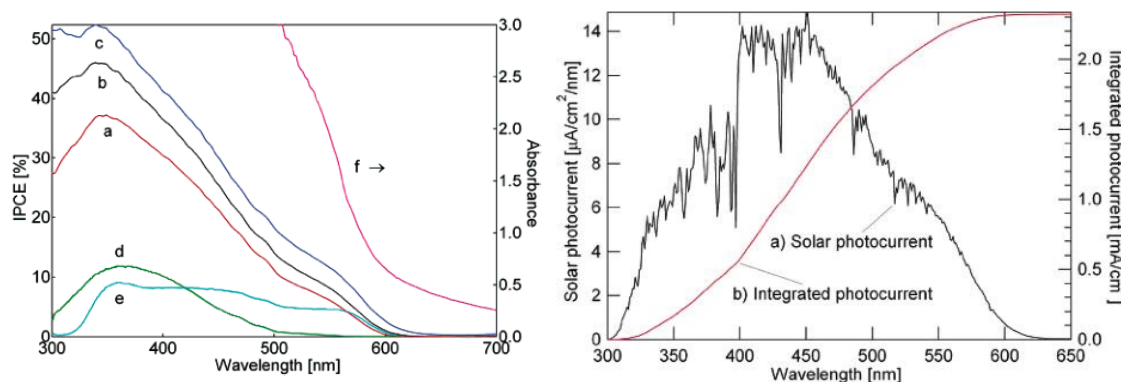
Figure 6.13: IPCE% values (left) and integrated photocurrent (right) recorded for a state of the art cobalt treated α-Fe$_2$O$_3$ photoanode. Figures reproduced from reference 141.

Furthermore, higher efficiencies can be achieved by using a different UV emitting dye with higher photon concentration yield and with an emission spectrum which better match the IPCE profile of the photoanode. By doing this a more efficient charge carrier separation could be achieved.

It is important to mention that a first set of experiments was carried out using three GaAs photovoltaic cells, however, given the poor quality of these cells it was not possible to control their current output maintaining a good fill factor and this resulted in a constant output of +1.85 V in operational conditions. When the chronoamperometry measurements were carried out on the fully operational reactor the current reached a stable average reading as high as 3.6 mA/cm^2. However, considering the high voltage applied on the PEC it was proposed that the high current value was caused by photo voltage driven electrolysis of water. The use of GaAs PV cell, however, is under consideration as it would further decrease the reactor overall cost per unit.

6.4   Conclusions

The prototype of a hybrid medium scale solar reactor consisting of a α-Fe$_2$O$_3$ based potoelectrochemical cell coupled with two luminescent solar concentrator plates and three Si photovoltaic cells has been herein developed. The design of the photoelectrochemical cell was chosen in order to reduce the overall cost per unit of the reactor. In fact, in a front side configuration the use of large area expensive transparent membranes could be avoided and the photoanode can be prepared on inexpensive highly conductive metal substrates, which are also suitable for roll to roll manufacturing. The photovoltaic cells, when in contact with a visible emitting LSC plate provide the required electrical bias to minimis electron/hole recombination following UV excitation of a α-Fe$_2$O$_3$ electrode by the

202

use of a LSC plate also. Two different dyes were used in the coating process of the glass plates considering their absorption profiles in different spectral regions and their emission at wavelengths which match the absorption of the α-Fe$_2$O$_3$ photoanode and the PV cells. From photocurrent measurements it was possible to define the condition in which the PEC cell is expected to reach maximum quantum efficiency, and chronoamperometry measurements were carried out in order to define the current output achieved. From these values it was possible to define the solar to hydrogen efficiency of the reactor developed, which was 0.1%; a significantly low value compared to the state of the art fuel reactors. The low STH efficiency achieved in these studies could be attributable to three main factors: i) the poor quality of the photoanodes employed over the course of these measurements, ii) the slight mismatch between the emission spectra of the UV plate and the IPCE% profile of the photoanode and iii) the lack of photon concentration occurring at the violet LSC. Optimising all these parameters could lead to a theoretically higher STH efficiency as demonstrated by the theoretical comparison with the state of the art α-Fe$_2$O$_3$ photoanodes.

Chapter VII

Concluding Remarks

The main objective of the PhD project reported in this thesis was to follow the dynamics of the photogenerated charge carriers in WO_3 photoanodes with the aim of providing mechanistic information on the processes limiting the water oxidation efficiency of this material (Chapter 3). Transient absorption spectroscopy operating in the micro-seconds to seconds timescales was the primary technique employed over the course of these studies in order to monitor the kinetics of photogenerated holes and electrons. Information on electron transport were also retrieved from transient photocurrent measurements.

A successful determination of the transient absorption fingerprints of holes and electrons was initially achieved and, in the presence of an efficient electron scavenger, we provided evidence of long-lived holes which are a requirement for the water oxidation reaction to occur. From the study of WO_3 electrodes in a fully operational photoelectrochemical cell it

was shown that the application of an external positive bias resulted in a decrease in electron/hole recombination and an increase of the charge carriers lifetime.

The lifetime of the photogenerated holes was found to be in the order of tens of milliseconds (30 ms), relatively shorter than the hole life-time determined for other metal oxide semiconductors such as TiO_2 and α-Fe_2O_3, and a quantitative correlation between photogenerated holes and photocurrent density was highlighted suggesting that the hole population in the valence band reaches saturation before they are transferred into solution. However, an overlap between the hole and electron signal complicates the determination of individual components of the hole and electron life-times.

A good quantitative correlation between photogenerated electrons and photocurrent density was also demonstrated and indicates a very slow electron transport through the film suggesting the presence of significant levels of trapping of photoelectrons at defect sites. Transient photocurrent measurements were employed to determine the dependence of the rate of electron transport on the excitation intensity and it was found to increase with increasing intensities, however, the electron transport rate still remains relatively slow, in the order of milliseconds (0.3 ms). The electron transport was also found to be relatively faster in thinner electrodes, however, remaining on the order of the milliseconds. These results indicates that the photo-oxidation efficiency of WO_3 photoanodes is limited by a slow electron transport which highlight the need to improve its rate in order to minimise fast electron/hole recombination and further increase the hole life-time. This could be achieved by an enhancement of the interconnectivity between the nano-particles which constitute the mesoporous films employed in the experiments described in this thesis.

Transient absorption spectroscopy was also employed in order to follow the charge carriers dynamics in hydrogen-treated rutile TiO_2 (H:TiO_2) nanowires with the aim of

understanding the factors controlling the very high STH efficiency for this material (Chapter 4). From the analysis of the transient traces and spectra recorded it has been highlighted an efficient suppression of fast electron/hole recombination in $H:TiO_2$ when compared with air-treated TiO_2 ($A:TiO_2$). In fact, a relatively high yield of both electrons and holes has been found at only –0.6 V vs Ag/AgCl in $H:TiO_2$, whereas it is necessary to apply a substantially higher electric current (–0.2 V vs Ag/AgCl) to $A:TiO_2$ in order to reach comparable electron and hole yields. From the analysis of the TA traces it has been found that the electron decay is well fitted at early times by a power law giving a lifetime of τ = 1.4×10^{-4} s suggesting that transport through the film is the main process involving the photogenerated electrons. On the other hand, the hole decay traces were well fitted by a combination of a power law and a single stretched exponential function in line with other widely studied semiconductors such as anatase TiO_2 and α-Fe_2O_3. The lifetime of the photogenerated hole was found to be τ = 0.15 ± 0.03 s for $H:TiO_2$ at – 0.6 V vs Ag/AgCl and 0.13 ± 0.02 s for $A:TiO_2$ at –0.2 V vs Ag/AgCl, suggesting that in both materials the photohole are enough long-lived in order to enable water oxidation in a complete photoelectrochemical cell. By the analysis of the hole transfer kinetics it was also possible to rule out a significant change in surface kinetics being an important factor behind the improved IPCE of $H:TiO_2$, confirming that the key factor leading to improved efficiency is an efficient suppression of electron/hole recombination.

Two side projects were also carried forward during the course of this PhD study: transient absorption and sum frequency generation spectroscopy were employed in the study of nano-crystalline (nc) TiO_2 (Chapter 5) and a medium scale proof of principle solar fuel reactor was developed (Chapter 6).

- Initial transient absorption studies on nc-TiO$_2$ in solutions with different pH's suggested a change in the mechanism of the photohole reaction with water in highly alkaline electrolytes highlighting the need to carry out experiments which could provide information on the nature of the surface intermediates involved during water oxidation. A sum frequency generation spectrometer was designed and set up with the aim of testing nc-TiO$_2$ films which were of greatest similarity to those employed during the transient absorption studies. The identification of four peaks assigned to physisorbed and chemisorbed methanol was successfully achieved confirming the possibility of using samples prepared using a doctor blade method with this technique. Initial sum frequency generation measurements at the interface nc-TiO$_2$/D$_2$O were also carried out and showed the presence of two broad signals which could be ascribed to asymmetric and symmetric stretches of D$_2$O adsorbed on the TiO$_2$ surface. However it is important to note that the amplitude and shape of these peaks does not allow a definitive assignment of the signals. Furthermore the physical degradation of the films employed in these studies when in the presence of an efficient electron scavenger highlighted the need to optimise the procedure of preparation of the samples in order to enable a more detailed study of the surface species in the presence of long-lived photoholes.

- A proof of principle hybrid reactor consisting of a α-Fe$_2$O$_3$ based photoelectrochemical cell coupled with two luminescent solar concentrators plates was also developed and tested during the course of this PhD. During the design process of the photoelectrochemical cell, particular attention was given to the cost per unit efficiency. A design which allowed a front side illumination of the α-Fe$_2$O$_3$ electrode was developed enabling in this way the preparation of the photoanode on highly conductive metal substrates and enabling the use of a small area transparent membrane (one of the main

factors which increases the cost per unit in currently employed medium to large scale reactors). Particular attention has also been given to the shape of the photoanodes employed in the reactor, reducing their active area in order to minimise resistive losses. The use of two solar concentrators (LSC) plates placed on top of each other and employed to irradiate the photoanode and a series of three Si photovoltaic cells (which provide the required electrical input to enable water oxidation) also represents an advantage because it increases the portion of the solar spectrum used compared to the present state of the art solar fuel reactors. Initial testing measurements on a proof of principle reactor were carried out providing encouraging results despite the low solar-to-hydrogen efficiency experimentally calculated (0.1%). These initial tests have highlighted the need to improve several factors such as the quality of the photoanodes employed and the photon concentration of the LSC plates in order to achieve higher solar-to-hydrogen efficiency.

Future works

- Despite good results being achieved from the studies of WO_3 photoanodes and the processes involving primarily photogenerated electrons being analysed and described, uncertainties on the kinetics of photogenerated holes still remain.

TAS studies in different electrolytes: Recent concerns rose over the competition between water and electrolytes ions for the photoholes have suggested the need to carry out transient absorption studies on WO_3 photoanodes in several electrolytes such as HCl, CH_3HSO_3 and H_2SO_4 in order to provide more information and highlight any possible difference in their kinetics.

- Sum frequency generation measurements also provided good initial results, however an improvement of the physical stability of the films employed during these experiments is required in order to allow further investigations.

SFG studies at the interface nc-TiO$_2$/D$_2$O in the presence of an applied bias: Considering the difficulties arisen when using AgNO$_3$ as an electron scavenger during the experiments described in Chapter V, a high yield of long-lived photoholes could be alternatively achieved by applying a positive bias to the nc-TiO$_2$ film. However, this would require the deposition of the nc-TiO2 paste on a metal conductive substrate and therefore a change in the actual set up of the spectrometer (SFG recorded in reflection instead of transmission)

- The test carried out on the hybrid PEC/LSC solar fuel reactor was encouraging, however the optimisation of several factors such as the choice of the UV dye species, the use of photoanodes with higher IPCE% values and the use of a highly conductive metal substrate in a front side configuration is required in order to provide better results.

Development of a dual PEC/LSC reactor: In order to achieve a water splitting reaction without the need of any external applied bias a reactor based on a photochatode/photoanode system could also be developed.

Bibliography

1)   G. Ciamician, "The Photochemistry of the Future" *Science,* **1912**, *36, 926*, 385

2)   Armaroli, A. and V. Balzani, "The Future of Energy Supply: Challenges and Opportunities" *Angewandte Chemie International Edition,* **2007**, *46*, 52

3)   Fujishima, A. and K. Honda, "Electrochemical Photolysis of Water at a Semiconductor Electrode" *Nature*, **1972**, *238*, 37

4)   P. J. Boddy, "Oxygen Evolution on Semiconducting TiO_2" *Journal of the Electrochemical Society,* **1968**, *115*, 199

5)   Chen, X., Shen, S., Guo, L. and S. S. Mao "Semiconductor-based Photocatalytic Hydrogen Generation" *Chemical Reviews*, **2010**, *110*, 6503

6)   Kudo, A. and Y. Miseki, "Heterogeneous Photocatalyst Materials for Water Splitting" *Chemical Society Reviews,* **2009**, *38*, 253

7)   F. E. Osterloh, "Inorganic Materials as Catalysts for Photochemical Splitting of Water" *Chemistry of Materials,* **2007**, *20*, 35

8)   Murphy, A. B.; Barnes, P. R. F.; Randeniya, L. K.; Plumb, I. C.; Grey, I. E. *et al.*, "Efficiency of Solar Water Splitting using Semiconductor Electrodes" *International Journal of Hydrogen Energy,* **2006**, *31*, 1999

9)   Chen, Z. B., Jaramillo, T. F., Deutsch, T. G., Kleiman-Shwarsctein, A., Forman, A. J. *et al.* "Accelerating Materials Development for Photoelectrochemical Hydrogen Production: Standards for Methods, Definitions, and Reporting Protocols" *Journal of Material Research,* **2010**, *25*, 3

10)   2010 Solar Technologies Market Report (Download available at the web address: www.nrel.gov/docs/fy12osti/51847.pdf)

11)   Walter, M. G., Warren, E. L., McKone, J. R., Boettcher, S. W., Mi, Q. *et al.* "Solar Water Splitting Cells" *Chemical Reviews*, **2010**, *110*, 11, 6446

12)   Pesci, F. M., Wang, G., Klug, D. R., Li, Y. and A. J. Cowan, "Efficient Suppression of Electron–Hole Recombination in Oxygen-Deficient Hydrogen-Treated TiO_2 Nanowires for Photoelectrochemical Water Splitting" *The Journal of Physical Chemistry C*, **2013**, *117*, 48, 25837

13)   Pesci, F. M., Cowan, A. J., Alexander, B. D., Durrant, J. R. And D. R. Klug, "Charge Carrier Dynamics on Mesoporous WO_3 during Water Splitting" *The Journal of Physical Chemistry Letters*, **2011**, *2,* 15, 1900

14)   Cowan, A. J., Barnett, C. J., Pendlebury, S. R., Barroso, M., Sivula, K., *et al.* "Activation Energies for the Rate-Limiting Step in Water Photooxidation by Nanostructured α-Fe_2O_3 and TiO_2" *Journal of the American Chemical Society*, **2011**, *133*, 26, 10134

15)   Cowan, A. J., Tang, J., Leng, W., Durrant, J. R., and D. R. Klug, "Water Splitting by Nanocrystalline TiO_2 in a Complete Photoelectrochemical Cell Exhibits Efficiencies Limited by Charge Recombination" *The Journal of Physical Chemistry C*, **2010**, *114*(9), 4208

16)   Tang, J., Durrant, J. R. And D. R. Klug, "Mechanism of Photocatalytic Water Splitting in TiO_2. Reaction of Water with Photoholes, Importance of Charge Carrier Dynamics, and Evidence for Four-hole Chemistry" *Journal of the American Chemical Society,* **2008**, 130, 42 13885

17)   Schmickler, W. and E. Santos "The Semiconductor-Electrolyte Interface." *Interfacial Electrochemistry*. Springer Berlin Heidelberg, **2010**. 117

18)   Archer, M. and A. J. Nozik, "Nanostructured and Photoelectrochemical Systems for Solar Photon Conversion" *Imperial College Press*, **2008**

19)   M. Grätzel, "Photoelectrochemical Cells" *Nature* **2001**, 414, 6861 338

20)   Nozik, A. J. And R. Memming, "Physical Chemistry of Semiconductor-Liquid Interfaces" *J. Phys. Chem.* **1996**, *100*, 13061

21)   J. A. Turner, "Energetics of the Semiconductor-Electrolyte Interface" *Journal of Chemical Education* **1983**, 60, 4, 327

22)   Bard, A. J.; Bocarsly, A. B.; Fan, F.-R. F.; Walton, E. G. And M. S. Wrighton, "The Concept of Fermi Level Pinning at Semiconductor/Liquid Junctions. Consequences for Energy Conversion Efficiency and Selection of Useful Solution Redox Couples in Solar Devices" *Journal of the American Chemical Society*, **1980**, 102, 3671

23)   Hong, S. J., Jun, H., Borse, P. H. and J. S. Lee "Size Effects of WO_3 Nanocrystals for Photooxidation of Water in Particulate Suspension and Photoelectrochemical Film Systems" *International Journal of Hydrogen Energy*, **2009**, *34*, 8, 3234

24)   P. V. Kamat, "Meeting the Clean Energy Demand: Nanostructure Architectures for Solar Energy Conversion" *The Journal of Physical Chemistry C, 2007*,111, 7 2834

25)   Bolton, J R., Stewart J. S. and J. S. Connolly "Limiting and Realizable Efficiencies of Solar Photolysis of Water", *Nature*, **1985**, 316, 6028, 495

26)   Park, J. H., Kim, S., and A. J. Bard, "Novel Carbon-Doped TiO^2 Nanotube Arrays with High Aspect Ratios for Efficient Solar Water Splitting" *Nano letters*, **2006**, *6*, 1, 24

27)   Khan, S. U., Al-Shahry, M., and W. B. Ingler, "Efficient Photochemical Water Splitting by a Chemically Modified n-TiO$_2$" *Science*, **2002**, *297*, 5590, 2243

28)   Chen, X, Liu L., Yu P. Y., and S. S. Mao "Increasing Solar Absorption for Photocatalysis with Black Hydrogenated Titanium Dioxide Nanocrystals" *Science*, **2011,** 331, 746

29)   Wang, G., Yichuan L., and Y. Li, "Oxygen-Deficient Metal Oxide Nanostructures for Photoelectrochemical Water Oxidation and other Applications" *Nanoscale*, **2012**, 4 6682

30)   Mi, Q., Ping, Y., Li, Y., Cao, B., Brunschwig, B. S., *et al.* "Thermally Stable N$_2$-Intercalated WO$_3$ Photoanodes for Water Oxidation" *Journal of the American Chemical Society*, **2012**, *134,* 44, 18318

31)   Miseki, Y., Kusama, H., Sugihara, H., and K. Sayama, "Cs-modified WO$_3$ Photocatalyst Showing Efficient Solar Energy Conversion for O$_2$ Production and Fe (III) Ion Reduction under Visible Light" *The Journal of Physical Chemistry Letters*, **2010**, *1*, 8, 1196

32)   Mi, Q., Coridan, R. H., Brunschwig, B. S., Gray, H. B., and N. S. Lewis, "Photoelectrochemical Oxidation of Anions by WO$_3$ in Aqueous and Nonaqueous Electrolytes" *Energy and Environmental Science*, **2013**, *6*, 9, 2646

33)   Mi, Q., Zhanaidarova, A., Brunschwig, B. S., Gray, H. B., and N. S. Lewis, "A Quantitative Assessment of the Competition between Water and Anion Oxidation at WO$_3$ Photoanodes in Acidic Aqueous Electrolytes" *Energy and Environmental Science*, **2012**, *5*, 2, 5694

34)   M. Anderman and J. H. Kennedy, *Semiconductor Electrodes*, ed. H.O. Finklea, Elsevier, **1998**.

35)   Marusak, L. A., Messier, R., and W. B. White, "Optical Absorption Spectrum of Hematite, α-Fe$_2$O$_3$ near IR to UV" *Journal of Physics and Chemistry of Solids*, **1980**, *41*, 9, 981

36)   Kim, J. Y., Magesh, G., Youn, D. H., Jang, J-W., Kubota, J., *et al.* "Single-Crystalline, Wormlike Hematite Photoanodes for Efficient Solar Water Splitting" *Science Reports*, **2013**, 3, 2681

37) Cowan, A. J. and J. R. Durrant, "Long-lived Charge Separated States in Nanostructured Semiconductor Photoelectrodes for the Production of Solar Fuels" *Chemical Society Reviews,* **2013***,* 42, 2281

38) B. A. Thrush, "The Genesis of Flash Photolysis" *Photochemical & Photobiological Sciences,* **2003**, 453

39) G. Porter, "Flash Photolysis and Spectroscopy. A New Method for the Study of Free Radical Reactions" *Proceedings of the Royal Society of London. A. Mathematical and Physical Sciences*, **1950**, 200, 1061, 284

40) Porter, G., and M. R. Topp. "Nanosecond Flash Photolysis" *Proceedings of the Royal Society of London. A. Mathematical and Physical Sciences*, **1970**, 315, 163

41) Bahnemann, D., Henglein, A., Lilie, J., and L. Spanhel "Flash Photolysis Observation of the Absorption Spectra of Trapped Positive Holes and Electrons in Colloidal Titanium Dioxide" *The Journal of Physical Chemistry*, **1984**, *88*, 4, 709

42) Wang, G., Wang, H., Ling, Y., Tang, Y., Yang, X., *et al.* "Hydrogen-Treated TiO_2 Nanowire Arrays for Photoelectrochemical Water Splitting" *Nano letters*, **2011**, *11*, 7, 3026

43) Bedja, I., Hotchandani, S., and P. V. Kamat, "Photoelectrochemistry of Quantized Tungsten Trioxide Colloids: Electron Storage, Electrochromic, and Photoelectrochromic Effects" *The Journal of Physical Chemistry*, **1993**, *97*, 42, 11064

44) Pendlebury, S. R., Barroso, M., Cowan, A. J., Sivula, K., Tang, J., *et al.* "Dynamics of Photogenerated Holes in Nanocrystalline α-Fe_2O_3 Electrodes for Water Oxidation Probed by Transient Absorption Spectroscopy" *Chemical Communications*, **2010**. *47*, 2, 716

45) Pendlebury, S. R., Cowan, A. J., Barroso, M., Sivula, K., Ye, J., *et al.* "Correlating Long-lived Photogenerated Hole Populations with Photocurrent Densities in Hematite Water Oxidation Photoanodes" *Energy & Environmental Science*, **2012**, *5*, 4, 6304

46) Lambert, A. G., Davies, P. B., and D. J. Neivandt, "Implementing the Theory of Sum Frequency Generation Vibrational Spectroscopy: A tutorial review" *Applied Spectroscopy Reviews,* **2005**, 40, 2, 103

47) Y. R. Shen, "The Principles of Nonlinear Optics" *New York, Wiley-Interscience, 1984, 575*

48)   Brillet, J., Cornuz, M., Le Formal, F., Yum, J-H., Grätzel, *et al.* "Examining Architectures of Photoanode–Photovoltaic Tandem Cells for Solar Water Splitting" *Journal of Material Research,* **2010**, 25, 1, 17

49)   Sivula, K., Le Formal, F., and M. Grätzel. "Solar Water Splitting: Progress Using Hematite (α-Fe_2O_3) Photoelectrodes" *ChemSusChem.,* **2011***, 4, 4. 432

50)   Brillet, J., Yum, J-H., Cornuz, M., Hisatomi, T., Solarska, R., *et al.* "Highly Efficient Water Splitting by a Dual-Absorber Tandem Cell" *Nature Photonics, 2012,* 6, 12, 824

51)   Batchelder, J. S., Zewail, A. H., and T. Cole, "Luminescent Solar Concentrators. 1: Theory of Operation and Techniques for Performance Evaluation" *Applied Optics*, **1979**, *18*(18), 3090

52)   Batchelder, J. S., Zewail, A. H., and T. Cole, "Luminescent Solar Concentrators. 2: Experimental and Theoretical Analysis of their Possible Efficiencies" *Applied Optics*, **1981**, *20*, 21, 3733

53)   Van Sark, W. G. J. H. M., Barnham, K. W., Slooff, L. H., Chatten, A. J., Büchtemann, A., *et al.* "Luminescent Solar Concentrators: a Review of Recent Results" *Optics Express [E]*, **2008**, *16*, 26, 21773

54)   Kennedy, M., McCormack, S. J., Doran, J., and B. Norton, "Modelling the Effect of Device Geometry on Concentration Ratios of Quantum Dot Solar Concentrators. In *Proceedings of ISES World Congress 2007 (Vol. I–Vol. V)* (pp. 1484-1488). Sprinter, **2009**.

55)   Technical details at http://www.instechlabs.com/Oxygen/polarographic/12505.php

56)   Fatt, I., Clark, L. C., and R. C. LaForce, "The Polarographic Oxygen Sensor: Its Theory of Operation and its Application in Biology, Medicine, and Technology" Cleveland: CRC Press, **1976**.

57)   Personal consultations with Martyn Fisher, Physics Department, Imperial College London, 2013.

58)   Xiao-e, L., Green, A. N., Haque, S. A., Mills, A., and J. R. Durrant, "Light-Driven Oxygen Scavenging by Titania/polymer Nanocomposite Films" *Journal of Photochemistry and Photobiology A: Chemistry*, **2004**, *162*, 2, 253

59)   Liu, B., and E. S. Aydil, "Growth of Oriented Single-crystalline Rutile TiO_2 Nanorods on Transparent Conducting Substrates for Dye-sensitized Solar Cells" *Journal of the American Chemical Society*, **2009**, *131*, 11, 3985

60) Santato, C., Odziemkowski, M., Ulmann, M., and J. Augustynski, "Crystallographically Oriented Mesoporous WO_3 Films: Synthesis, Characterization, and Applications" *Journal of the American Chemical Society*, **2001**, *123,* 43, 10639

61) Liang, Y., and R. van de Krol, "Influence of Si Dopant and SnO_2 Interfacial Layer on the Structure of the Spray-deposited Fe_2O_3 films" *Chemical Physics Letters*, **2009**, *479,* 1, 86

62) Deepa, M., Srivastava, A. K., Sood, K.N., and S. A. Agnihotry, "Nanostructured Mesoporous Tungsten Oxide Films with Fast Kinetics for Electrochromic Smart Windows" *Nanotechnology,* **2006**, 17, 10, 2625

63) Niklasson, G. A., and C. G. Granqvist, "Electrochromics for Smart Windows: Thin Films of Tungsten Oxide and Nickel Oxide, and Devices Based on These" *Journal of Material Chemistry, 2007*, 17, 2, 127

64) Vallejos, S., Stoycheva, T., Umek, P., Navio, C., Snyders, *et al.* "Au Nanoparticle-Functionalised WO_3 Nano-Needles and their Application in High Sensitivity Gas Sensor Devices" *Chemical Communications,* **2011**, 47, 1 565

65) Xie, Z., Zhu, Y., Xu, J., Huang, H., Chen, D., *et al.* "Porous WO_3 with Enhanced Photocatalytic and Selective Gas Sensing Properties" *CrystEngComm.*, **2011**, *13,* 21, 6393

66) Alexander, B. D., Kulesza, P. J., Rutkowska, I., Solarska, R., and J. Augustynski "Metal Oxide Photoanodes for Solar Hydrogen Production" *Journal of Material Chemistry*, **2008**, *18,* 20, 2298

67) Solarska, R., Alexander, B. D., and J. Augustynski, "Electrochromic and Structural Characteristics of Mesoporous WO_3 Films Prepared by a Sol-Gel Method" *Journal of Solid State Electrochemistry*, **2004**, *8*, 10, 748

68) Reichman, B., and A. J. Bard, "The Electrochromic Process at WO_3 Electrodes Prepared by Vacuum Evaporation and Anodic Oxidation of W" *Journal of The Electrochemical Society*, **1979**, *126*, 4, 583

69) Marsen, B., Miller, E. L., Paluselli, D., and R. E. Rocheleau, "Progress in Sputtered Tungsten Trioxide for Photoelectrode Applications" *International Journal of Hydrogen Energy*, **2007**, *32*, 15, 3110

70)   Baeck, S. H., Choi, K. S., Jaramillo, T. F., Stucky, G. D., and E. W. McFarland, "Enhancement of Photocatalytic and Electrochromic Properties of Electrochemically Fabricated Mesoporous WO_3 Thin Films" *Advanced Materials*, **2003**, *15*, 15, 1269

71)   Hao, J., Studenikin, S. A., and M. Cocivera, "Transient Photoconductivity Properties of Tungsten Oxide Thin Films Prepared by Spray Pyrolysis" *Journal of Applied Physics*, **2001**, *90*, 10, 5064

72)   Solarska, R., Alexander, B. D., Braun, A., Jurczakowski, R., Fortunato, G., *et al.* "Tailoring the Morphology of WO_3 Films with Substitutional Cation Doping: Effect on the Photoelectrochemical Properties" *Electrochimica Acta*, **2010**, *55*, 26, 7780

73)   Cole, B., Marsen, B., Miller, E., Yan, Y., To, B., *et al.* "Evaluation of Nitrogen Doping of Tungsten Oxide for Photoelectrochemical Water Splitting" *The Journal of Physical Chemistry C*, **2008**, *112*, 13, 5213

74)   Solarska, R., Królikowska, A., and J. Augustynski, "Silver Nanoparticle Induced Photocurrent Enhancement at WO_3 Photoanodes" *Angewandte Chemie International Edition*, **2010**, *49*, 43, 7980

75)   Liu, Q., Chen, Q., Bai, J., Li, J., Li, J., *et al.* "Enhanced Photoelectrocatalytic Performance of Nanoporous WO_3 Photoanode by Modification of Cobalt–Phosphate (Co–Pi) Catalyst" *Journal of Solid State Electrochemistry*, **2014**, *18*, 1, 157

76)   Seabold, J. A., and K. S. Choi, "Effect of a Cobalt-based Oxygen Evolution Catalyst on the Stability and the Selectivity of Photo-oxidation Reactions of a WO_3 Photoanode" *Chemistry of Materials*, **2011**, *23,* 5, 1105

77)   Darwent, J. R., and A. Mills, "Photo-Oxidation of Water Sensitized by WO_3 Powder" *Journal of the Chemical Society, Faraday Transactions,* **1982**, *2*, *78*, 359

78)   Desilvestro, J., and M. Grätzel, "Photoelectrochemistry of Polycrystalline n-WO_3: Electrochemical Characterization and Photoassisted Oxidation Processes" *Journal of Electroanalytical Chemistry and Interfacial Electrochemistry*, **1987**, *238*, 129

79)   Solarska, R., Jurczakowski, R., and J. Augustynski, "A Highly Stable, Efficient Visible-light Driven Water Photoelectrolysis System Using a Nanocrystalline WO_3 Photoanode and a Methane Sulfonic Acid Electrolyte" *Nanoscale*, **2012**, *4*, 5, 1553

80)   Patil, P. R., and P. S. Patil, "Transient Photoconductivity Measurements of Ultrasonic Spray Pyrolyzed Tungsten Oxide Thin Films" *Materials Research Bulletin*, **2000**, *35*, 6, 865

81)   Solarska, R., Santato, C., Jorand-Sartoretti, C., Ulmann, M., and J. Augustynski, "Photoelectrolytic Oxidation of Organic Species at Mesoporous Tungsten Trioxide Film Electrodes Under Visible Light Illumination" *Journal of applied electrochemistry*, **2005**, *35*, 7-8, 715

82)   Erbs, W., Desilvestro, J., Borgarello, E., and M. Grätzel, "Visible-light-induced Oxygen Generation from Aqueous Dispersions of Tungsten (VI) Oxide" *The Journal of Physical Chemistry*, **1984**, *88*, 18, 4001

83)   Hirakawa, T., and P. V. Kamat, "Charge Separation and Catalytic Activity of Ag@TiO$_2$ Core-shell Composite Clusters under UV-irradiation" *Journal of the American Chemical Society*, **2005**, *127*, 11, 3928

84)   Duonghong, D., Borgarello, E., and M. Grätzel, M. "Dynamics of Light-induced Water Cleavage in Colloidal Systems" *Journal of the American Chemical Society*, **1981**, *103*, 16, 4685

85)   Barroso, M., Cowan, A. J., Pendlebury, S. R., Grätzel, M., Klug, D. R., *et al.* "The Role of Cobalt Phosphate in Enhancing the Photocatalytic Activity of α-Fe$_2$O$_3$ toward Water Oxidation" *Journal of the American Chemical Society*, **2011**, *133*, 38, 14868

86)   Wang, H., Lindgren, T., He, J., Hagfeldt, A., and S. E. Lindquist, "Photolelectrochemistry of Nanostructured WO$_3$ Thin Film Electrodes for Water Oxidation: Mechanism of Electron Transport" *The Journal of Physical Chemistry B*, **2000**, *104*, 24, 5686

87)   Pendlebury, S. R., Cowan, A. J., Barroso, M., Sivula, K., Ye, J., *et al.* "Correlating Long-lived Photogenerated Hole Populations with Photocurrent Densities in Hematite Water Oxidation Photoanodes" *Energy & Environmental Science*, **2012**, *5*, 4, 6304

88)   Cowan, A. J., Leng, W., Barnes, P. R., Klug, D. R., and J. R. Durrant, "Charge carrier separation in nanostructured TiO$_2$ photoelectrodes for water splitting" *Physical Chemistry Chemical Physics*, **2013**, *15*, 22, 8772

89)   Nelson, J. "Continuous-time Random-walk Model of Electron Transport in Nanocrystalline TiO$_2$ Electrodes" *Physical Review B*, **1999**, *59*, 23, 15374

90)   Barzykin, A. V., and M. Tachiya "Mechanism of Charge Recombination in Dye-Sensitized Nanocrystalline Semiconductors: Random Flight Model" *The Journal of Physical Chemistry B*, **2002**, *106*, 17, 4356

91)   Hotchandani, S., Bedja, I., Fessenden, R., and P. V. Kamat, "Electrochromic and Photoelectrochromic Behavior of Thin WO_3 Films Prepared from Quantum Size Collodal Particles. *Langmuir*, **1994**, *10*, 1, 17

92)   Leland, J. K., and A. J. Bard, "Electrochemical Investigation of the Electron-transfer Kinetics and Energetics of Illuminated Tungsten Oxide Colloids" *Journal of Physical Chemistry*, **1987**, *91*, 19, 5083

93)   Pendlebury, S. R., Charge Carrier Dynamics in Hematite Photoanodes for Solar Water Oxidation, PhD Thesis, Imperial College London, **2012**.

94)   Kambe, S., Nakade, S., Kitamura, T., Wada, Y. And S. Yanagida, "Influence of the Electrolytes on Electron Transport in Mesoporous TiO_2-Electrolyte Systems" *The Journal of Physical Chemistry B*, **2002**, *106*, 11, 2967

95)   Solbrand, A., Lindström, H., Rensmo, H., Hagfeldt, A., Lindquist, S. E., *et al.* "Electron Transport in the Nanostructured TiO_2-Electrolyte System Studied with Time-Resolved Photocurrents" *The Journal of Physical Chemistry B*, **1997**, *101*, 14, 2514

96)   Tacca, A., Meda, L., Marra, G., Savoini, A., Caramori, S., *et al.* "Photoanodes Based on Nanostructured WO_3 for Water Splitting" *ChemPhysChem*, **2012**, *13*, 12, 3025

97)   Personal consultations with Dr. Bruce Alexander, Greenwich University, 2013

98)   Pan, X., Yang, M. Q., Fu, X., Zhang, N. and Y. J. Xu, "Defective TiO_2 with Oxygen Vacancies: Synthesis, Properties and Photocatalytic Applications" *Nanoscale*, **2013**, *5*, 9, 3601

99)   Jiang, X., Zhang, Y., Jiang, J., Rong, Y., Wang, Y. *et. al.* "Characterization of Oxygen Vacancy Associates within Hydrogenated TiO_2: a Positron Annihilation Study" *The Journal of Physical Chemistry C*, **2012**, *116*, 42, 22619

100)   Cooper, J. K., Ling, Y., Longo, C., Li, Y., and J. Z. Zhang, "Effects of Hydrogen Treatment and Air Annealing on Ultrafast Charge Carrier Dynamics in ZnO Nanowires under in Situ Photoelectrochemical Conditions" *The Journal of Physical Chemistry C*, **2012**, *116*, 33, 17360

101)   Yoshihara, T., Katoh, R., Furube, A., Tamaki, Y., Murai, M., *et al.* "Identification of Reactive Species in Photoexcited Nanocrystalline TiO_2 Films by Wide-Wavelength-Range (400-2500 nm) Transient Absorption Spectroscopy" *The Journal of Physical Chemistry B*, **2004**, *108*, 12, 3817

102) Yoshihara, T., Tamaki, Y., Furube, A., Murai, M., Hara, K., *et al.* "Effect of pH on Absorption Spectra of Photogenerated Holes in Nanocrystalline TiO_2 Films" *Chemical physics letters*, **2007**, *438*, 4, 268

103) Tamaki, Y., Furube, A., Murai, M., Hara, K., Katoh, R., *et al.* "Dynamics of Efficient Electron–Hole Separation in TiO_2 Nanoparticles Revealed by Femtosecond Transient Absorption Spectroscopy under the Weak-Excitation Condition" *Physical Chemistry Chemical Physics*, **2007**, *9*, 12, 1453

104) P. Zawadzki, "Absorption Spectra of Trapped Holes in Anatase TiO_2" *The Journal of Physical Chemistry C*, **2013**, *117*, 17, 8647

105) Zawadzki, P., Jacobsen, K. W., and J. Rossmeisl, "Electronic Hole Localization in Rutile and Anatase TiO_2–Self-Interaction Correction in Δ-SCF DFT" *Chemical Physics Letters*, **2011**, *506*, 1, 42

106) Nelson, J., Haque, S. A., Klug, D. R., and J. R. Durrant, "Trap-Limited Recombination in Dye-Sensitized Nanocrystalline Metal Oxide Electrodes" *Physical Review B*, **2001**, *63*, 20, 205321

107) Katoh, R., Murai, M., and A. Furube, "Electron–Hole Recombination in the Bulk of a Rutile TiO_2 Single Crystal Studied by Sub-Nanosecond Transient Absorption Spectroscopy" *Chemical Physics Letters*, **2008**, *461*, 4, 238

108) Liu, L., Peter, Y. Y., Chen, X., Mao, S. S., and D. Z. Shen, "Hydrogenation and Disorder in Engineered Black TiO_2" *Physical review letters*, **2013**, *111*, 6, 065505

109) W. W. Gärtner, "Depletion-Layer Photoeffects in Semiconductors" *Physical Review*, **1959**, *116*, 1, 84

110) H. Gerischer, "Electrochemical Behavior of Semiconductors under Illumination" *Journal of the Electrochemical Society*, **1966**, *113*, 11, 1174

111) Soedergren, S., Hagfeldt, A., Olsson, J., and S. E. Lindquist, "Theoretical Models for the Action Spectrum and the Current-Voltage Characteristics of Microporous Semiconductor Films in Photoelectrochemical Cells" *The Journal of Physical Chemistry*, **1994**, *98*, 21, 5552

112) Bisquert, J., Garcia-Belmonte, G., and F. Fabregat-Santiago, "Modelling the Electric Potential Distribution in the Dark in Nanoporous Semiconductor Electrodes" *Journal of Solid State Electrochemistry*, **1999**, *3*, 6, 337

113) D. C. Cronemeyer, "Infrared Absorption of Reduced Rutile TiO_2 Single Crystals" *Physical Review*, **1959**, *113*, 5, 1222

114) Kim, J., Monllor-Satoca, D., and W. Choi, "Simultaneous Production of Hydrogen with the Degradation of Organic Pollutants using TiO_2 Photocatalyst Modified with Dual Surface Components" *Energy & Environmental Science*, **2012**, *5*, 6, 7647

115) He, X., Cai, Y., Zhang, H., and C. Liang, "Photocatalytic Degradation of Organic Pollutants with Ag Decorated Free-Standing TiO_2 Nanotube Arrays and Interface Electrochemical Response" *Journal of Materials Chemistry*, **2011**, *21*, 2, 475

116) Imanishi, A., Okamura, T., Ohashi, N., Nakamura, R., and Y. Nakato, "Mechanism of Water Photooxidation Reaction at Atomically Flat TiO_2 (Rutile)(110) and (100) Surfaces: Dependence on Solution pH" *Journal of the American Chemical Society*, **2007**, *129*, 37, 11569

117) Nakamura, R., Okamura, T., Ohashi, N., Imanishi, A., and Y. Nakato, "Molecular Mechanisms of Photoinduced Oxygen Evolution, PL Emission, and Surface Roughening at Atomically Smooth (110) and (100) n-TiO_2 (Rutile) Surfaces in Aqueous Acidic Solutions" *Journal of the American Chemical Society*, **2005**, *127*, 37, 12975

118) Nakamura, R., and Y. Nakato, "Primary Intermediates of Oxygen Photoevolution Reaction on TiO_2 (Rutile) Particles, Revealed by in situ FTIR Absorption and Photoluminescence Measurements" *Journal of the American Chemical Society*, **2004**, *126*, 4, 1290

119) Nakamura, R., Imanishi, A., Murakoshi, K., and Y. Nakato, "In Situ FTIR Studies of Primary Intermediates of Photocatalytic Reactions on Nanocrystalline TiO_2 Films in Contact with Aqueous Solutions" *Journal of the American Chemical Society*, **2003**, *125*, 24, 7443

120) Yang, X., and N. Tamai, "How Fast is Interfacial Hole Transfer? In Situ Monitoring of Carrier Dynamics in Anatase TiO_2 Nanoparticles by Femtosecond Laser Spectroscopy" *Physical Chemistry Chemical Physics*, **2001**, *3*, 16, 3393

121) Crawford, S., Thimsen, E., and P. Biswas, "Impact of Different Electrolytes on Photocatalytic Water Splitting" *Journal of The Electrochemical Society*, **2009**, *156*, 5, H346

122) Wang, C. Y., Groenzin, H., and M. J. Shultz, "Molecular Species on Nanoparticulate Anatase TiO_2 Film Detected by Sum Frequency Generation: Trace Hydrocarbons and Hydroxyl Groups" *Langmuir*, **2003**, *19*, 18, 7330

123) Wang, C. Y., Groenzin, H., M. J. Shultz, "Comparative Study of Acetic Acid, Methanol, and Water Adsorbed on Anatase TiO$_2$ Probed by Sum Frequency Generation Spectroscopy" *Journal of the American Chemical Society*, **2005**, *127*, 27, 9736

124) Wang, C. Y., Groenzin, H., and M. J. Shultz, "Direct Observation of Competitive Adsorption between Methanol and Water on TiO$_2$: An in situ Sum-Frequency Generation Study" *Journal of the American Chemical Society*, **2004**, *126*, 26, 8094

125) Wang, C. Y., Groenzin, H., and M. J. Shultz, "Surface Characterization of Nanoscale TiO$_2$ Film by Sum Frequency Generation using Methanol as a Molecular Probe" *The Journal of Physical Chemistry B*, **2004**, *108*, 1, 265

126) Uosaki, K., Yano, T., and S. Nihonyanagi, "Interfacial Water Structure at as-Prepared and UV-Induced Hydrophilic TiO$_2$ Surfaces Studied by Sum Frequency Generation Spectroscopy and Quartz Crystal Microbalance" *The Journal of Physical Chemistry B*, **2004**, *108*, 50, 19086

127) Nelson, J., Eppler, A. M., and I. M. Ballard, "Photoconductivity and Charge Trapping in Porous Nanocrystalline Titanium Dioxide" *Journal of photochemistry and photobiology A: Chemistry*, **2002**, *148*, 1, 25

128) Eppler, A. M., Ballard, I. M., and J. Nelson, "Charge Transport in Porous Nanocrystalline Titanium Dioxide" *Physica E: Low-dimensional Systems and Nanostructures*, **2002**, *14*, 1, 197

129) Rowland, B., Kadagathur, N. S., Devlin, J. P., Buch, V., Feldman, T., and M. J. Wojcik, "Infrared Spectra of Ice Surfaces and Assignment of Surface-Localized Modes from Simulated Spectra of Cubic Ice" *The Journal of chemical physics*, **1995**, *102*, 8328

130) Ayers, G. P., and A. D. E. Pullin, "The IR Spectra of Matrix Isolated Water Species - I. Assignment of Bands to H$_2$O, D$_2$O and HDO Dimer Species in Argon Matrices" *Spectrochimica Acta Part A: Molecular Spectroscopy*, **1976**, *32*, 10, 1629

131) Carver, C., Ulissi, Z., Ong, C. K., Dennison, S., and G. H. Kelsall, "Modelling and Evaluation of a Photoelectrochemical Reactor for H$_2$ Production" *ECS Transactions*, **2010**, 28, 26, 103

132) Carver, C., Ulissi, Z., Ong, C. K., Dennison, S., Kelsall, G. H., *et al.* "Modelling and Development of Photoelectrochemical Reactor for H$_2$ Production" *International Journal of Hydrogen Energy*, **2012**, *37*, 3, 2911

133) Weber, W. H., and J. Lambe, "Luminescent Greenhouse Collector for Solar Radiation" *Applied Optics*, **1976**, *15*, 2299

134) Goetzberger, A., and W. Greube, "Solar Energy Conversion with Fluorescent Collectors" *Applied Physics*, **1977**, *14*, 2, 123

135) Currie, M. J., Mapel, J. K., Heidel, T. D., Goffri, S., and M. A. Baldo, "High-Efficiency Organic Solar Concentrators for Photovoltaics" *Science*, **2008**, *321*, 5886, 226

136) Sholin, V., Olson, J. D., and S. A. Carter, "Semiconducting Polymers and Quantum Dots in Luminescent Solar Concentrators for Solar Energy Harvesting" *Journal of applied physics*, **2007**, *101*, 12, 123114

137) Chatten, A. J., Barnham, K. W. J., Buxton, B. F., Ekins-Daukes, N. J., and M. A. Malik, "Quantum Dot Solar Concentrators" *Semiconductors*, **2004**, *38*, 8, 909

138) Barnham, K., Marques, J. L., Hassard, J., and P. OBrien, "Quantum-Dot Concentrator and Thermodynamic Model for the Global Redshift" *Applied Physics Letters*, **2000**, *76*, 9, 1197

139) http://www.idex-hs.com/materials/guide/PEEK.aspx

140) Inaba, M., Kinumoto, T., Kiriake, M., Umebayashi, R., Tasaka, A., *et al.* "Gas Crossover and Membrane Degradation in Polymer Electrolyte Fuel Cells" *Electrochimica Acta*, **2006**, *51*, 26, 5746

141) Kay, A., Cesar, I., and M. Grätzel, "New Benchmark for Water Photooxidation by Nanostructured α-Fe_2O_3 Films" *Journal of the American Chemical Society*, **2006**, *128*, 49, 15714

Appendix: Summary of Permissions for Third Party Copyright Works

Page Number	Type of work: text, figure, etc.	Source work	Copyright holder & year	Work out of copyright	Permission to re-use	Permission requested
Page 77	Figure	Nano Letters(2011), vol 11, 7 3026-3033	© 2011 American Chemical Society		✓	
Page 129	Figure	The Journal of Physical Chemistry C (2013), vol 117, 48 25837-25844	©2013 American Chemical Society		✓	
Page 133	Figure	The Journal of Physical Chemistry C (2013), vol 117, 48 25837-25844	©2013 American Chemical Society		✓	
Page 140	Figure	The Journal of Physical Chemistry C (2013), vol 117, 48 25837-25844	©2013 American Chemical Society		✓	
Page 141	Figure	The Journal of Physical Chemistry C (2013), vol 117, 48 25837-25844	©2013 American Chemical Society		✓	
Page 143	Figure	The Journal of Physical Chemistry C (2013), vol 117, 48 25837-25844	©2013 American Chemical Society		✓	
Page 144	Figure	Nano Letters(2011), vol 11, 7 3026-3033	© 2011 American Chemical Society		✓	
Page 150	Figure	Chemical Physics Letters (2007), vol 438, 4 268-273	© 2007 Elsevier B. V.		✓	
Page 200	Figure	Journal of the American Chemical Society (2006), vol 128, 49, 15714-15721	© 2006 American Chemical Society		✓	

Permission to reuse Figures from Nano Letters, **2011**, vol 11, 7 3026-3033 (Figures at pages 77 and 144 in the thesis)

Copyright Clearance Center

RightsLink®

Home   Account Info   Help

ACS Publications
MOST TRUSTED. MOST CITED. MOST READ.

Title: Hydrogen-Treated TiO2 Nanowire Arrays for Photoelectrochemical Water Splitting

Author: Gongming Wang, Hanyu Wang, Yichuan Ling, Yuechao Tang, Xunyu Yang, Robert C. Fitzmorris, Changchun Wang, Jin Z. Zhang, and Yat Li

Publication: Nano Letters

Publisher: American Chemical Society

Date: Jul 1, 2011

Copyright © 2011, American Chemical Society

Logged in as:
Federico Pesci

LOGOUT

PERMISSION/LICENSE IS GRANTED FOR YOUR ORDER AT NO CHARGE

This type of permission/license, instead of the standard Terms & Conditions, is sent to you because no fee is being charged for your order. Please note the following:

- Permission is granted for your request in both print and electronic formats, and translations.
- If figures and/or tables were requested, they may be adapted or used in part.
- Please print this page for your records and send a copy of it to your publisher/graduate school.
- Appropriate credit for the requested material should be given as follows: "Reprinted (adapted) with permission from (COMPLETE REFERENCE CITATION). Copyright (YEAR) American Chemical Society." Insert appropriate information in place of the capitalized words.
- One-time permission is granted only for the use specified in your request. No additional uses are granted (such as derivative works or other editions). For any other uses, please submit a new request.

If credit is given to another source for the material you requested, permission must be obtained from that source.

BACK   CLOSE WINDOW

Permission to reuse Figures from The Journal of Physical Chemistry C, **2013**, vol 117, 48 25837-25844 (Figures at pages 129, 133, 140, 141 and 143 in the thesis)

225

b. **Adapter's License** means the license You apply to Your Copyright and Similar Rights in Your contributions to Adapted Material in accordance with the terms and conditions of this Public License.

c. **Copyright and Similar Rights** means copyright and/or similar rights closely related to copyright including, without limitation, performance, broadcast, sound recording, and Sui Generis Database Rights, without regard to how the rights are labeled or categorized. For purposes of this Public License, the rights specified in Section 2(b)(1)-(2) are not Copyright and Similar Rights.

d. **Effective Technological Measures** means those measures that, in the absence of proper authority, may not be circumvented under laws fulfilling obligations under Article 11 of the WIPO Copyright Treaty adopted on December 20, 1996, and/or similar international agreements.

e. **Exceptions and Limitations** means fair use, fair dealing, and/or any other exception or limitation to Copyright and Similar Rights that applies to Your use of the Licensed Material.

f. **Licensed Material** means the artistic or literary work, database, or other material to which the Licensor applied this Public License.

g. **Licensed Rights** means the rights granted to You subject to the terms and conditions of this Public License, which are limited to all Copyright and Similar Rights that apply to Your use of the Licensed Material and that the Licensor has authority to license.

h. **Licensor** means the individual(s) or entity(ies) granting rights under this Public License.

i. **Share** means to provide material to the public by any means or process that requires permission under the Licensed Rights, such as reproduction, public display, public performance, distribution, dissemination, communication, or importation, and to make material available to the public including in ways that members of the public may access the material from a place and at a time individually chosen by them.

j. **Sui Generis Database Rights** means rights other than copyright resulting from Directive 96/9/EC of the European Parliament and of the Council of 11 March 1996 on the legal protection of databases, as amended and/or succeeded, as well as other essentially equivalent rights anywhere in the world.

k. **You** means the individual or entity exercising the Licensed Rights under this Public License. **Your** has a corresponding meaning.

Section 2 – Scope
a. License grant.

1. Subject to the terms and conditions of this Public License, the Licensor hereby grants You a worldwide, royalty-free, non-sublicensable, non-exclusive, irrevocable license to exercise the Licensed Rights in the Licensed Material to:

A. reproduce and Share the Licensed Material, in whole or in part; and
B. produce, reproduce, and Share Adapted Material.

2. *Exceptions and Limitations*. For the avoidance of doubt, where Exceptions and Limitations apply to Your use, this Public License does not apply, and You do not need to comply with its terms and conditions.

3. *Term*. The term of this Public License is specified in Section 6(a).

4. *Media and formats*; technical modifications allowed. The Licensor authorizes You to exercise the Licensed Rights in all media and formats whether now known or hereafter created, and to make technical modifications necessary to do so. The Licensor waives and/or agrees not to assert any right or authority to forbid You from making technical modifications necessary to exercise the Licensed Rights, including technical modifications necessary to circumvent Effective Technological Measures. For purposes of this Public License, simply making modifications authorized by this Section 2(a)(4) never produces Adapted Material.

5. *Downstream recipients*

A. *Offer from the Licensor* – Licensed Material. Every recipient of the Licensed Material automatically receives an offer from the Licensor to exercise the Licensed Rights under the terms and conditions of this Public License.

B. *No downstream restrictions*. You may not offer or impose any additional or different terms or conditions on, or apply any Effective Technological Measures to, the Licensed Material if doing so restricts exercise of the Licensed Rights by any recipient of the Licensed Material.

6. *No endorsement*. Nothing in this Public License constitutes or may be construed as permission to assert or imply that You are, or that Your use of the Licensed Material is, connected with, or sponsored, endorsed, or granted official status by, the Licensor or others designated to receive attribution as provided in Section 3(a)(1)(A)(i).

b. Other rights.

1. Moral rights, such as the right of integrity, are not licensed under this Public License, nor are publicity, privacy, and/or other similar personality rights; however, to the extent possible, the Licensor waives and/or agrees not to assert any such rights held by the Licensor to the limited extent necessary to allow You to exercise the Licensed Rights, but not otherwise.

2. Patent and trademark rights are not licensed under this Public License.

3. To the extent possible, the Licensor waives any right to collect royalties from You for the exercise of the Licensed Rights, whether directly or through a collecting society under any voluntary or waivable statutory or compulsory licensing scheme. In all other cases the Licensor expressly reserves any right to collect such royalties.

Section 3 – License Conditions
Your exercise of the Licensed Rights is expressly made subject to the following conditions.

a. Attribution

1. If You Share the Licensed Material (including in modified form), You must:

A. retain the following if it is supplied by the Licensor with the Licensed Material:

i. identification of the creator(s) of the Licensed Material and any others designated to receive attribution, in any reasonable manner requested by the Licensor (including by pseudonym if designated);

ii. a copyright notice;

iii. a notice that refers to this Public License;

iv. a notice that refers to the disclaimer of warranties;

v. a URI or hyperlink to the Licensed Material to the extent reasonably practicable;

B. indicate if You modified the Licensed Material and retain an indication of any previous modifications; and

C. indicate the Licensed Material is licensed under this Public License, and include the text of, or the URI or hyperlink to, this Public License.

2. You may satisfy the conditions in Section 3(a)(1) in any reasonable manner based on the medium, means, and context in which You Share the Licensed Material. For example, it may be reasonable to satisfy the conditions by providing a URI or hyperlink to a resource that includes the required information.

3. If requested by the Licensor, You must remove any of the information required by Section 3(a)(1)(A) to the extent reasonably practicable.

4. If You Share Adapted Material You produce, the Adapter's License You apply must not prevent recipients of the Adapted Material from complying with this Public License.

Section 4 – Sui Generis Database Rights
Where the Licensed Rights include Sui Generis Database Rights that apply to Your use of the Licensed Material:

a. for the avoidance of doubt, Section 2(a)(1) grants You the right to extract, reuse, reproduce, and Share all or a substantial portion of the contents of the database;

b. if You include all or a substantial portion of the database contents in a database in which You have Sui Generis Database Rights, then the database in which You have Sui Generis Database Rights (but not its individual contents) is Adapted Material; and

c. You must comply with the conditions in Section 3(a) if You Share all or a substantial portion of the contents of the database.

For the avoidance of doubt, this Section 4 supplements and does not replace Your obligations under this Public License where the Licensed Rights include other Copyright and Similar Rights.

Section 5 – Disclaimer of Warranties and Limitation of Liability
a. Unless otherwise separately undertaken by the Licensor, to the extent possible, the Licensor offers the Licensed Material as-is and as-available, and makes no representations or warranties of any kind concerning the Licensed Material, whether express, implied, statutory, or other. This includes, without limitation, warranties of title, merchantability, fitness for a particular purpose, non-infringement, absence of latent or other defects, accuracy, or the presence or absence of errors, whether or not known or discoverable. Where disclaimers of warranties are not allowed in full or in part, this disclaimer may not apply to You.

b. To the extent possible, in no event will the Licensor be liable to You on any legal theory (including, without limitation, negligence) or otherwise for any direct, special, indirect, incidental, consequential, punitive, exemplary, or other losses, costs, expenses, or damages arising out of this Public License or use of the Licensed Material, even if the Licensor has been advised of the possibility of such losses, costs, expenses, or damages. Where a limitation of liability is not allowed in full or in part, this limitation may not apply to You.

c. The disclaimer of warranties and limitation of liability provided above shall be interpreted in a manner that, to the extent possible, most closely approximates an absolute disclaimer and waiver of all liability.

Section 6 – Term and Termination
a. This Public License applies for the term of the Copyright and Similar Rights licensed here. However, if You fail to comply with this Public License, then Your rights under this Public License terminate automatically.

b. Where Your right to use the Licensed Material has terminated under Section 6(a), it reinstates:

1. automatically as of the date the violation is cured, provided it is cured within 30 days of Your discovery of the violation; or

2. upon express reinstatement by the Licensor.For the avoidance of doubt, this Section 6(b) does not affect any right the Licensor may have to seek remedies for Your violations of this Public License.

c. For the avoidance of doubt, the Licensor may also offer the Licensed Material under separate terms or conditions or stop distributing the Licensed Material at any time; however, doing so will not terminate this Public License.

d. Sections 1, 5, 6, 7, and 8 survive termination of this Public License.

Section 7 – Other Terms and Conditions
a. The Licensor shall not be bound by any additional or different terms or conditions communicated by You unless expressly agreed.

b. Any arrangements, understandings, or agreements regarding the Licensed Material not stated herein are separate from and independent of the terms and conditions of this Public License.

Section 8 – Interpretation
a. For the avoidance of doubt, this Public License does not, and shall not be interpreted to, reduce, limit, restrict, or impose conditions on any use of the Licensed Material that could lawfully be made without permission under this Public License.

b. To the extent possible, if any provision of this Public License is deemed unenforceable, it shall be automatically reformed to the minimum extent necessary to make it enforceable. If the provision cannot be reformed, it shall be severed from this Public License without affecting the enforceability of the remaining terms and conditions.

c. No term or condition of this Public License will be waived and no failure to comply consented to unless expressly agreed to by the Licensor.

d. Nothing in this Public License constitutes or may be interpreted as a limitation upon, or waiver of, any privileges and immunities that apply to the Licensor or You, including from the legal processes of any jurisdiction or authority.

Permission to reuse Figures from Chemical Physics Letters, **2007**, vol 438, 4 268-273

(Figure at page 150 of the thesis)

ELSEVIER LICENSE
TERMS AND CONDITIONS

Jul 15, 2014

This is a License Agreement between Federico M Pesci ("You") and Elsevier ("Elsevier") provided by Copyright Clearance Center ("CCC"). The license consists of your order details, the terms and conditions provided by Elsevier, and the payment terms and conditions.

All payments must be made in full to CCC. For payment instructions, please see information listed at the bottom of this form.

Supplier	Elsevier Limited The Boulevard,Langford Lane Kidlington,Oxford,OX5 1GB,UK
Registered Company Number	1982084
Customer name	Federico M Pesci
Customer address	637 Kingston Rd
	London, SW20 8SA
License number	3430470920953
License date	Jul 15, 2014
Licensed content publisher	Elsevier
Licensed content publication	Chemical Physics Letters
Licensed content title	Effect of pH on absorption spectra of photogenerated holes in nanocrystalline TiO2films
Licensed content author	Toshitada Yoshihara,Yoshiaki Tamaki,Akihiro Furube,Miki Murai,Kohjiro Hara,Ryuzi Katoh
Licensed content date	20 April 2007
Licensed content volume number	438
Licensed content issue number	4–6
Number of pages	6
Start Page	268
End Page	273
Type of Use	reuse in a thesis/dissertation
Portion	figures/tables/illustrations
Number of figures/tables /illustrations	1
Format	electronic
Are you the author of this Elsevier article?	No

Will you be translating?	No
Title of your thesis/dissertation	Metal Oxide Semiconductors Employed as Photocatalysts during Water Splitting
Expected completion date	Jul 2014
Estimated size (number of pages)	230
Elsevier VAT number	GB 494 6272 12
Permissions price	0.00 GBP
VAT/Local Sales Tax	0.00 GBP / 0.00 GBP
Total	0.00 GBP

Terms and Conditions

7. Reservation of Rights: Publisher reserves all rights not specifically granted in the combination of (i) the license details provided by you and accepted in the course of this licensing transaction, (ii) these terms and conditions and (iii) CCC's Billing and Payment terms and conditions.

8. License Contingent Upon Payment: While you may exercise the rights licensed immediately upon issuance of the license at the end of the licensing process for the transaction, provided that you have disclosed complete and accurate details of your proposed use, no license is finally effective unless and until full payment is received from you (either by publisher or by CCC) as provided in CCC's Billing and Payment terms and conditions. If full payment is not received on a timely basis, then any license preliminarily granted shall be deemed automatically revoked and shall be void as if never granted. Further, in the event that you breach any of these terms and conditions or any of CCC's Billing and Payment terms and conditions, the license is automatically revoked and shall be void as if never granted. Use of materials as described in a revoked license, as well as any use of the materials beyond the scope of an unrevoked license, may constitute copyright infringement and publisher reserves the right to take any and all action to protect its copyright in the materials.

9. Warranties: Publisher makes no representations or warranties with respect to the licensed material.

10. Indemnity: You hereby indemnify and agree to hold harmless publisher and CCC, and their respective officers, directors, employees and agents, from and against any and all claims arising out of your use of the licensed material other than as specifically authorized pursuant to this license.

11. No Transfer of License: This license is personal to you and may not be sublicensed, assigned, or transferred by you to any other person without publisher's written permission.

12. No Amendment Except in Writing: This license may not be amended except in a writing signed by both parties (or, in the case of publisher, by CCC on publisher's behalf).

13. Objection to Contrary Terms: Publisher hereby objects to any terms contained in any purchase order, acknowledgment, check endorsement or other writing prepared by you, which terms are inconsistent with these terms and conditions or CCC's Billing and Payment terms and conditions. These terms and conditions, together with CCC's Billing and Payment terms and conditions (which are incorporated herein), comprise the entire agreement between you and publisher (and CCC) concerning this licensing transaction. In the event of any conflict between your obligations established by these terms and conditions and those established by CCC's Billing and Payment terms and conditions, these terms and conditions shall control.

14. Revocation: Elsevier or Copyright Clearance Center may deny the permissions described in this License at their sole discretion, for any reason or no reason, with a full refund payable to you. Notice of such denial will be made using the contact information provided by you. Failure to receive such notice will not alter or invalidate the denial. In no event will Elsevier or Copyright Clearance Center be responsible or liable for any costs, expenses or damage incurred by you as a result of a denial of your permission request, other than a refund of the

230

amount(s) paid by you to Elsevier and/or Copyright Clearance Center for denied permissions.

LIMITED LICENSE

The following terms and conditions apply only to specific license types:

15. **Translation**: This permission is granted for non-exclusive world **English** rights only unless your license was granted for translation rights. If you licensed translation rights you may only translate this content into the languages you requested. A professional translator must perform all translations and reproduce the content word for word preserving the integrity of the article. If this license is to re-use 1 or 2 figures then permission is granted for non-exclusive world rights in all languages.

16. **Posting licensed content on any Website**: The following terms and conditions apply as follows: Licensing material from an Elsevier journal: All content posted to the web site must maintain the copyright information line on the bottom of each image; A hyper-text must be included to the Homepage of the journal from which you are licensing at http://www.sciencedirect.com/science/journal/xxxxx or the Elsevier homepage for books at http://www.elsevier.com; Central Storage: This license does not include permission for a scanned version of the material to be stored in a central repository such as that provided by Heron/XanEdu.

Licensing material from an Elsevier book: A hyper-text link must be included to the Elsevier homepage at http://www.elsevier.com . All content posted to the web site must maintain the copyright information line on the bottom of each image.

Posting licensed content on Electronic reserve: In addition to the above the following clauses are applicable: The web site must be password-protected and made available only to bona fide students registered on a relevant course. This permission is granted for 1 year only. You may obtain a new license for future website posting.

For journal authors: the following clauses are applicable in addition to the above: Permission granted is limited to the author accepted manuscript version* of your paper.

*Accepted Author Manuscript (AAM) Definition: An accepted author manuscript (AAM) is the author's version of the manuscript of an article that has been accepted for publication and which may include any author-incorporated changes suggested through the processes of submission processing, peer review, and editor-author communications. AAMs do not include other publisher value-added contributions such as copy-editing, formatting, technical enhancements and (if relevant) pagination.

You are not allowed to download and post the published journal article (whether PDF or HTML, proof or final version), nor may you scan the printed edition to create an electronic version. A hyper-text must be included to the Homepage of the journal from which you are licensing at http://www.sciencedirect.com/science/journal/xxxxx. As part of our normal production process, you will receive an e-mail notice when your article appears on Elsevier's online service ScienceDirect (www.sciencedirect.com). That e-mail will include the article's Digital Object Identifier (DOI). This number provides the electronic link to the published article and should be included in the posting of your personal version. We ask that you wait

until you receive this e-mail and have the DOI to do any posting.

Posting to a repository: Authors may post their AAM immediately to their employer's institutional repository for internal use only and may make their manuscript publically available after the journal-specific embargo period has ended.

Please also refer to Elsevier's Article Posting Policy for further information.

18. **For book authors** the following clauses are applicable in addition to the above: Authors are permitted to place a brief summary of their work online only.. You are not allowed to download and post the published electronic version of your chapter, nor may you scan the printed edition to create an electronic version. **Posting to a repository:** Authors are permitted to post a summary of their chapter only in their institution's repository.

20. **Thesis/Dissertation**: If your license is for use in a thesis/dissertation your thesis may be submitted to your institution in either print or electronic form. Should your thesis be published commercially, please reapply for permission. These requirements include permission for the Library and Archives of Canada to supply single copies, on demand, of the complete thesis and include permission for UMI to supply single copies, on demand, of the complete thesis. Should your thesis be published commercially, please reapply for permission.

Elsevier Open Access Terms and Conditions

Elsevier publishes Open Access articles in both its Open Access journals and via its Open Access articles option in subscription journals.

Authors publishing in an Open Access journal or who choose to make their article Open Access in an Elsevier subscription journal select one of the following Creative Commons user licenses, which define how a reader may reuse their work: Creative Commons Attribution License (CC BY), Creative Commons Attribution – Non Commercial - ShareAlike (CC BY NC SA) and Creative Commons Attribution – Non Commercial – No Derivatives (CC BY NC ND)

Terms & Conditions applicable to all Elsevier Open Access articles:

Any reuse of the article must not represent the author as endorsing the adaptation of the article nor should the article be modified in such a way as to damage the author's honour or reputation.

The author(s) must be appropriately credited.

If any part of the material to be used (for example, figures) has appeared in our publication with credit or acknowledgement to another source it is the responsibility of the user to ensure their reuse complies with the terms and conditions determined by the rights holder.

Additional Terms & Conditions applicable to each Creative Commons user license:

CC BY: You may distribute and copy the article, create extracts, abstracts, and other revised

versions, adaptations or derivative works of or from an article (such as a translation), to include in a collective work (such as an anthology), to text or data mine the article, including for commercial purposes without permission from Elsevier

CC BY NC SA: For non-commercial purposes you may distribute and copy the article, create extracts, abstracts and other revised versions, adaptations or derivative works of or from an article (such as a translation), to include in a collective work (such as an anthology), to text and data mine the article and license new adaptations or creations under identical terms without permission from Elsevier

CC BY NC ND: For non-commercial purposes you may distribute and copy the article and include it in a collective work (such as an anthology), provided you do not alter or modify the article, without permission from Elsevier

Any commercial reuse of Open Access articles published with a CC BY NC SA or CC BY NC ND license requires permission from Elsevier and will be subject to a fee.

Commercial reuse includes:

- Promotional purposes (advertising or marketing)

- Commercial exploitation (e.g. a product for sale or loan)

- Systematic distribution (for a fee or free of charge)

Please refer to Elsevier's Open Access Policy for further information.

21. **Other Conditions**:

v1.7

If you would like to pay for this license now, please remit this license along with your payment made payable to "COPYRIGHT CLEARANCE CENTER" otherwise you will be invoiced within 48 hours of the license date. Payment should be in the form of a check or money order referencing your account number and this invoice number 501352532. Once you receive your invoice for this order, you may pay your invoice by credit card. Please follow instructions provided at that time.

Make Payment To:
Copyright Clearance Center
Dept 001
P.O. Box 843006
Boston, MA 02284-3006

For suggestions or comments regarding this order, contact RightsLink Customer Support: customercare@copyright.com or +1-877-622-5543 (toll free in the US) or +1-978-646-2777.

Permission to reuse Figures from The Journal of the American Chemical Society, **2006**,

vol 128, 49, 15714-15721 (Figure at page 200 of the thesis)

Copyright Clearance Center · **RightsLink**®

ACS Publications
MOST TRUSTED. MOST CITED. MOST READ.

Title: New Benchmark for Water Photooxidation by Nanostructured α-Fe2O3 Films

Author: Andreas Kay, Ilkay Cesar, and, and Michael Grätzel*

Publication: Journal of the American Chemical Society

Publisher: American Chemical Society

Date: Dec 1, 2006

Copyright © 2006, American Chemical Society

Logged in as:
Federico Pesci
Account #:
3000811817

LOGOUT

PERMISSION/LICENSE IS GRANTED FOR YOUR ORDER AT NO CHARGE

This type of permission/license, instead of the standard Terms & Conditions, is sent to you because no fee is being charged for your order. Please note the following:

- Permission is granted for your request in both print and electronic formats, and translations.
- If figures and/or tables were requested, they may be adapted or used in part.
- Please print this page for your records and send a copy of it to your publisher/graduate school.
- Appropriate credit for the requested material should be given as follows: "Reprinted (adapted) with permission from (COMPLETE REFERENCE CITATION). Copyright (YEAR) American Chemical Society." Insert appropriate information in place of the capitalized words.
- One-time permission is granted only for the use specified in your request. No additional uses are granted (such as derivative works or other editions). For any other uses, please submit a new request.

If credit is given to another source for the material you requested, permission must be obtained from that source.

BACK · CLOSE WINDOW

16/07/2014 11:41